Effect of Axial Compression on Flexural Strength of Freshwater and Saline Ice

By

©Taha Anwar

A thesis submitted to the

School of Graduate Studies

in partial fulfillment of the requirements for the degree of

Master of Engineering

Faculty of Engineering and Applied Science

Memorial University of Newfoundland

May 2024

St. John's, Newfoundland and Labrador, Canada

Abstract

In the design of bridges, wind turbine towers, offshore structures and ice-class ships for operations in ice-prone regions, sloped structures may be employed to promote flexural failure of level ice to reduce loads on the structure. During such interactions, the ice sheet does not fail in pure bending since a component of the applied force at the sloped interface results in an axial load that induces a compressive stress in the ice. The net effect of this axial component is that the corresponding compressive stresses balance with flexure-induced tensile stresses in the outmost fibres of the ice. As a result, the apparent flexural strength of the ice is expected to increase with increasing axial compression, since larger bending forces would be required to generate sufficient tension to trigger fracture. In ice load prediction models for sloped structures, an in-plane compression (IPC) factor is applied to calculated loads to account for increased flexural strength which is empirically determined to be 1.5. While the method of superposition may be used to assess combined loading effects for elastic structures, assessing such effects in ice is more complex since the behaviour of ice is not purely elastic. The relationship between axial compression and the flexural strength of freshwater and saline ice is studied experimentally to assess how the flexural failure behaviour of the ice changes for different levels of in-plane compression factor. A series of experiments on freshwater ice have been conducted for compression levels at 75%, 135% and 185% of unconfined flexural strength for ram speeds of 0.1 mm/s, 1.0 mm/s and 10.0 mm/s. Compression levels tested for saline ice correspond to IPC of 35%, 70% and 125%. These results indicate that in-plane compression can significantly increase the apparent flexural strength of the ice, ranging anywhere from 50 to 300%. These results highlight the need for further work in this area to better understand this phenomenon and assess implications for design. This new testing approach provides a

promising direction for further examination of these important effects, including extending this work to larger beam sizes and different temperature ranges.

Acknowledgement

Completing my master's research program has been one of the most challenging endeavours I have undertaken in my life which would not have been possible on my own in the very least. Thus, I would like to mention all the great and wonderful people who helped make this research project a success.

First and foremost, I am extremely grateful to my master's supervisor, Dr. Rocky Taylor, whose relentless support, guidance and commitment from day one of the research program enabled me to accomplish this monumental task. His efforts in coordinating access to lab facilities, enhancing my learning experience through fieldwork and attending conferences and supporting me in pursuing an industrial internship abroad all made my program a very rewarding one. I am very thankful to have had him as my supervisor for my master's program through whom I have learned a lot.

Next, I would like to express my sincerest gratitude to NRC for their invaluable support in enabling me to complete my experimental program at their Cold Room facility. I want to especially thank Dr. Jungyong Wang at NRC who oversaw my research work there and offered very valuable input throughout the testing phase and later in data analysis and review of my written works. The testing would also not have been possible without Mr. Austin Bugden's assistance who made sure the lab was ready for my tests every day for more than 2 months straight. His broad experience with physical ice testing and his willingness to train me with lab equipment is greatly appreciated.

I would also like to thank C-CORE for allowing our research team to use their facilities for storage of sea ice samples until start of testing. I would like to acknowledge Mr. Jan Thijssen for his conceptualization of the research topic, Mr. Rob Pritchett for allowing us to use his equipment for

confinement frame, Mr. Soroosh Afzali for helping me with instrumentation selection and Mr. Andrew MacNeill for his encouragement.

At Memorial University, I want to mention my professors from my undergraduate degree: Dr. Geoff Rideout, Dr. Sam Nakhla, Dr. Ali Nasiri, Dr. Oscar DeSilva and Dr. Nana Baafour, who had the greatest impact on me by developing my keen interest in mechanical engineering and who were highly supportive during my pursuit of master's degree. I would also like to thank Mr. Dave Snook, Mr. Gordon Whelan and notably Mr. Simon Ernst from the Tech Services departments at Memorial University who were critical in keeping testing plan on track through their timely delivery of fabricated parts and modifications.

Funding from School of Graduate Studies, Memorial University; Hibernia Management and Development Company Ltd. (HMDC), Natural Sciences and Engineering Research Council of Canada (NSERC) and InnovateNL is duly acknowledged. I am also very thankful to the selection committee of Albert George Hatcher Memorial Scholarship who recognized my potential and chose me for this very prestigious award.

My friends in St. John's were like a second family to me thousands of miles away from home who were there for me through the highs and lows of the program. To Juanita Hennessey, Bahareh Haghighat, everyone else at the Internationalization Office, Adrian Dobre, Pritom Chakraborty, Victor Anyidoho and Mobin Abdolalipour I simply want to say thank you for all your support.

Last but most importantly, I want to dedicate my work to my beloved family. To my father, Dr. Muhammad Abaidullah Anwar who instilled in me the value of discipline and perseverance, to my mother, Rukhsana Anwar, who showed me unconditional love and support, to my sister Haleema, who encouraged me to go after things I want in life, to my younger sister Hajra, who taught me to

play hard after working hard and to my younger brother, Hasan, who is my best friend; you all are my favorite people and I would not be where I am today without you.

Contents

List of Tables

List of Figures

1. Introduction

1.1. Overview

Cold, offshore regions are gaining interest as future sites of economic development owing to potential for offshore windfarms for sustainable energy production [1] and new shipping routes emerging from reduced ice cover [2]. Hence the field of ice load calculation [3, 4], simulation [5, 6] and model testing [7] against sloped marine structures is receiving increased attention as sloped structures tend to result in lower ice loads than vertical ones [8]. The flexural strength of ice is a related research area of interest as it is a significant input parameter for models used to calculate loads against sloped structures [9].

Moving ice can impart significant loads on marine and offshore structures in ice-prone waters in Arctic and sub-Arctic regions. Typically for such structures, ice loads are a primary factor driving the structural design and design methodologies need to account for the effect of local ice pressure as well as global loads on the structure [8].

When the ice fails against a sloped structure, the maximum forces acting on the structure will be influenced by the strength of the ice which in turn is affected by factors such as thickness, speed, salinity, temperature and microstructure [10]. For level ice interactions, the failure mode of the ice against the sloped surface will be a combination of compressive and flexural failure modes. Ice may also fail along a shear plane at some angle relative to the vertical. Designs that can induce the flexural failure are generally favored since the ice fails more easily in this mode and correspondingly the ice can transmit less force to the structure when failing in flexure rather than in pure compression. When ice with a symmetric cross-section is undergoing downward flexure, the top half of the ice experiences tension while the bottom half experiences compression [11].

Due to the relatively low strength of ice under tensile conditions [10], the tension experienced by ice in flexure initiates the crack and eventually breaks up the ice sheet.

Sloped structures are designed to take advantage of lower flexural strength to promote break up and clearing of the ice [12]. During such interactions, in addition to inducing flexural stresses from the vertical component of the contact forces as shown by the vertical force (V) in Figure 1-1, the horizontal component of the contact force (H) also induces an axial compressive component of stress in the ice. The deflection of ice sheet is also illustrated as it rides up the slope as well as the weight of the ice sheet (W) and buoyancy force (B) acting on it through the center of gravity (Cg). Eccentric force (H) and vertical force (V) at the slope induce flexural moment in the ice sheet. Internal shear force (V_{int}), horizontal force (H_{int}) and reaction moment (M_R) also emerge at the free end of the ice sheet which are equal but opposite in direction to forces H and V and the induced moment, respectively. The waterline is represented by the dotted line.

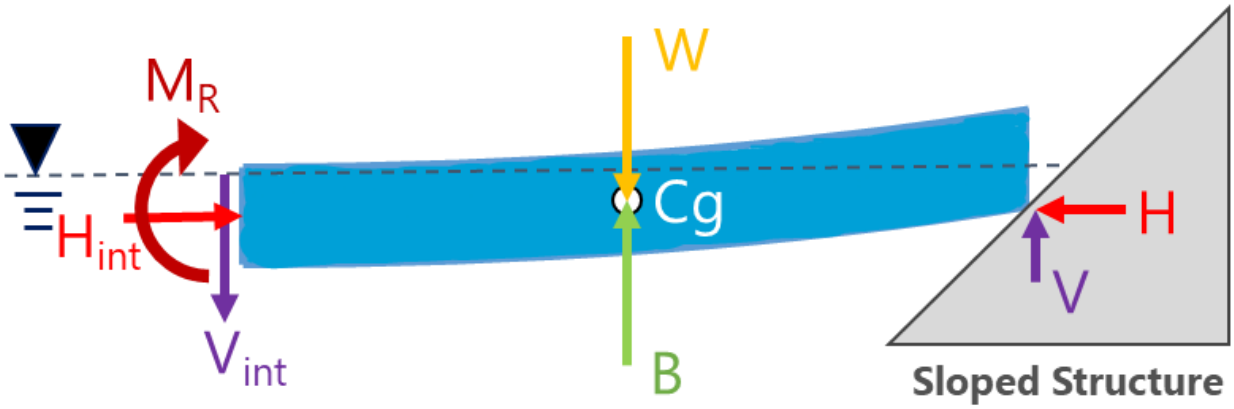

Figure 1-1 - Increase in flexural strength due to axial compression.

These in-plane compressive stresses counteract flexure-induced tensile stresses in the ice sheet, resulting in reduced net tensile stresses. Thus, the amount of bending force required to fail a beam will increase with an increase of axial confinement and it will result in potentially higher forces on

the structure [13]. The model developed by Ken and Croasdale [14] (referred to as the Croasdale model in subsequent sections) was developed for ice loads against sloped structures and accounts for this increase in strength using an in-plane compression factor which is empirically determined to be 1.5 [13]. This translates to total horizontal load increase of 50% on the structure.

1.2. Purpose

Much experimental work has been completed to characterize the flexural strength of ice. A recent study by Aly et al. [15] compiled 2,073 freshwater and 2,843 sea-ice beam bending test data from the literature between 1959 and 2017, with particular emphasis on scale effects on flexural strength. More region specific and full-scale tests have also been completed in recent years [9, 16, 17]. The tests include a wide variety of conditions such as 3-point and 4-point bending tests, in-situ and lab conditions, as well as large-scale and small-scale testing. It is noted that in all such tests, loading is in pure flexure and to date ice behaviour under combined axial and flexural loading have not been reported.

To address this gap, a series of experiments were conducted using lab-grown polycrystalline ice and naturally occurring sea-ice where ice beams were tested for flexural strength under axial compression.

The main objective of the research project was to study the effect of different levels of axial compression on the flexural strength of ice. The in-plane compression factor which is defined as the ratio of axially applied stress to the flexural strength of ice was varied from 1.0-3.0, where, at 1.0, there is no axial compression, all the way up to 3.0. This will help determine if the compression factor of 1.5 is appropriate for the ice load models or whether or not a higher or lower factor should be used. The upper limit of in-plane compression effect will also be determined.

The second objective of this project was to compare the in-plane compression effect for saline and freshwater ice. Sea ice samples were collected during a field program while the freshwater ice was grown in a laboratory using distilled, deaerated water.

The third objective was to observe the failure mechanism of ice samples under combined loading using high speed camera video recording to compare failure mechanism with those observed during simple flexural tests.

2. Literature Review

2.1. Sea Ice Formation

The following description of sea ice growth and first year ice is based on [8] which focuses on the Arctic region. Different ice growth stages and associated values have only been presented in this section as a reference to the general process. Region specific differences and variations should be accounted for ice load analysis and application.

Sea water unlike fresh water becomes denser as it gets closer to its freezing temperature for all water with salinity greater than 24.7 parts per thousand (ppt). Therefore, when upper layers of seawater are cooled, they sink lower due to higher density and achieve stability with lower layers. Next, the warmer and/or lower salinity water replaces the upper layers. This mixing process continues until top 10-20 m of sea has been cooled to the freezing temperature where freezing process is initiated. Seawater with salinity of 35 ppt has a freezing point of -1.8ºC.

If ambient air temperature remains at -1.8ºC or cooler, small ice crystals a few centimeters in length begin to appear and float to upper layers of the cooled seawater. This layer is called frazil ice. Then, a thin slush layer forms as these crystals are joined together which is called grease ice. This layer of ice acts to dampen small water waves. If conditions are favourable, ice rinds of solid ice form from the crystals coalescing which can be up to 5 cm thick. Wave action can break this ice into disc shaped pancake ice which can be 3 to 30 cm thick.

The next stage of ice that is formed is called young ice. Young ice is formed by pancake ice and remnants of rind ice freezing together into a 5-30 cm thick solid, stable layer. Outer edges of individual pancake ice may be visible as rings in the frozen layer. This layer has ice crystals that are 1 mm in diameter approximately. These crystals generally have random orientation but can

have a more regular orientation depending on formation conditions and this type of ice is called granular ice. As salt is completely rejected from the grains as the water freezes, the forming ice is pure. Brine, air and gas pockets may form in the ice as liquid and gas can get trapped in the layer. These brine pockets may combine to form brine channels running through the thickness of the ice-sheet. Brine volume of sea ice has a significant effect on its flexural strength.

2.1.1. First-year ice

First-year ice is defined as ice sheet that has only experienced a single season of growth and all of it melts away during the warm season. After a solid layer of ice has formed, the ice formation mechanism changes and continues down from the bottom surface. The ice growth starts off quickly but slows down as the ice gets thicker which has an insulating effect. This new layer is called secondary ice which has elongated crystals anywhere from 1-10 cm long or even longer. The long crystals form due to preferred direction of heat flux being vertical. Maximum amount of energy is removed from freezing in the vertical direction and thus the crystals grow downwards. In calm and/or waters with directional waves, the columnar crystals will have a preferred direction in the horizontal plane, however, if the ice drifts around and/or the water waves are very irregular, the columnar crystals will not have a preferred horizontal plane direction but will be horizontally isotropic. Thick first year ice can reach thicknesses of greater than 120 cm.

2.1.2. Sea Ice structure

Typical sea ice structure along the vertical direction is shown in Figure 2-1. There is snow cover at the top followed by snow-ice transition and then transition layer. Above the transition zone, the ice has granular structure as illustrated in the thin-section. Past the transition zone, is the columnar zone with large and elongated grains. In the transition zone, a mix of both columnar and granular grains can be observed. Brine drainage channels are also shown in the ice layer.

Figure 2-2 shows thin sections of sea ice sample taken from North-West Barents Sea. The large size of grains can be seen in horizontal cross-section in Figure 2-2a. The columnar shape along the vertical direction can be observed in Figure 2-2b.

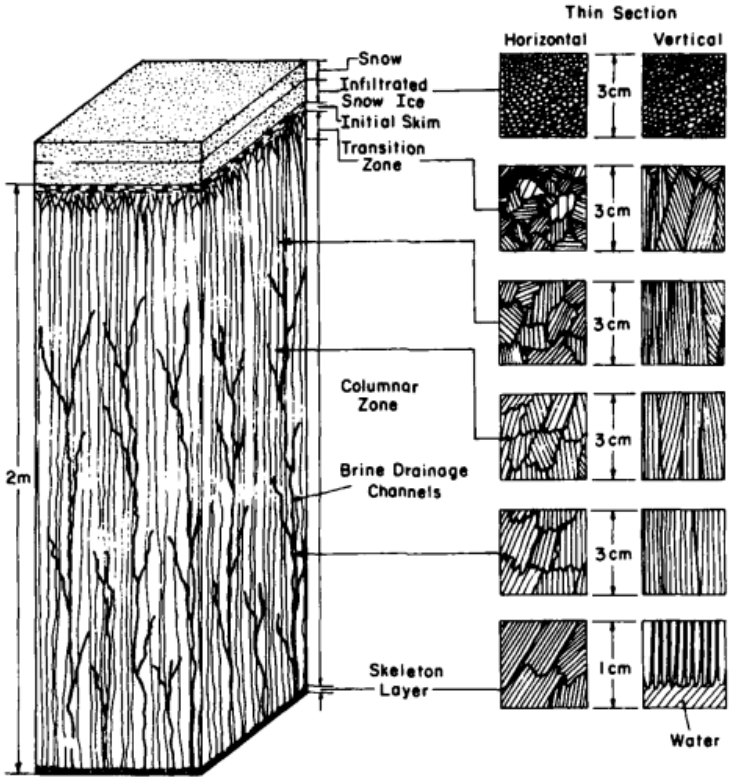

Figure 2-1 - Different layers of sea ice and their microstructure are shown for Greenland sea ice cover. Reproduced from [19].

Figure 2-2 - Thin sections of sea ice from North-West Barents Sea is shown (a.) is horizontal cross-section and (b.) is vertical. Reproduced from [9].

2.1.3. Temperature profile

During the winter months, the ice sheet has a linear temperature profile where the bottom of the ice sheet remains at the freezing temperature of sea ice which is -1.8ºC and the top layer may be at much colder temperature within 1.0ºC of ambient air temperature [10]. During warmer months, the temperature profile assumes a C-shape where the upper layers of the ice approach the warmer air temperatures [10].

One such evolution is shown in Figure 2-3 for fast ice off Zhongshan Station which is a Chinese research in Antarctica [20]. In November, sea ice has a linear temperature profile compared to depth. During the melting month of December, the characteristic C-shape is seen where top layer warms up above the freezing temperature. Similar changes in temperature profile are also provided by Carnat et. Al [21] and Johnston and Timco [22].

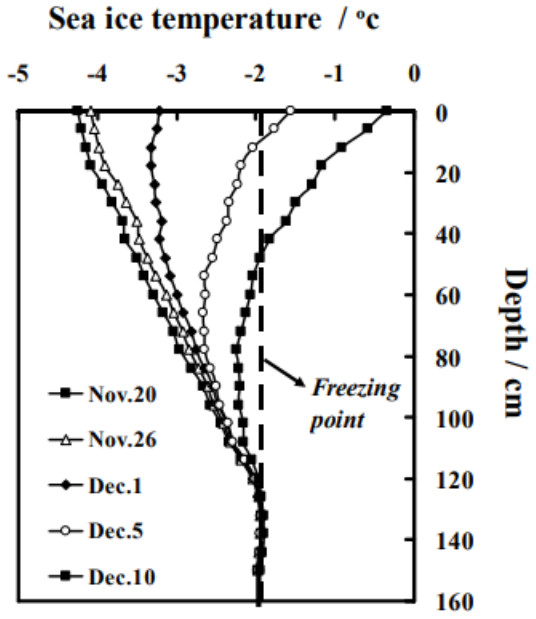

Figure 2-3 - Temperature profile changes from winter to warming season. Reproduced from [20].

2.2. Ice Loads on Sloped Structures

Sloped structures are of high interest for Engineering design since as they encourage ice failure in flexure compared to vertical walled structures where crushing failure dominates [23]. When a beam undergoes upward flexion, the lower fibers of ice experience tensile stresses while top ones experience compressive stresses. Given that ice is weaker in tension than in compression [24], and that flexural failure is triggered by tensile failure, lower ice loads are seen by the structure making sloped structures very attractive in offshore structural designs.

2.2.1. Croasdale Model

The Croasdale 3D model for ice load calculations is one of a number of models for calculating the load of ice sheet acting against sloping structures. This method is based on elastic beam bending theory and is one of the two models suggested by ISO 19906 for ice-sloped structure interaction calculations [25]. The various processes that the model accounts for as illustrated by [14] are shown in Figure 2-4. The figure has been modified from original source for simplicity.

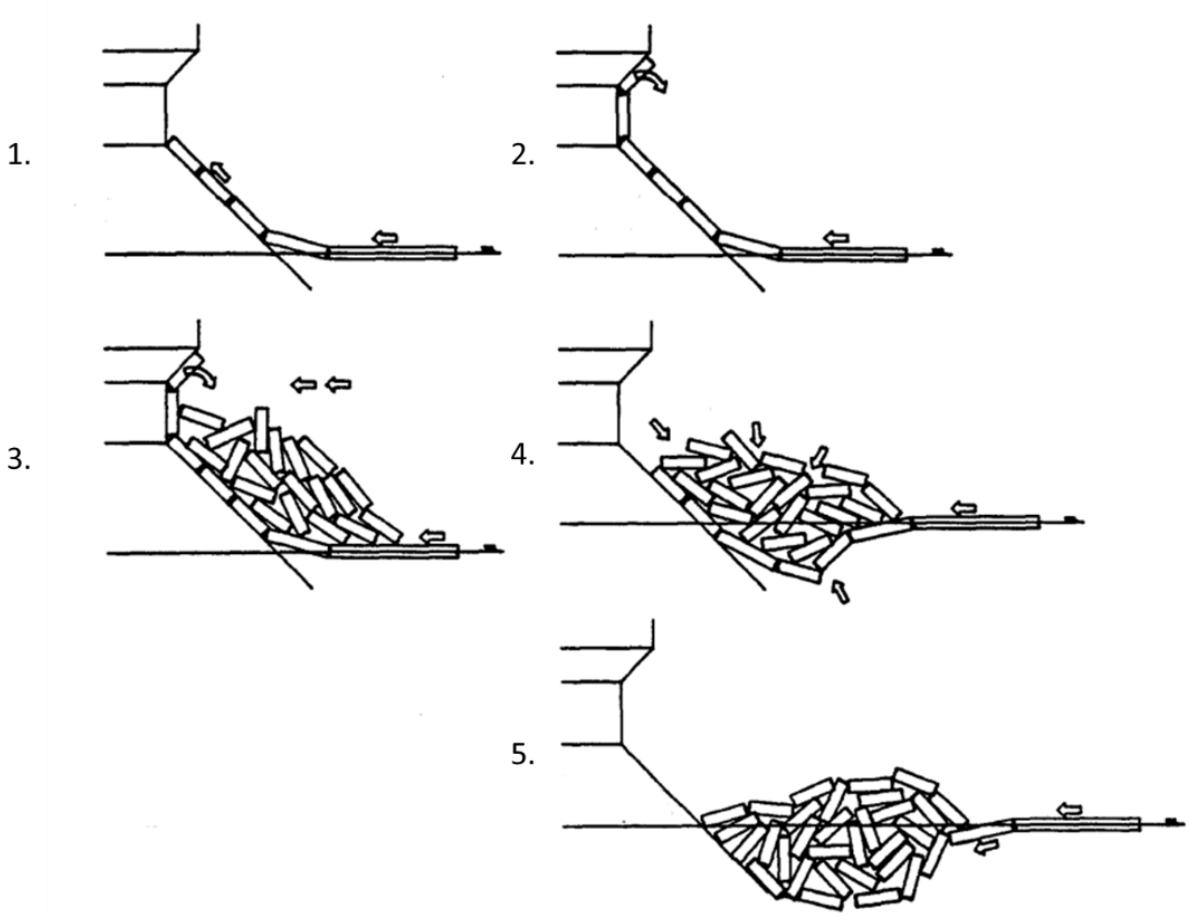

Figure 2-4 – Failure process of ice sheet against a sloped structure as presented by Croasdale's 3D model. Adapted from [14].

As shown in Figure 2-4, in stage 1, two processes are shown as ice rides up a slope. The first is larger ice piece breaking into small pieces due to bending failure, and second, pushing the smaller ice sections up the slope. In stage 2, the ice force rotates the pieces upright against the vertical portion of structures. In stage 3, the process of rubbling is shown. As ice is pushed up the vertical section, the ice pieces fall off and collect in front of the sloping structure the weight of which is initially supported by the ice sheet. The ice sheet pushes through this rubble and fails against the slope. In stage 4, the weight of the rubble breaks the ice sheet. In stage 5, for wide structures, the rubble remains in front of the slope and the approaching ice sheet now fails against the rubble

instead of the slope. For narrow structures, the rubble is usually cleared and process repeats from stage 1.

Based on these processes, the Croasdale model calculates five load components as follows:

- H_B, the breaking force for ice breaking in bending
- H_P, force for pushing the ice through the ice rubble
- H_R, the force needed to push ice blocks up the slope through ice rubble
- H_L, force for lifting the ice rubble on top of approaching ice sheet before failure
- H_T, force needed for turning ice blocks at top of the slope

The total load seen by the structure is sum of all these five components

$$H_{Total} = H_B + H_P + H_R + H_L + H_T \quad (1)$$

2.2.2. In-plane compression effect

In-plane compression effect is also incorporated into load calculations in the Croasdale model by multiplying the total load with a corrective factor I_p [26].

$$H_{Total} = (H_B + H_P + H_R + H_L + H_T)I_p \quad (2)$$

In-plane compression factor arises due to horizontal forces acting on the ice sheet by the slope. On an inclined slope, the resultant force on ice by the structure can be resolved into vertical and horizontal components as shown in Figure 2-5. The vertical force, V, acts to break the sheet in bending, however, the horizontal force, H, has a compressive effect on the ice sheet which reduces the tensile stresses in the ice sheet thereby making the ice stronger in flexure and exerting higher loads on the structure.

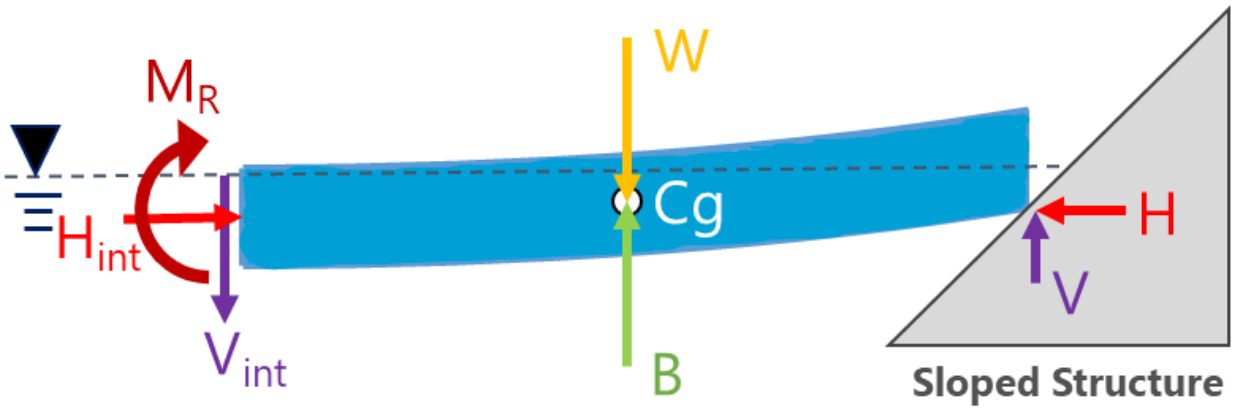

Figure 2-5 – Forces acting on the ice sheet from sloped structure.

The in-plane compression effect is shown in Figure 2-6. Assuming that ice is a homogenous and perfectly elastic material, in pure bending, the outermost fibers the of ice will have equal stresses in tension and compression [11]. The tensile stresses help fail the ice in flexure. Due to the compressive action of the horizontal forces, the combined loading results in the stress distribution changing where the total compressive stresses increase and the net tensile stresses decrease. Due to this decrease in maximum tensile stresses, the ice requires a higher applied force. This higher force requirement in turn translates into a higher apparent flexural strength.

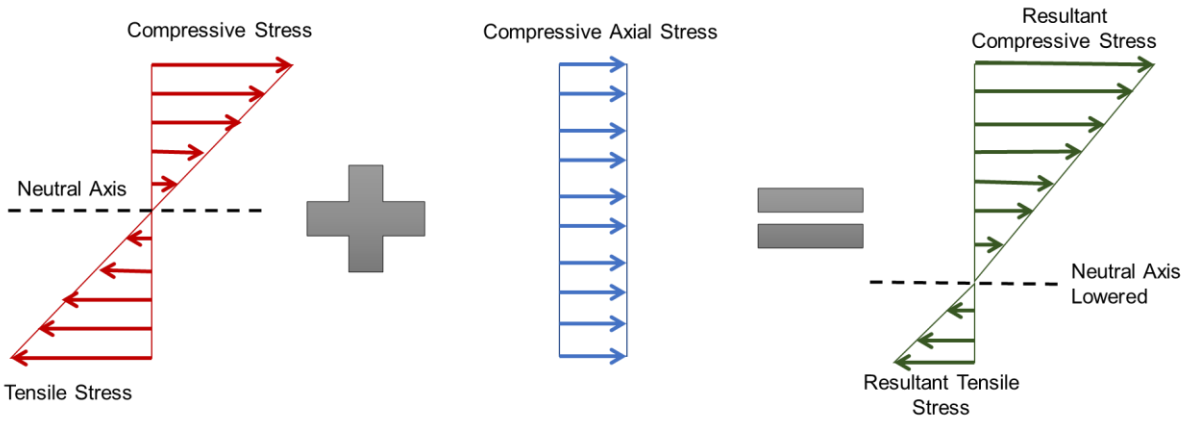

Figure 2-6 – Combined effect of stress distribution due to bending and axial compression.

The in-plane compression factor, I_p, is defined as ratio of increased flexural strength of ice due to compression, $\sigma_{f,compressed}$, to the nominal flexural strength of ice with no compression, $\sigma_{f,uncompressed}$.

$$I_p = \frac{\sigma_{f,compressed}}{\sigma_{f,uncompressed}} \quad (3)$$

In the Croasdale model, an I_p factor of 1.5 is used to account for increased flexural strength which has been derived empirically [26]. This implies the flexural strength of ice is 50% greater than nominal flexural strength when there are in-plane compression forces. A probabilistic assessment of level ice loads done using a Monte-Carlo type simulation based on the Croasdale model showed that I_p factor has a significant impact on the loads seen by the structure. For an I_p of 1.5, the load was 196% of when using I_p of 1.0 [13] emphasizing the need for accurate determination of the I_p factor to apply for load calculations.

2.3. Flexural Strength Testing

Flexural strength is seen as an index test rather than a material property of ice [10]. While ice is a viscoelastic material, it is assumed to be elastic and homogenous to apply elastic beam bending theory and use derived equations to calculate flexural strength [15]. Ice can be tested in-situ with cantilever tests or with simple beam tests with either 3- or 4-point loading. The 4-point test is preferred for beam tests as a zone of maximum moment develops between the indenters and the ice fails where it is the weakest [15] giving an accurate estimate of strength. An advantage of 4-poitnt bending is that the region of ice between the top indenters has constant bending moment and zero shear. Ice under 4-point symmetric flexural testing is shown in Figure 2-7.

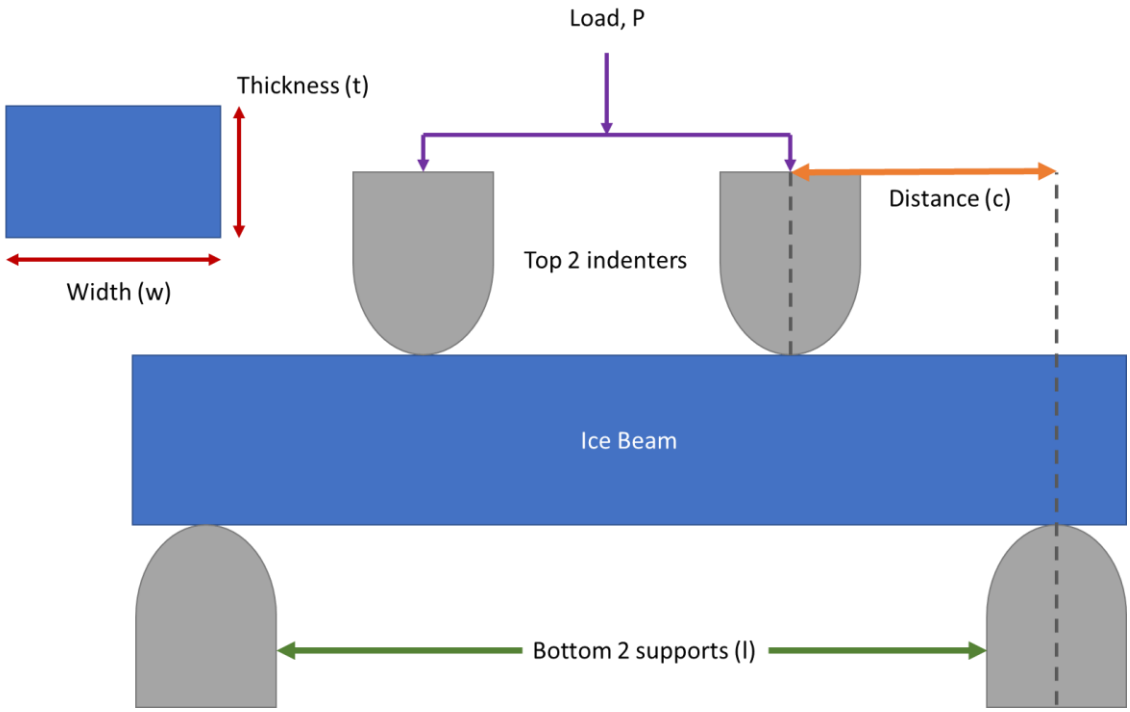

Figure 2-7 – 4-point symmetric bending test is shown for flexural strength measurement.

Bending strength is calculated using the following formula [27]:

$$\sigma_f = \frac{3Pc}{wt^2} \quad (4)$$

Where P is load applied to the beam by top indenters, c is distance between inner and outer indenter, w is width of ice beam and t is thickness of ice beam as shown in Figure 2-7.

For the sake of uniformity between flexural tests, Schwarz et al [27] recommends having beam length between seven to ten times that of thickness, beam width to be one to two times the beam thickness and beam width to be ten times the size of ice crystals for freshwater ice. The supports and indenters should also be rounded so as to not introduce stress concentrations and local indentations at points of load application [28].

2.4. Strength Tests to Study Axial Compression Effects

Flexural strength of both freshwater and saline ice is a widely researched topic as it is a significant input for calculating ice resistance of ships, ice forces on sloped structures, bearing capacity of ice cover, breakup of an oncoming ice sheet undergoing ridging, ice breakage of oncoming waves and other such ice load calculation models [9]. A recent study by Aly [15] compiled 2,073 freshwater and 2,843 sea-ice beam bending test data from the literatures between 1959 and 2017, with particular emphasis on scale effects on flexural strength. This work highlights the extensive number of flexural tests done for both saline and freshwater ice. More region specific and full-scale tests have also been completed in recent years [9, 16, 17]. These tests include a wide variety of conditions including 3-point and 4-point bending tests, in-situ and lab conditions, as well as large-scale and small-scale testing.

2.5. Factors Affecting Flexural Strength of Ice

Flexural strength of ice depends on factors such as temperature, loading direction, grain structure, grain size, test type (cantilever, 3-point and 4-point), loading rate, beam size and for saline ice, salinity and brine volume [31]. Some of these factors are well studied in the literature such as temperature, specimen size and brine volume while others have not been studied thoroughly since these details are often not reported by investigators [31]. The following sections look at effect of grain size, strain rate, temperature, brine volume and beam size on flexural strength of freshwater and saline ice.

2.5.1. Grain Size

One such factor is grain size which is the measure of size of individual crystals each with a specific orientation that exist in materials. For freshwater flexural strengths, under controlled conditions, it has been shown that ice with smaller grain size has higher flexural strength and the effect is

statistically significant [32, 24]. For ice crystals five times smaller than larger crystals, the increase in strength can be between 50 to 100 % [24]. However, ice grain structure can also influence the flexural strength of ice where structures with larger ice crystals can also have increased flexural strength due to a different failure mechanism [24].

For flexural strength of saline ice, apart from limited literature available, there is no consensus on whether the grain size is a significant factor. If flexural strength of saline ice for a given grain size is extrapolated to 0% brine volume, it is similar to flexural strength of freshwater ice of similar grain size [33]. This points to grain size controlling the strength, however, it is also argued that for saline ice, grain size has no appreciable effect on tensile strength [33].

Flexural strength of ice can be looked at as brittle failure in tension [17] as the failure originates in tensile fibers of the bending ice. In tension, strong tensile strength-grain size relationship is apparent for freshwater and glacial ice samples as shown in Figure 2-8 for different temperatures and strain rates [35].

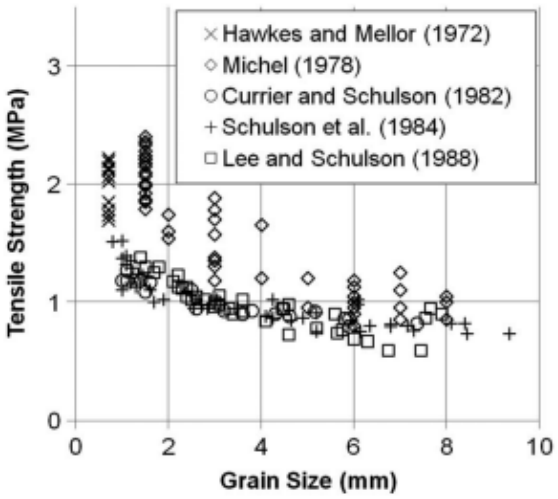

Figure 2-8 – Tensile strength – grain size relationship plotted for various sources of freshwater and glacial tests. Reproduced from [35].

Tensile strength increases as grain size decreases and this is due to existence of large number of grain boundaries compared to the number of dislocations that limit dislocation movement.

The relationship between flexural strength of sea ice and grain size is not well established due to complex ice structure. Nonetheless, it is important to maintain consistent grain size in testing to ensure grain size effects are controlled.

2.5.2. Strain Rate

Ice is considered to be an anisotropic, viscoelastic brittle material where stress is a time-dependent [36]. Therefore, mechanical properties of ice are affected by strain rate. The relationship between compressive strength and strain rate of both freshwater [37, 38, 39, 40] and saline ice [17, 41] have been well-studied in the literature. For low strain rates, the compressive strength increases with strain rate until it reaches a ductile to brittle transition strain that exists around 10^{-3} s^{-1} strain rate [42] as shown in Figure 2-9. Ice behaves in a ductile manner before this limit and in a brittle manner at higher strain rates. There is considerable randomness in ice behaviour at high strain rates beyond the transition limit. It is thought that ice either reaches maximum strength at transition strain value and then fails in brittle manner at higher strain rates and decreases in strength [38, 39]. Alternatively, it has also been noted from some conditions that ice continues to increase in strength or at least achieves plateau, failing in brittle manner, as strain rate is increased [38, 39]. Since dislocation movement in ice is linked to temperature and time-dependent processes, these mechanisms play an important role in strain rate and temperature dependent behaviour of ice. For a more detailed discussion of these phenomenon the reader is referred to Schulson and Duval [43].

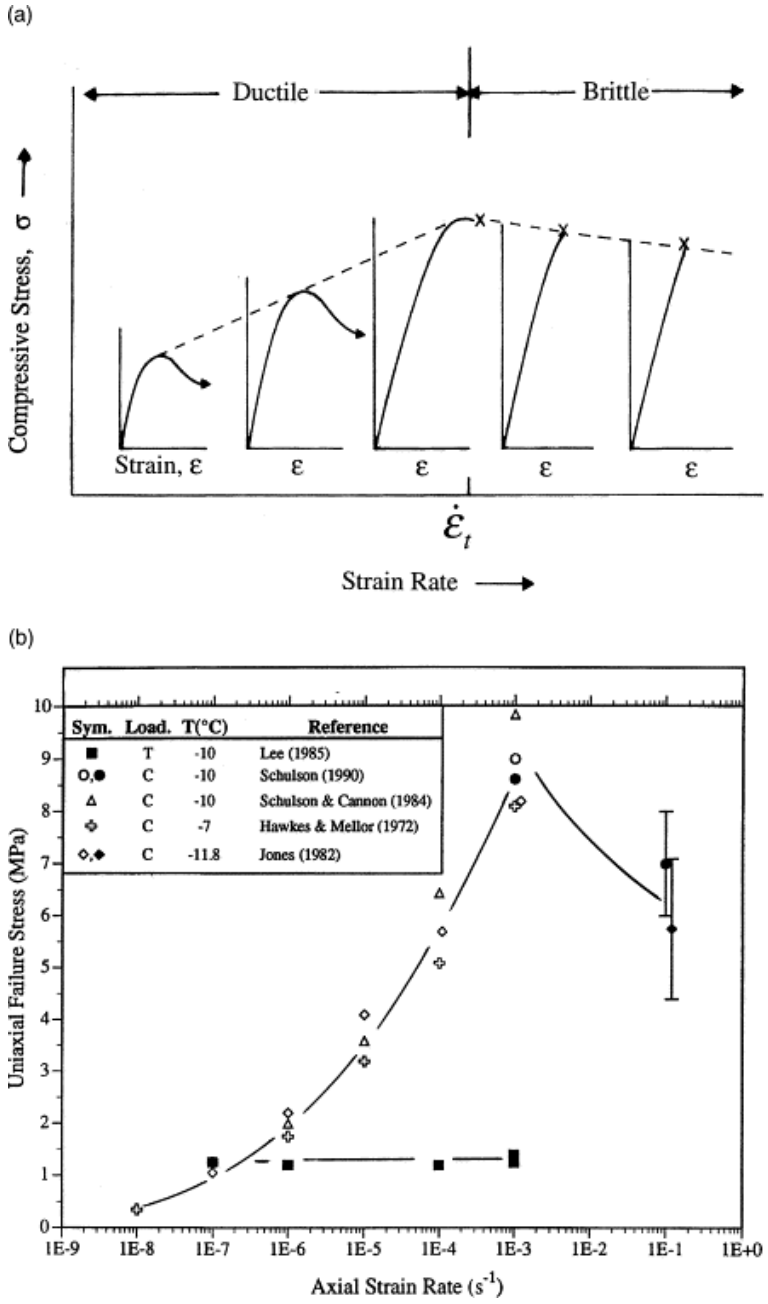

Figure 2-9 – (a.) Stress-strain profiles before and after ductile to brittle transition is illustrated for uniaxial compressive stress; (b.) Compressive stress relationship with strain rate is shown for tests by various researchers. Reproduced from [42].

As with grain size effect, the relationship between flexural strength and strain rate has not been studied extensively [44]. Presently there is no agreement on the flexural strength-strain rate effect, it is either believed that there is no such effect [10] or that the strength increases slightly at high

strain rates [44]. This is attributed to failure time being very short for practical applications and strength not being accurately measured if the sampling rate is too small [44].

Displacement can either be measured using sensors physically in contact with ice samples such as LVDTs and strain gauges which have an inherent disadvantage of introducing stress concentrations in the sample or using the displacement of indenters with the assumption that testing system is mechanically stiff enough to not influence the results [44]. The flexural strain rate is calculated using following equation derived from Timoshenko's Beam Bending Theory [45, 46]:

$$\dot{\epsilon} = \frac{hs}{\left(lc - \frac{4}{3}c^2\right)} \quad (5)$$

Where h is beam height, s is ram speed, l is distance between outer supports, c is distance between outer and inner support as illustrated in Figure 2-7.

Digital image correlation (DIC) is a new method by which strain can be more accurately determined from comparison of before and after images captured at high frame rates [47] and is a promising approach to better map the evolution of strain fields during experiments. Although such techniques could not be applied during in-situ tests and imaging of ice can present challenges due to low contrast differences between adjacent ice particles in a given specimen.

There are limited tests looking at flexural strength-strain rate relationship for ice types other than lab-grown freshwater. Depending on the accumulation temperature and testing temperature, the bending strength was seen to either increase or decrease with strain rate between the range 10^{-5} and 10^{-2} s^{-1} for atmospheric ice [34]. For iceberg ice tested at -11ºC, flexural strength was 26% stronger for lower strain rate 10^{-5} than 10^{-3} s^{-1} [45]. For first year sea ice at Tarsiut Island, no

relationship was observed although it could be attributed to very few number of tests conducted on the ice [48]. Two sets of sea ice testing gave inconclusive results about strain rate effect [41, 49]. Flexural strength increased with strain for cantilever beam tests but when inertial effects are subtracted, there was no apparent strain rate effect [41].

2.5.3. Temperature effects on flexural strength

Temperature is shown to affect flexural strength of both freshwater and saline ice as well and has been studied more thoroughly in literature. Closer to melting temperature, Ice behaves in a ductile manner and is prone to creep whereas at colder temperatures flexural strength increases and ice fails in a brittle fashion [36]. A very comprehensive compilation of flexural strength present in the literature was done by Timco and O'Brien for saline and freshwater ice [31]. The results showed that there was very large scatter in data for freshwater flexural strength at different temperatures and there was no clear relationship, however, the flexural strength of sea ice did increase with decreasing temperature as seen in Figure 2-10 [31].

For more recent tests, there is an evidence for both freshwater ice increasing in flexural strength as temperature is decreased [45, 50, 51] and flexural strength is not as affected by temperature [9, 52]. Flexural strength is observed to increase at a higher rate between 0 and -5 ºC and at a lower rate for lower temperatures [45]. Temperature gradient within the sample also tends to play a significant role in flexural strength of ice. Compared to isothermal samples, for ice samples with large temperature differences between top and bottom surfaces, flexural strength can decrease up to 55% [24]. Figure 2-11 shows Timco and O'Brien's original compilation plot and new testing of freshwater ice overlain on the plot to demonstrate the increasing flexural strength of freshwater ice with decreasing temperature relationship [51]. White ice refers to ice with high porosity giving it an opaque apparent while clear ice is more transparent.

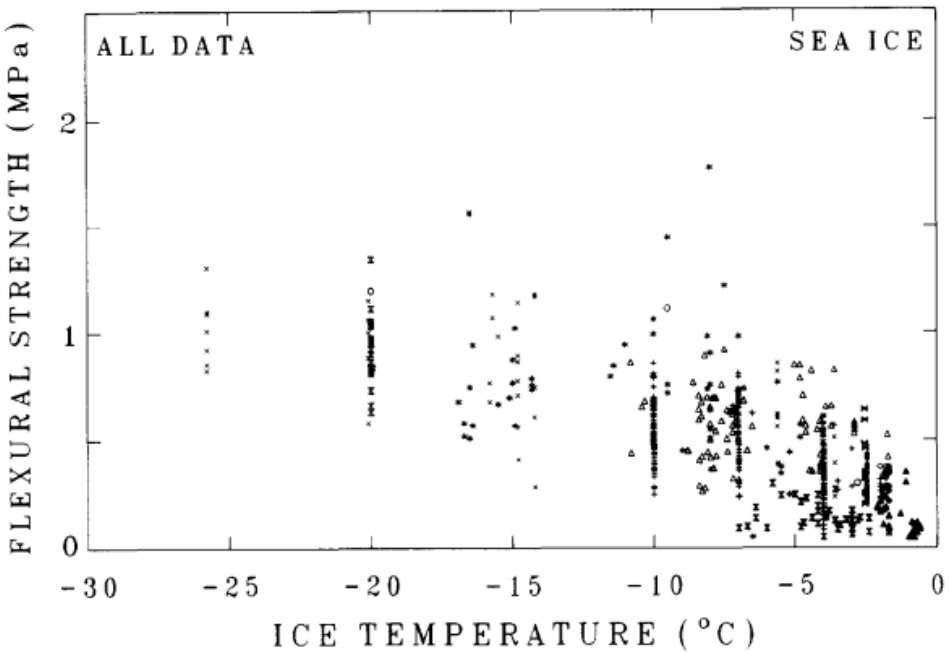

Figure 2-10 – Flexural strength data from various investigations plotted against temperature for sea ice. Reproduced from [31].

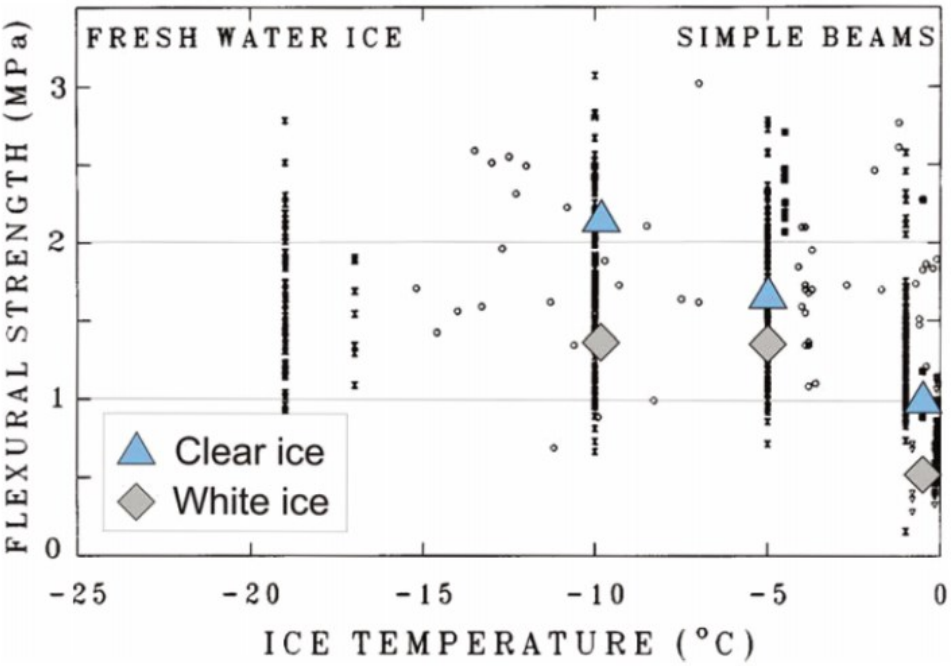

Figure 2-11 - Average flexural strength of tests done by [51] *plotted on by* [31]. *Reproduced from* [51].

2.5.4. Brine volume

Brine volume is one of the most commonly reported properties for saline ice as there is a very strong relationship between brine volumes and flexural strength. Timco and O'Brien's compilation of flexural strengths and their salinities is most comprehensive and used as a baseline for comparison in literature although the relationship should only be applied to first year sea-ice growing in winter season [31]. The relationship is as follows, where $\sqrt{v_b}$ is square root of brine-volume which is dependent on salinity and temperature:

$$\sigma_f = 1.76 \cdot e^{5.88\sqrt{v_b}} \qquad (6)$$

2.5.5. Beam Size

Scale effects have recently been established by Aly for both freshwater and saline ice where flexural strength is seen to decrease with increasing beam volume [55]. 2073 freshwater and 2843 sea-ice beam tests have been analyzed to determine relationships between flexural strength and relative volumes [55].

Plot of these results are provided in Figure 2-12. For saline ice, due to dependency on brine volume and temperature, all data has been normalized to a reference temperature of -10ºC and salinity of 5 ppt [55]. As seen in Figure 2-12, freshwater ice tends to be stronger than saline ice, however, it does start to converge at larger beam volumes for normalized data.

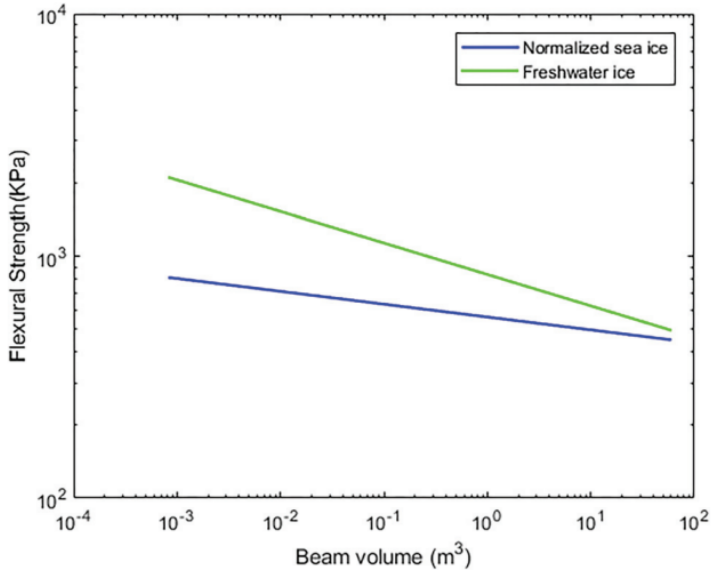

Figure 2-12 – Scale effects are demonstrated for freshwater ice and normalized sea ice. Reproduced from [55].

2.6. Flexural Strength Definitions

In this thesis three different forms of flexural strengths are discussed: simple flexural strength, apparent flexural strength and nominal flexural strength and they are defined as follows:

- Simple flexural strength – This is the form of flexural strength generally used in the literature where there is no axial compression (e.g. unconfined specimens). Simple flexural strength here has been defined as extreme stresses in the outermost fibres of the material undergoing flexural loading that cause tensile cracking. This stress is calculated using the elastic beam bending equation. While simple flexural strength is not a material property since, it is dependent on beam geometry, it is an important index value that is easy to model and measure. In the following chapters, flexural strength with no axial confinement has been referred to as simple flexural strength.

- Apparent flexural strength – Apparent flexural strength is the extreme stresses in the outermost fibers of an ice sample that is axially confined at the ends of the ice beam based solely on the elastic beam bending equation not accounting for axial compression effects. In the following chapters, when the term flexural strength is used for ice beams under compression, it refers to apparent flexural strength unless otherwise stated.
- Nominal flexural strength – Nominal flexural strength is similar to apparent flexural strength where the axial confinement stress is subtracted from the extreme stresses in the outermost fibers of the ice using the principle of superposition.

In Figure 2-13(a) the stress profile of an ice beam in flexural loading under axial compression is shown. The outermost fiber stress in this case ultimately determines the nominal flexural strength of ice beam. When axial stress component (b) is subtracted from (a) we get the stress profile shown in (c) and the extreme outermost fiber stress in this case is the apparent flexural strength.

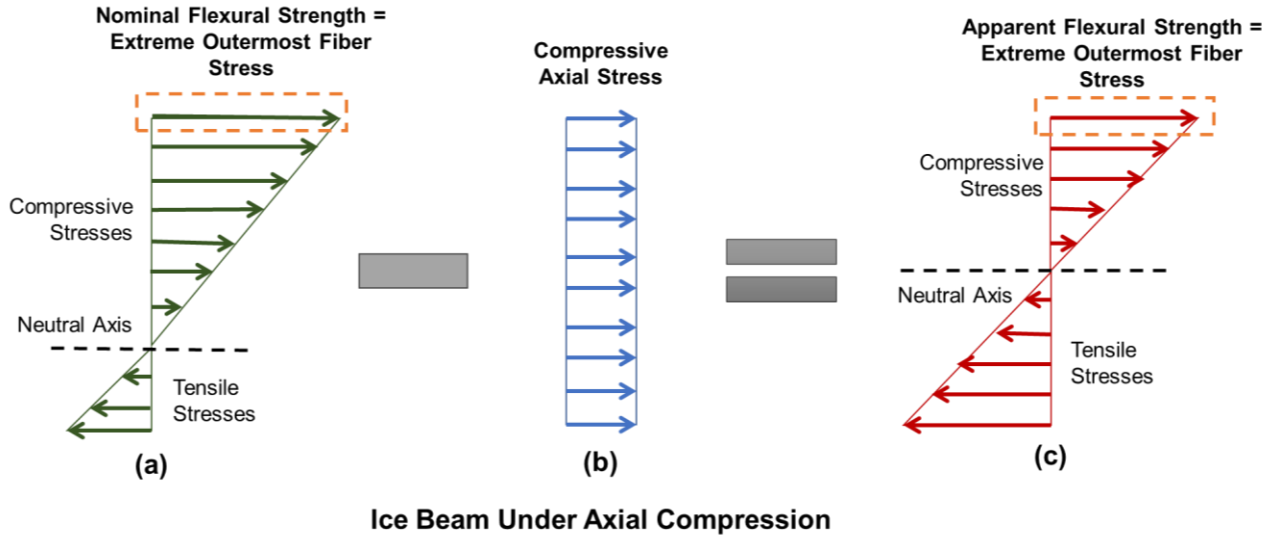

Figure 2-13 – Using principle of superposition to differentiate between nominal and apparent flexural strengths.

2.7. Summary

Flexural strength of ice is a significant input for many ice load calculation models including ones for sloped structures as it represents an index value of ice strength undergoing bending stressed. In the Croasdale model for ice loads against sloped structures, an in-plane compression factor is used to account for increase in flexural strength due to axial compressive forces. Empirically, this factor is set at 1.5 translating to 50% increase in flexural strength. Despite the large body of literature available on simple flexural test on ice, no publicly accessible data is available on flexural test under in-plane compression.

Ice is a naturally occurring geophysical material that is present as sea ice and its flexural strength depends on various factors such as grain size, temperature, brine volume for sea ice and size and speed of ice sheet. Ice flexural strength generally tends to increase as grain size increases and temperature and brine volume decrease. New tests to address these gaps in data and understanding for flexural strength under axial confinement are needed. The work presented in this thesis aim to help address these gaps.

3. Experimental Methodology

3.1. Scope

Despite the large amount of research focused on the characterization of flexural strength of ice under different conditions, to date, no work has been done to directly study the effect of axial compression on flexural strength of ice. Given the significance of in-plane compression effect and it's effect on ice load calculation using the Croasdale model for sloped structures, a novel testing method was devised and is presented in this chapter to study the effect of axial compression on flexural strength of ice. The effect of strain rate on flexural strength for different compressions was also analyzed.

For the apparatus, Boroojerdi [29] used a confinement frame for her shear test under confinement studies which was reused and modified for the purposes of the tests. Boroojerdi's set up is shown in Figure 3-1 and further details about adapting this frame for testing are given in section 3.6.

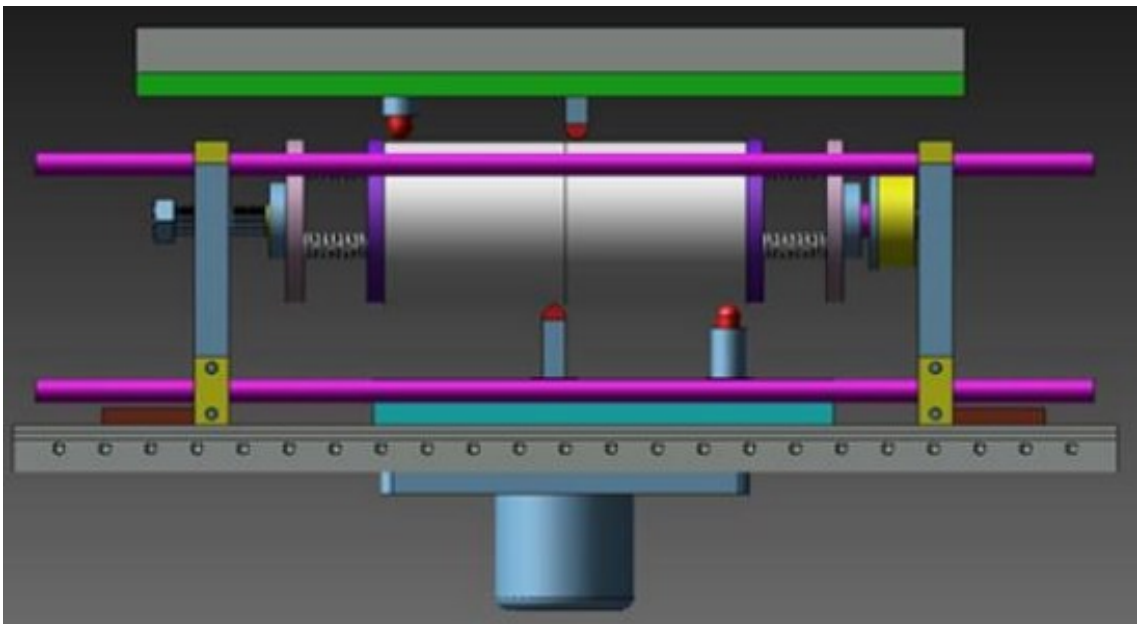

Figure 3-1 – Confinement frame used by Boroojerdi to apply axial pressure to cylindrical ice samples. Reproduced from [29].

3.2. Testing Sequence

In the first set of tests, simple 4-point bending tests were done on freshwater and saline ice beams to calculate their unconfined (simple) flexural strengths and compare them with values in literature. Tests were done for three different ram speeds: 0.1, 1.0 and 10.0 mm/s with at least three repetitions for both confined and unconfined tests.

The ram speeds translate into strain rates of 4.67×10^{-4}, 4.67×10^{-3} and 4.67×10^{-2} using the following equation taken from [45]:

$$strain\ rate = \frac{h \cdot s}{l \cdot c - \frac{4}{3}c^2} \quad (7)$$

Where h is the beam thickness, s is ram speed in mm/s, l is the distance between bottom supports and c is distance between bottom and top support as illustrated in Figure 2-7. All dimensions are in mm. In the remainder of this thesis, 4.67×10^{-4}, 4.67×10^{-3} and 4.67×10^{-2} strain rates are also referred to as lo (low), med (medium) and hi (high) for simplicity which has been summarized in *Table 3-1*.

Table 3-1 – Strain levels and associated strain values tested.

Strain level	**Strain Rates**
Low	4.67×10^{-4}
Medium	4.67×10^{-3}
High	4.67×10^{-2}

After determining the baseline unconfined (simple) flexural strengths for freshwater and saline ice, a percentage of the simple flexural strength value was applied as axial pressure for confined flexural strength. This was repeated for different confinement levels at the three strain rates. For freshwater ice, the in-plane compression confinement levels were 75%, 135% and 185%. For saline ice, the compression levels were 35%, 70% and 125%.

3.3. Freshwater Ice

The polycrystalline ice for freshwater flexural tests was made using the vacuum mold process as it offers the benefit of removing the air out of the ice mold and improves water flooding during preparation, resulting in very high-quality ice samples with few defects caused by presence of air bubbles. To make the ice sample, initially, ice cubes from an ice making machine were crushed into smaller pieces using an ice crusher which were then separated into different sizes using sieves. The grain size for the ice was chosen to be under 5 mm to ensure grain to beam width ratio remained more than 1:10 as the nominal width of the beam was 50.8 mm. Ice seed between U.S. sieve sizes #4 and #6 which have sieve openings of 4.75 mm and 3.35 mm respectively, were collected to populate the ice mold as shown in Figure 3-2a.

a. b. c.

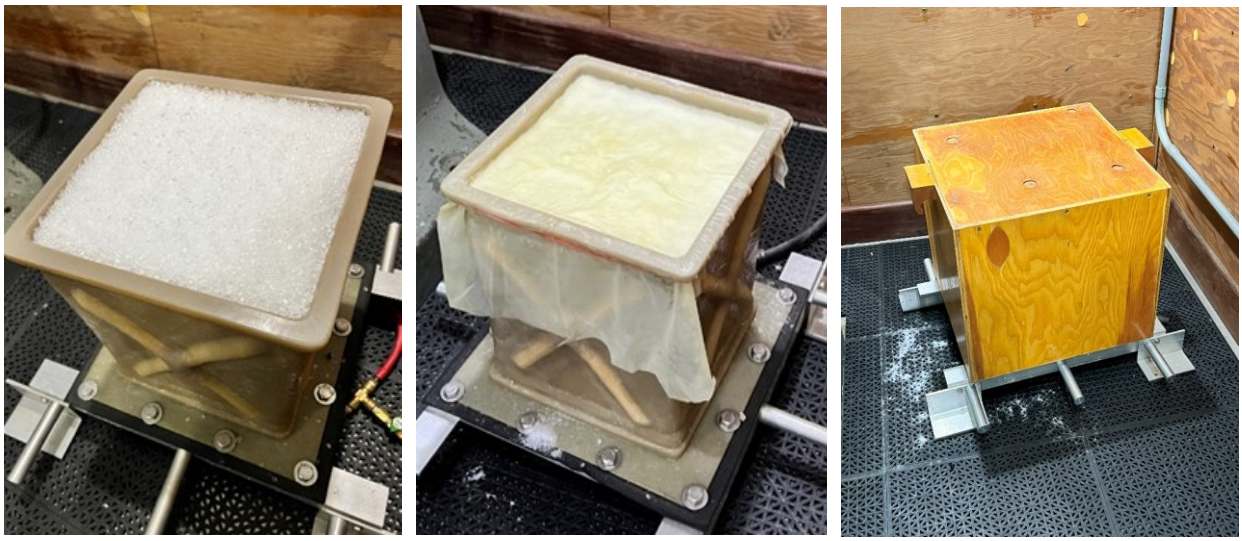

Figure 3-2 – (a.) Ice mold populated with crushed ice of desired grain size; (b.) Ice mold sealed to create a vacuum for water flooding; and (c.) mold covered in a box with insulating foam on the inside.

Once the mold was filled, the top opening was sealed using silicon grease and a rubber sheet as shown in b and a vacuum pump was connected to create negative pressure in the mold. Then, the mold was flooded with distilled, de-aerated water until the water reached the top of the mold and wetted the sheet at which point the water flow was cut off, vacuum pump disconnected, mold covered with an insulation box (c) and left to freeze in the cold room for several days with temperature maintained at -10 ºC. The insulated box is insulated on the four sides and top, with the bottom exposed to promote freezing from the bottom up to further promote air rejection and create bubble free specimens.

Once the ice block had solidified completely after 3-4 days of freezing, it was cut into multiple 25.4 mm thick slabs using a band saw. Each of these slabs were then further cut into beams with nominal length of 203 mm and width of 50.8 mm to be used for flexural testing. A sample of these beams is shown in Figure 3-3.

Figure 3-3 – Ice beams cut out of polycrystalline ice block made using the vacuum mold method.

3.4. Saline Ice

3.4.1. Saline ice sample collection

Saline ice cores were collected from a field work campaign completed on 6th April 2022 on landfast ice of Pistolet Bay located at the Northern tip of Newfoundland Island and a 5-minute drive from Town of Raleigh. The coordinates were approximately 51.549° N, 55.744° W. As seen in Figure 3-4 (taken from Google Maps) the site is less than 50 meters away from the Raleigh Harbor, which has a L-shaped wharf in the figure.

Figure 3-4 – Location of fieldwork site is shown by the red bubble. Source: Google Maps

This site was chosen by consulting a nautical chart of Pistolet Bay to ensure that frozen ice will not reach the seabed. Site with water depth between 1-2 meters was selected as, based on the Freezing Degree Days analysis of regional ice thickness, the ice was not expected to be deeper than 80 cm. Previous expeditions were also conducted around the same site between 2016 and

2019 where the local ice thicknesses ranged from 50 to 90 cm. Selecting a shallow water depth also has the added safety advantage of minimizing risk in case a person falls through as they can stand on the seafloor and be quickly brought to safety.

On the day of the field work and the day prior, the chosen site was scoped out on foot to make sure that the area was accessible and safe to work. A visual survey was done to make sure that the ice is stable and there are no visible deformities such as ridges and cracks. Thickness measurements were taken by coring ice using an ice auger, submerging the Kovacs ice thickness gauge into the cored hole and then tugging it upwards as shown in Figure 3-5. This flattens the T-bar which presses against the bottom of the ice sheet serving as the bottom reference. The thickness of ice sheet is measured using the attached measuring tape.

a. b.

Figure 3-5 – (a.) Kovacs ice thickness gauge; and (b.) ice thickness being measured using the gauge thickness.

After verifying that the ice was of sufficient thickness, ice cores were drilled using Kovacs ice corer as shown in Figure 3-6. The drilling was done with cordless drills and then manually with handlebars.

a. b.

Figure 3-6 – (a.) Kovacs ice corer; and (b.) corer being drilled into the ice sheet.

Ice cores were generally 800 mm in length which were cut into approximately 250 mm sections using a handsaw as shown in Figure 3-7. The 250 mm cores were stored in coolers where each core was separated from the other using bubble wrap so that the cores did not freeze together as seen in Figure 3-8. The cores were stored on their sides to help reduce brine drainage.

Figure 3-7 – Cores cut into smaller sections that can fit inside the cooler using a handsaw.

Figure 3-8 – Cores stored in the cooler separated by bubble wrap.

Once the sample collection was done, an additional core was extracted to determine the temperature profile by taking measurements at 100 mm intervals along the core. Air and sea water

temperatures were also taken. The coolers were then transported to an industrial freezer and left overnight. Then they were driven to Deer Lake airport the next day and flown to St. John's. In St. John's, the coolers were stored in C-CORE's reefer units set at temperature of -15 ºC and kept there until testing.

3.4.2. Saline ice sample preparation

In September 2022, the coolers with ice cores in them were moved from C-CORE's reefer unit to NRC's cold room both of which were maintained at -15 ºC. Each cylindrical core was cut into two prisms of nominal sizes 25x50x210 mm using a bandsaw. The ends of these prisms were milled after tempering to produce fine and parallel surfaces so that confinement force would be applied to the ends evenly and there would be no local loading. Some of the samples prepared for testing are shown in Figure 3-9. The long axis of the beams are parallel to direction of growth of ice sheet as shown in Figure 3-10.

Figure 3-9 – Saline ice prisms prepared for flexural testing.

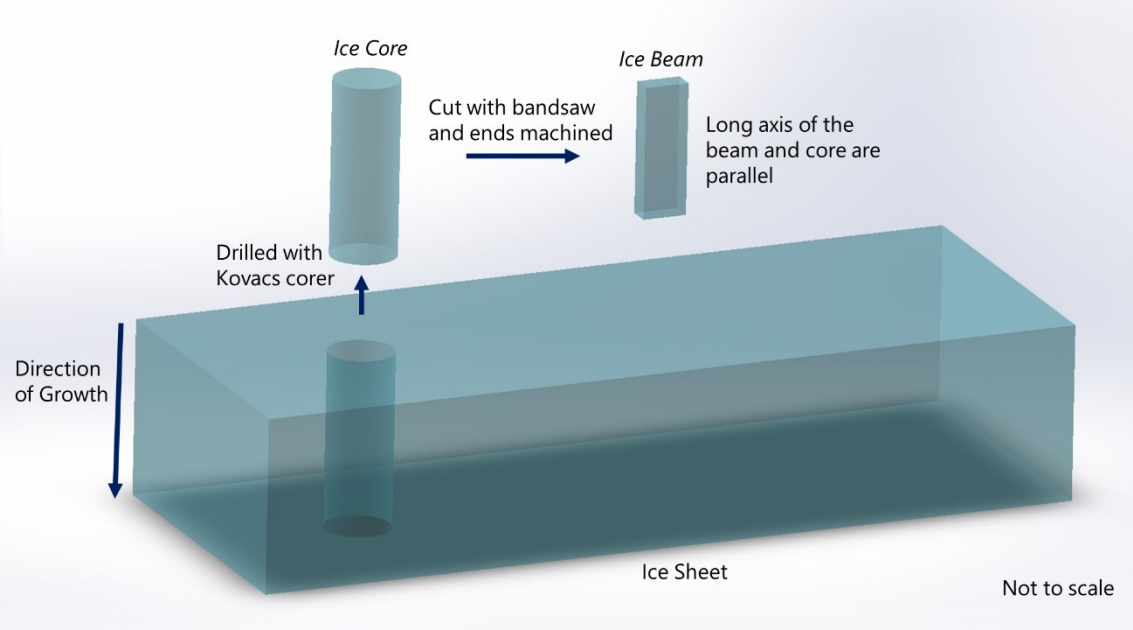

Figure 3-10 – Orientation of ice beams and cores relative to the ice sheet are shown.

3.4.3. Saline sample tempering

To ensure that sample temperature was same for both freshwater and saline ice, -10 ºC, a tempering process was used to bring the saline ice samples up to -10 ºC from -15 ºC. This was done by drilling a small hole to the center of the sample and measuring the time taken for the temperature to rise at the geometric center point of the ice prism immediately before being moved out of the -15 ºC room and into the MTS testing cold room set at -10 ºC.

Temperature was measured every 15 minutes until the center point temperature of -10 ºC was achieved. The total time taken for the equilibration was 70 minutes. Therefore, a tempering duration of at least 75 minutes was chosen for the samples before they were tested. Temperature readings at the start and end of the tempering are shown in Figure 3-11.

a.

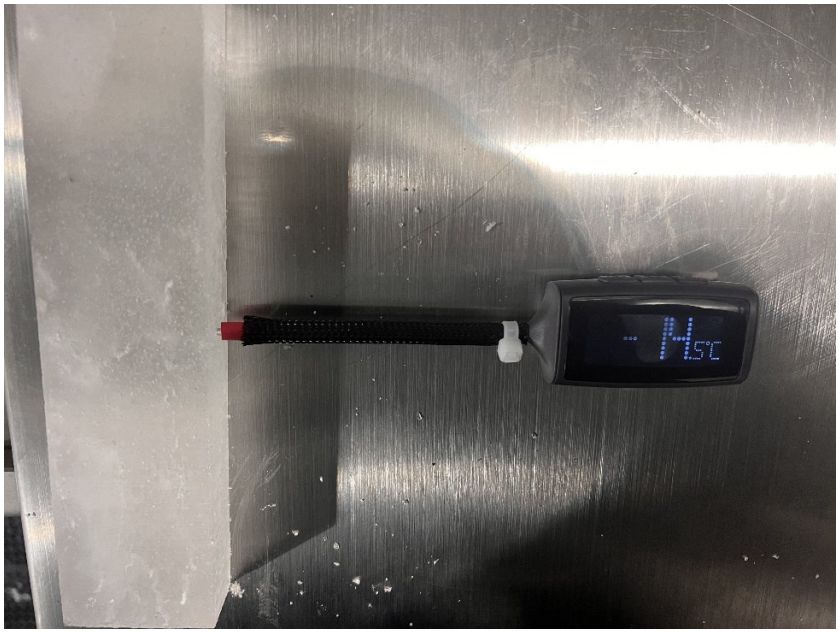

b.

Figure 3-11 – Centrepoint temperature of the sample before moving to -10 ºC room (a.) and temperature stabilized to -10 ºC (b.)

3.4.4. Salinity measurements

A YSI Pro 30 Salinity Meter was used to measure the salinity of saline ice samples. First, the meter's calibration was verified using calibration solutions of 1413 µS/cm and 35 ppt salinity.

Then, several thin discs were cut from the end of ice cores to be placed in sealed plastic bags and left overnight for the ice to melt and stabilize with room temperature.

The following day, salinity of each of these melted ice discs was measured by pouring the water in a graduated cylinder and submerging the salinity meter probe fully in the melted water. After ensuring the water temperature was same as room temperature (23 ºC), the salinity measurements were recorded. The graduated cylinder was washed multiple times with distilled water between each of the measurements so that any remaining salts from previous measurements did not affect the following ones. The complete set up is shown in Figure 3-12.

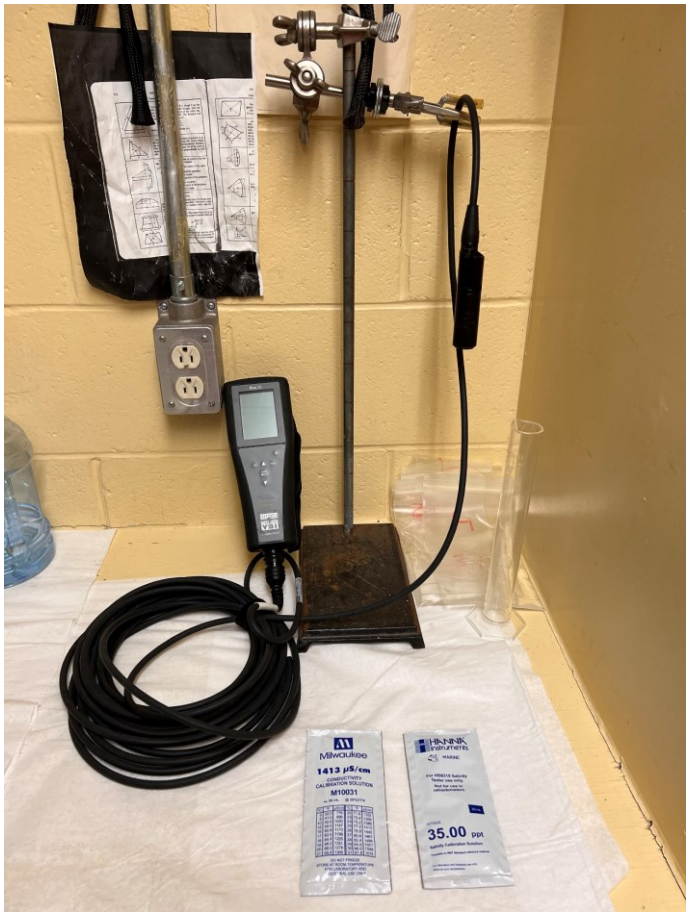

Figure 3-12 – Salinity measurement device connected to probe via a cable. The calibration solutions graduated cylinder and melted saline ice samples are also shown.

3.5. Microstructural analysis

Microstructural analysis of ice samples was done using a thin sectioning method [56]. The ice samples were taken as perpendicular cross-sections of the ice cores as illustrated in Figure 3-13. In this method, samples of ice are freeze welded onto glass slides that are heated up using a hot plate. When ice comes in contact with the warm slides, the ice melts cooling the glass and also leaving a layer of water between the unfrozen ice and glass. When left in a cold room after wiping off excess water, this melted water refreezes and adheres the ice sample to the glass.

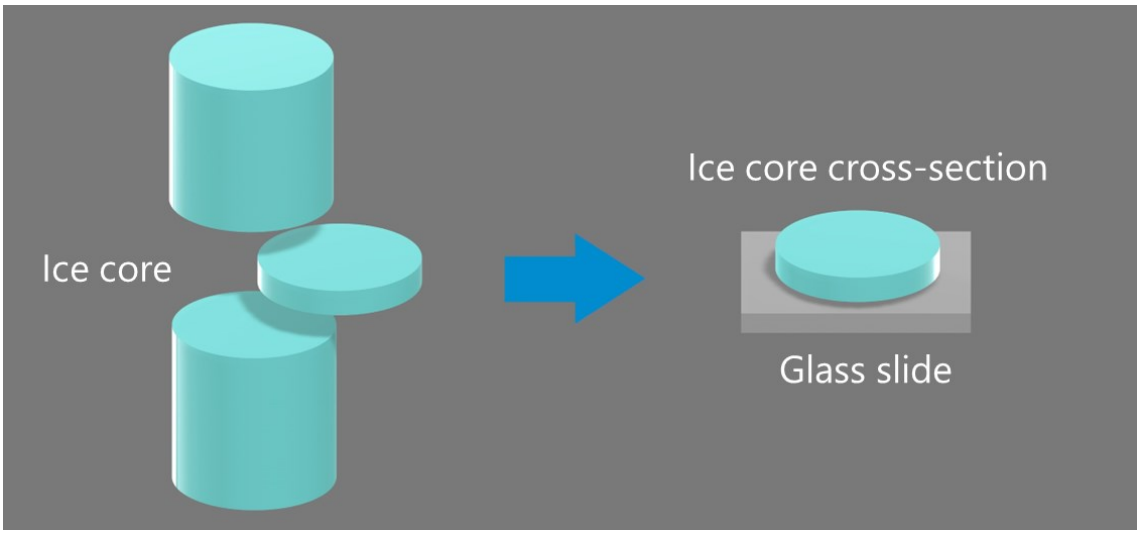

Figure 3-13 – Ice core cross-sections used for thin sectioning are shown.

This glass slide is then attached to Leitz 1400 Sledge Microtome on the specimen holder which is connected to an air pump creating negative pressure over the surface of the holder. When the slide is placed on the holder and air pump valve closed, the suction pressure keeps the slide fixed to the holder. The setup is shown in Figure 3-14a.

This allowed the sample to be easily moved back and forth with the sledge. By aligning the top surface of the sample right under the microtone blade and selecting a thickness increment, a small layer of ice is shaved off by the blade each time the sledge is pulled back and forth. The microtome

sledge elevation raises automatically by the selected increment upon completion of each stroke of the cutting process, resulting in a method that progressively reduces the thickness of the thin section until the desired thickness is achieved which is usually between 0.5 and 1 mm. The prepared thin section is then removed from the microtome stage and placed in a viewing box with polarized back light to observe and photograph the grain structure as shown in Figure 3-14b. Thin-sections prepared for freshwater and saline ice are given in Sections 4.2 and 5.1.3, respectively.

a. b.

Figure 3-14 – (a.) Microtome setup; and (b.) grain structure of saline ice.

3.6. Testing Apparatus

Testing was done in the MTS machine located in the cold room at National Research Council (NRC) facility in St. John's, NL. The testing temperature was selected to be -10 ^{o}C for all tests. A specially designed compression frame was used that allowed placement of ice samples on two indenters while axial load was applied on either end through discs attached to springs. The springs allow for compliance so that pressure is applied evenly across the surface and to minimize creep relaxation in the ice. The compression frame rested on an aluminum plate and was held in place using screws which were attached to the bottom crosshead of the MTS machine. A loadcell was installed between the end plate of the compression frame and the disc to measure the axial load applied to the ice sample. Different amounts of axial loading were applied to the sample via the threaded rod where one end was connected to the compression discs and other had a nut welded onto it where a torque converter was be attached. Torque was delivered to the torque converter by a cordless Makita drill.

The upper section of the bending test apparatus had two LVDTs and two supports on a dovetail connection and was connected to the MTS crosshead by a pivot joint. The pivot joint was used to ensure that when the flexural load was applied, the plate could rotate so that both top bending supports were fully seated on the ice sample and apply load evenly. A loadcell was installed between the pivot joint housing and the MTS top crosshead to measure the flexural load. Regular and high speed videos were also recorded to study the physical behaviour of ice beams in testing.

The complete set up is shown in Figure 3-15 followed by a close view of an ice sample fully loaded axially and indenters preloaded right before initiating the flexural test in Figure 3-16.

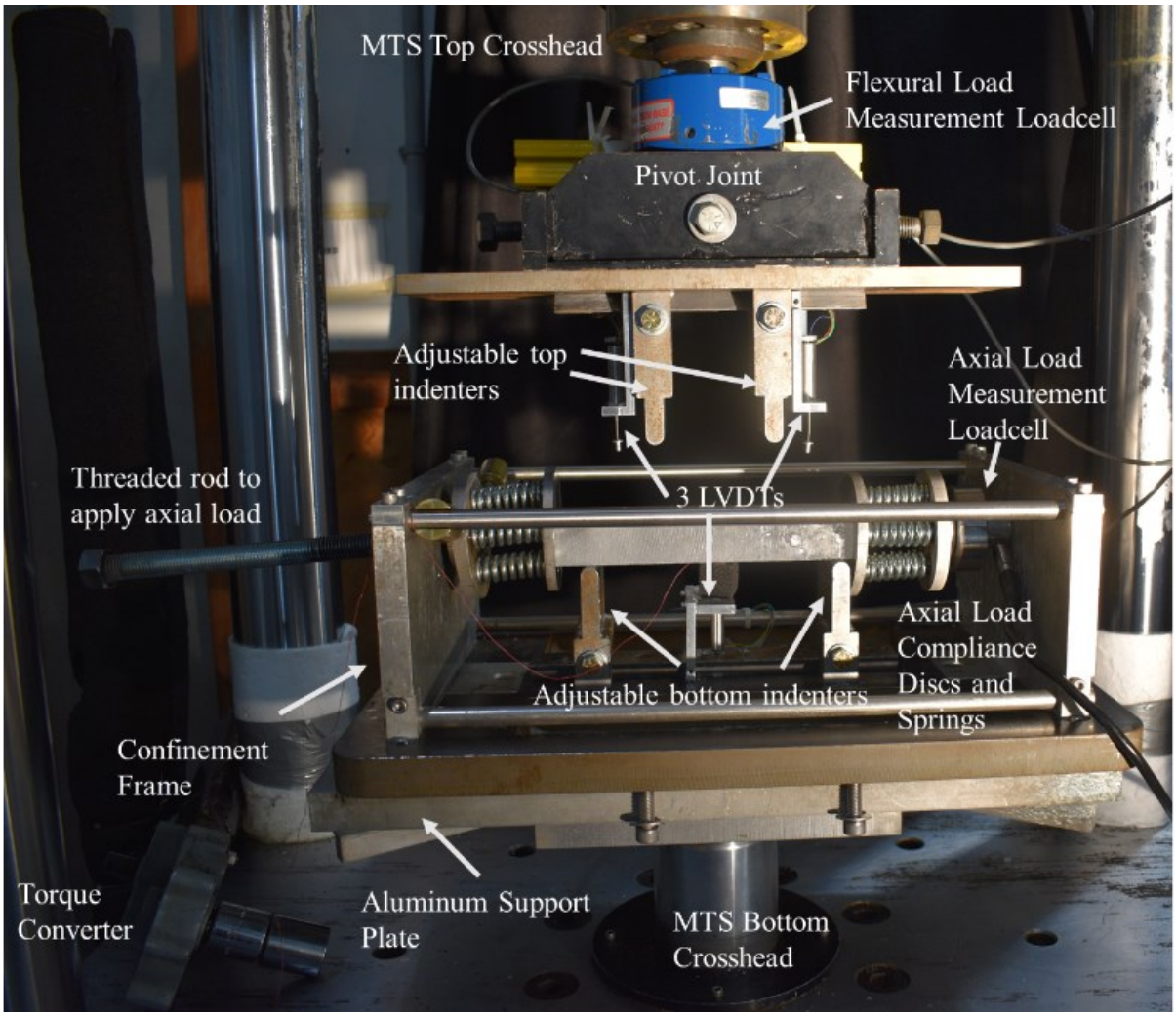

Figure 3-15 – 4-point bending test setup with axial compression frame installed in the MTS machine.

Figure 3-16 – Ice sample preloaded by indenters and axially loaded by plates and springs.

3.7. Sample loading

For confined flexural tests, first the sample was placed on the supports and then, an axial load was applied with the drill and torque converter corresponding to the desired compression level. Next, the bottom crosshead was slowly raised until load was sensed in the flexural strength loadcell when the top indenters contacted the sample. Each sample was pre-loaded up to 50-100 N before the flexural test commenced to make sure that both indenters were firmly contacting the sample and there was no give in the upper plate. The distance between top indenters was selected to be 82.5 mm while for the bottom indenters it was 178 mm to ensure that there was enough overhang of the ice sample on either side of the indenters where axial loading could be applied by the discs without physically interfering with the indenters or LVDT mounts. Samples were loaded in bending until complete failure. All data was collected using the NRC in-house DAQ system to which all the load cells and LVDTs were connected. Data was collected at a sampling frequency of 5k Hz and all channels had analog filtering at 1 kHz. LVDTs had an inherent 250 Hz filter. Data was also recorded and stored on a computer by the MTS system for flexural load values and displacement for data redundancy.

To ensure axial load was applied to end of the beams and to minimize the possibility of any moments being applied, following steps were taken:

- Ends of the ice beams were milled to obtain perpendicular surfaces to the axis of ice beams
- The springs used between the platens in the apparatus were of equal lengths and spring constants. The springs were also uniformly distributed between the platens.
- Through visual inspection, it was ensured that the sample was seated on both indenters (e.g. no gap or light was visible between the contact points and the sample) and that the platens were perpendicular to the beam after the sample had been axially loaded.

4. Confined Freshwater Ice Four-Point Beam Tests

4.1. Apparent Flexural Strength Test Results

In total, 56 flexural strength tests were completed for the freshwater series. Test data with all the measured variables are provided in Table 4-1. The peak values from flexural load cell during testing was used to calculate the apparent flexural strength (extreme fiber stresses) with the standard equation derived from beam bending theory without adjusting for confinement stresses [11]:

$$\sigma_f = \frac{3p(l-c)}{2wt^2} \quad (8)$$

Where p is peak load, l is distance between bottom supports, c is distance between top supports, w is width of the beam and t is the thickness as shown in Figure 2-7.

Table 4-1 – Raw data for apparent flexural strength of freshwater ice tests.

Target Compression %	Strain Rate	Index #	Test #	Failure Time [s]	Flexural Strength [MPa]	MTS Displacement [mm]	Right LVDT [mm]	Left LVDT [mm]	Center LVDT [mm]	Compressive Stress [MPa]	Measured Compression %
0	$4.67x10^{-4}$ (Low)	1	7	1.401	1.631	0.140	0.027	0.045	0.099	-	-
		2	8	3.258	1.752	0.328	0.088	0.059	0.134	-	-
		3	9	1.358	1.420	0.138	0.066	0.050	0.062	-	-
		4	14	1.452	1.688	0.142	0.033	0.040	0.103	-	-
		5	15	1.370	1.631	0.138	0.032	0.035	0.096	-	-
	$4.67x10^{-3}$ (Medium)	6	4	0.164	1.451	0.162	0.067	0.032	0.086	-	-
		7	5	0.137	1.676	0.130	0.032	0.035	0.101	-	-
		8	6	0.188	1.754	0.188	0.032	0.035	0.156	-	-
		9	12	0.165	1.752	0.164	0.038	0.037	0.109	-	-
		10	13	0.232	1.620	0.227	0.222	0.000	0.125	-	-
	Continued on next page										

Target Compression %	Strain Rate	Index #	Test #	Failure Time [s]	Flexural Strength [MPa]	MTS Displacement [mm]	Right LVDT [mm]	Left LVDT [mm]	Center LVDT [mm]	Compressive Stress [MPa]	Measured Compression %
	Continuing from previous page										
0	$4.67x10^{-2}$ (High)	11	1	0.021	1.866	0.154	0.038	0.048	0.133	-	-
		12	2	0.019	1.240	0.136	0.100	0.060	0.076	-	-
		13	3	0.025	1.794	0.191	0.056	0.051	0.139	-	-
		14	10	0.018	1.664	0.118	0.042	0.038	0.064	-	-
		15	11	0.023	1.815	0.176	0.067	0.053	0.096	-	-
		16	16	0.021	1.668	0.170	0.044	0.066	0.128	-	-
75	$4.67x10^{-4}$ (Low)	17	37	44.601	6.248	4.458	2.902	2.184	3.604	1.247	71
		18	45	51.197	5.471	5.123	2.881	2.689	9.586	1.210	69
		19	46	42.813	5.876	4.278	2.732	2.626	6.838	1.279	73
		20	47	45.665	5.636	4.566	2.571	2.746	6.817	1.252	71
	$4.67x10^{-3}$ (Medium)	21	38	1.735	5.260	1.727	0.977	0.916	0.154	1.316	75
		22	39	1.895	4.840	1.892	0.965	0.947	1.513	1.260	72
		23	40	1.452	4.799	1.444	0.834	0.829	0.310	1.274	72
		24	48	1.885	4.736	1.877	1.127	1.116	3.279	1.260	71
		25	50	2.506	4.678	2.506	1.357	1.309	3.994	1.260	72
		26	51	1.506	4.698	1.500	0.789	0.869	1.817	1.268	72
	$4.67x10^{-2}$ (High)	27	41	0.112	3.951	1.077	0.652	0.606	0.039	1.314	75
		28	42	0.112	4.121	1.083	0.715	0.649	0.214	1.362	77
		29	43	0.132	3.806	1.275	0.572	0.567	0.022	1.335	76
		30	52	0.120	4.142	1.148	0.603	0.782	1.213	1.287	73
		31	53	0.087	3.459	0.819	0.502	0.430	0.919	1.316	75
		32	54	0.170	3.208	1.650	1.620	0.177	1.398	1.255	71
135	$4.67x10^{-4}$ (Low)	33	17	39.838	6.130	3.986	1.593	1.491	5.995	2.232	127
		34	18	31.456	7.176	3.147	1.376	1.512	4.532	2.422	138
		35	19	32.279	6.702	3.224	1.367	1.459	4.979	2.208	125
		36	30	31.156	4.998	3.122	1.682	2.428	4.567	2.440	139
		37	32	37.795	5.836	3.777	2.486	2.234	5.408	2.117	120
		38	33	39.285	4.955	3.931	2.318	2.613	5.474	2.355	134
		39	34	41.120	5.732	4.114	2.690	2.450	5.684	2.312	131
		40	35	47.796	6.044	4.785	3.136	2.718	6.367	2.339	133
	Continued on next page										

Target Compression %	Strain Rate	Index #	Test #	Failure Time [s]	Flexural Strength [MPa]	MTS Displacement [mm]	Right LVDT [mm]	Left LVDT [mm]	Center LVDT [mm]	Compressive Stress [MPa]	Measured Compression %
Continuing from previous page											
135	$4.67x10^{-3}$ (Medium)	41	20	3.858	5.454	3.860	1.512	1.595	4.270	2.347	133
		42	21	1.761	5.335	1.754	0.705	0.995	1.889	2.395	136
		43	22	1.825	6.052	1.823	1.113	1.171	2.572	2.478	141
		44	23	1.941	5.852	1.940	1.222	1.181	0.823	2.462	140
		45	24	2.500	6.797	2.500	1.221	2.258	3.093	1.864	106
	$4.67x10^{-2}$ (High)	46	25	0.248	5.180	2.427	3.391	0.176	0.228	2.464	140
		47	26	0.124	5.394	1.190	0.722	0.892	0.203	2.472	140
		48	27	0.073	4.862	0.683	0.252	0.460	-0.005	2.288	130
		49	28	0.074	6.051	0.701	0.220	0.340	0.000	2.336	133
		50	29	0.115	6.473	1.095	0.573	0.699	0.227	2.702	153
185	$4.67x10^{-4}$ (Low)	51	69	36.445	2.809	3.647	3.046	2.105	3.475	3.292	187
		52	70	16.920	3.439	1.695	1.260	0.881	1.609	3.340	190
	$4.67x10^{-3}$ (Medium)	53	64	1.807	5.410	1.806	0.956	0.775	1.125	3.241	184
		54	65	2.456	5.293	2.459	1.968	1.239	1.761	3.180	180
	$4.67x10^{-2}$ (High)	55	66	0.136	5.605	1.322	0.351	0.448	1.082	3.319	188
		56	68	0.160	5.350	1.553	1.067	0.613	1.078	3.410	194

4.2. Microstructure

Figure 4-1 shows four thin-sections of random ice samples taken from freshwater polycrystalline ice mold. The images are shown in monochrome to better outline the grains. A 10 mm scale is also provided in Figure 4-1a. As visible, the grains are equiaxed with random orientation and are of similar sizes. No structural defects are visible. These observations were consistent for all ice beams that were cut out of the mold as seen in Figure 3-3. The ice beams had virtually no voids or air bubbles. As grain size can affect the flexural strength of ice as discussed in Section 2.5.1, a consistent grain size was used for all freshwater flexural tests to minimize any grain size effect.

The ASTM grain size interception method [57] was used to calculate the average grain diameter of the ice samples which was 3.66 mm which falls between the sieve sizes used for ice mold which were 4.75 and 3.35 mm.

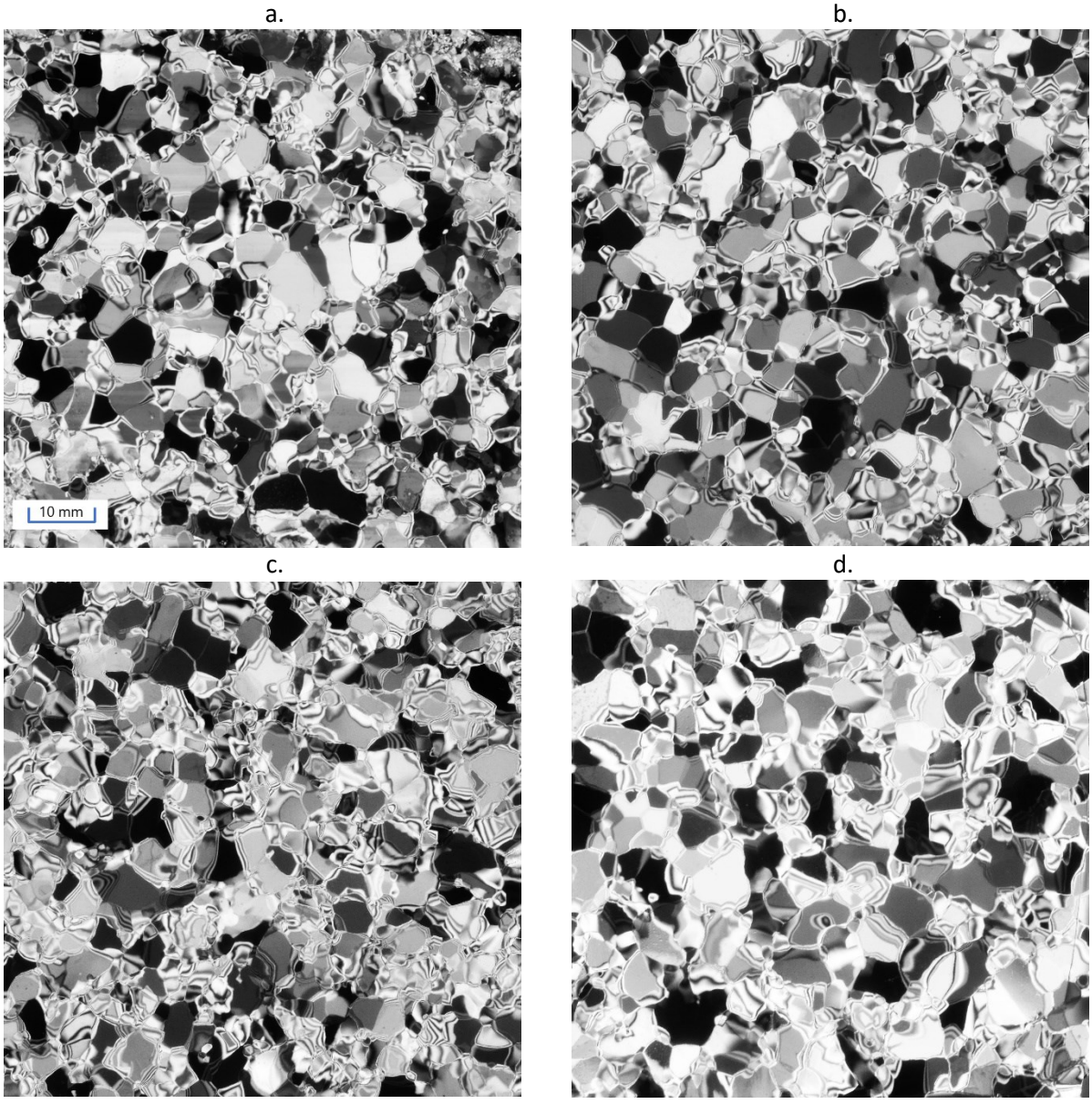

Figure 4-1- Four representative thin sections of ice samples taken from polycrystalline ice mold.

4.3. Unconfined Flexural Tests

Flexural strength test results where no compression is applied (15 tests) are plotted against results from tests in the literature for 4-point bending tests compiled by Aly [15]. The beam size in the literature spans from 0.0002 m^3 to 0.0046 m^3 and temperatures range from -0.5 to -55 ºC. The current test beam nominal volume is 0.00027 m^3 with a fixed temperature of -10 ºC. As seen in Figure 4-2, at the chosen volume of current tests, the data fits in well with the overall scatter and general trend of increasing strength with decreasing volume. The power law line of best fit was determined using Excel for the literature data points shown in blue and the equation is as follows. The test data shown in orange points fall close to the power line of best fit.

$$Flexural\ Strength\ [kPa] = 742.95x(Beam\ Volume)^{-0.112} \quad (9)$$

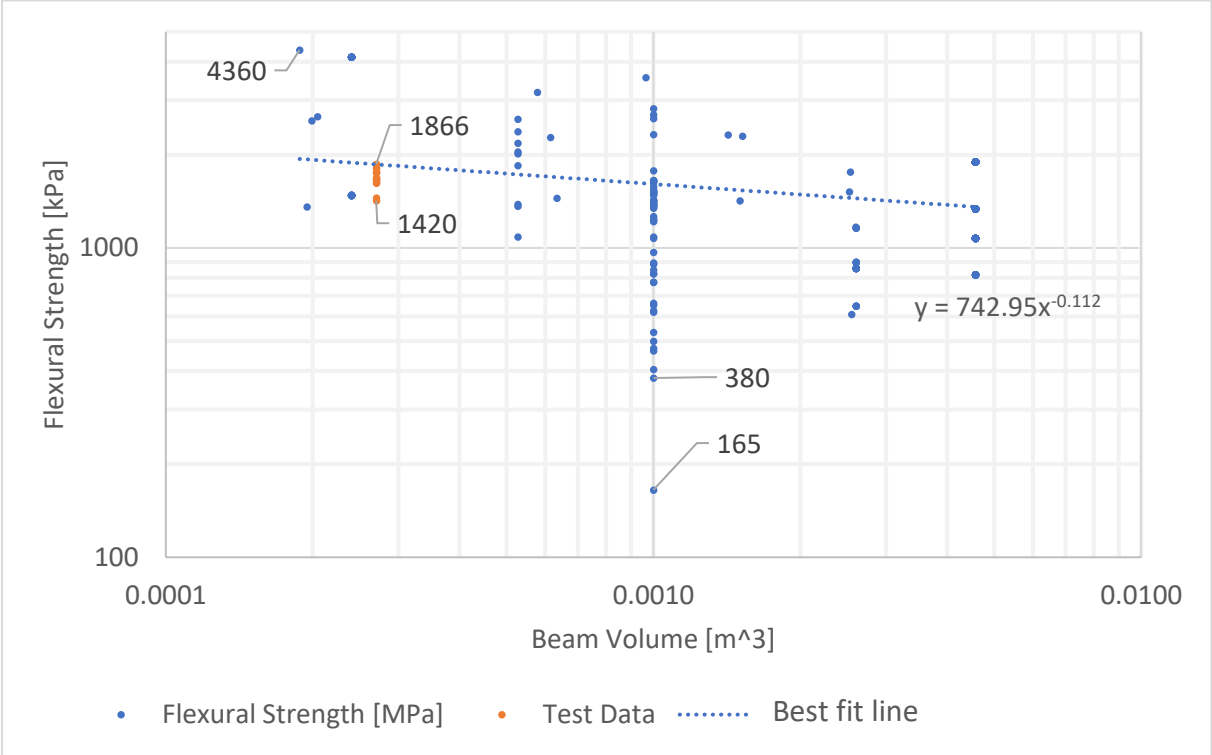

Figure 4-2 – Flexural strength against beam volume is plotted for current test in orange points and tests done reported in literature in blue points [15].

Compared to other clusters of tests done for specific beam volumes, the variation for current tests is very small ranging from 1420 to 1866 kPa. This can be attributed to the very high quality of ice samples made using the vacuum mold method which resulted in ice with virtually no defects and consistent grain size for all samples.

Results for unconfined (simple) flexural tests categorized by strain rates are shown in the plot below along with the averages of the repetitions in blue triangles. As shown in Figure 4-3, there is a relatively small amount variability between tests done for each of the strain rates. The average flexural strength for high strain rate was 1.76 MPa, about 0.1 MPa higher than medium and low speeds both of which had very similar flexural strengths, 1.62 and 1.65 MPa. It can be observed that there is not a strong relationship between strain rate and flexural strength for unconfined ice.

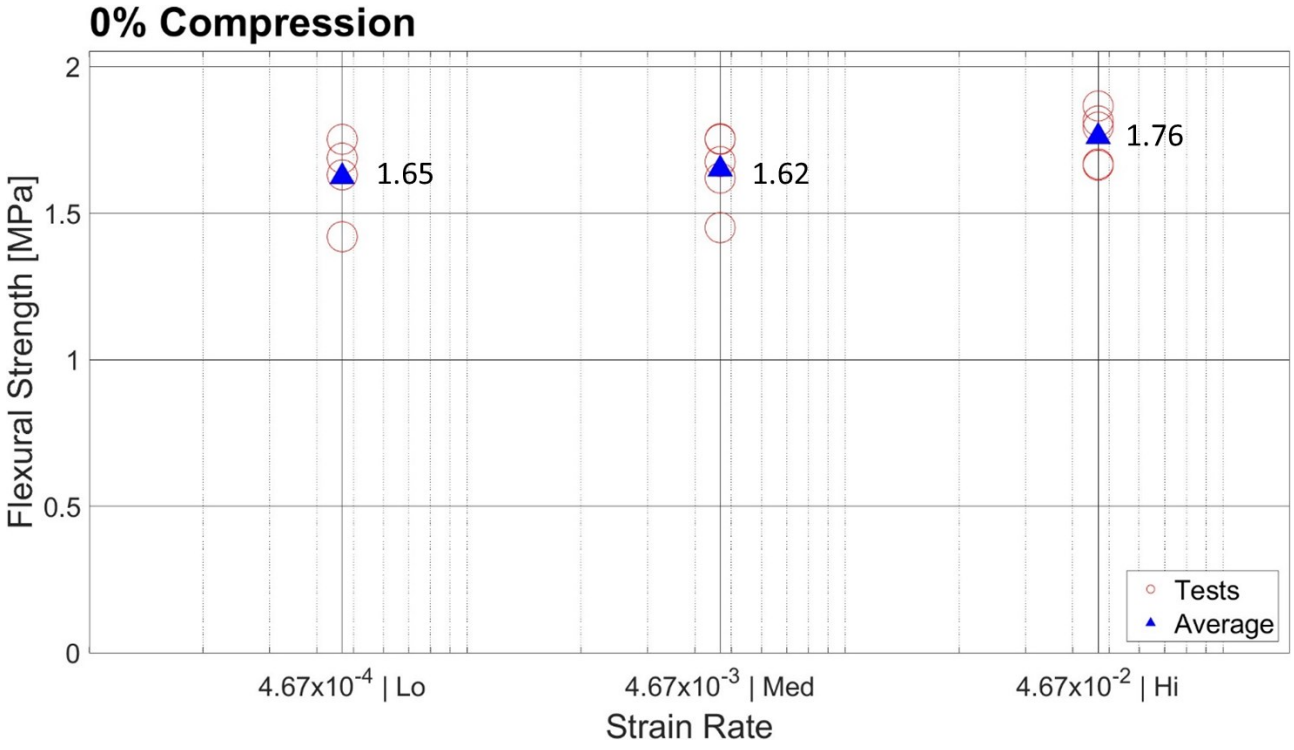

Figure 4-3 – Test results of simple flexural tests with no compression. Blue bars are individual tests and orange bars are average for each strain rate.

From these results, it can be concluded that there is no strong strain rate effect for unconfined flexural tests. It is understood that flexural failure is triggered by failure in tensile fibers of ice beam and tensile strength is not dependent on strain rate [58].

Based on these results, the average of all three strain rates was calculated to be 1.68 MPa. This value was used as a baseline unconfined flexural strength for different levels of axial stresses to be applied for confined tests. For example, for the 75% compression case, 75% of 1.68 MPa was applied as an axial stress of (1.26 MPa). The load value (F) applied to the ice beam ends was calculated using equation (10) as the product of the target axial stress (σ_a) and the cross-sectional area (A_c) of the beam, which was nominally 1290 mm^2. This was done for all three compression levels (and corresponding IPC values): 75% (IPC = 1.75), 135% (IPC = 2.35) and 185% (IPC = 2.85).

$$\sigma_a = \frac{F}{A_c} \qquad (10)$$

For the confined flexural strength tests, apparent flexural strengths have been presented, where the axial compression component has not been subtracted from the calculated flexural strength values.

4.4. Flexural Tests under Axial Compression

4.4.1. Low Compression Flexure Tests (IPC 75%)

In Figure 4-4 the plot shows results of individual tests at the three strain rates and their average in the blue triangles. Compared to the baseline flexural strength of 1.68 MPa for the unconfined case, this amount of compression has had a very strong influence on the flexural strengths. For the low-strain case, the average enhanced flexural strength is 3.46 times the baseline strength. We see that within repetitions for each speed, there is low variation. However, a strong relationship between strain rate and average flexural strength is apparent where the flexural strength decreases with

higher strain rates. The average flexural strength for the low-strain tests is 5.81 MPa, which is nearly 1.5 times the average flexural strength of 3.78 MPa for the high strain rate.

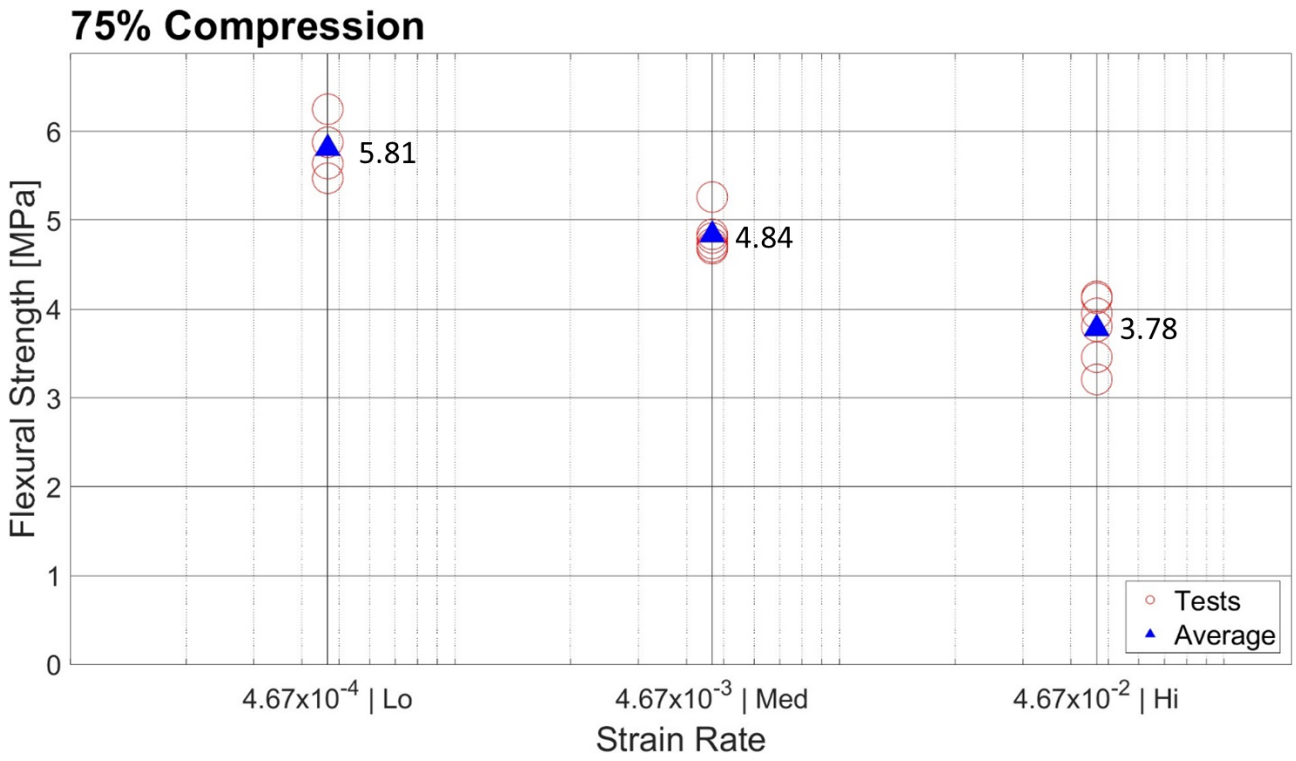

Figure 4-4 – Flexural strength for ice measured at 75% compression for different strain rates.

Table 4-2 summarizes the increase in flexural strength for IPC 75%. The strength increases between 225 to 346% for different strain rate cases.

Table 4-2 – Summary of ratio of enhanced flexural strength to unconfined baseline for different strain rates for IPC 75%.

Strain rate	Average Flexural Strength [MPa]	Flexural Strength Ratio
low	5.81	346%
med	4.84	288%
high	3.78	225%

4.4.2. Medium Compression Flexure Test (IPC 135%)

Figure 4-5 shows flexural test results for 135% compression level.

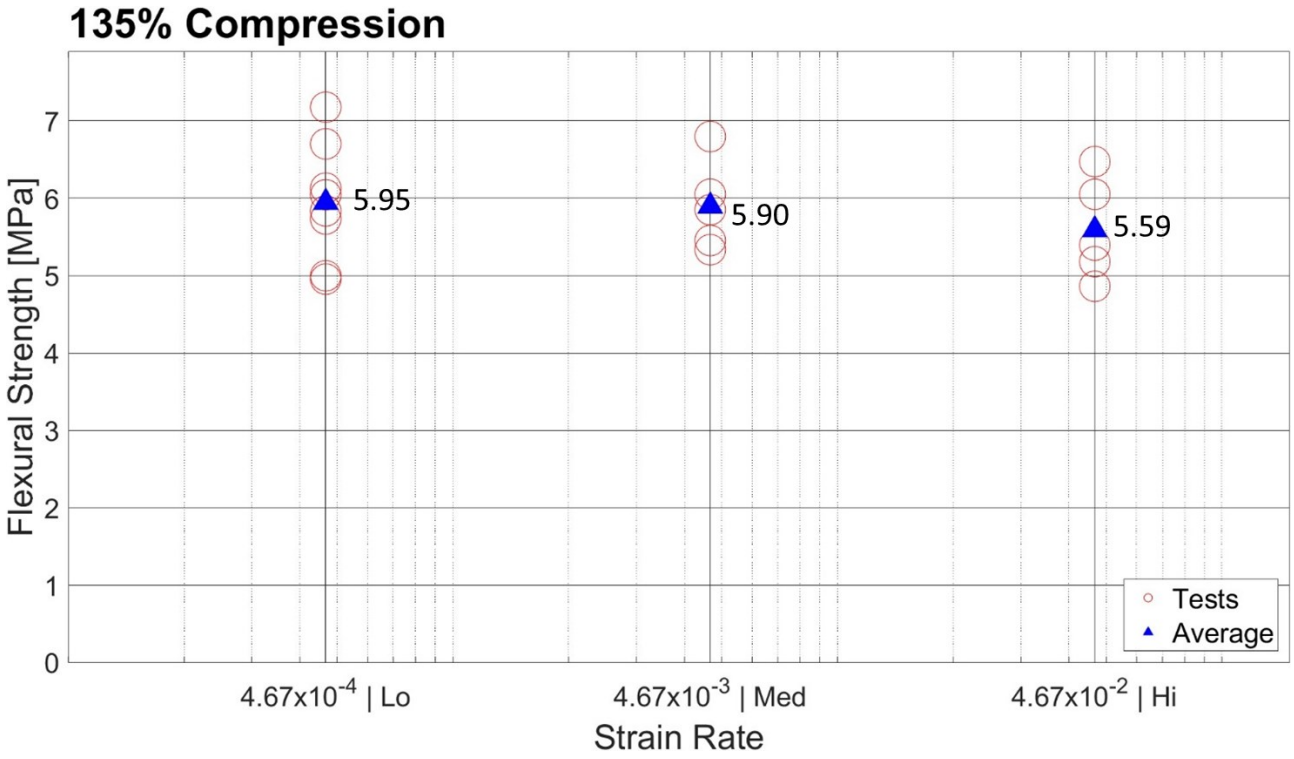

Figure 4-5- Flexural strength tests for different strain rates for IPC 135%.

Compared to the IPC 75% case, while there is higher variation observed within individual groups of strain rates, there is a smaller strain rate effect observed at IPC 135% as shown in *Table 4-3*. The average flexural strength increase is similar for low and medium strain rate at around 350% while it is slightly lower for high strain rate at 333%. There is little difference between average flexural strength increase for IPC 75% and IPC 135% for low strain rate while the difference increases with strain rate.

Table 4-3 – Summary of ratio of enhanced flexural strength to unconfined baseline for different strain rates for IPC 135%.

Strain rate	Average Flexural Strength [MPa]	Flexural Strength Ratio
low	5.95	355%
med	5.90	351%
high	5.59	333%

4.4.3. High Compression Flexure Test (IPC 185%)

There were only two repetitions completed for this case as the objective was to find out the maximum level of compression that could be applied on the ice sample on which a bending test could be performed to try to determine the upper limit of the flexural strength. Slightly higher compression was used initially but the sample failed by buckling before the sample could be evaluated in flexure. So, it was reduced to 185%. The testing procedure was also modified where the top and bottom indenters were in contact with the sample before the compression was applied so that sample could be tested immediately. The results are shown in Figure 4-6.

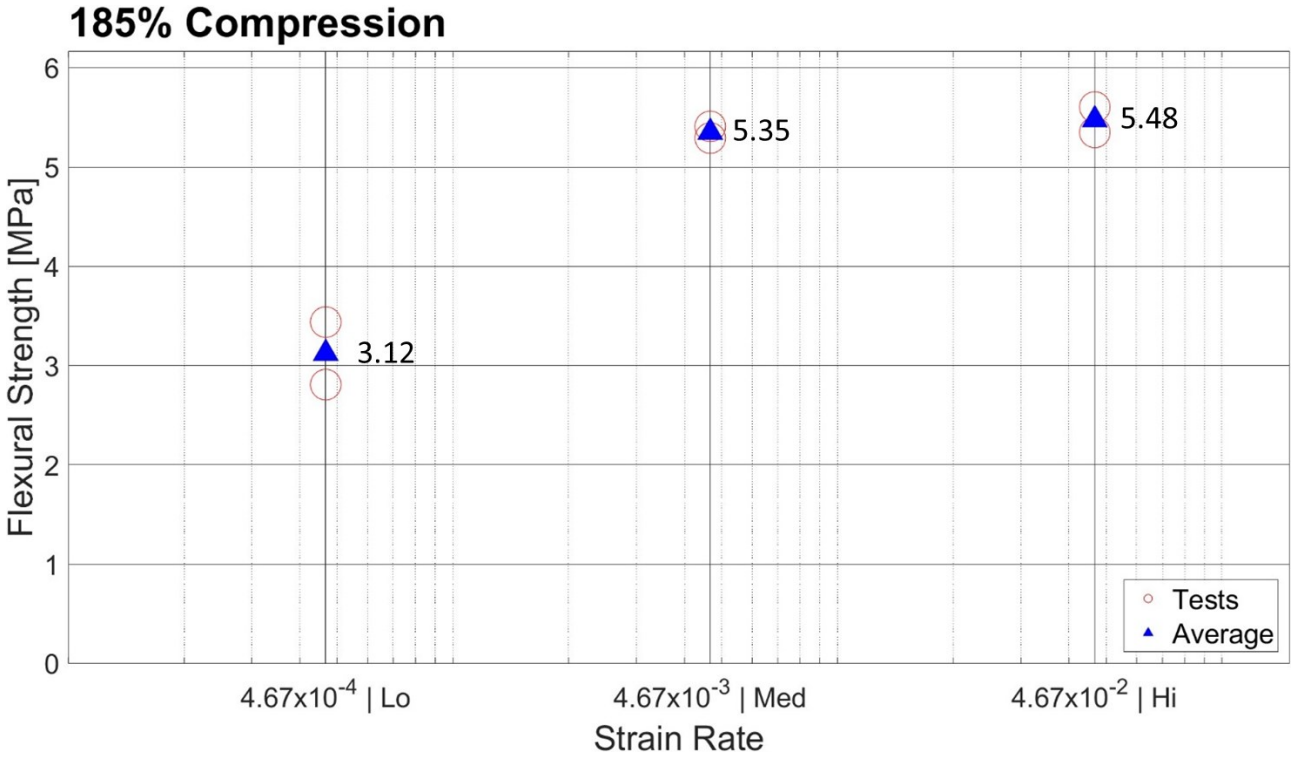

Figure 4-6 – Results of flexural test for IPC 185%.

For the previous two cases of IPC 75% and IPC 135%, the slow strain rate had the highest average flexural strength, whereas for 185% case, the high strain rate has the highest strength as

summarized in *Table 4-4*. The slow strain rate strength of 185% is about half of the higher strain rate cases although the increase in strength is still significantly higher than no compression case.

Table 4-4 – Summary of ratio of enhanced flexural strength for IPC 185% as compared to unconfined baseline for different strain rates.

Strain rate	Average Flexural Strength [MPa]	Flexural Strength Ratio
low	3.12	186%
med	5.35	318%
high	5.48	326%

Potential reasoning for the change in trend for the 185% case is that the very high levels of compression introduced significant weakness in the ice beam structure due to damage under compression and may induce damage-enhanced buckling prior to flexural failure. The two images below in Figure 4-7 show ice sample that was tested at 185% compression and slow speed. In the top image the sample has just been axially loaded to the desired compression level of 185%.

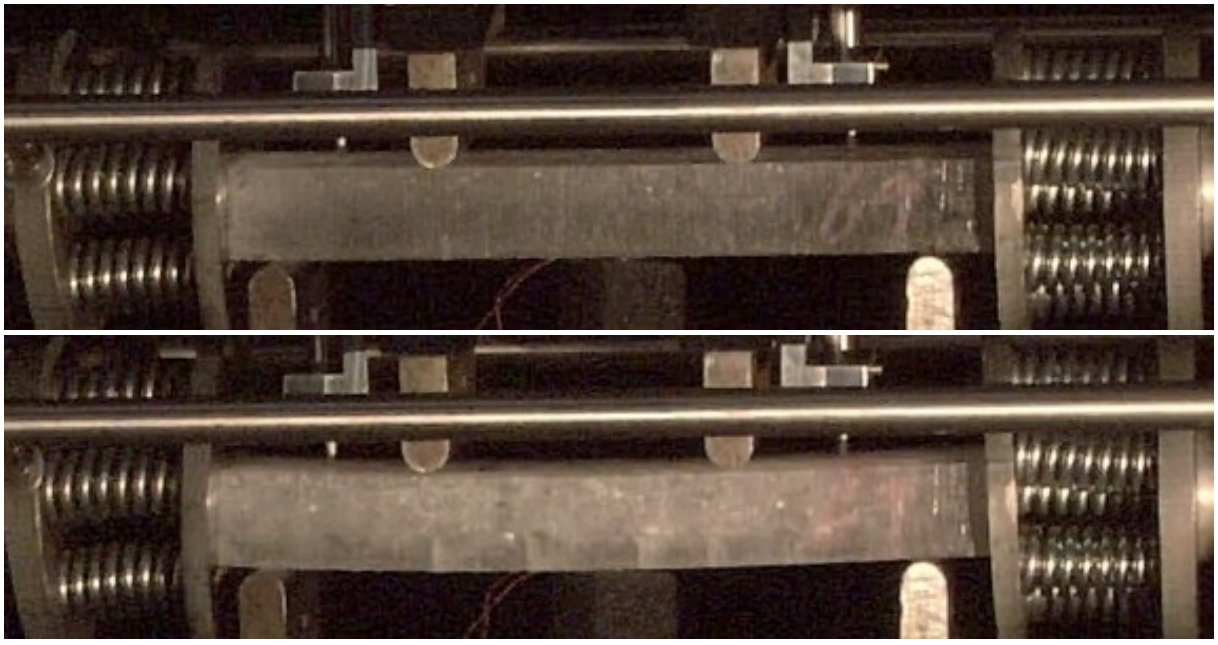

Figure 4-7 – Sample 69 tested at IPC 185% shown right after axial loading (top) and right before flex test (bottom).

For this loading scenario, before flexural loading is initiated in the MTS machine, the sample has already begun to buckle and several cracks have formed on the bottom half of the beam as shown in the bottom image in Figure 4-7. The sample also had a cloudy appearance due to microcracks forming in the sample. The progressive accumulation of micro-cracking damage prior to slow loading plays a significant role in reduced strength of ice under high confinement conditions.

Figure 4-8 shows the load and displacement traces for test 69 completed at 185% compression and low strain rate shown in Figure 4-7. It can be seen that the flexural load does not increase until around 14 seconds while the ram displacement and center LVDT readings do increase during this time period. Increasing LVDT readings while vertical loading remains zero confirms that the beam is buckling from the high axial compression prior to the load from the indenters is applied to the sample. The center LVDT reads 0.5 mm at the start of the test which indicates that the beam center has already deflected.

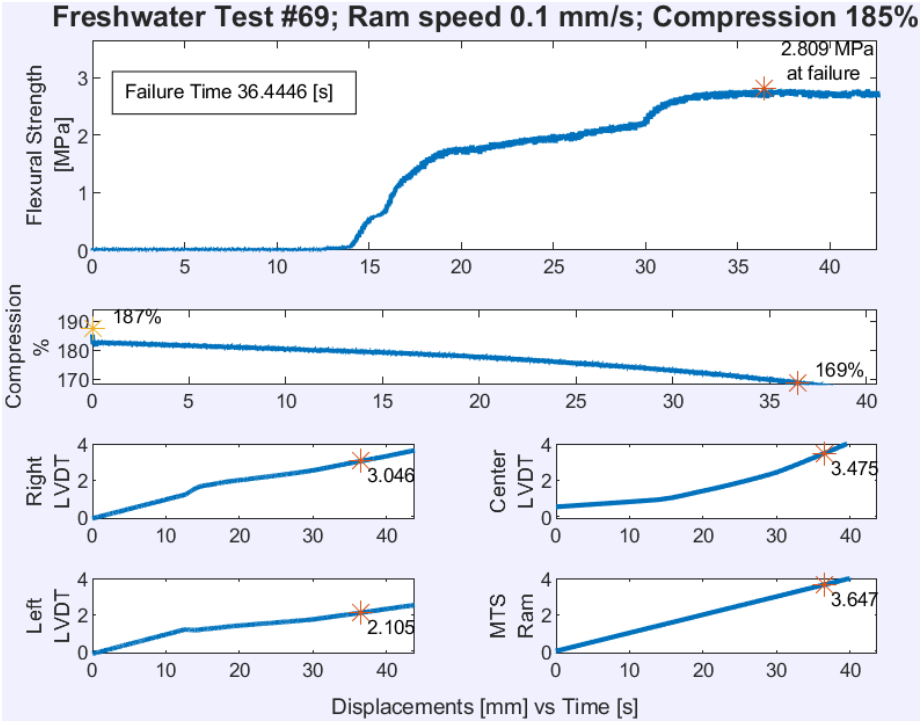

Figure 4-8 – Group plot showing load and displacement trace for test 69.

4.5. Summary of Apparent Flexural Strength

In Figure 4-9, average apparent flexural strength is plotted against strain rates for different compression levels on a logarithmic axis. We can see that for IPC 75%, the flexural strength has a strong relationship with strain rate where strength decreases as strain rate increases. For IPC 135%, the flexural strength remains the same with a slight decrease at high strain rate. The flexural strength is highest for all strain rates for IPC 135% compared to other compression levels. For IPC 185%, the strength is lowest at low strain rate, increases for medium strain rate and remains steady for high strain rate. The base line strength of 1.68 MPa is also plotted for no compression case.

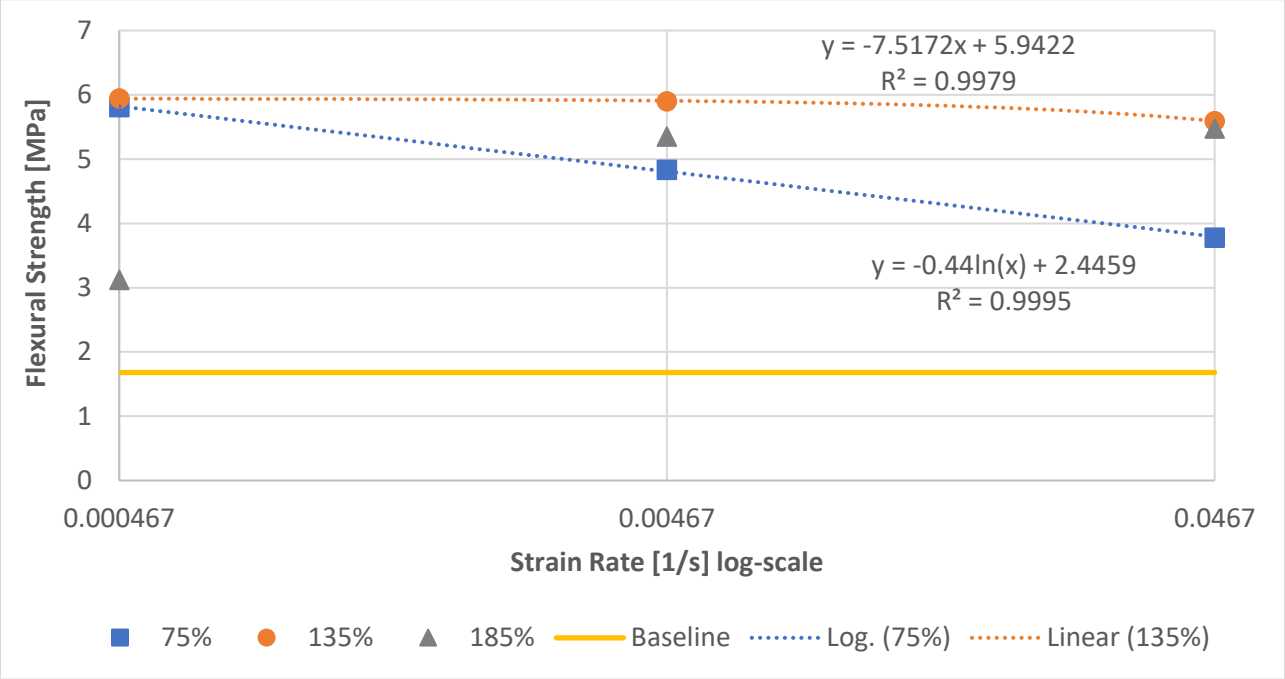

Figure 4-9 – Apparent flexural strength plotted against strain rates for different compression levels.

The power law curve of best fit for 75% compression flexural strength $\sigma_{f,75\%}$ versus strain rate, $\dot{\varepsilon}$, with a R^2 value of 0.995 is given by following equation:

$$\sigma_{f,75\%} = -0.44 \ln \dot{\varepsilon} + 2.4459 \qquad (11)$$

The linear best fit for 135% compression flexural strength $\sigma_{f,135\%}$ versus strain rate, $\dot{\varepsilon}$, with a R^2 value of 0.998 can be described by following equation:

$$\sigma_{f,135\%} = -7.5172\dot{\varepsilon} + 5.942 \qquad (12)$$

Overall, we see in Figure 4-10 that there is an increasing trend for flexural strength as compression level is increased from IPC 75% to IPC 135%. Between IPC 135% and IPC 185%, slow rate strength drops significantly, strengths at medium rates also drops slightly while high speed strength increases slightly. The strengths appear to converge as the compression level increases. Strengths are similar for 135% compression with for all three strain rates. Figure 4-11 shows the average apparent strength flexural strength values for the data plotted in Figure 4-10. Figure E 3 in Appendix E - Additional Plots and Analysis also plots all apparent test data points with the averages shown in Figure 4-11.

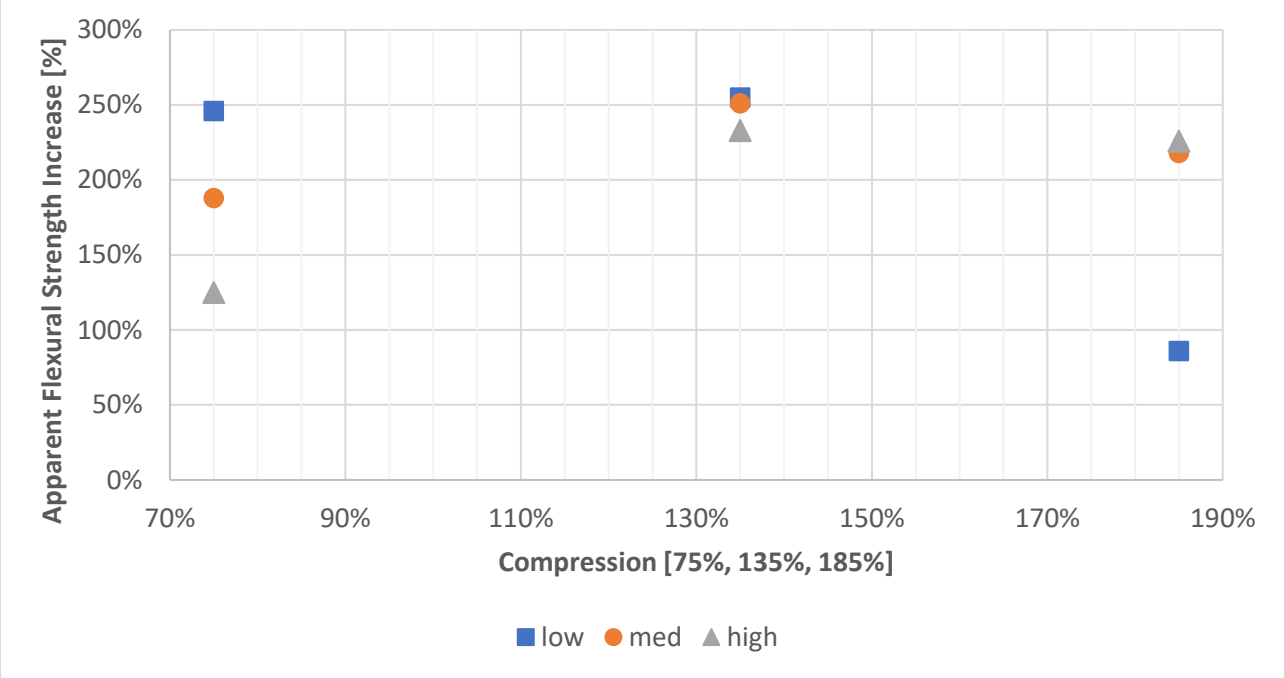

Figure 4-10 – Apparent freshwater flexural strength increase plotted against test compression levels for different strain rates.

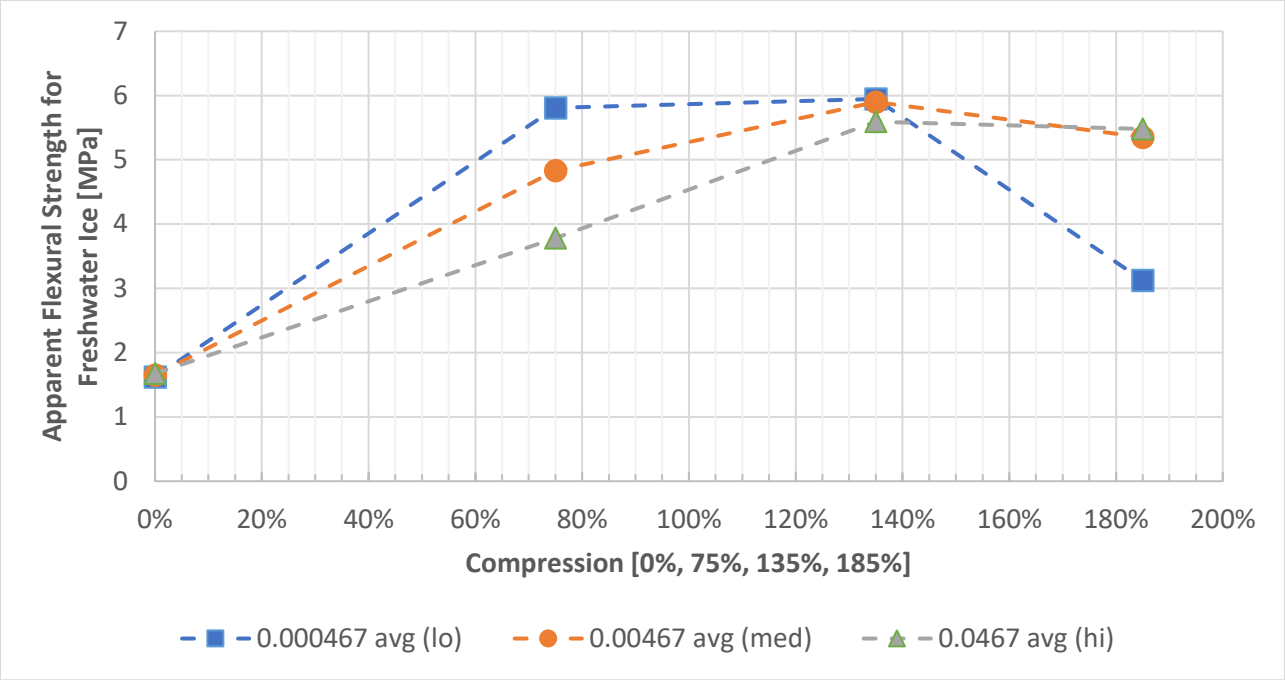

Figure 4-11 – Average values of apparent freshwater flexural strengths plotted against test compression levels for different strain rates.

4.6. Summary of Nominal Flexural Strength

In nominal flexural strength, the axial component has been subtracted from apparent flexural strength to observe the trends in flexural strength using the following formula:

$$\sigma_{f,ratio} = \frac{\sigma_{f,compressed} - \sigma_{a,compressed}}{\sigma_{f,nominal\ 0\ compression}} \quad (13)$$

Where $\sigma_{f,compressed}$ is flexural strength of ice under confinement, $\sigma_{a,compressed}$ is the axial confinement pressure applied to the sample and $\sigma_{f,nominal\ 0\ compression}$ is the unconfined flexural strength of ice.

In Figure 4-12, we see that trends have changed compared to the apparent flexural strength. These results suggest that the confinement effect is most significant for the lower range of compression level where the strength increase ranges from 50% to 170%. At medium compression, the strength

increase is slightly more than 100% for all strain rates. At 185% compression, the flexural strength increases drops to 50% for low and medium strain rates and by 100% for high strain rate indicating that there is no strength in ice at this combination of compression and strain. The convergence effect can still be observed where there is a clear strain rate effect at 75% but strength values are identical for all strain rates at 135% compression. Figure 4-13 shows the average nominal flexural strength values for the data plotted in Figure 4-12. Figure E 4 in Appendix E - Additional Plots and Analysis also plots all nominal test data points with the averages shown in Figure 4-13.

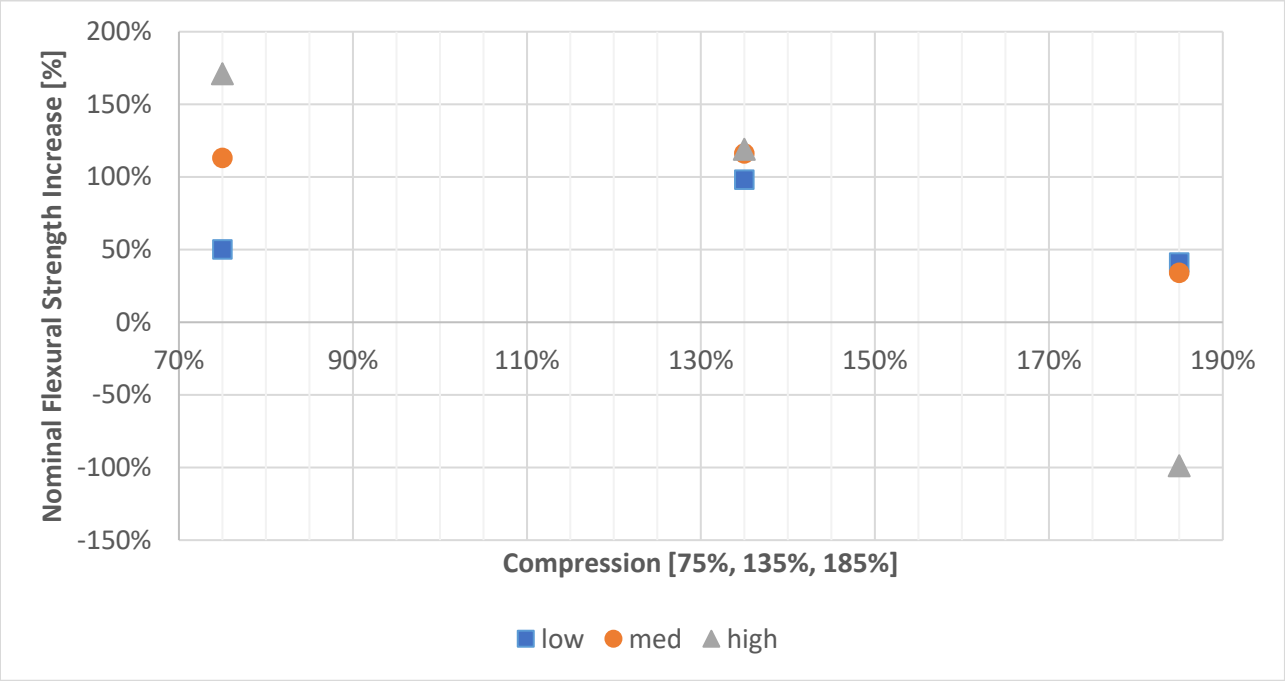

Figure 4-12 – Nominal freshwater flexural strength increase plotted against test compression levels for different strain rates.

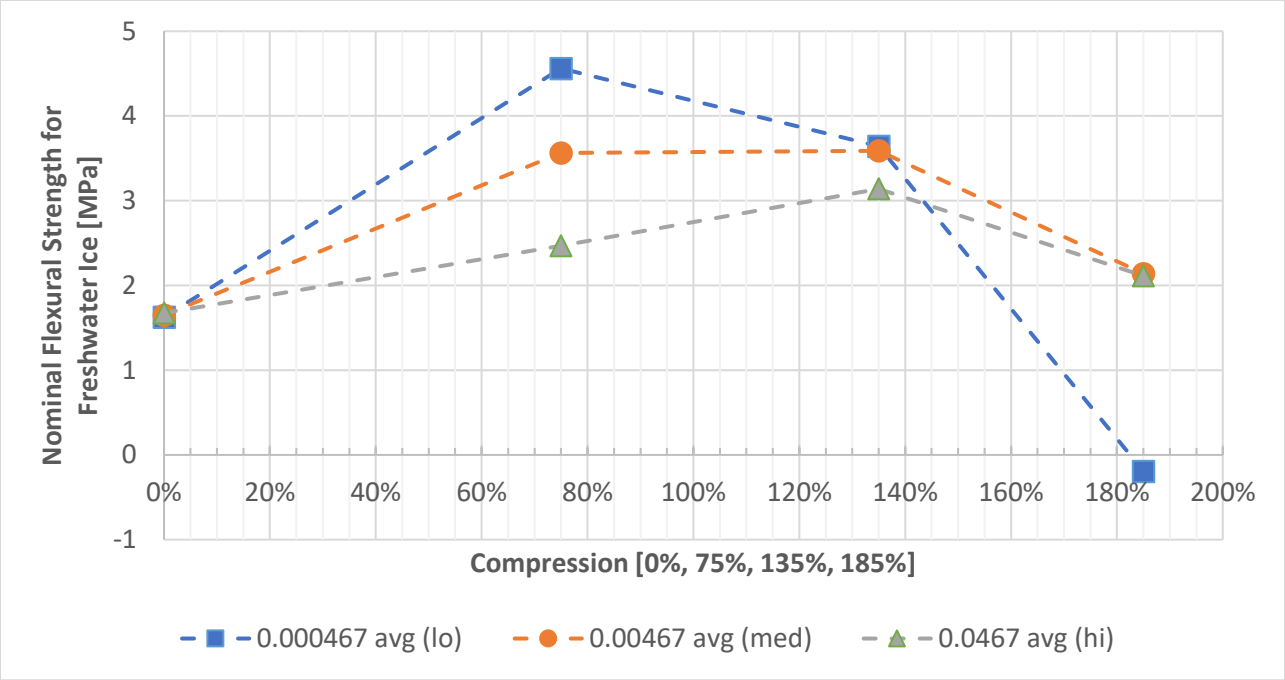

Figure 4-13 – Average values of nominal freshwater flexural strengths plotted against test compression levels for different strain rates.

4.7. Deflection Analysis

Figure 4-14 shows average deflection measured by MTS ram displacement and center LVDT with standard deviation error bars for IPC 0%, 75% and 135% cases for all strain rates. Error bars are not given for IPC 185% as only two repetitions were done.

Center LVDT was positioned in the test setup to measure midpoint deflection of the beam where the failure was most likely expected to occur. As mentioned previously, the strain rate effect is apparent for IPC 75% and IPC 135% cases compared to unconfined case owing to different failure mechanisms, which is discussed further in the next section. There is no effect of strain rate on deflection for unconfined flexural tests. For compression tests, the deflection decreases as strain rate increases. Deflection measured by center LVDT is higher than MTS displacement for low strain rate, similar for medium strain rate and lower for high strain rate. The variance can be attributed to large overall and local deformations in the sample at low strain rate compared to

higher strain tests. LVDT reading generally has higher variation than MTS readings as LVDT is measuring local displacement which can be highly variable while MTS ram is displacement controlled and measurement is the travel of the ram. Compared to flexural strength trend for IPC 135%, there is a strong relationship of average displacements decreasing with increasing strain rate. Two LVDT measurements for IPC 135% high strain rate (tests #27 and 28) were not included in the average as they were not recorded due to equipment failure.

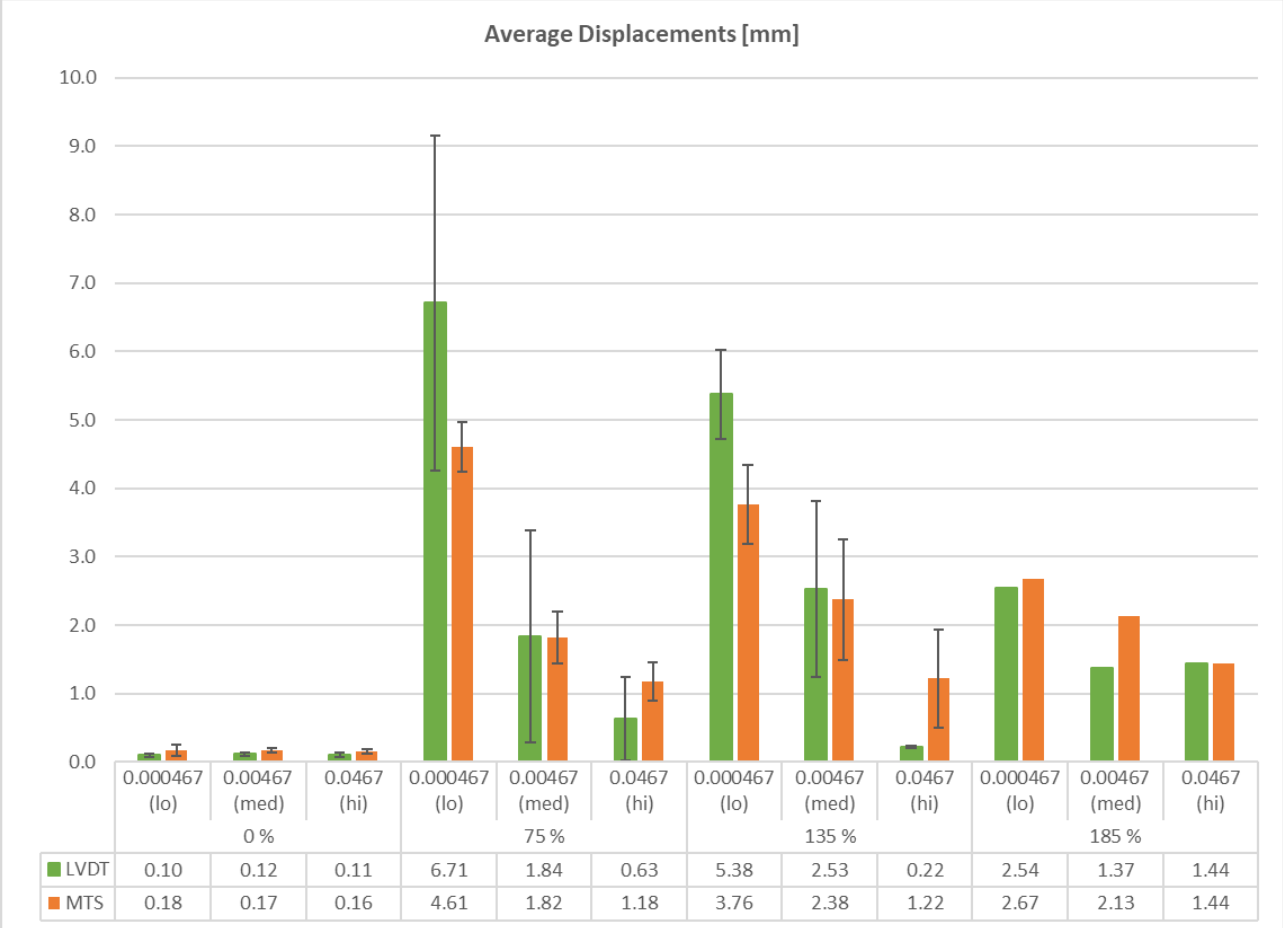

	0.000467 (lo)	0.00467 (med)	0.0467 (hi)	0.000467 (lo)	0.00467 (med)	0.0467 (hi)	0.000467 (lo)	0.00467 (med)	0.0467 (hi)	0.000467 (lo)	0.00467 (med)	0.0467 (hi)
	0 %			75 %			135 %			185 %		
LVDT	0.10	0.12	0.11	6.71	1.84	0.63	5.38	2.53	0.22	2.54	1.37	1.44
MTS	0.18	0.17	0.16	4.61	1.82	1.18	3.76	2.38	1.22	2.67	2.13	1.44

Figure 4-14 – Average displacements shown for different compression levels and three strain rates: $4.67x10^{-4}$ (low), $4.67x10^{-3}$ (medium) and $4.67x10^{-2}$(high).

4.8. Failure Mechanism

For simple 4-point bending tests, all samples failed due to planar fracture parallel to the end surfaces of the beam. This is an expected fracture surface as observed by Gow et al [24]. One of the surfaces of a failed sample is shown in Figure 4-15.

Figure 4-15 – Fracture surface of ice beam in simple flexural loading.

For the combined loading tests, high speed video recording up to 18,000 frames per second was used to record some of the tests to observe the failure. The sample failed too rapidly to look at failure sequence with a regular speed camera.

All samples failed somewhere in the volume of ice between the top indenters due to compressive failure of ice in the top portion of the beam. Tensile cracks were observed in the bottom sections of the sample for low compression tests, but these never propagated sufficiently to trigger beam failure as the compressive forces acted to stabilize the tensile cracks as the tips grew towards the neutral axis. In Figure 4-16a, the testing had just begun for ice sample in 75% compression and high strain rate. In Figure 4-16b, we observe a crack forming in the bottom layer of the sample as shown in the yellow circle. In Figure 4-16c, failure has begun as the top layers get crushed by

compression. The crushing does not extend outside the region between the top indenters. By the time shown in Figure 4-16d, the sample has failed completely. The first crack occurs within 0.044 seconds and complete failure occurs by 0.112 seconds.

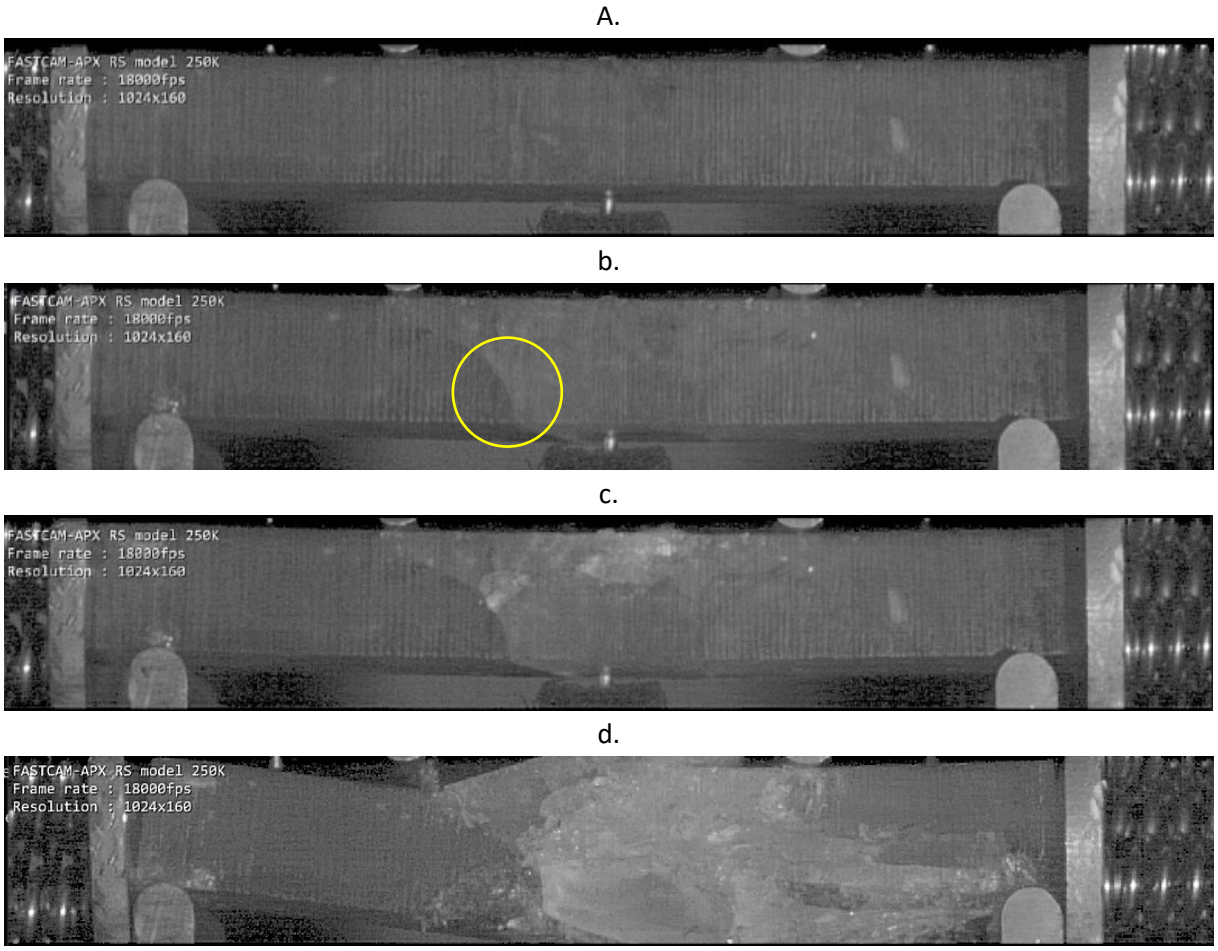

Figure 4-16 – Failure sequence of ice sample in combined loading.

For higher compression levels, tensile cracks were not observed in some of the videos, however the samples still failed by processes originating from the top (compressive) region of the ice specimen.

The influence of multiple mechanisms can be seen in Figure 4-17 for a sample that was loaded to 135% compression and tested at low strain rate. In Figure 4-17a, it may be seen how much the sample deformed during testing. In Figure 4-17b, the effect of compressive forces in the top layer

is seen, in which microcracking is much more concentrated in the region between the top indenters. Some bulging in this section may also be observed. In Figure 4-17c, extensive tensile cracking on the underside of the bottom portion of the beam may also be observed.

a.

b.

c.

Figure 4-17 – Sample that did not fail completely for 135% compression and low speed. (a.) side view of the sample; (b.) top view; and (c.) bottom view.

The approximate locations of the top and bottom indenters of the sample are shown in *Figure 4-18*.

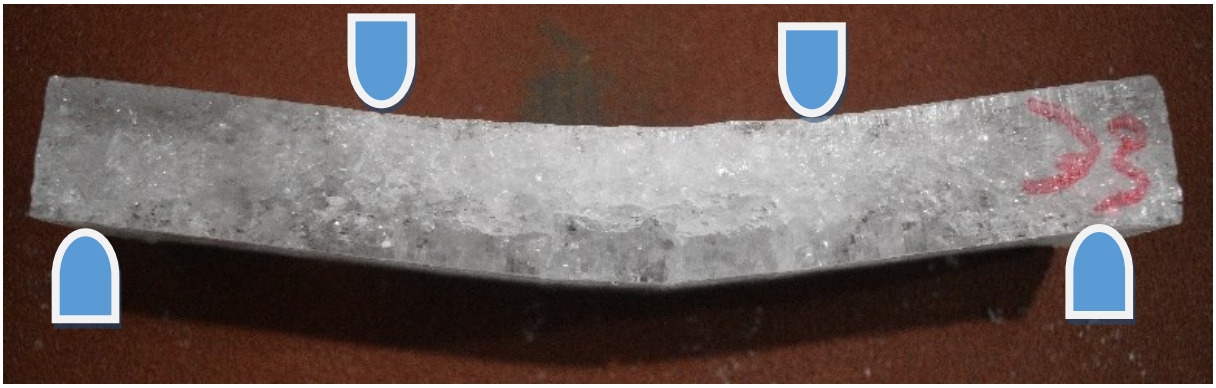

Figure 4-18 – Ice sample with approximate indenter locations.

In the slow speed test (Figure 4-19a), the sample does not fail at peak stress, but rather after achieving peak stress, there is some stress reduction (e.g. damage enhanced creep). The medium and high-speed test samples fail suddenly, characterized by an instant drop in stress as shown in Figure 4-19b and c. In both cases the samples fail at the peak stress. Failure times are also shown in each plot. Some characteristic sawtooth profiles were also observed in slow strain tests as seen around 25 seconds in Figure 4-19a. System ringing was also observed for fast strain tests as shown by waves in the load trace between 0.07 and 0.12 seconds in Figure 4-19c.

a.

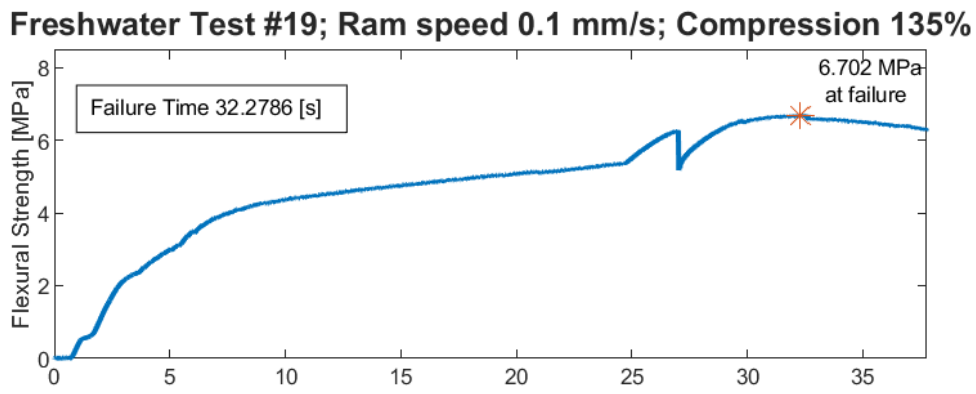

b.

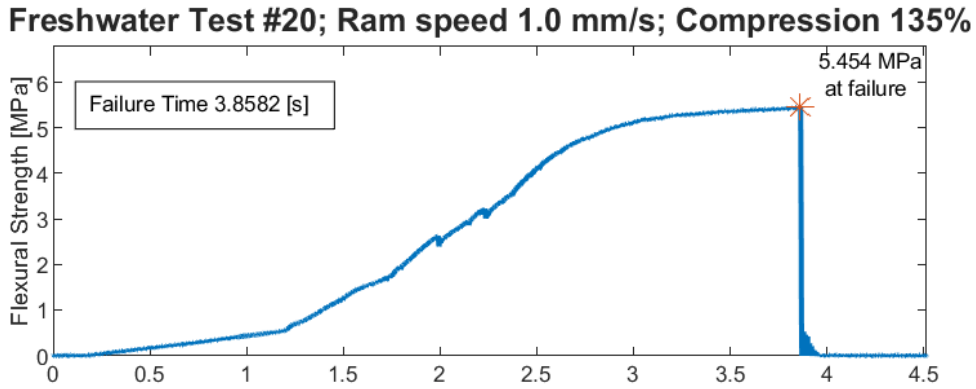

c.

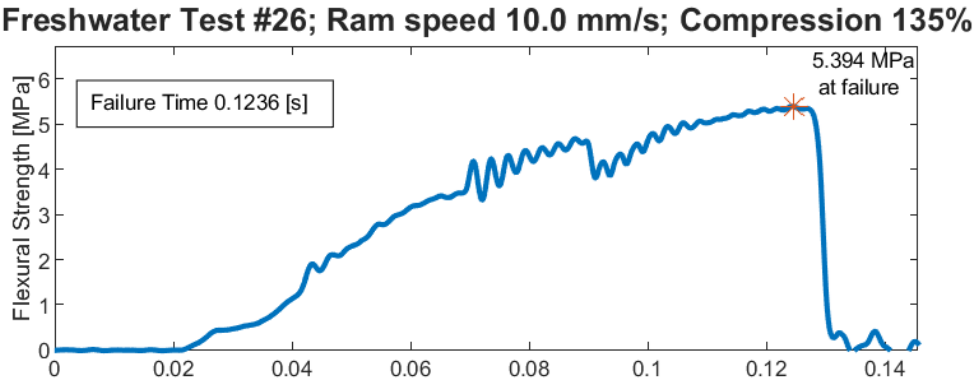

Figure 4-19 – Load traces for different strain rates are shown for 135% compression tests.

Complete load traces for tests in Figure 4-19 (19, 20 and 26) are shown together in the following plot. Flexural load is applied at 20 seconds for all tests. The failure load reduction occurs for 60 seconds after peak load achieved at around 30 seconds. This is distinctly different from medium and high strain rate failure (Figure 4-20 & Figure 4-21) where the load drops to zero immediately.

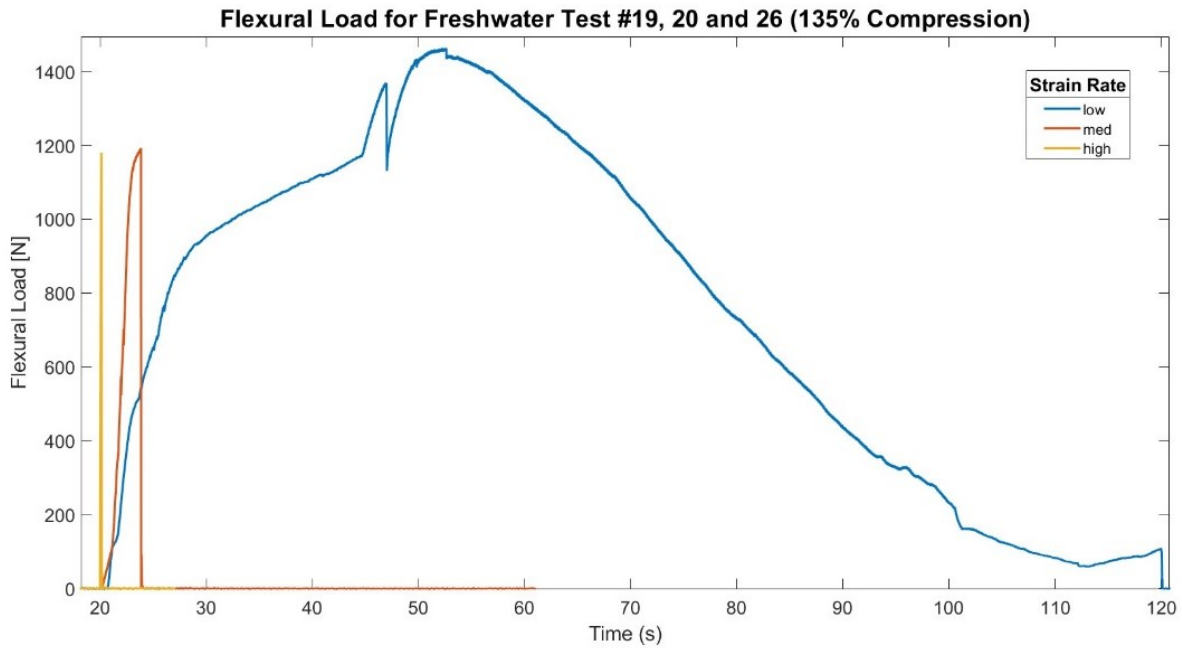

Figure 4-20 – Load trace for tests 19, 20 and 26.

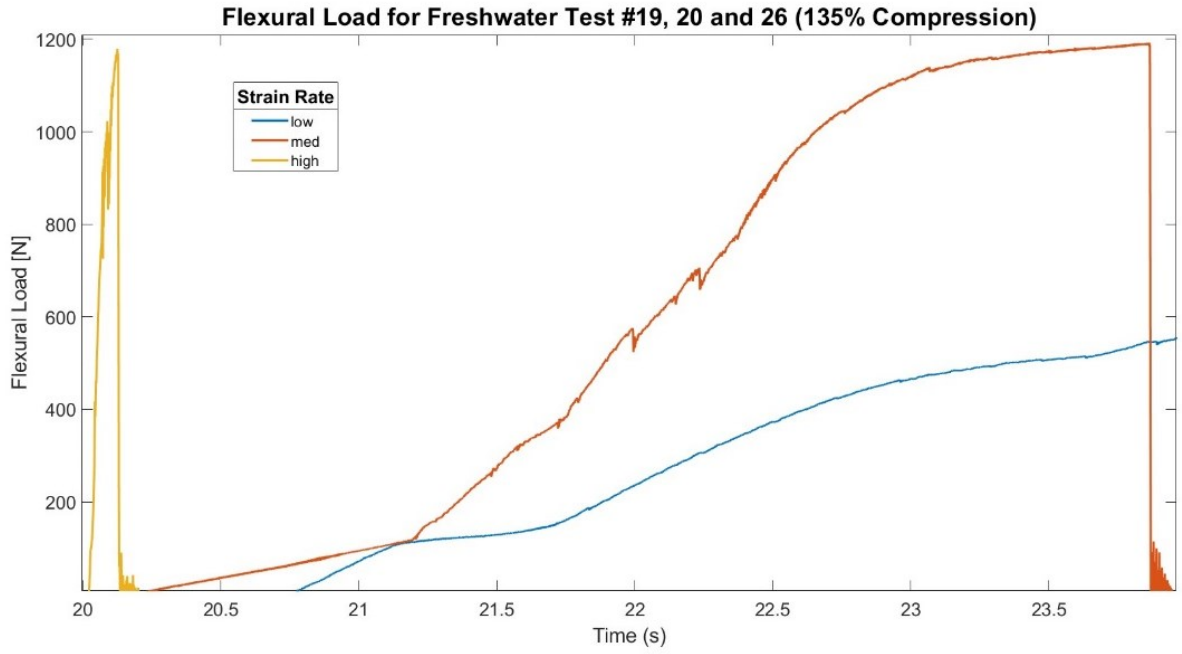

Figure 4-21 – Load trace in Figure 4-20 zoomed in for medium and high strain rate test.

Figure 4-22 shows the ice beams at different compressions: 75% (a) 135% (b) and 185% (c) at medium strain rate right before failure captured from high-speed videos. The level of microcracking in the area above the neutral axis is very distinct for low, medium and high compression where microcracks can be observed throughout the sample for IPC 185% and very few for IPC 75%. Only a few tensile cracks can be observed in the IPC 75% case and several throughout the length of the sample for the IPC 185% cases. There isn't noticeable damage on the compression ends for Figure 4-22a and b, but damage on left end of Figure 4-22c is very apparent which may indicate crushing failure.

a.

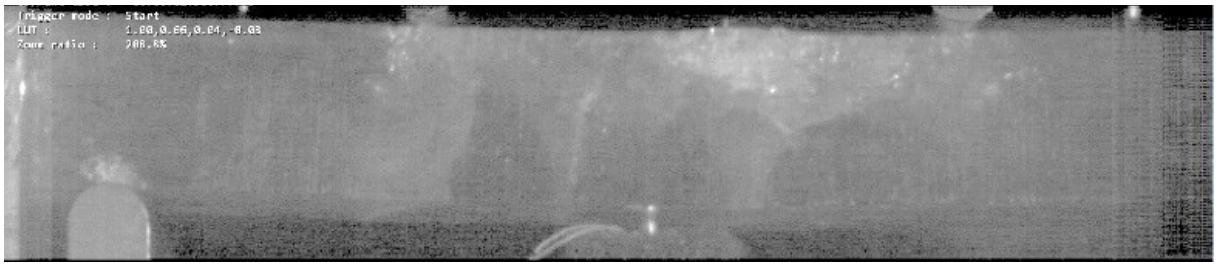

b.

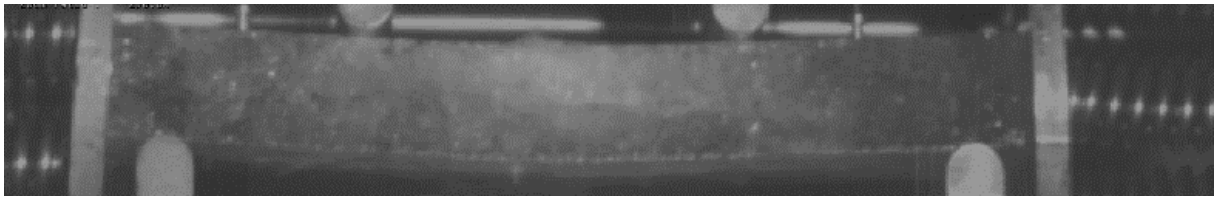

c.

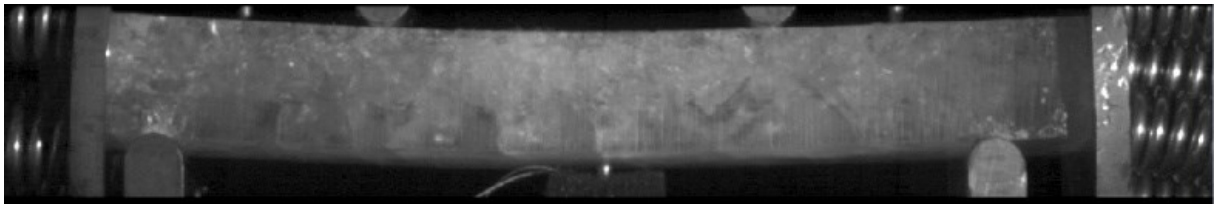

Figure 4-22 – Damage in the ice beam right before failure is shown for different compression levels: (a.) 75%; (b.) 135%; and (c.) 185% at medium strain rate.

4.9. Buckling Analysis

As buckling was observed as a failure mechanism at higher compression levels (185%), buckling critical load was calculated for the beam geometry and ice properties. Due to the very small

slenderness ratio of the beam, Johnson's parabola formula was used for buckling load calculation instead of Euler's formula as it tends to grossly overpredict the load values as seen in Figure 4-23 [59]. All calculation details are provided in Table E 1 in Appendix E - Additional Plots and Analysis

For the purposes of buckling calculations, the Young's Modulus of ice was assumed to be 9 Gpa [58]. The transition slenderness ratio was calculated to be 167 under which Johnson formula should be used. The slenderness ratio for the beam was determined to be 27, which was much lower than the transition ratio.

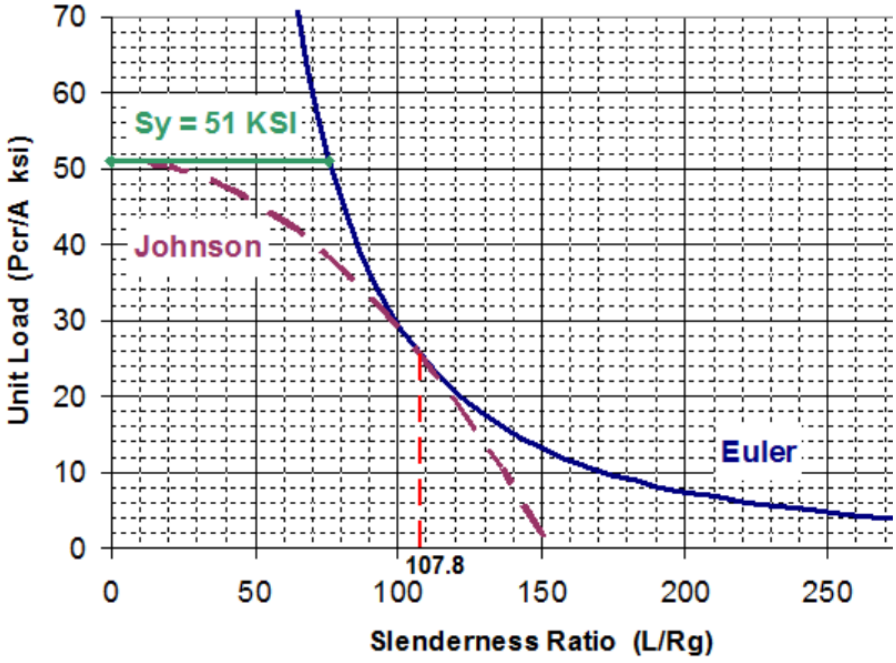

Figure 4-23 – Critical buckling load limit lines for Euler and Johnson formula are compared for a given beam geometry and material. Reproduced from [59].

Compressive strength of ice is an input for Johnson formula. One test was done to determine the compressive strength of ice by loading a sample in the confinement frame and applying axial load at a loading rate of ~180 N/s until failure. The compressive strength was measured to be 6.4 MPa.

Based on these values, the theoretical buckling load is calculated to be ~8100 N while axial load applied at 185% compression was ~3300 N. The discrepancy could be due to using a compressive strength value derived from a single compressive test therefore multiple compressive tests should be done to obtain a more reliable compressive strength test value. Tests should also be done with freshwater mold ice to obtain an accurate young's modulus of the ice.

4.10. Summary

A total of 56 tests on lab-grown freshwater ice were completed at three different strain rates for simple flexural tests and three compression levels: 75, 135 and 185%. Microstructural analysis of the ice samples showed that ice had random orientation and consistent grain size. Visual inspection of the ice samples also showed that samples were defect free.

Compared to other 4-point flexural tests reported in the literature, the unconfined flexural tests fit in well with general trends of the data for the beam volume chosen for the tests. Strain rate did not have an observable effect on the unconfined flexural strength, which was expected due to the failure mechanism originating from tensile failure. Perpendicular and planar fracture was also observed which is characteristic of unconfined flexural failure as described in literature.

For flexural tests under axial confinement, average flexural strength was significantly enhanced, increasing between about 125% to 250%. Clear strain rate effects were observed for the IPC 75% case where strength decreased with increasing strain rate. No strain rate effect was seen for the IPC 135% case; however, the flexural strength was highest and similar for all strain rates at around 250%. For the IPC 185% case, the high confinement changed the failure mode and buckling started to influence the failure mechanism. Average midpoint deflection by LVDT and MTS readings did show strong strain rate effect for both the IPC 75% or IPC 135% cases.

In contrast to tensile dominated planar fracture, the confined samples failed from upper most fibers under compression. Tensile cracks did form, however the compressive loading acted to suppress the crack tip growth and prevented unstable tensile crack growth. Studying the load and stress traces revealed that low strain rate samples failed slowly while higher strain rates failed in a sudden fashion.

5. Confined Saline Ice Four-Point Beam Tests

5.1. Sample Characteristics

5.1.1. Temperature Profile

As discussed in Chapter 3, temperatures were taken at 10 cm intervals for a single ice core following extraction during field work at Pistolet Bay. The total ice core length taken was 95 cm with 13 cm of snow and 19 cm of snow ice. The seawater temperature was -1.7 ºC and air temperature +0.6 ºC. Table 5-1 summarizes the temperatures taken at each distance from core bottom.

Table 5-1 - Temperature readings taken at set distance from the bottom of the core.

Distance from core bottom (cm)	Temperature (C)
10	-1.7
20	-1.8
30	-1.9
40	-1.9
50	-1.7
60 (Snow ice interface)	-1.7
70	-1.7
~80 (Snow-snow ice)	-0.6
Top of snow	-0.5
Air temperature	+0.6

Figure 5-1 plots distance from core bottom against the measured temperatures. From this figure, a partial “C-shape” is apparent associated with warming weather as the snow layer of the core is almost 1.5 ºC warmer than the coolest temperature recorded in the bottom of core around 30-40 cm at -1.9 ºC.

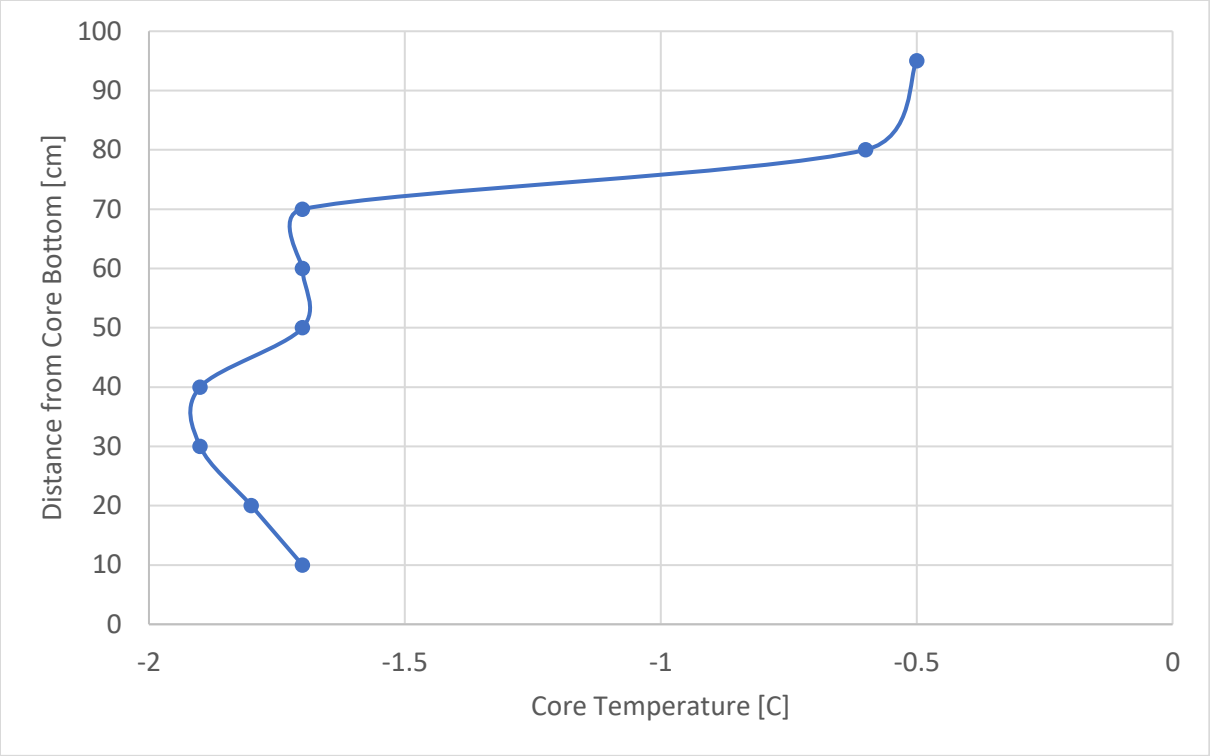

Figure 5-1 - Plot of core distance against core temperature is provided.

5.1.2. Salinity

The ice cores were stored in coolers for transportation and transfer to the testing lab. Five random samples from each cooler were taken for salinity testing and the results are given in Table 5-2 below. The salinity of the samples varied from 1.4 to 2.9 ppt with an average salinity of 2.1 ppt at average room temperature of 22.8 ºC. This value of salinity is lower than standard reported salinity of 4-6 ppt for arctic first year ice towards end of winter [60]. Care was taken to reduce brine drainage by storing ice samples at -15 ºC however, ideally, ice should be stored at -27 ºC or colder to minimize drainage but no storage facilities were available that operated at this temperature. Hence, as brine drainage introduces a source of uncertainty to the test data, in-situ tests are recommended in future to determine salinities and to verify if any brine drainage has occurred prior to testing.

Table 5-2 - Measured salinity and temperature of each sample.

Sample #	Cooler	Salinity [ppt]	Temperature [C]
1	1	1.8	22.8
2	1	2.5	22.8
3	1	1.9	22.8
4	1	2.1	22.7
5	1	1.9	22.7
1	2	2.1	22.7
2	2	2.2	22.9
3	2	1.4	23
4	2	1.4	23
5	2	2.9	22.9
6	2	2.4	22.6
Average		2.1	22.8

5.1.3. Grain Size Analysis

Random ice samples from coolers were selected for thin section analysis to determine grain structure and size. The orientation of cross-sections are shown in Figure 3-13. As expected, there was a distinct snow ice layer and columnar grains layer observed deeper in the cores. These two distinct layers are shown in Figure 5-2 for one of the cores. In Figure (a), the small, randomly oriented crystals can be seen throughout the section while in b, small grains can be seen at the top of section and larger (green rectangle), elongated crystals can be seen in the lower layers (blue rectangle). The orientation of the thin section is same as the ice core. Scales with 0.1 cm graduations are also included in the figures. It should be noted that crystals on the edges of Figure 5-2(b) are not part of the original microstructure and are formed from refreezing of melted water during preparation of thin sections (white boxes).

In loading against sloped structures in the field, ice will experience bending along the horizontal plane rather than vertical. Therefore, microstructural orientation will be in the horizontal direction rather than the vertical direction considered here.

a. b.

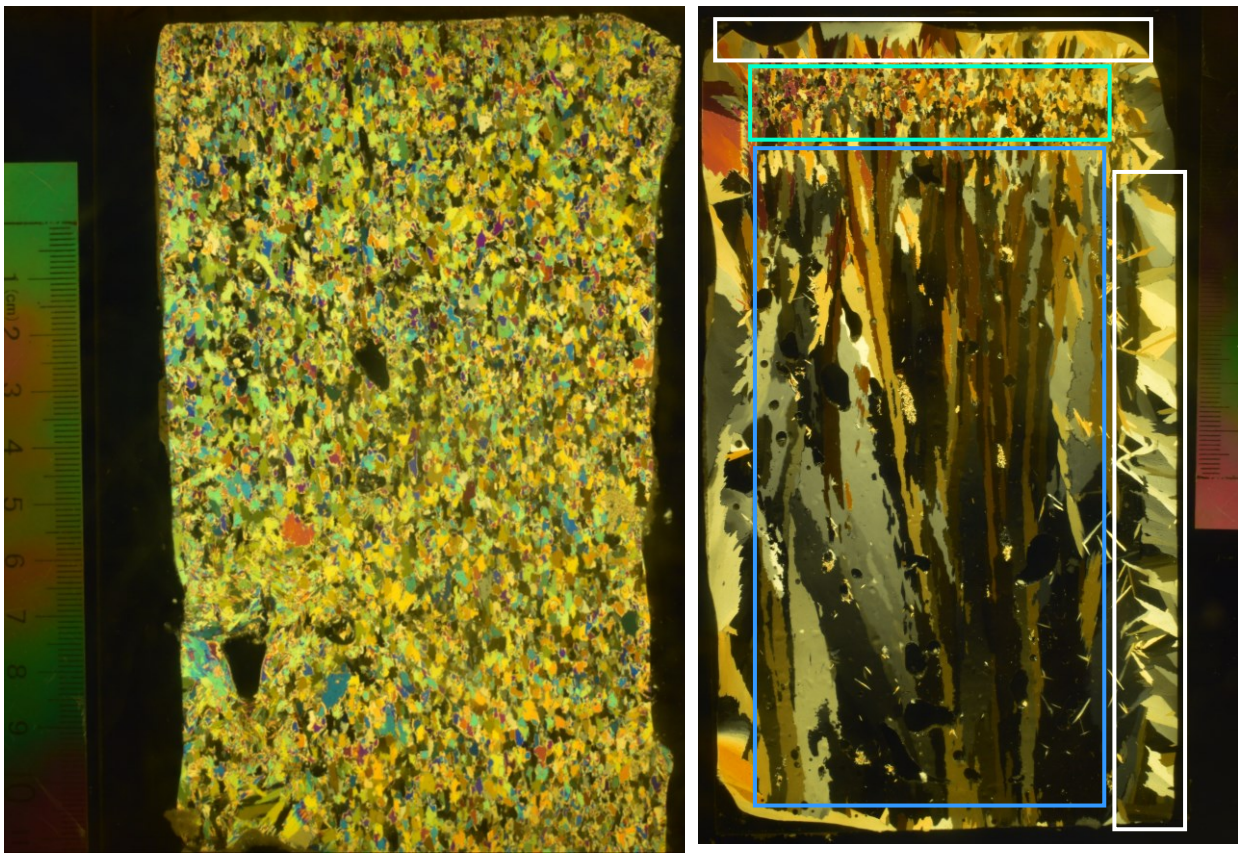

Figure 5-2 - Thin sections of an ice core showing (a.) granular layer; and (b.) columnar grains.

The grain size of columnar crystals was determined by applying the ASTM grain size method on thin sections of four cross-sections of random ice cores as shown in Figure 5-3. The results are summarized in *Table 5-3* where average columnar grain size varies from 0.56 to 0.64 cm.

a.

b.

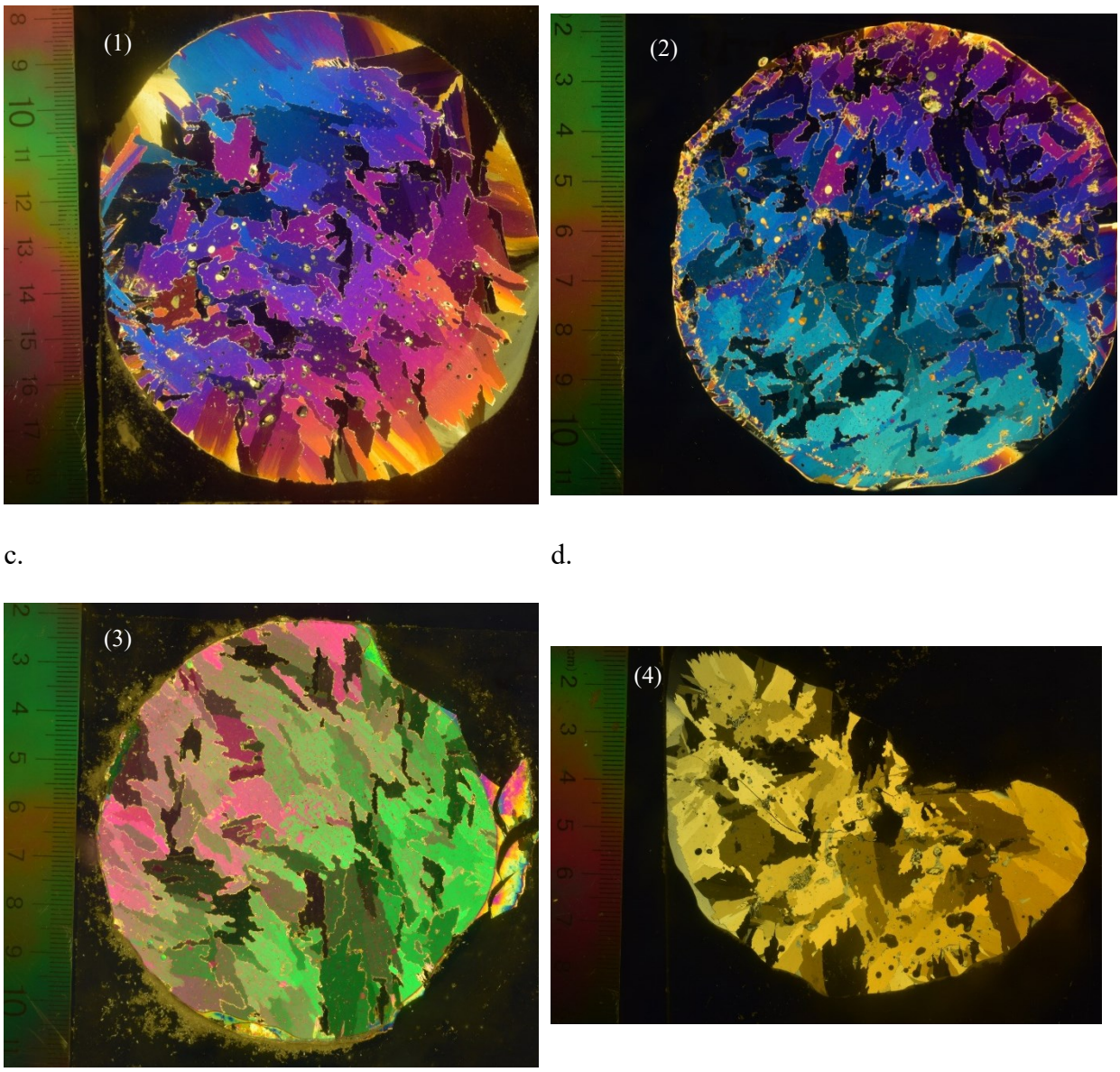

c.

d.

Figure 5-3 - Four thin sections (a.-d.) of cross-section samples of ice cores used for grain size analysis.

Figure 5-4 shows cross sections of samples that show the granular microstructure of snow-ice layer. *Table 5-3* summarizes the grain size which ranges from 0.93 and 1.0 mm.

a. b.

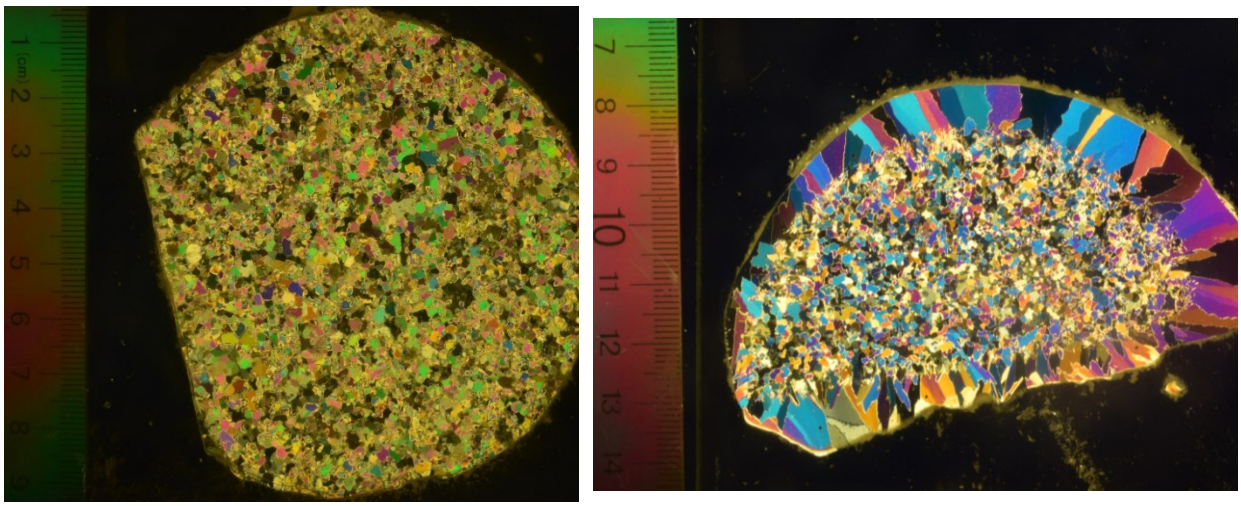

Figure 5-4 - Thin sections of two sample cross-sections showing granular microstructure.

Table 5-3 – Average grain size in [cm] for each sample.

Sample #	Average Grain Size [cm]
*Figure 5-3*a	0.64
*Figure 5-3*b	0.63
*Figure 5-3*c	0.56
*Figure 5-3*d	0.61
*Figure 5-4*a	0.93
*Figure 5-4*b	1.00

5.1.4. Grain Size Uniformity in Beams

The saline ice core's long axis was parallel to growth direction of ice sheet as illustrated in Figure 3-10. This results in some slight variation in grain size from one end of the beam to the other which adds some variability for saline ice tests. Additional saline ice specimens extracted perpendicular to ice sheet growth direction so that beam microstructure is consistent along the long axis as visualized in Figure 5-5 are recommended for future test programs.

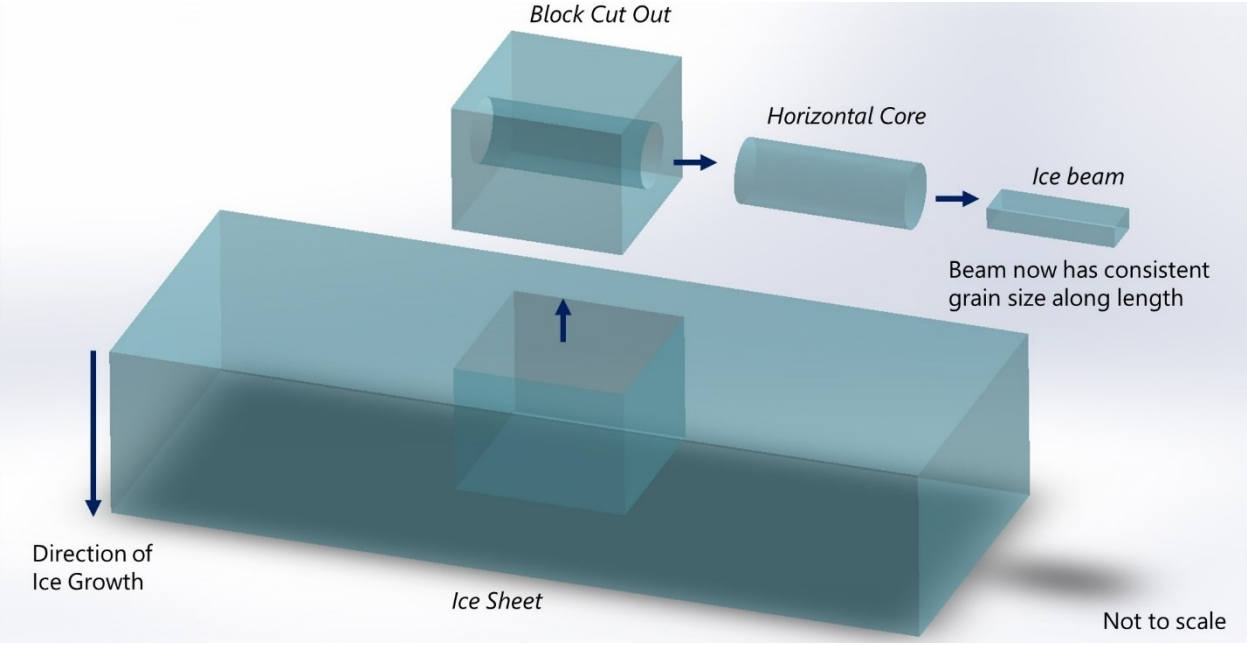

Figure 5-5 - Coring method to reduce variability in ice beam grain structure along the length.

5.2. Saline Apparent Flexural Strength Test Results

In total, 43 flexural strength tests were completed for the saline series. Test data with all the measured variables are provided in Table 5-4. The peak values from flexural load cell during testing was used to calculate the apparent flexural strength (extreme fiber stresses) with the standard equation derived from beam bending theory [11]:

$$\sigma_f = \frac{3p(\mathrm{l} - \mathrm{c})}{2\mathrm{w}t^2} \quad (13)$$

Where p is peak load, l is distance between bottom supports, c is distance between top supports, w is width of the beam and t is the thickness.

Table 5-4 - Raw data for apparent flexural strength of freshwater ice tests.

Target Compression [%]	Strain Rate	Index #	Test #	Failure Time [s]	Flexural Strength [MPa]	MTS Displacement [mm]	Right LVDT [mm]	Left LVDT [mm]	Center LVDT [mm]	Axial Load [N]	Compressive Stress [MPa]	Measured Compression [%]
0	$4.67x10^{-4}$ (Low)	1	1	1.988	1.767	0.195	0.120	0.132	0.077	-	-	-
		2	2	2.596	1.327	0.262	0.063	0.361	0.000	-	-	-
		3	3	5.578	2.624	0.558	0.040	0.658	0.166	-	-	-
		4	10	0.393	1.592	0.385	0.704	0.086	0.115	-	-	-
		5	13	4.809	1.478	0.487	0.032	0.584	0.094	-	-	-
	$4.67x10^{-3}$ (Medium)	6	4	0.132	1.202	0.126	0.030	0.058	0.077	-	-	-
		7	5	0.312	0.964	0.306	0.004	0.536	0.034	-	-	-
		8	6	0.461	0.898	0.452	0.312	1.115	0.084	-	-	-
		9	11	0.448	2.494	0.442	0.046	0.064	0.054	-	-	-
		10	12	0.253	1.817	0.247	0.094	0.113	0.132	-	-	-
	$4.67x10^{-2}$ (High)	11	7	0.022	1.494	0.174	0.132	0.319	0.067	-	-	-
		12	8	0.018	1.400	0.130	0.033	0.050	0.096	-	-	-
		13	9	0.086	1.611	0.805	1.574	1.248	0.390	-	-	-
35	$4.67x10^{-4}$ (Low)	14	36	40.000	3.000	2.000	4.895	5.759	5.000	708	0.595	41
		15	37	37.861	3.178	3.789	1.809	1.969	6.177	713	0.529	36
		16	38	30.724	2.810	3.070	1.812	1.706	3.157	681	0.603	41
	$4.67x10^{-3}$ (Medium)	17	39	4.307	3.429	4.310	2.846	2.172	7.871	686	0.531	36
		18	40	4.208	2.959	4.211	2.868	2.342	7.184	689	0.555	38
		19	41	4.278	3.070	4.280	2.552	2.115	7.584	694	0.510	35
	$4.67x10^{-2}$ (High)	20	42	0.187	2.220	1.825	1.101	0.663	2.494	702	0.526	36
		21	43	0.123	2.265	1.192	0.683	0.576	1.469	713	0.555	38
		22	44	0.232	2.592	2.279	1.458	0.955	3.509	684	0.571	39

Continued on next page

Target Compression [%]	Strain Rate	Index #	Test #	Failure Time [s]	Flexural Strength [MPa]	MTS Displacement [mm]	Right LVDT [mm]	Left LVDT [mm]	Center LVDT [mm]	Axial Load [N]	Compressive Stress [MPa]	Measured Compression [%]
Continuing from previous page												
70	$4.67x10^{-4}$ (Low)	23	26	26.422	3.838	2.642	2.433	0.756	2.171	1188	1.015	69
		24	27	32.943	4.639	3.293	2.038	1.900	4.166	1300	0.991	68
		25	28	34.796	4.904	3.475	2.230	2.043	4.577	1314	1.071	73
	$4.67x10^{-3}$ (Medium)	26	29	3.895	4.234	3.893	2.831	2.213	5.455	1327	1.089	75
		27	30	3.073	4.775	3.076	1.656	1.500	3.996	1330	1.049	72
		28	31	4.864	5.165	4.864	2.888	3.181	8.769	1311	0.975	67
		29	35	2.038	3.722	2.036	1.136	1.339	1.628	1322	1.023	77
	$4.67x10^{-2}$ (High)	30	32	0.210	3.787	2.056	0.516	1.710	1.906	1391	1.121	78
		31	33	0.113	2.916	1.083	0.592	0.339	0.930	1324	1.140	75
		32	34	0.133	2.914	1.285	0.743	0.626	1.134	1306	1.097	70
125	$4.67x10^{-4}$ (Low)	33	14	39.816	5.980	3.982	2.056	2.401	4.565	2459	1.872	128
		34	15	31.527	5.095	3.159	2.156	2.029	4.516	2451	1.848	127
		35	16	32.420	5.097	3.244	2.099	1.619	4.226	2414	1.874	128
		36	17	49.477	7.008	4.945	3.323	2.624	6.010	2566	1.912	131
	$4.67x10^{-3}$ (Medium)	37	18	3.582	7.304	3.584	1.915	1.955	0.000	2491	1.874	128
		38	19	1.708	4.949	1.707	0.665	0.790	1.704	1898	1.442	99
		39	20	3.638	6.007	3.637	2.625	1.838	4.824	2323	1.701	117
		40	21	3.006	6.257	3.003	1.647	1.749	4.056	2494	1.938	133
	$4.67x10^{-2}$ (High)	41	22	0.091	3.545	0.858	0.303	0.498	0.382	2272	1.826	125
		42	23	0.179	4.075	1.752	0.313	1.355	0.926	1546	1.199	82
		43	24	0.123	4.553	1.150	0.484	0.500	0.860	2435	1.834	126
		44	25	0.119	4.924	1.145	0.352	0.712	0.782	2245	1.698	116

5.3. Simple Flexural Strength Tests

5.3.1. Normalizing Data

Twelve (12) saline ice beams were tested for simple flexural strength at three different strain rates to determine the baseline strength and for comparison with literature data compiled by Aly [15] for the specific beam volume of 0.00027 m^3. Due to salinity being a significant factor affecting saline ice strength, the test results were normalized to 5 ppt salinity and -10 ºC testing temperature as done by Aly [15] for all saline test data for equal comparison. The salinity of current ice samples was assumed to be 2.1 ppt as described in Section 5.1.2. Equation (14) is used to calculate the normalized strength $\sigma_{normalized}$ [15]. $\sigma_{measured}$ is the strength measured during testing, $\sigma_{reference}$ is the reference strength for 5 ppt salinity and -10 ºC testing temperature (765 kPa) from Aly's model and σ_{model} is the strength predicted by Aly's model for a given test salinity and temperature.

$$\sigma_{normalized} = \sigma_{measured} \cdot \frac{\sigma_{reference}}{\sigma_{model}} \quad (14)$$

Equation (15) is the model equation determined by Aly [15] used to calculate strength predicted by his model for a given brine volume, v_b.

$$\sigma_{model} = 1.73e^{-4.89\sqrt{v_b}} \quad (15)$$

Equation (16) is used to calculate the brine volume where S is salinity in ppt and $|T|$ is absolute temperature in ºC.

$$v_b = S \cdot \left(\frac{49.185}{|T|} + 0.532\right) \quad (16)$$

Measured flexural strength and normalized strengths are provided in Table 5-5 for different strain rates and their repetitions. The normalized strength varies from a minimum of 0.67 MPa to a maximum of 1.50 MPa.

Table 5-5 - Measured and normalized flexural strength of saline ice beams.

Speed [mm/s]	Index	Repetition #	Measured Strength [MPa]	Normalized Strength [MPa]
0.1	1	1	1.767	1.33
	2	2	1.327	1.00
	3	3	1.592	1.19
	4	4	1.478	1.11
1.0	5	1	1.202	0.90
	6	2	0.964	0.72
	7	3	0.898	0.67
	8	4	2.000	1.50
	9	5	1.817	1.36
10	10	1	1.494	1.12
	11	2	1.400	1.05
	12	3	1.611	1.21

5.3.2. Comparison with Literature

Figure 5-6 shows the current test data plotted with flexural tests in literature against their beam volumes compiled by Aly [15]. The saline model relationship determined by Aly [15] is also plotted as a line which is given by Equation (17) where V is beam volume in m^3, V_1 is standard beam volume 1 m^3, and v_b is brine volume.

$$\sigma_f = 1324 \cdot \left(\frac{V}{V_1}\right)^{-0.054} \cdot e^{-4.969 \cdot \sqrt{v_b}} \quad (17)$$

As seen in the plot, the current test data fits well the general trend of higher average flexural strengths as the beam volume increases. The data points are close to the saline model equation line as well. Compared to other tests the scatter of data is smaller. The higher variability in the data can be attributed to the different types of tests in literature plotted such as 3-point, 4-point, cantilever, lab and field tests.

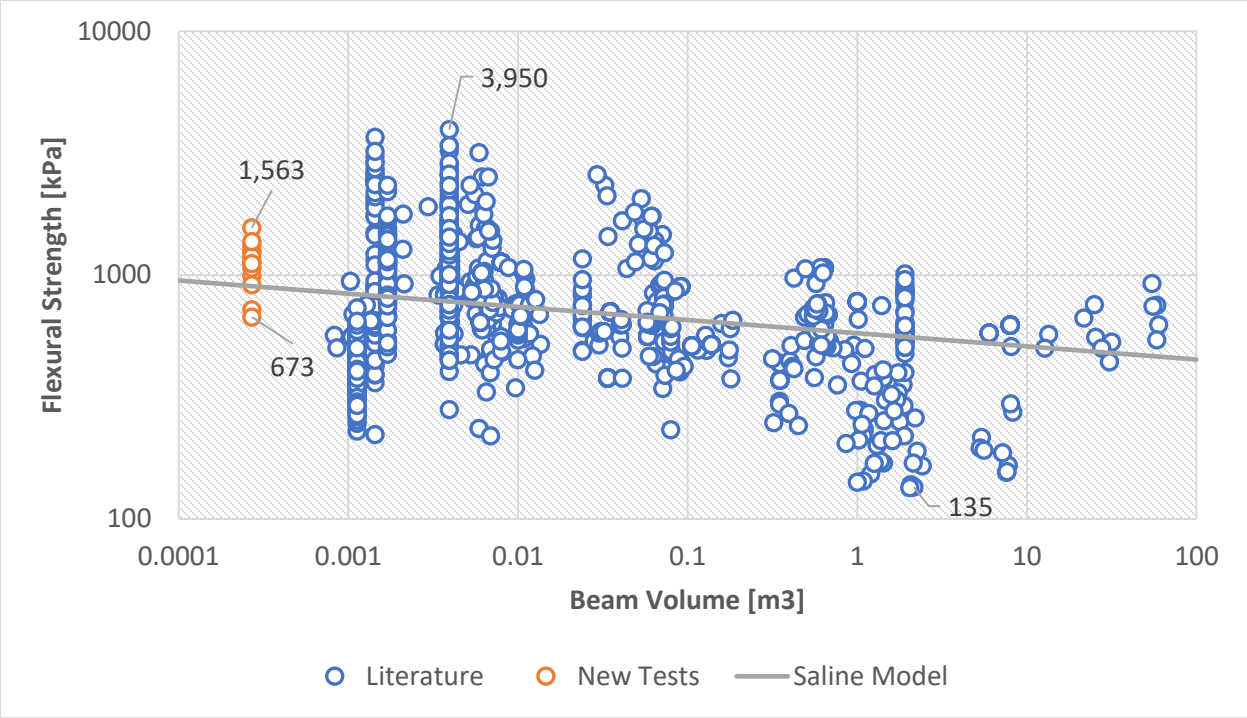

Figure 5-6 - Plot of normalized test data, normalized literature data and saline model.

5.3.3. Summary

Figure 5-7 plots flexural strength of saline ice beams divided by different strain rates along with average strength. For low strain rate, the average strength is 1.54 MPa, 1.48 MPa for medium strain rate and 1.50 MPa for high strain rate. High variability is observed for medium strain rate tests, which can be attributed to non-uniformity in the specimens arising from voids and existence of brine pockets and channels as seen in Figure 5-8. No strong relationship between strain rate and flexural strength is observed like freshwater tests. The baseline average for saline tests for compression tests is taken to be 1.51 MPa which is 11% less than baseline average strength for freshwater ice which was 1.68 MPa. This is expected due to the imperfect nature of the structure of saline ice which causes it to be weaker and fail more easily.

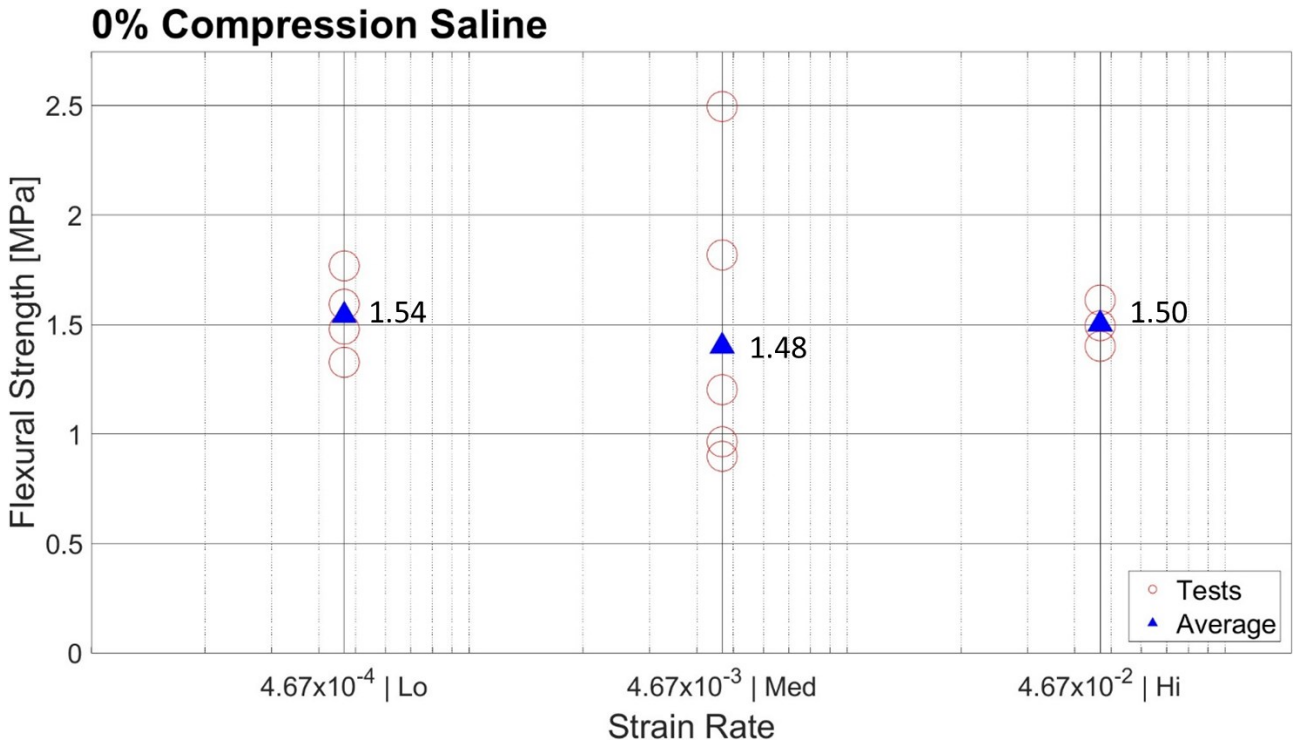

Figure 5-7 - Flexural strength of saline ice beams separated by strain rate.

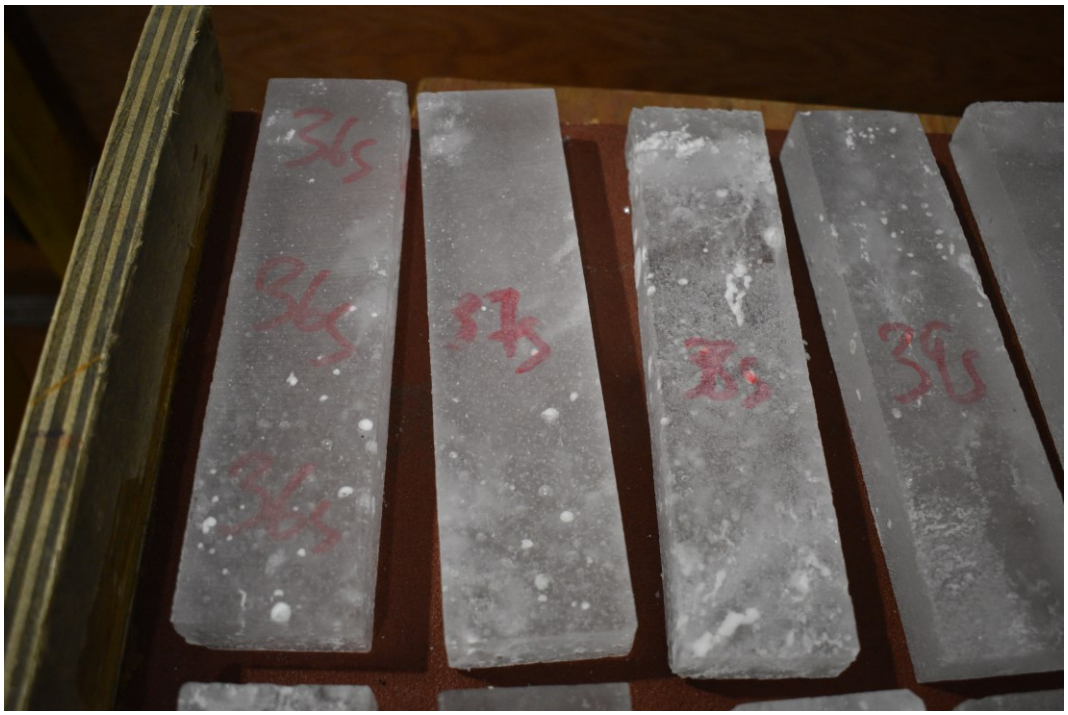

Figure 5-8 - Saline ice samples showing different types and amounts of imperfections.

5.4. Flexural Tests under Axial Compression

5.4.1. Low Compression Flexure Tests (SW-IPC 35%)

In Figure 5-9 the plot shows results of individual tests at the three strain rates and their average in blue triangles. Compared to the baseline flexural strength of 1.46 MPa for the unconfined case, this amount of compression has had a strong influence on the flexural strength. For the low and medium strain rates, the flexural strength increase is nearly two times that of baseline strength. As observed for freshwater tests, the strength increase is smaller for higher strain rate at 1.62 times that of baseline. Percentage changes are given in *Table 5-6*.

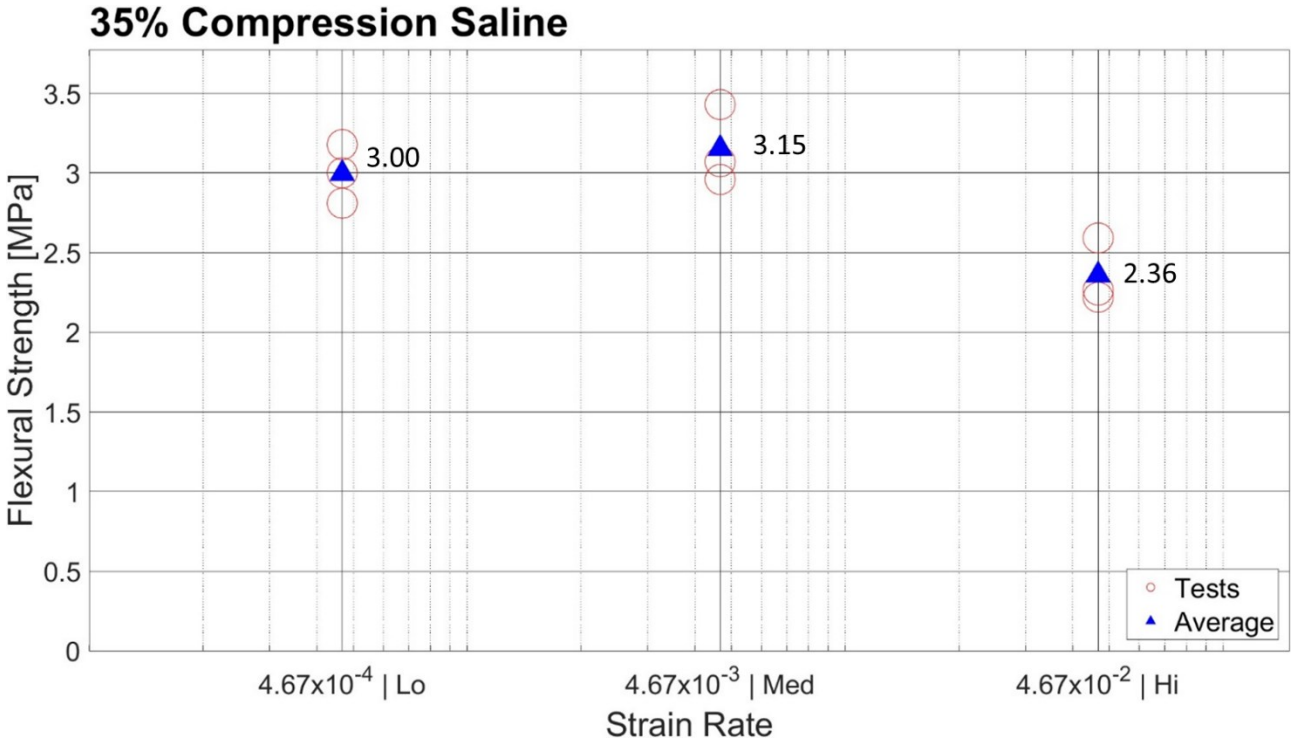

Figure 5-9 - Flexural strength of saline ice measured at different strain rates for 35% compression.

Table 5-6 - Summary of ratio of enhanced flexural strength to unconfined baseline for different strain rates for IPC 135% case.

Strain rate	Average Flexural Strength [MPa]	Flexural Strength Ratio
low	3.00	205%
med	3.15	216%
high	2.36	162%

5.4.2. Medium Compression Flexure Tests (SW-IPC 70%)

Figure 5-10 shows individual flexural strengths for IPC 70% case for different strain rates which is almost 1.5 times that of low compression 35%. Average for each strain rate is also shown.

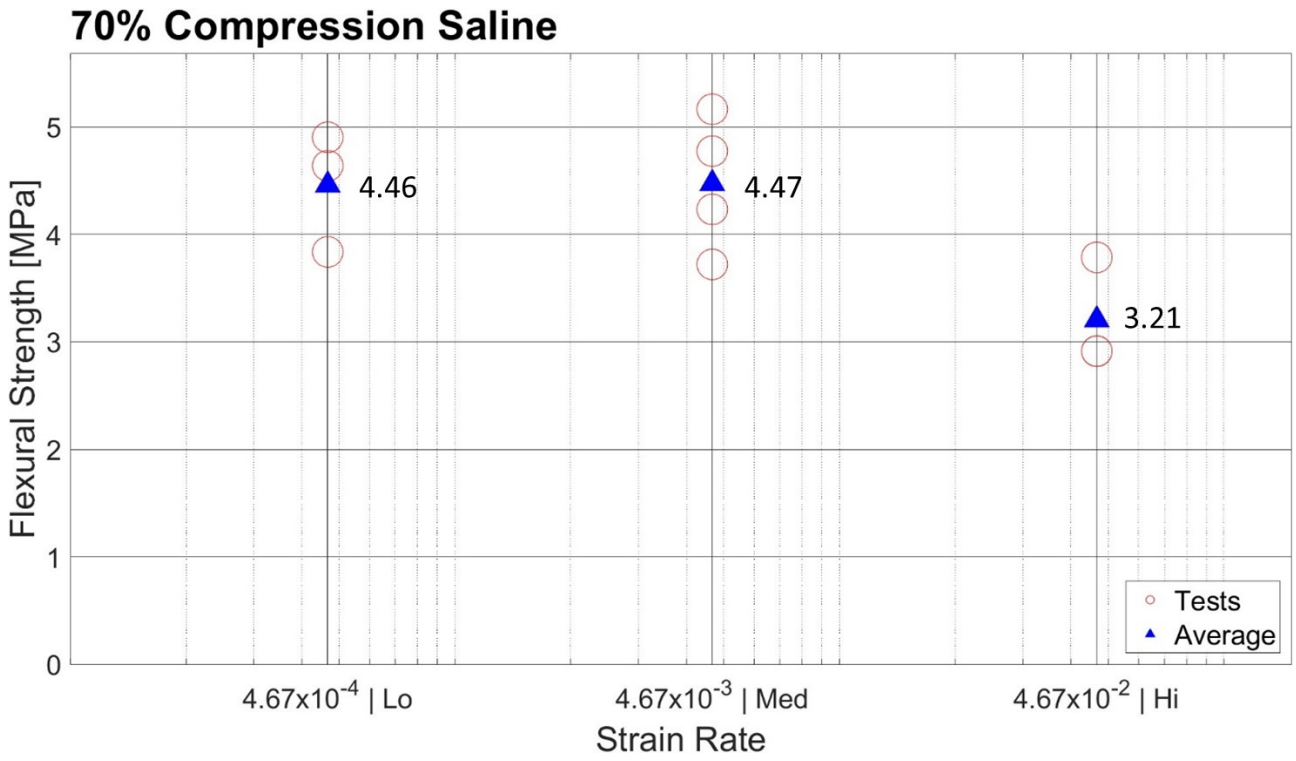

Figure 5-10 - Flexural strength of SW-IPC70% Tests at different strain rates.

Table 5-7 summarizes the percentage increase compared to baseline strength for each strain rate case. We can see that for low and medium strain rates, the strength has increased by nearly another 100% more compared to the 35% compression case and reaching 300%. Continuing from the

previous trend, the high strain rate strength is lower than the slower strain rates although the strength has increased from 162 to 220 %. There is greater variability between different repetitions for each strain rate as evidenced by larger spread of data points compared to low compression case.

Table 5-7 - Summary of ratio of enhanced flexural strength to unconfined baseline for different strain rates for 70% compression case.

Strain rate	Average Flexural Strength [MPa]	Flexural Strength Ratio
low	4.46	305%
med	4.47	306%
high	3.21	220%

5.4.3. High Compression Flexure Tests (SW-IPC 125%)

Figure 5-11 shows individual flexural strengths for 125% compression case while *Table 5-8* lists the percentage increase in flexural strength for each strain rate case. For 125% compression, the strength for low and medium strain rates again increases by another 100% compared to 70% compression to reach about 400% of baseline strength. As seen with the other two compression levels, the high strain strength is lower than slower speeds but has still increased from 70% and is nearly 300% strength of baseline value of 1.46 MPa. In terms of percentage deviation from , the variation between 125% and 70% compression cases are similar.

Table 5-8 - Summary of ratio of enhanced flexural strength to unconfined baseline for different strain rates for SW-IPC125% Tests.

Strain rate	Average Flexural Strength [MPa]	Flexural Strength Ratio
low	5.80	397%
med	6.13	420%
high	4.27	293%

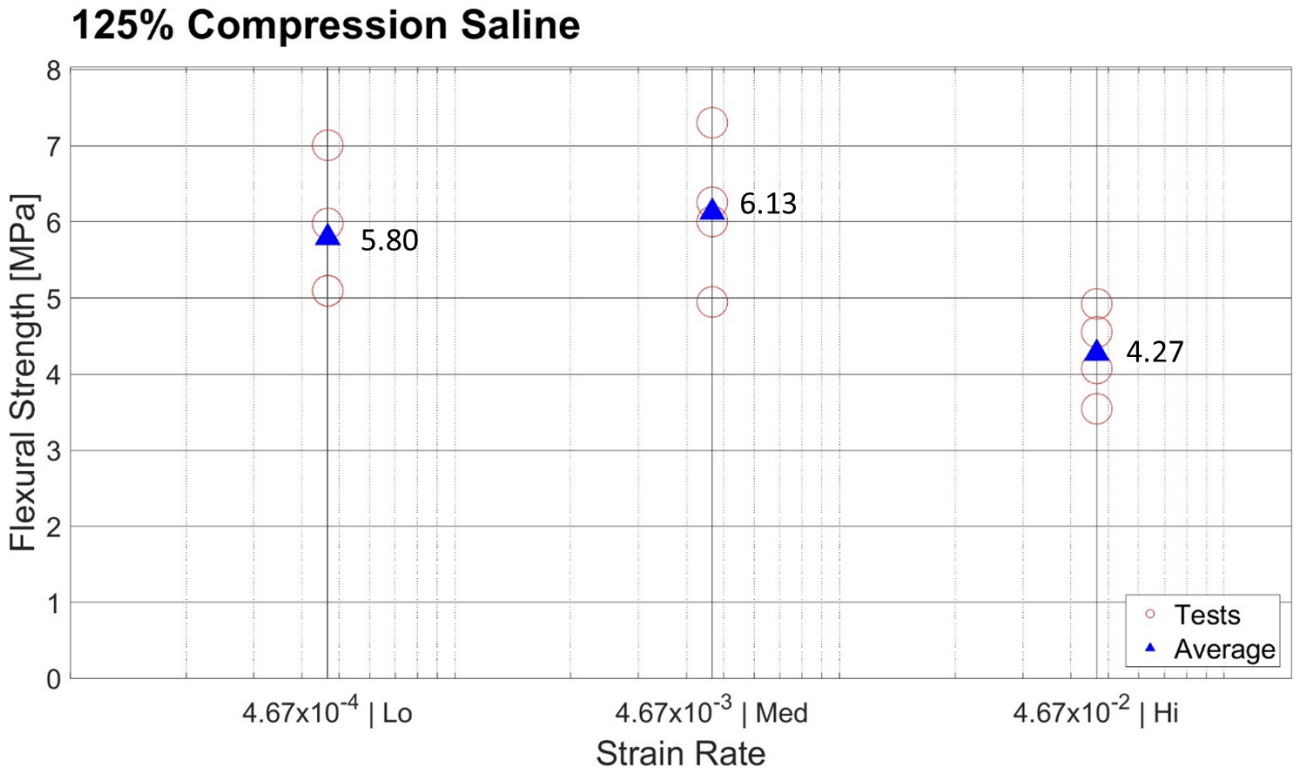

Figure 5-11 - Flexural strength of saline ice measured at different strain rates for SW-IPC125% Tests.

5.5. Summary of Apparent and Nominal Flexural Strength

Apparent flexural strength is the flexural strength as experienced during interaction with structures. Nominal flexural strength accounts for the applied compressive axial stress and subtracts it from the outer fibre stress to study the trends in flexural strengths.

In Figure 5-12, flexural strength is plotted against strain rates for different compression levels on a logarithmic x-axis along with baseline strength of 1.46 MPa. For all 3 compression levels (35, 70 and 125%), flexural strengths are similar for low and medium strain rates and decrease for the high strain rate. The decrease in strength at high strain rate compared to low and medium is highest for IPC 125% and lowest for IPC 35%. As discussed in the previous section, strength is highest for all strain rates at IPC 125% followed by IPC 70% and then IPC 35%. Strength-strain

relationships are described by power law equations for all the compressions as follows. All strain values have been divided by a factor of 4.67.

The power line of best fit for IPC 35% flexural strength $\sigma_{f,35\%}$ versus strain rate, $\dot{\varepsilon}$, with a R^2 value of 0.923 is given by Equation (18):

$$\sigma_{f,35\%} = 3.1146e^{-5.873\dot{\varepsilon}} \qquad (18)$$

Next, the power line of best fit for 70% compression flexural strength $\sigma_{f,70\%}$ versus strain rate, $\dot{\varepsilon}$, with a R^2 value of 0.989 can be described by Equation (19):

$$\sigma_{f,70\%} = 4.5497e^{-7.46\dot{\varepsilon}} \qquad (19)$$

Lastly, the power line of best fit for 125% compression flexural strength $\sigma_{f,125\%}$ versus strain rate, $\dot{\varepsilon}$, with a R^2 value of 0.931 can be described by Equation (20):

$$\sigma_{f,125\%} = 6.0613e^{-7.392\dot{\varepsilon}} \qquad (20)$$

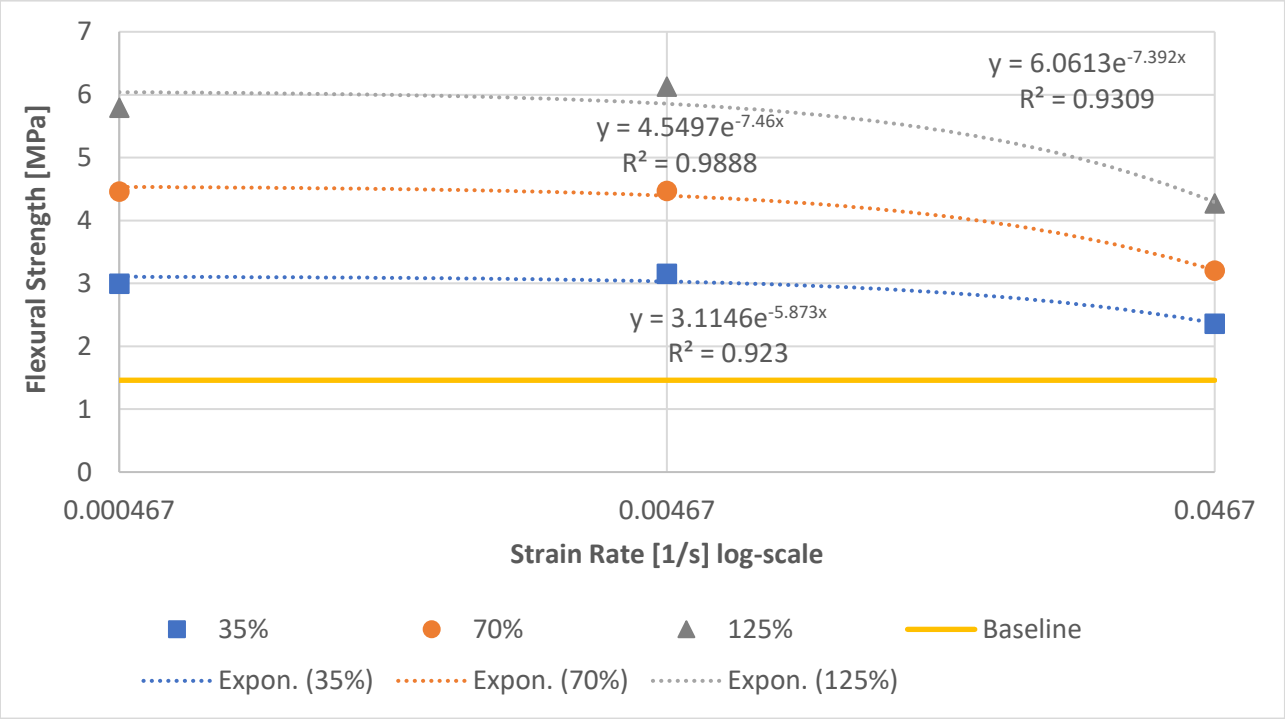

Figure 5-12 – Apparent flexural strength plotted against strain rates for different compression levels.

Overall, we see in Figure 5-13 that there is an increasing trend for flexural strength as compression level is increased. The increase in strength is similar for low and medium strain rates. At high strain rate, the strength increase is lower for all compression levels. As compression increases, the difference in strength between low-medium and high strain rate also increases as seen in the diverging trend in Figure 5-13. For IPC 35%, the strength increase is 100%, for IPC 70%, the strength increase doubles to 200% and for IPC 125%, the strength increase reaches a maximum of 300% for low and medium strain rates. For high strain rate, the maximum strength increase is nearly 200% for IPC 125% and minimum is about 50% for IPC 35%. Figure 5-14 shows the average apparent strength flexural strength values for the data plotted in Figure 5-13. Figure E 5 in Appendix E - Additional Plots and Analysis also plots all apparent test data points with the averages shown in Figure 5-14.

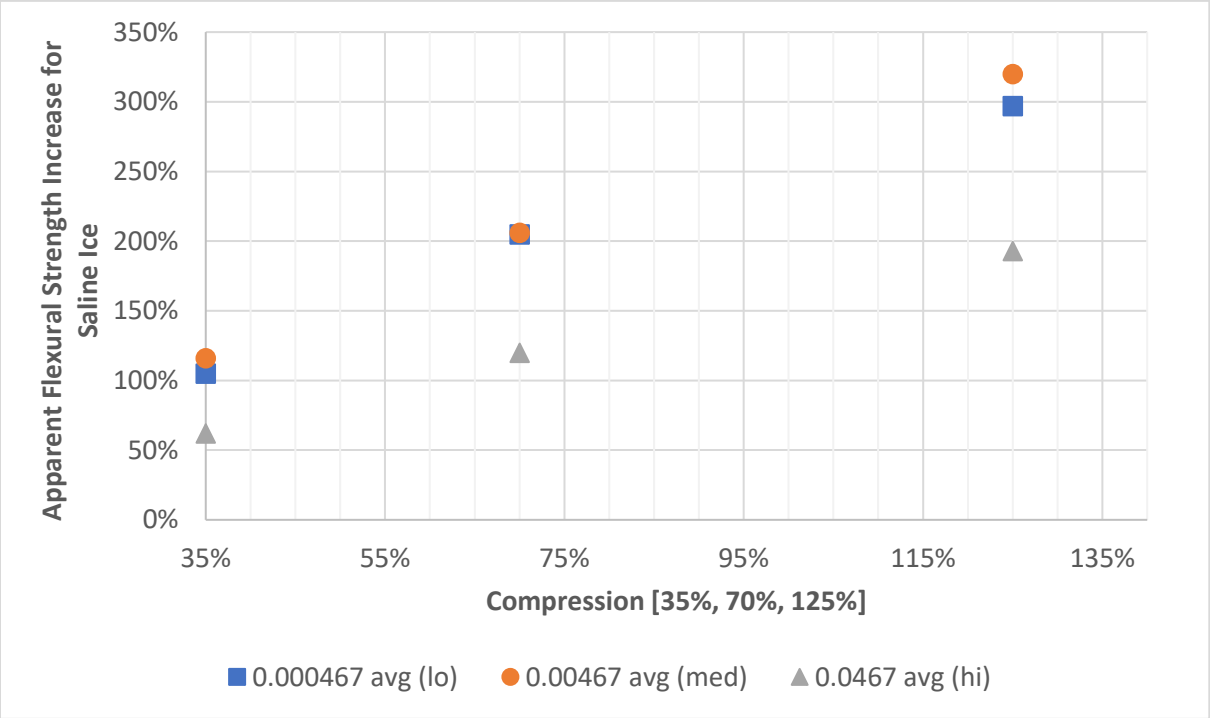

Figure 5-13 – Apparent flexural strength increase plotted against test compression levels for different strain rates.

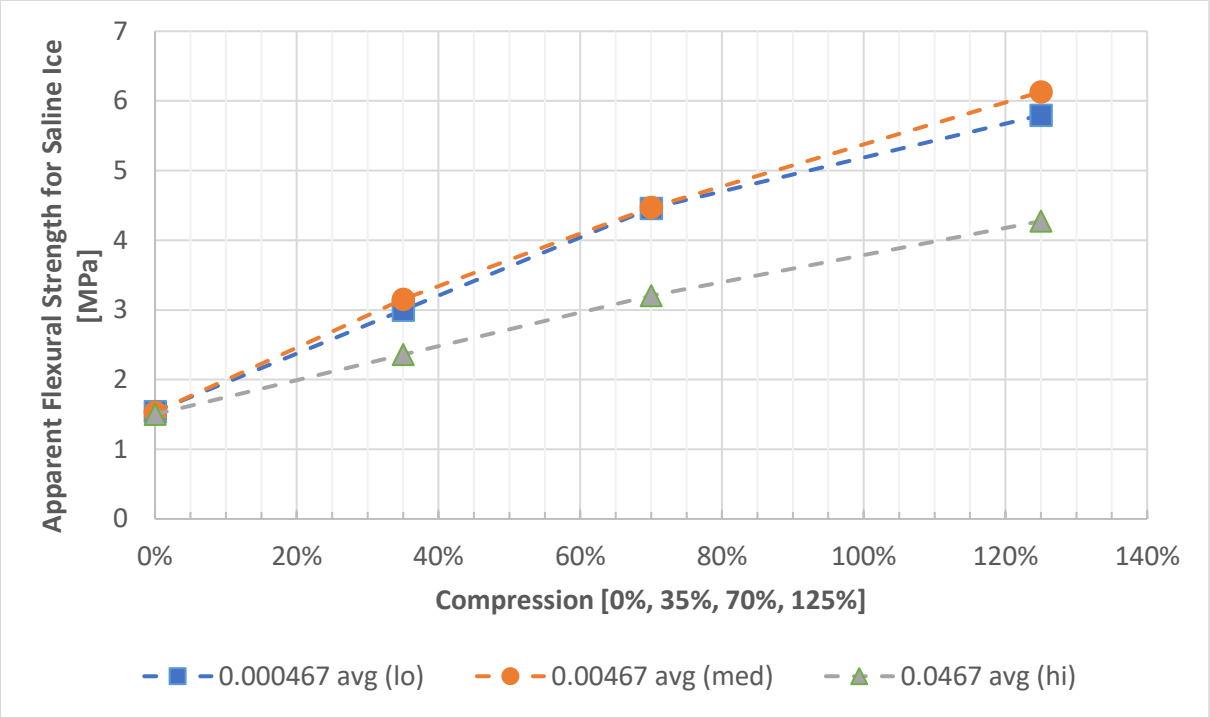

Figure 5-14 - Average values of apparent freshwater flexural strengths plotted against test compression levels for different strain rates.

Figure 5-15 shows nominal flexural strength increase for different compression levels at low, medium and high strain rates where the amount of axial stress applied to sample has been subtracted from the flexural strength measurements. Similar trends are preserved as seen in Figure 5-13, where the strength increases with compression level and high strain rate strength is lower than low and medium strain rate cases. One notable distinction between the two plots is that the difference between low/medium strain and high strain is more pronounced as compression increases more for nominal strengths than apparent strengths. Figure 5-16 shows the average apparent strength flexural strength values for the data plotted in Figure 5-15. Figure E 6 in Appendix E - Additional Plots and Analysis also plots all nominal test data points with the averages shown in Figure 5-16.

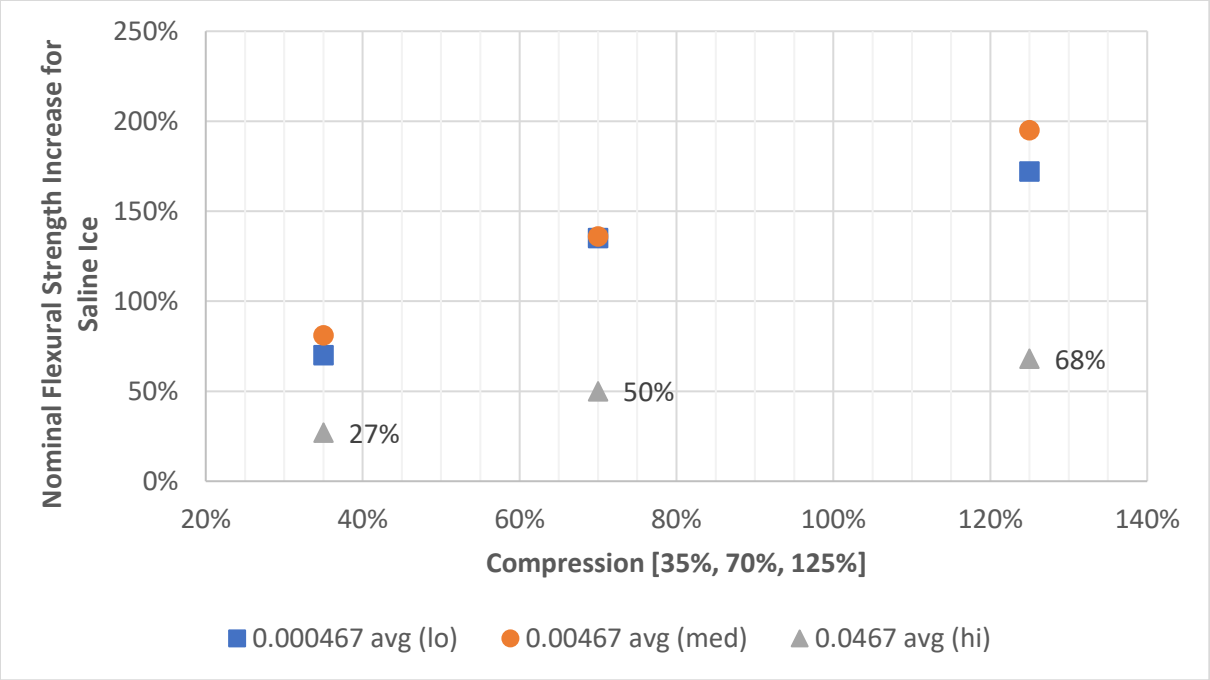

Figure 5-15 – Nominal flexural strength increase plotted against test compression levels for different strain rates.

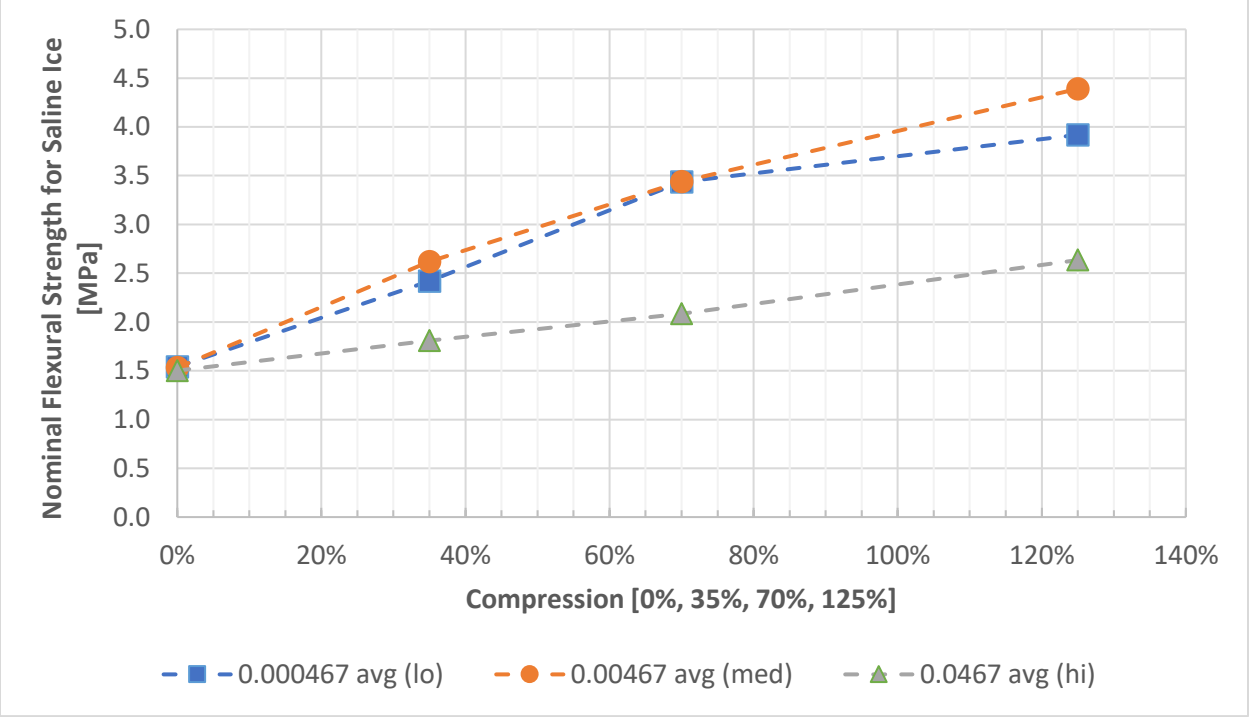

Figure 5-16 - Average values of nominal saline flexural strengths plotted against test compression levels for different strain rates.

5.6. Deflection Analysis

Figure 5-17 shows average displacements and with their standard deviation parts plotted for all compression levels and high ($4.67x10^{-2}$), medium ($4.67x10^{-3}$) and low ($4.67x10^{-4}$) strain rates. Generally, we observe that LVDT readings are higher than MTS measurements for all compression cases except the high strain readings for IPC 70% and IPC 125%. The reason could be that the MTS ram was displacement controlled and applied force over the whole sample while the LVDT measured the displacement at a specific point and was influenced strongly by physical changes occurring at the center of the sample which were more prone to cracking and sections of ice breaking. This also explains the generally larger standard deviation bars for LVDT compared to MTS.

In terms of trends, for simple unconfined flexural tests, there is no strain rate effect as expected and is consistent with observations for freshwater tests as well. This is due to the samples failing due to tensile fracture which is generally independent of strain rate effects. For IPC 35% and IPC 70%, the high strain rate tests have the smallest deflections while medium strain rates have the highest average deflection. The low strain rate tests have deflections slightly smaller than medium strain rate cases. This is quite different from freshwater tests where the average deflection decreased as strain rate increased for 75% and 135% compression with low strain tests having highest deflections and high strain rates having lowest average deflections. The IPC 125% case is slightly different where strength decreases as strain rate increases which was the general observation for freshwater tests.

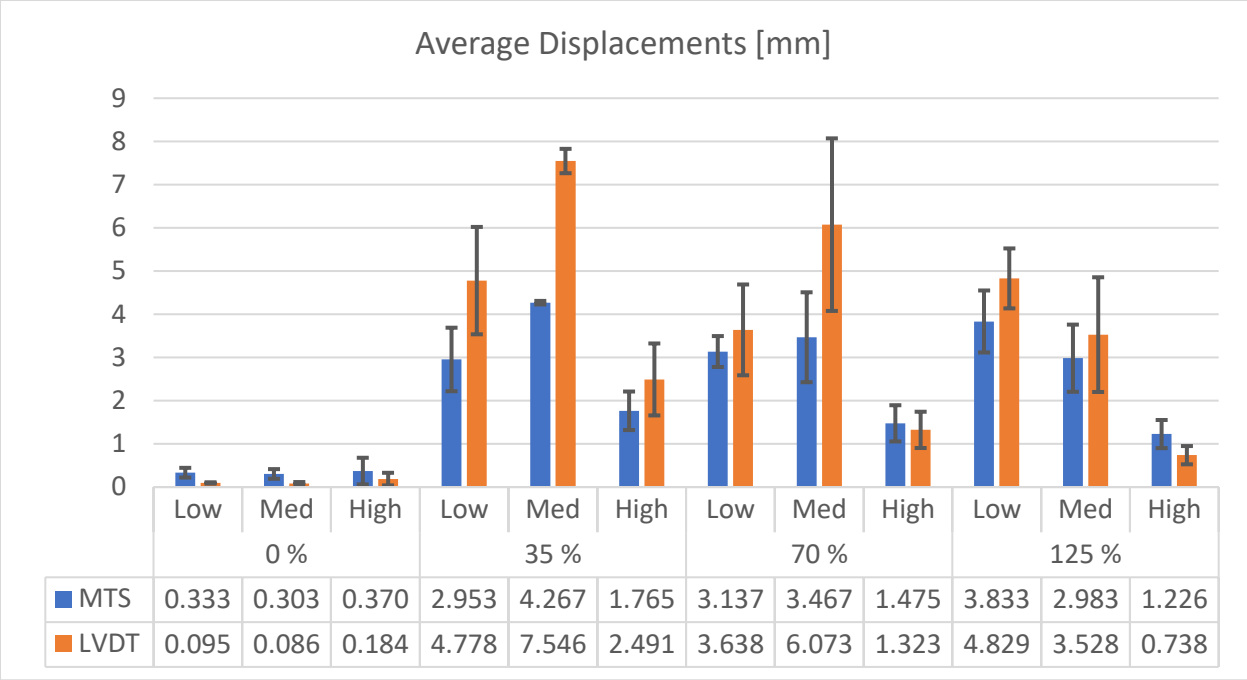

	Low	Med	High	Low	Med	High	Low	Med	High	Low	Med	High
	0 %			35 %			70 %			125 %		
MTS	0.333	0.303	0.370	2.953	4.267	1.765	3.137	3.467	1.475	3.833	2.983	1.226
LVDT	0.095	0.086	0.184	4.778	7.546	2.491	3.638	6.073	1.323	4.829	3.528	0.738

Figure 5-17 - Average midpoint displacement measured using LVDT and MTS are summarized for all compression levels and associated strain rates: (Low = $4.67x10^{-4}$, Med = $4.67x10^{-3}$ and High = $4.67x10^{-}$)^{2}

5.7. Failure Mechanism

Planar fracture of ice beam in simple flexural tests was also observed for saline ice. The cracks originated from bottom of beam (tensile) and the sample failed upon complete crack through. The failure location was limited between top indenters for all thirteen (13) samples that were tested. One notable difference compared to the freshwater samples was that the fracture surface is not perfectly parallel to ends of the beam and this could be due to imperfections and voids within the sample which also influenced where the sample failed. Figure 5-18 shows samples 10, 11, 13 and 12 in order after failure, depicting the different failure locations and angled fracture surface.

Figure 5-18 - Saline ice samples tested in 4-point bending tests.

For 35% compression, the failures were characterized by a single vertical tensile crack in the bottom at the boundary of top indenters, shown in Figure 5-19b, progressing into a horizontal crack (c). For high strain, the crack is at a sharp normal angle while for lower strains, the crack propagation from vertical to horizontal is more rounded. After separation, the entire strength of ice is carried by a thin "bridge" of ice (c) and failure occurs when top of this section fails from compression (d).

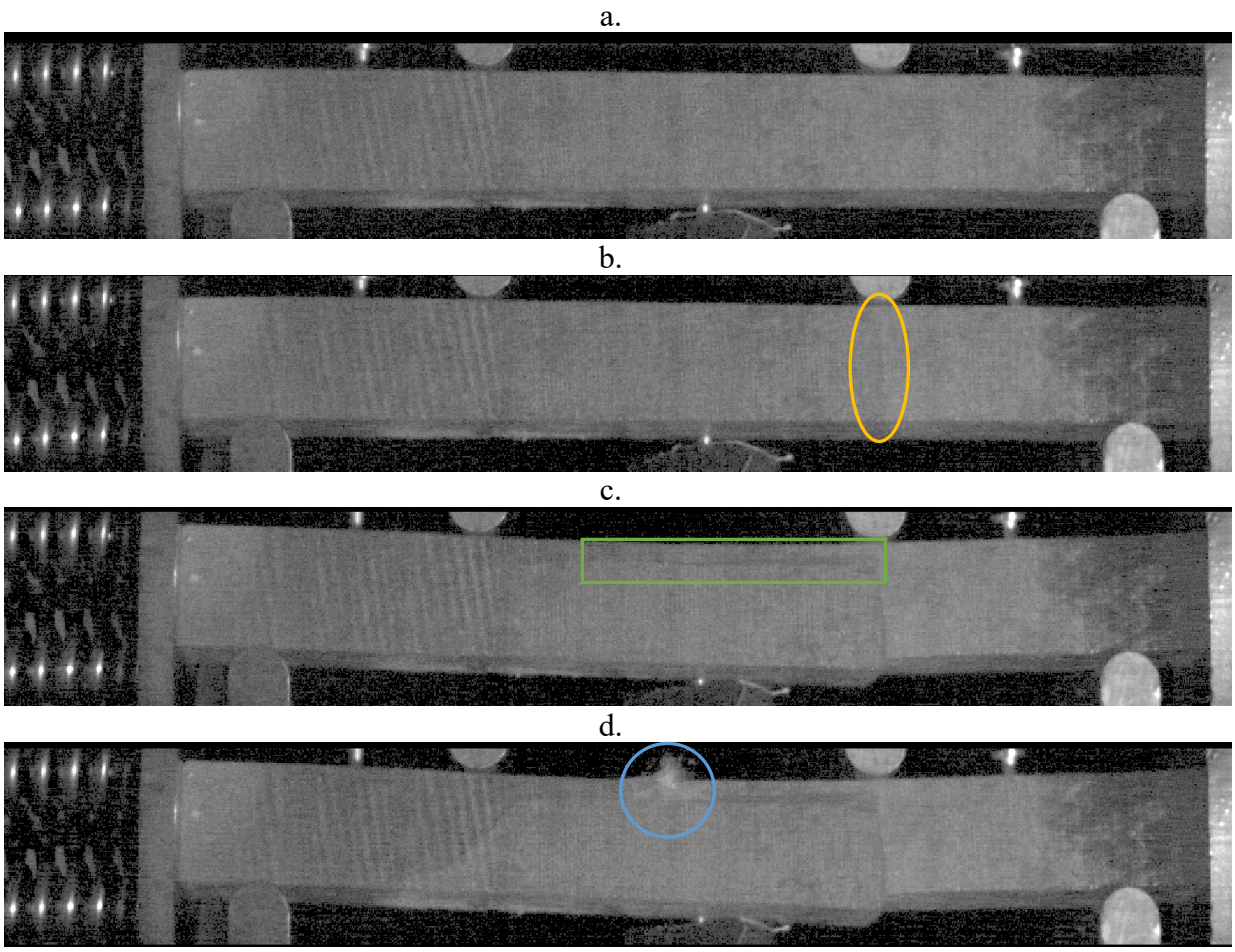

Figure 5-19 - Sequence of failure for ice sample at IPC 35% at high strain rate.

Similar "bridging" is shown for IPC 35% at lower strain rates in Figure 5-20. The crack from vertical to horizontal was more rounded and the intact layer is also noticeably thicker than the high strain rate which can explain the higher flexural strength seen for lower strain rates.

For IPC 70%, usually two cracks were observed with each one under an indenter as seen in Figure 5-21b and failure originating from crushing in the top (c). For high strain tests, the vertical cracks do not propagate further into horizontal ones as seen for IPC 35%. The unbroken section is thicker (Figure 5-22a) than ones seen for IPC 35% in Figure 5-20. This can be explained by higher compressive loads deepening the neutral axis thus increasing the thickness of ice and its ability to

bear higher stresses. In some tests, the tensile crack was close to the center of the sample rather than under an indenter (Figure 5-22b).

a.

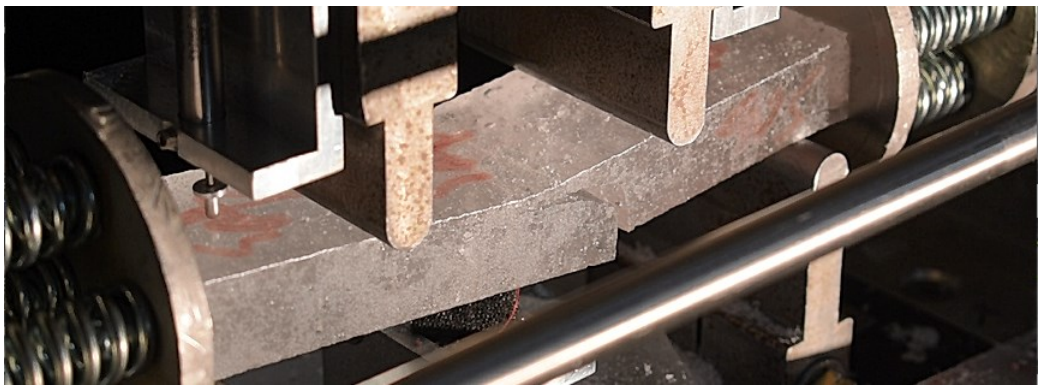

b.

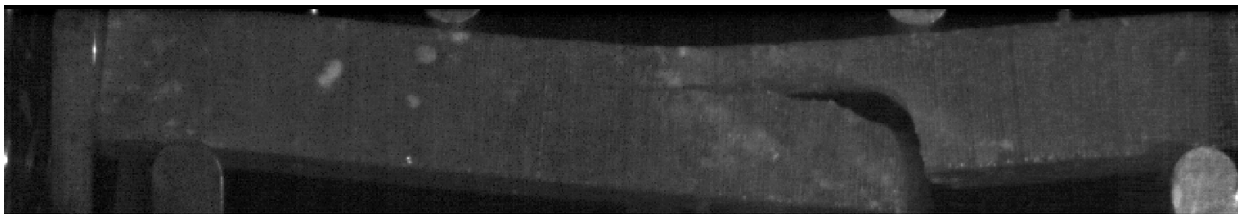

Figure 5-20 - Sample before failure for IPC 35% and (a.) low strain rate; and (b.) medium strain rate.

a.

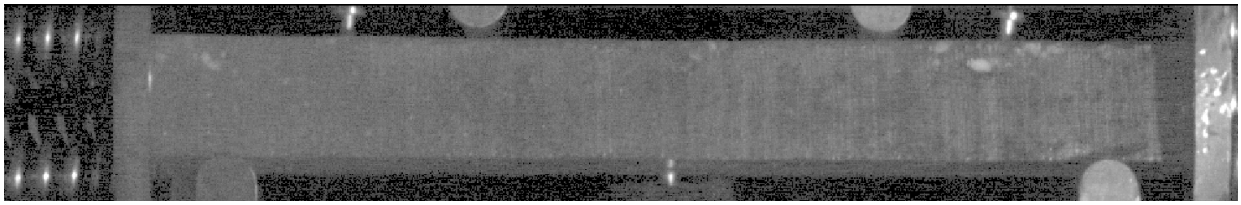

b.

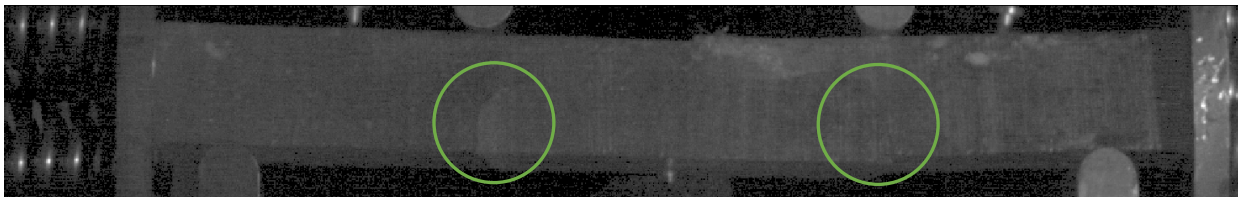

c.

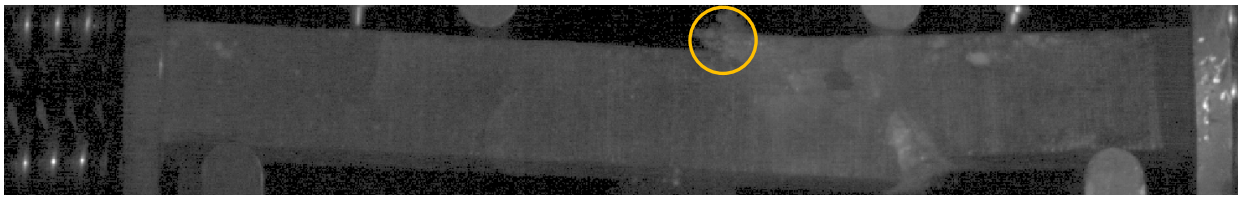

Figure 5-21 - Failure sequence for sample under 70% compression and high strain rate.

a.

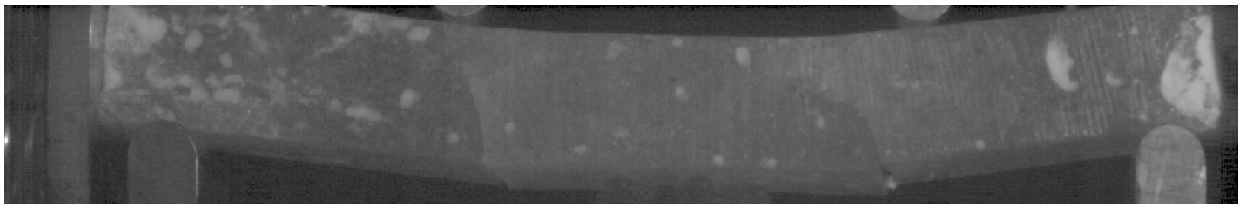

b.

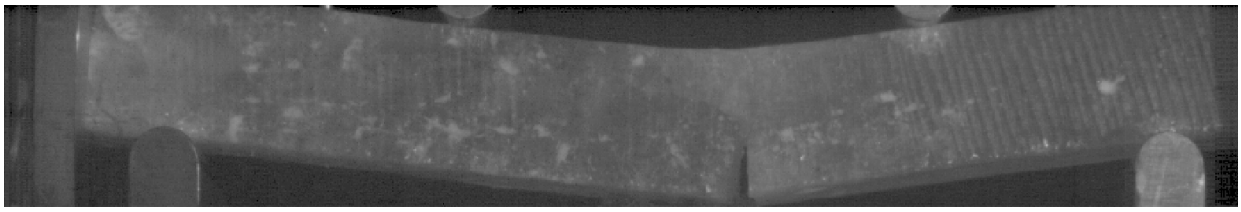

Figure 5-22 - two tests for IPC 70% at low strain rate.

In the case of IPC 125%, multiple tensile cracks were observed for all strain rates between the boundaries of the top indenters. Four of them have been labeled and can be seen evenly spread between the top indenters in Figure 5-23 for a sample for IPC 125% and high strain rate. The cracks also do not penetrate very deep into the sample.

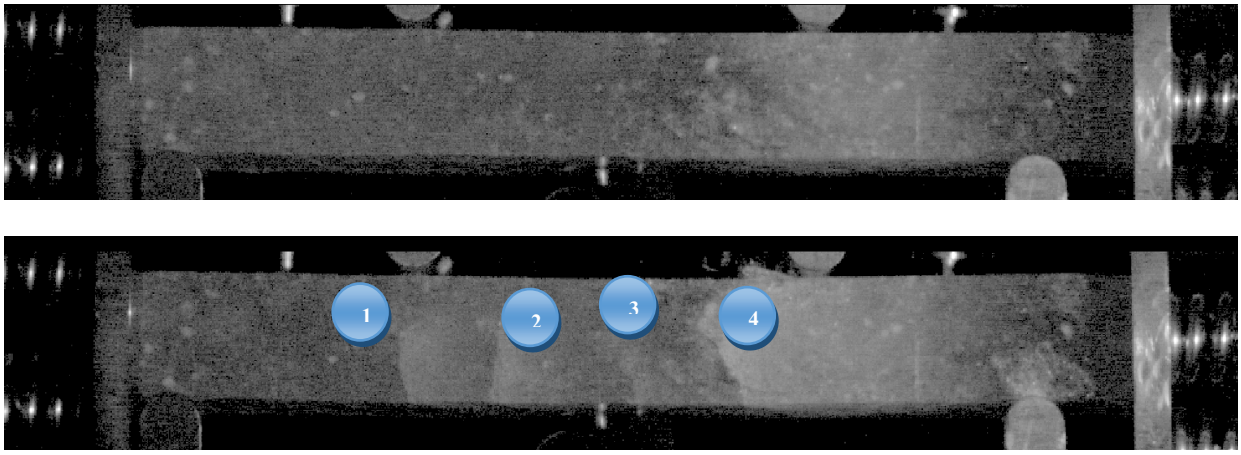

Figure 5-23 - Sample failing under IPC 125% and high strain rate.

In medium and low strain rate tests under IPC 125%, several tensile cracks also emerged between the indenters and a very high level of damage from microcracks accumulated in the compressive layer which was observed from freshwater tests. This can be seen for medium strain rate in Figure 5-24a and low strain rate in (b).

a.

b.

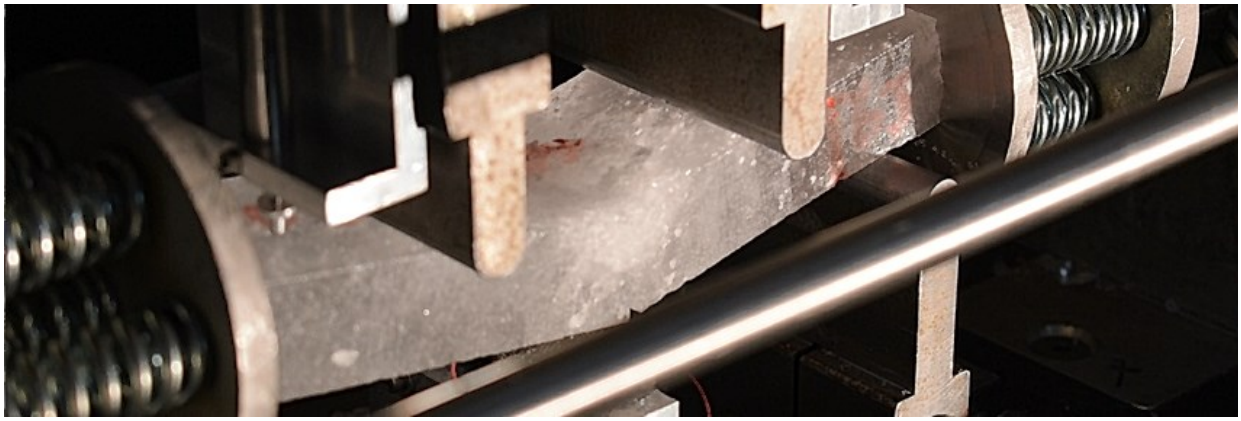

Figure 5-24 - Sample undergoing testing for IPC 125% with (a.) medium strain rate; and (b.) low strain rate.

Tensile cracks on the underside of the sample for a low strain rate test which did not fail completely are shown in Figure 5-25.

Figure 5-25 - Tensile cracks of a partially failed sample.

General crack profiles for different compression levels that were observed during testing are shown in Figure 5-26. For lower compression levels, it was observed that the tensile cracks originating from the bottom turn at a near 90-degree angle towards the top of the sample and grow along the length resulting in separation of a thin layer that carries the entire load applied to the ice sample. For higher compression levels, this layer increases in thickness allowing the ice sample to carry more load. The cracking is also more rounded as it develops from a vertical to horizontal direction.

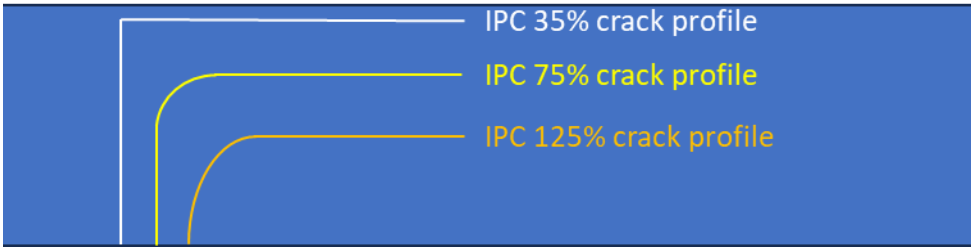

Figure 5-26- Changes in cracking profile as IPC increases.

Figure 5-27 shows characteristic load traces seen for saline tests for low, medium and high strain rates, for IPC 70% case. For low strain rate, there was slow load reduction after achieving peak load indicating damage enhanced creep which was also seen in freshwater tests. Similar load reduction is apparent for medium strain rate as well, but it is shorter in duration followed by instantaneous load drop. By comparison, for the high strain rate case shown in Figure 5-28, the load drops to zero as soon as peak force occurs a indicating brittle fracture. For the freshwater tests, the load drop was instantaneous for both high and medium strain tests. In saline tests, some medium strain rate tests exhibited instantaneous load drop while others show slow load release as seen in Figure 5-27.

In general, the saw-tooth profile was also more commonly observed for medium and low strain rate tests for IPC 35% and IPC 70% as seen in Figure 5-28.

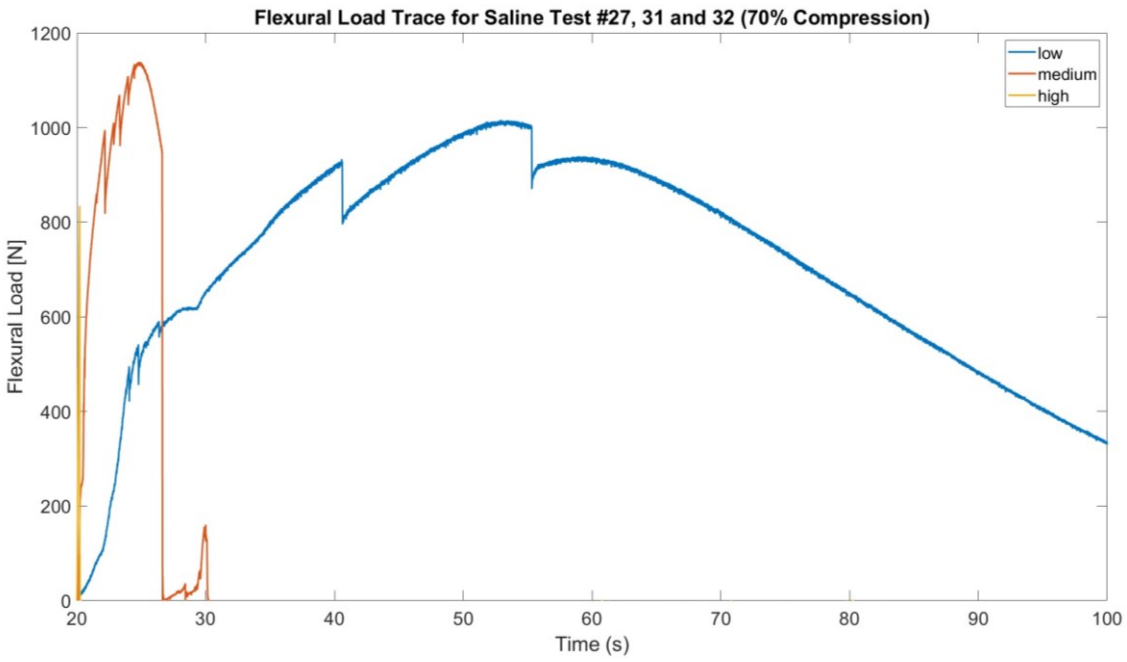

Figure 5-27 - Load trace for 70% compression showing three different strain rates.

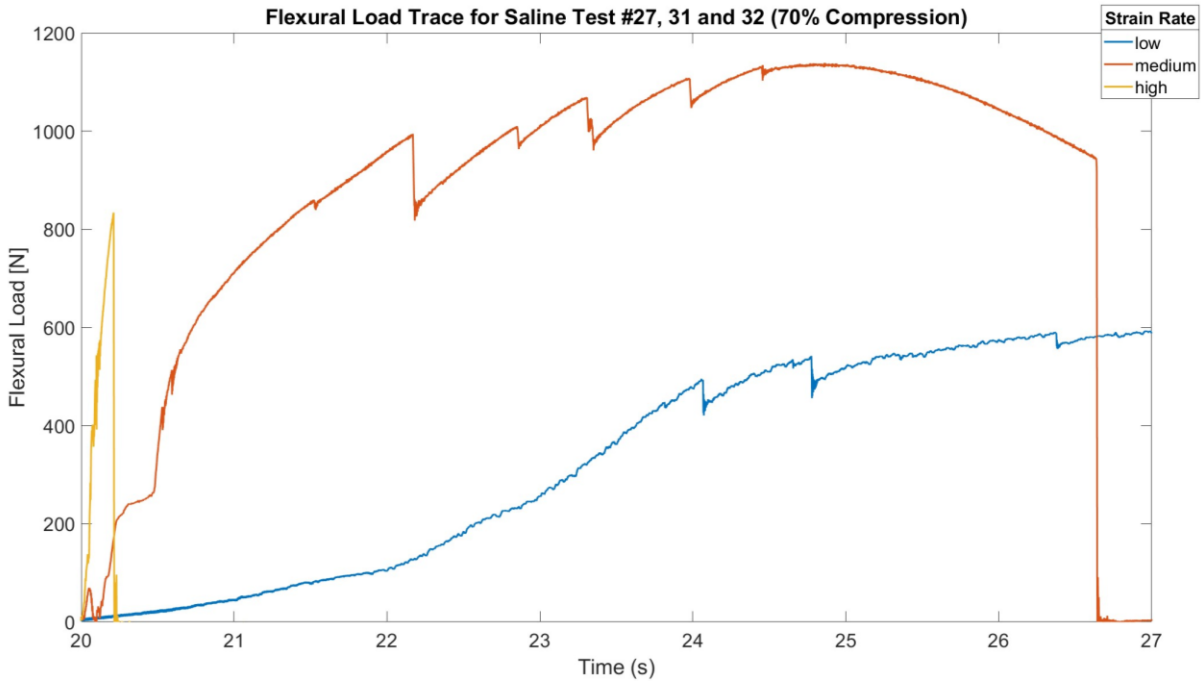

Figure 5-28 - Load trace from Figure 5-27 zoomed in to show high and medium strain rate.

5.8. Summary

Forty-three (43) flexural strength tests on saline ice samples, collected from Pistolet Bay in April 2022, were conducted at three different strain rates for unconfined conditions, as well as three compression levels: 35, 70 and 125%. Salinity tests on random samples showed that average salinity was 2.1 ppt. Microstructural analysis of ice samples showed that the ice had both fine, granular randomly oriented snow ice layer which had average grain size of 1 mm and long columnar grains deeper in the sample with average grain width around 6 mm. The samples had imperfections such as brine channels and voids, which are common for naturally occurring saline ice.

Compared to other 4-point flexural tests done in the literature, the simple flexural test results from this study fit well with general trends of the data for the beam volume chosen for the tests. Current test data and literature data was normalized to 5 ppt salinity and -10 ºC temperature for equivalent comparison. Strain rate did not have an observable effect on simple flexural strength which was expected due to failure mechanism being dominated by tensile failure.

For confined flexural tests, flexural strength was enhanced, significantly increasing anywhere from about 50% to 300%. Low and Medium strain rate tests for all three compression levels had similar strength values while high strain test had lowest strength for all compression levels. Average midpoint deflection by LVDT and MTS readings showed that medium strain tests had highest average deflection for IPC 35% and IPC 70% followed by slightly lower deflection for low strain test and lowest for high strain. In the case of IPC 125%, the average deflection decreased as strain increased from low to high.

In contrast to complete tensile crack through for simple flexural tests, the samples under axial compression failed from upper most fibers under compression. Tensile cracks initially form but

only penetrate partially into the sample and a thin section of ice that separates at the top carries the entire load until it fails. As compression levels are increased and strain levels decreased, the thickness of this “bridge” section increases allowing it to carry more load and increasing sample’s flexural strength. Studying the load and stress traces revealed that low strain rate samples showed evidence of damage enhanced creep while higher strain rates failed in brittle fashion.

6. Conclusions and Recommendations

6.1. Summary

Sloped structures are utilized in the design of structures for ice-prone waters to help reduce ice loads since the slope causes the ice to fail in flexure and ice is weaker in this failure mode. This effect is influenced by a phenomenon known as in-plane compression. The force from the slope on ice can be resolved into vertical and horizontal components where the former bends the ice and breaks it in flexure and the latter compresses the ice and counteracts flexure induced tensile stresses. In ice load models for sloped structures (e.g. Croasdale [26]), an in-plane compression factor (IPC) of 1.5 is applied to all load calculations to account for this effect, which was empirically derived. The in-plane compression effect arises when flexural strength of ice increases due to existence of axial compressive stresses that tend to suppress crack growth. To the present, no physical testing had been done to study this effect and assess its validity.

To study the in-plane compression effect, 56 tests were done on lab grown freshwater ice samples and 44 tests done on saline ice samples prepared from ice cores collected at Pistolet Bay in April 2022. The nominal size was selected to be 50 mm wide, 25 mm thick and 200 mm long (2 inches x 1 inch x 8 inches). The first set of tests were done to determine the baseline flexural strength under no compression and compare them against tests reported in the literature. The average freshwater flexural strength was found to be 1.76 MPa, while for saline it was found to be 1.49 MPa. Both baseline flexural strengths were within the range expected from the literature. Three different strain rates were also tested for each ice type and no clear strain rate effect was observed.

Microstructural analysis using thin sectioning showed that freshwater samples had polycrystalline structure with randomly oriented grains and minimal defects. The average grain size was found to be 3.6 mm. For saline ice samples, snow ice and columnar grains were observed. Snow ice had

small, randomly oriented, granular grains while columnar grains below the snow ice were elongated. The grain size for snow ice crystals was under 1.0 mm while the width of columnar grains ranged from 5.6 to 6.4 mm.

After unconfined, simple flexural tests, samples were tested under three different compression levels at 3 strain rates and at least three repetitions. For freshwater samples, the compression levels were 75%, 135% and 185%, where 75% compression is defined as an applied axial pressure equal to 75% of flexural strength. For saline samples, the compression levels were 35%, 70% and 125%.

In freshwater tests, large increases in flexural strengths were observed ranging from 125% to 250% which was achieved at IPC 135%. Clear strain rate effects were also observed for IPC 75% where strength increased as strain rate decreased. For IPC 135%, the strength was similar for all strain rates. The IPC 185% condition was only tested to determine the upper envelope of in-plane compression effect because at very high compression levels, the samples started to buckle before they could be tested indicating that in-plane compression effect does not increase indefinitely. Deflection measurements showed that there was a clear strain rate effect for IPC 75% and IPC 135% cases where average midpoint deflection increased with decreasing strain rate. Load traces for the medium and high strain rate tests illustrated an instant drop in the load value at peak load indicating brittle failure while for low strain rate, there was slow load release after achieving peak load representing damage enhanced creep failure.

Large increases in apparent flexural strengths were also seen for saline tests which ranged from 50% to 300%, the maximum of which was reached at IPC 125%. However, the strain effect was different from freshwater, although it was consistent for all three compression levels. Both medium strain rate and low strain rate flexural strengths were similar, with flexural strength values for the medium strain rates being slightly higher. High strain rate flexural strengths were considerably

lower than low/medium strain rates. When looking at midpoint deflection for IPC 30% and IPC 70%, medium strain rate tests had the highest average deflection followed by slightly less midpoint deflection for low strain rate tests. The smallest deflections at failure correspond to high strain rate tests. For IPC 125%, the deflection trend was similar to that observed for freshwater tests where deflection increased as strain rate decreased. Studying the load traces revealed that low strain rate samples showed evidence of damage enhanced creep by slow load release beyond the peak load prior to failing. While saline ice loaded higher strain rates failed in a brittle fashion with a characteristic instant load drop.

In terms of the failure mechanisms of unconfined simple flexural tests, the sample fails when the tensile cracks form at the bottom of the sample and propagate through the entire thickness. The mechanism transforms into multi-mode failure for samples subjected to axial confinement. While tensile cracks still form first, they do not extend all the way through the sample. Instead, the samples fail when the beam section above the neutral axis fails from compressive failure. The failure in these cases always originated from the top layer of ice where there is formation and coalescence of dense clouds of microcracks.

Based on these results, the mechanism and conditions under which in-plane compression effect applies have been observed proving its validity and importance for ice load calculations on sloped structures. The upper limit of this effect has also been established. Currently, an empirical factor of 1.5 is applied to load calculations represents a 50% increase in strength. From laboratory testing, strength increase of up to 300% for very small samples was achieved under conditions of low strain and very high compression levels. The significant increase warrants a closer look at this phenomenon, since failure under such conditions is dominated by compressive failure which is highly scale dependent. Studies on how the current work could be used to enhance the load

prediction models is needed. The strength increase was highly very strain rate dependent suggesting that in-plane compression factor could change based on ice floe speeds during interaction with a sloped structures.

6.2. Future Work

The research presented in this thesis is first of its kind and therefore there are several ways in which the work can be expanded upon to gain a better understanding of the in-plane compression effect:

- Scale effects in compressive failure are known to be highly important [61]. The interplay between scale effects in compression and the results observed from these tests is an essential area of further study.
- Temperature and beam volume were two major variables that were controlled in the testing. It is known that ice flexural strength increases with colder temperatures and decreases with increasing beam size due to scale effects. Compared to literature, the tested beam volume was amongst the smallest beams tested in the past. Therefore, larger beam sizes over a temperature range should be tested to investigate the in-plane compression effect and its applicability to larger ice beams.
- More compression levels should be tested for IPC values between the range of 0-100% for both saline and freshwater ice to determine at what compression level the in-plane compression starts to become effective. Linking these results with natural phenomena such as pack ice pressure to study if it has any effect on the flexural strength of ice is an important future topic.
- Upper limit of in-plane compression effect for saline ice should be determined as was done for freshwater ice.

- In-plane compression effect implementation in ice load models should be reviewed to see how the data from new testing can be used to enhance the load models.
- The saline ice cores were cut in the vertical direction. Horizontal sections should also be tested in future to further assess grain orientation effects on increased flexural strength with IPC.
- Efforts to minimize brine drainage were made by careful handling of samples and storing them at -15 degrees C prior to testing. However, it is likely that some drainage did occur. Salinities could not be measured in the field and were only recorded prior to testing. In future, tests should be done in the field to minimize the brine drainage effect.
- Ice was assumed to be effectively elastic in the analysis. Future works should study viscoelastic effects.
- In the current test design and set-up, a fixed amount of axial pressure was applied to the sample before flexural loading was applied at various strain rates. For future tests, axial and flexural loads should be applied simultaneously at a constant axial to flexural load ratio. This testing method will better simulate the evolution of ice loads as it interacts with sloped structures. The tests should also be repeated for a range of axial to flexural load ratios to account for different sloping angles.
- To determine accurate critical buckling loads, additional compressive strength tests should be done for specific ice types to obtain accurate values. Tests should also be done for each ice type to determine the sample's Young's Modulus. Compressive strength and Young's Modulus are the two material property parameters that are used to calculate buckling loads.

6.3. Concluding Remarks

The purpose of this research program was to study the increase in flexural strength of ice due to in-plane compression effect. The specific objectives were to test different axial compression levels at different strain rates, determine any differences between saline and freshwater ice and lastly, to observe and qualify the failure mechanism. The results showed a clear trend between in-plane axial compression and strain rate on flexural strength and differences in trends when it came to ice type. A general failure mechanism was also observed.

The testing methodology and gathered results form an important first step in understanding the in-plane compression effect in more detail. The work presented can be used to enhance ice load prediction models against sloped structures. Following the recommendations will offer even deeper understanding of the phenomenon resulting in more accurate load prediction and safer marine structural design in future.

References

[1] A. Wang, M. Tang, Q. Zhao, Y. Liu, B. Li, Y. Shi and J. Sui, "Analysis of sea ice parameters for the design of an offshore wind farm in the Bohai Sea," *Ocean Engineering,* vol. 239, 2021.

[2] N. Melia, K. Haines and E. Hawkins, "Sea ice decline and 21st century trans-Arcticshipping routes," *Geophysical Research Letters,* 2016.

[3] C. Sinsabvarodom, W. Chai, B. J. Leira, K. V. Høyland and A. Naess, "Uncertainty assessments of structural loading due to first year ice based on the ISO standard by using Monte-Carlo simulation," *Ocean Engineering,* vol. 198, 2020.

[4] K. Croasdale, J. Thijssen and N. Allyn, "Ice load signatures for ridge actions on wind turbines with conical collars," in *Port and Ocean Engineering under Arctic Conditions*, Delft, 2019.

[5] Z. Chen, Y. He, C. Huang, Y. Ren and M. Wu, "Numerical Simulation of Sloping Structure-Level Ice Interaction Based on SPH-FEM Conversion Algorithm," in *ISOPE*, Virtual, 2020.

[6] F. Wang, Z.-J. Zou, L. Zhou, Y.-Z. Ren and S.-Q. Wang, "A simulation study on the interaction between sloping marine structure and level ice based on choesive element model," *Cold Regions Science and Technology,* vol. 149, pp. 1-15, 2018.

[7] I. Lemström, A. Polojärvi, O. Puolakka and J. Tuhkuri, "Load distributions in the ice-structure interaction process in shallow water," *Ocean Engineering,* vol. 258, 2022.

[8] C. Daley, Sea Ice Engineering for ships and offshore structures, St. John's, 2020.

[9] M. Karulina, A. Marchenko, E. Karulin, D. Sodhi, A. Sakharov and P. Chistyakov, "Full-scale flexural strength of sea ice and freshwater ice in Spitsbergen Fjords and North-West Barents Sea," *Applied Ocean Research,* vol. 90, 2019.

[10] G. Timco and W. Weeks, "A review of the engineering properties of sea ice," *Cold Regions Science and Technology,* vol. 60, pp. 107-129, 2010.

[11] J. Gere and B. Goodno, Mechanics of Materials, Stanford: Cengage Learning, 2012.

[12] J. S. Tibbo, "Flexural Failure of Sea Ice - Analysis of Interactions at the Confederation Bridge and Assessment of Selected Prediction Technique," University of Calgary, Calgary, 2010.

[13] J. Thijssen, M. Fuglem and K. Croasdale, "Probabilistic Assessment of Muti-Year Sea Ice Loads on Upward Sloping Arctic Structures," in *Offshore Technology Conference*, St. John's, 2016.

[14] K. R. Croasdale and A. B. Cammaert, "An Improved Method For The Calculation Of Ice Loads On Sloping Structures In First-Year Ice," *Hydrotechnical Construction,* vol. 28, no. 3, pp. 46-51, 1994.

[15] M. Aly, "Analysis of Scale Effect in Ice Flexural Strength," Memorial University of Newfoundland, St. John's, 2018.

[16] M. Suominen, R. Repin, L. Lu, F. Li and P. Kujala, "Flexural Strength of Freshwater Ice in Saimaa Area," in *Port and Ocean Engineering under Arctic Conditions*, Moscow, 2021.

[17] Q. Wang, Z. Li, P. Lu, Y. Xu and Z. Li, "Flexural and compressive strength of the landfast sea ice in the Prydz Bay, East Antarctic," The Cryosphere, 2022.

[18] T. Sanderson, Ice Mechanics and Risks to Offshore Structures, Norwell, MA: Kluwer Academic Publishers, 1988.

[19] W. F. Weeks, "Physical properties of the ice cover of the Greenland Sea," CRREL, Hanover, NH, 1982.

[20] R. Lei, Z. Li, Z. Zhang, Y. Chen and Y. Dou, "Physical characteristics of fast ice off Zhongshan Station during austral summer," in *POAC*, Dalian, 2007.

[21] G. Carnat, T. Papakyriakou, N. Geilfus, F. Brabant, B. Delille, M. Vancooppenolle, G. Gilson, J. Zhou and J. L. Tison, "Investigations on physical and textural properties of Arctic

first-year sea ice in the Amundsen Gulf, Canada, November 2007-June 2008 (IPY-CFL system study)," *Journal of Glaciology,* vol. 59, no. 217, 2013.

[22] M. Johnston and G. Timco, "Temperature changes in first year arctic sea ice during the decay," in *16th IAHR International Symposium on Ice*, Dunedin, 2002.

[23] S. Ji, S. Di and S. Liu, "Analysis of ice load on conical structure with discrete element method," *International Journal for ComputerAided Engineering and Software,* vol. 32, no. 4, pp. 1121-1134, 2015.

[24] A. J. Gow and H. T. Ueda, "Structure And Temperature Dependence Of The Flexural Properties Of Laboratory Freshwater Ice Sheets," in *Cold Regions Science and Technology*, Amsterdam, 1988.

[25] International Standard, "Petroleum and natural gas industries - Arctic offshore structures," ISO, Geneva, 2010.

[26] K. Croasdale, T. Brown, C. Wong, N. Shrestha, G. Li, W. Spring, M. Fuglem and J. Thijssen, "Improved Equations for the Actions of Thick Level Ice on Sloping Platforms," in *Offshore Technology Conference*, St. John's, 2016.

[27] J. Schwarz, R. Frederking, V. Gavrillo, I. Petrov, K.-I. Hirayama, M. Mellor, P. Tryde and K. Vaudrey, *Standardized Testing Methods For Measuring Mechanical Properties Of Ice,* Amsterdam: Cold Regions Science and Technology, 1981.

[28] ITTC, "Test methods for model ice properties," in *International Towing Tank Conference*, 2014.

[29] M. T. Boroojerdi, "Investigation of the Role of Freeze Bonds on the Development of Ice Rubble Strength," Memorial University of Newfoundland, St. John's, Canada, 2020.

[30] M. T. Boorojerdi, E. Bailey, M. Ghobadi and R. Taylor, "Experimental Study on Shear Strength of Freeze Bonds in Freshwater Ice," in *Arctic Technology conference*, St. John's, NL, 2016.

[31] G. Timco and S. O'Brien, "Flexural strength equation for sea ice," in *Cold Regions Science and Technology*, 1994.

[32] G. Timco and R. Frederking, "Comparative Strengths of Freshwater Ice," in *Cold Regios Science and Technology*, Amsterdam, 1982.

[33] G. Timco and R. Frederking, "Flexural Strength and Fracture Toughness of Sea Ice," in *Cold Regions Science and Technology*, Amsterdam, 1982.

[34] M. Kermani, M. Farzaneh and R. Gagnon, "Bending strength and effective modulus of atmospheric ice," *Cold Regions Science and Technology,* vol. 53, no. 2, pp. 162-169, 2008.

[35] W. Colgan and L. U. Arenson, "Open-Pit Glacier Ice Excavation: Brief Review," *Journal of Cold Regions Engineering ,* vol. 27, pp. 223-243, 2013.

[36] H. Han, W. Huang and Z. Li, "Flexural Strength and Effective Modulus of Large Columnar-Grained Freshwater Ice," *Journal of Cold Regions Engineering,* vol. 30, no. 2, 2016.

[37] L. W. Gold, "Engineering Properties Of Fresh-water Ice," *Journal of Glaciology,* vol. 19, no. 81, 1977.

[38] H. Kim and J. N. Keune, "Compressive strength of ice at impact strain rates," *Journal Material Science,* vol. 42, 2007.

[39] C. Qi, J. Lian, Q. Ouyang and X. Zhao, "Dynamic Compressive Strength and Failure of Natural Lake Ice Under Moderate Strain Rates at Near Melting Point Temperature," *Latin American Journal of Solids and Structures,* vol. 14, pp. 1669-1694, 2017.

[40] A. Kovacs, "Estimating the full-scale flexural and compressive strength of first-year sea ice," *JOURNAL OF GEOPHYSICAL RESEARCH,,* vol. 102, pp. 8681-8689, 1997.

[41] J. Schwarz and W. F. Weeks, "Engineering Properties of Sea Ice," *Journal of Glaciology,* vol. 19, no. 81, 1977.

[42] E. M. Schulson, "Brittle Failure of Ice," *Engineering Fracture Mechanics,* vol. 68, no. 17-18, pp. 1839-1887, 2001.

[43] E. Schulson and P. Duval, Creep and fracture of ice, Cambridge University Press, 2009.

[44] A. Wang and S. Ji, "Flexural Strength of Sea Ice," *Encyclopedia of Ocean Engineering,* pp. 575-583, 2020.

[45] R. Gagnon and P. Gammon, "Characterization and flexural strength of iceberg and glacier ice," *Journal of Galciology,* vol. 41, no. 137, pp. 103-111, 1995.

[46] S. Timoshenko and D. H. Young, Elements of Strength of Materials, D. Van Nostrand Company, 1968.

[47] A. Wang, Z. W. X. Chen, S. Ji, Y. Liu and L. Qing, "Brief communication: Full-field deformation measurement for uniaxial compression of sea ice using the digital image correlation method," in *The Cryosphere*, 2019.

[48] D. Blanchet, R. Abdelnour and G. Comfort, "Mechanical Properties Of First-Year Sea Ice At Tarsiut Island," *Journal of Cold Regions Engineering,* vol. 11, no. 1, pp. 59-83, 1997.

[49] Y. Xiu, Z. Li, Q. Wang, H. Han, Z. Zong, Y. Zu and Y. Zhang, "Experimental study on flexural strength and effective elastic modulus of granular ice in the Bohai Sea, China," *Frontiers in Energy Research,* vol. 10, 2022.

[50] A. Murdza, E. M. Schulson and C. E. Renshaw, "Strengthening of columnar-grained freshwater ice through cyclic flexural loading," *Journal of Glaciology,* pp. 1-11, 2020.

[51] P. D. Barrette, "A laboratory study on the flexural strength of white ice and clear ice from the Rideau Canal skateway," *Canadian Journal of Civil Engineering,* 2011.

[52] A. Marchenko, M. Kraulina, E. Karulin and P. Chistyakov, "Flexural Strength of Ice Reconstructed from Field Tests with Cantilever Beams and Laboratory Tests with Beams and Disks," in *POAC 17*, Busan, Korea, 2017.

[53] G. Frankenstein and R. Garner, *Equations for determining the brine volume of sea ice from -0.5 to -22.9 C,* Hanover: CRREL, 1967.

[54] S.-y. Ji, A.-l. Wang, J. Su and Q.-j. Yue, "Experimental Studies on Elastic Modulus and Flexural Strength of Sea Ice in the Bohai Sea," *Journal of Cold Regions Engineering,* vol. 25, no. 4, 2011.

[55] M. Aly, R. Taylor, E. B. Dudley and I. Turnbull, "Scale Effect in Ice Flexural Strength," *Journal of Offshore Mechanics and Arctic Engineering,* vol. 141, 2019.

[56] R. M. W. Frederking, D. Blanchet, I. Jordaan, K. Kennedy, N. Sinha and E. Stander, "Field tests on ice indentation at medium scale, ice island," National Research Council of Canada, 1989.

[57] A. International, *Standard Test Methods for Determining Average Grain Size,* West Conshohocken: ASTM, 2021.

[58] J. J. Petrovic, "Review of Mechanical Properties of Ice and Snow," *Journal of Materials Science,* vol. 38, pp. 1-6, 2003.

[59] W. Dornfeld, "Fairfield University School of Engineering," 26 October 2023. [Online]. Available: http://www.faculty.fairfield.edu/wdornfeld/ME311/MEEG3311MachineDesignNotes07.pdf. [Accessed 4 February 2024].

[60] M. O. Jeffries, "sea ice," Encyclopedia Brittanica, 18 December 2023. [Online]. Available: https://www.britannica.com/science/sea-ice. [Accessed 29 January 2024].

[61] R. Taylor, "Analysis of scale effect in compressive ice failure and implications for design," Memorial University of Newfoundland, St. John's, 2010.

[62] J. H. Currier and E. M. Schulson, "The tensile strength of ice as a function of grain size," *Acta Metallurgica,* vol. 30, no. 8, pp. 1511-1514, 1982.

[63] I. Gribanov, R. Taylor and R. Sarracino, "Application of cohesive zone model to the fractureprocess of freshwater polycrystalline ice under flexural loading," in *IOP Conference Series: Earth and Environmental Science*, 2018.

Appendix A - Freshwater Ice Tests Raw Data Table

Table A 1 - Raw Data for 0% Compression Tests on Freshwater Ice.

Index #	Test #	Ram Speed [mm/s]	Failure Time [s]	Target Compression %	Flexural Strength [MPa]	MTS Displacement [mm]	Right LVDT [mm]	Left LVDT [mm]	Center LVDT [mm]	Axial Load [N]	Cross-sectional Area [mm^2]	Compressive Stress [MPa]	Measured Compression %
1	7	0.1	1.401	0	1.631	0.140	0.027	0.045	0.099	-	1232	-	-
2	8	0.1	3.258	0	1.752	0.328	0.088	0.059	0.134	-	1226	-	-
3	9	0.1	1.358	0	1.420	0.138	0.066	0.050	0.062	-	1263	-	-
4	14	0.1	1.452	0	1.688	0.142	0.033	0.040	0.103	-	1232	-	-
5	15	0.1	1.370	0	1.631	0.138	0.032	0.035	0.096	-	1238	-	-
6	4	1	0.164	0	1.451	0.162	0.067	0.032	0.086	-	1231	-	-
7	5	1	0.137	0	1.676	0.130	0.032	0.035	0.101	-	1252	-	-
8	6	1	0.188	0	1.754	0.188	0.032	0.035	0.156	-	1228	-	-
9	12	1	0.165	0	1.752	0.164	0.038	0.037	0.109	-	1242	-	-
10	13	1	0.232	0	1.620	0.227	0.222	0.000	0.125	-	1206	-	-
11	1	10	0.021	0	1.866	0.154	0.038	0.048	0.133	-	1293	-	-
12	2	10	0.019	0	1.240	0.136	0.100	0.060	0.076	-	1210	-	-
13	3	10	0.025	0	1.794	0.191	0.056	0.051	0.139	-	1312	-	-
14	10	10	0.018	0	1.664	0.118	0.042	0.038	0.064	-	1231	-	-
15	11	10	0.023	0	1.815	0.176	0.067	0.053	0.096	-	1217	-	-
16	16	10	0.021	0	1.668	0.170	0.044	0.066	0.128	-	1241	-	-

Note: Ram speeds 0.1, 1 and 10 mm/s correspond to strain rates 4.67×10^{-4}, 4.67×10^{-3} and 4.67×10^{-2} respectively.

Table A 2 - Raw Data for 75% Compression Tests on Freshwater Ice.

Index #	Test #	Ram Speed [mm/s]	Failure Time [s]	Target Compression %	Flexural Strength [MPa]	MTS Displacement [mm]	Right LVDT [mm]	Left LVDT [mm]	Center LVDT [mm]	Axial Load [N]	Cross-sectional Area [mm^2]	Compressive Stress [MPa]	Measured Compression %
17	37	0.1	44.601	75	6.248	4.458	2.902	2.184	3.604	1719	1359	1.247	71
18	45	0.1	51.197	75	5.471	5.123	2.881	2.689	9.586	1666	1357	1.210	69
19	46	0.1	42.813	75	5.876	4.278	2.732	2.626	6.838	1711	1352	1.279	73
20	47	0.1	45.665	75	5.636	4.566	2.571	2.746	6.817	1674	1347	1.252	71
21	38	1	1.735	75	5.260	1.727	0.977	0.916	0.154	1789	1349	1.316	75
22	39	1	1.895	75	4.840	1.892	0.965	0.947	1.513	1741	1360	1.260	72
23	40	1	1.452	75	4.799	1.444	0.834	0.829	0.310	1754	1366	1.274	72
24	48	1	1.885	75	4.736	1.877	1.127	1.116	3.279	1719	1345	1.260	71
25	50	1	2.506	75	4.678	2.506	1.357	1.309	3.994	1698	1326	1.260	72
26	51	1	1.506	75	4.698	1.500	0.789	0.869	1.817	1727	1352	1.268	72
27	41	10	0.112	75	3.951	1.077	0.652	0.606	0.039	1682	1288	1.314	75
28	42	10	0.112	75	4.121	1.083	0.715	0.649	0.214	1733	1285	1.362	77
29	43	10	0.132	75	3.806	1.275	0.572	0.567	0.022	1730	1275	1.335	76
30	52	10	0.120	75	4.142	1.148	0.603	0.782	1.213	1749	1344	1.287	73
31	53	10	0.087	75	3.459	0.819	0.502	0.430	0.919	1690	1306	1.316	75
32	54	10	0.170	75	3.208	1.650	1.620	0.177	1.398	1714	1349	1.255	71

Note: Ram speeds 0.1, 1 and 10 mm/s correspond to strain rates 4.67×10^{-4}, 4.67×10^{-3} and 4.67×10^{-2} respectively.

Table A 3 - Raw Data for 135% Compression Tests on Freshwater Ice.

Index #	Test #	Ram Speed [mm/s]	Failure Time [s]	Target Compression %	Flexural Strength [MPa]	MTS Displacement [mm]	Right LVDT [mm]	Left LVDT [mm]	Center LVDT [mm]	Axial Load [N]	Cross-sectional Area [mm^2]	Compressive Stress [MPa]	Measured Compression %
33	17	0.1	39.838	135	6.130	3.986	1.593	1.491	5.995	2934	1316	2.232	127
34	18	0.1	31.456	135	7.176	3.147	1.376	1.512	4.532	3148	1299	2.422	138
35	19	0.1	32.279	135	6.702	3.224	1.367	1.459	4.979	2886	1300	2.208	125
36	30	0.1	31.156	135	4.998	3.122	1.682	2.428	4.567	2910	1197	2.440	139
37	32	0.1	37.795	135	5.836	3.777	2.486	2.234	5.408	3052	1438	2.117	120
38	33	0.1	39.285	135	4.955	3.931	2.318	2.613	5.474	3111	1322	2.355	134
39	34	0.1	41.120	135	5.732	4.114	2.690	2.450	5.684	3046	1320	2.312	131
40	35	0.1	47.796	135	6.044	4.785	3.136	2.718	6.367	3095	1325	2.339	133
41	20	1	3.858	135	5.454	3.860	1.512	1.595	4.270	3084	1310	2.347	133
42	21	1	1.761	135	5.335	1.754	0.705	0.995	1.889	3062	1277	2.395	136
43	22	1	1.825	135	6.052	1.823	1.113	1.171	2.572	3073	1238	2.478	141
44	23	1	1.941	135	5.852	1.940	1.222	1.181	0.823	3100	1258	2.462	140
45	24	1	2.500	135	6.797	2.500	1.221	2.258	3.093	2352	1261	1.864	106
46	25	10	0.248	135	5.180	2.427	3.391	0.176	0.228	3108	1256	2.464	140
47	26	10	0.124	135	5.394	1.190	0.722	0.892	0.203	3049	1232	2.472	140
48	27	10	0.073	135	4.862	0.683	0.252	0.460	-0.005	2985	1304	2.288	130
49	28	10	0.074	135	6.051	0.701	0.220	0.340	0.000	3087	1324	2.336	133
50	29	10	0.115	135	6.473	1.095	0.573	0.699	0.227	3108	1152	2.702	153

Note: Ram speeds 0.1, 1 and 10 mm/s correspond to strain rates 4.67×10^{-4}, 4.67×10^{-3} and 4.67×10^{-2} respectively.

Table A 4 - Raw Data for 185% Compression Tests on Freshwater Ice.

Index #	Test #	Ram Speed [mm/s]	Failure Time [s]	Target Compression %	Flexural Strength [MPa]	MTS Displacement [mm]	Right LVDT [mm]	Left LVDT [mm]	Center LVDT [mm]	Axial Load [N]	Cross-sectional Area [mm^2]	Compressive Stress [MPa]	Measured Compression %
51	69	0.1	36.445	185	2.809	3.647	3.046	2.105	3.475	4219	1278	3.292	187
52	70	0.1	16.920	185	3.439	1.695	1.260	0.881	1.609	4419	1329	3.340	190
53	64	1	1.807	185	5.410	1.806	0.956	0.775	1.125	4299	1318	3.241	184
54	65	1	2.456	185	5.293	2.459	1.968	1.239	1.761	4211	1317	3.180	180
55	66	10	0.136	185	5.605	1.322	0.351	0.448	1.082	4336	1314	3.319	188
56	68	10	0.160	185	5.350	1.553	1.067	0.613	1.078	4328	1275	3.410	194

Note: Ram speeds 0.1, 1 and 10 mm/s correspond to strain rates 4.67×10^{-4}, 4.67×10^{-3} and 4.67×10^{-2} respectively.

Appendix B - Freshwater Ice Individual Test Plots

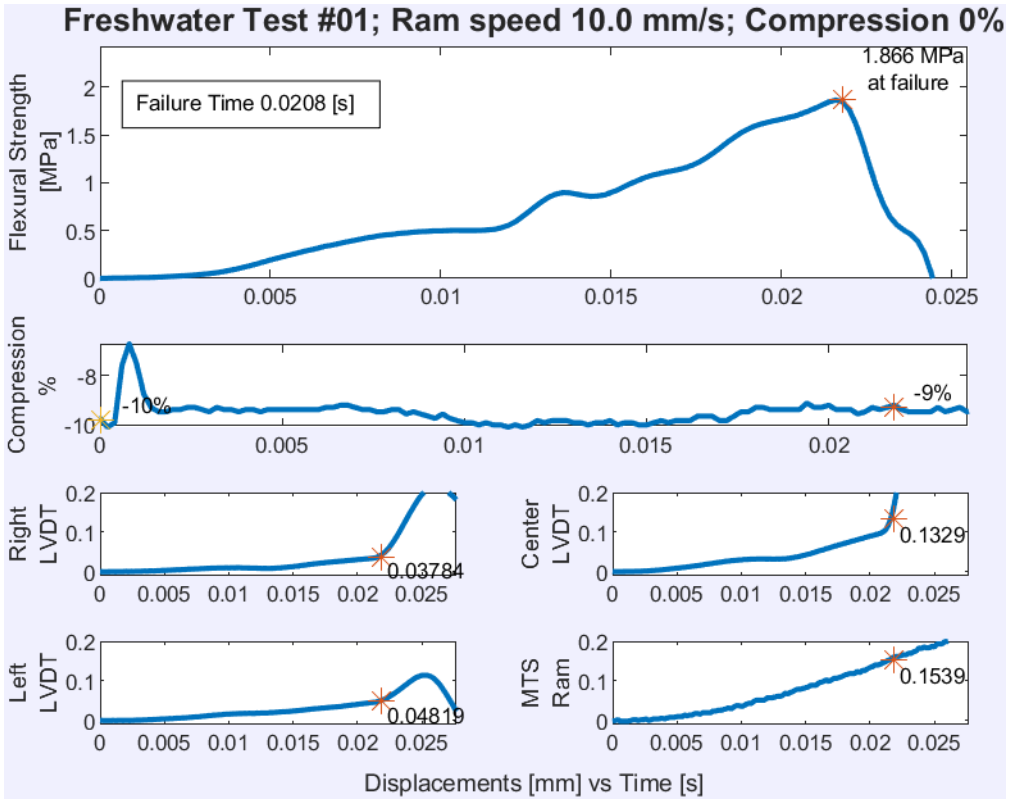
Freshwater Test #01; Ram speed 10.0 mm/s; Compression 0%
Failure Time 0.0208 [s]
1.866 MPa
at failure
Flexural Strength [MPa]
Compression %
-10%
-9%
Right LVDT
0.03784
Center LVDT
0.1329
Left LVDT
0.04819
MTS Ram
0.1539
Displacements [mm] vs Time [s]

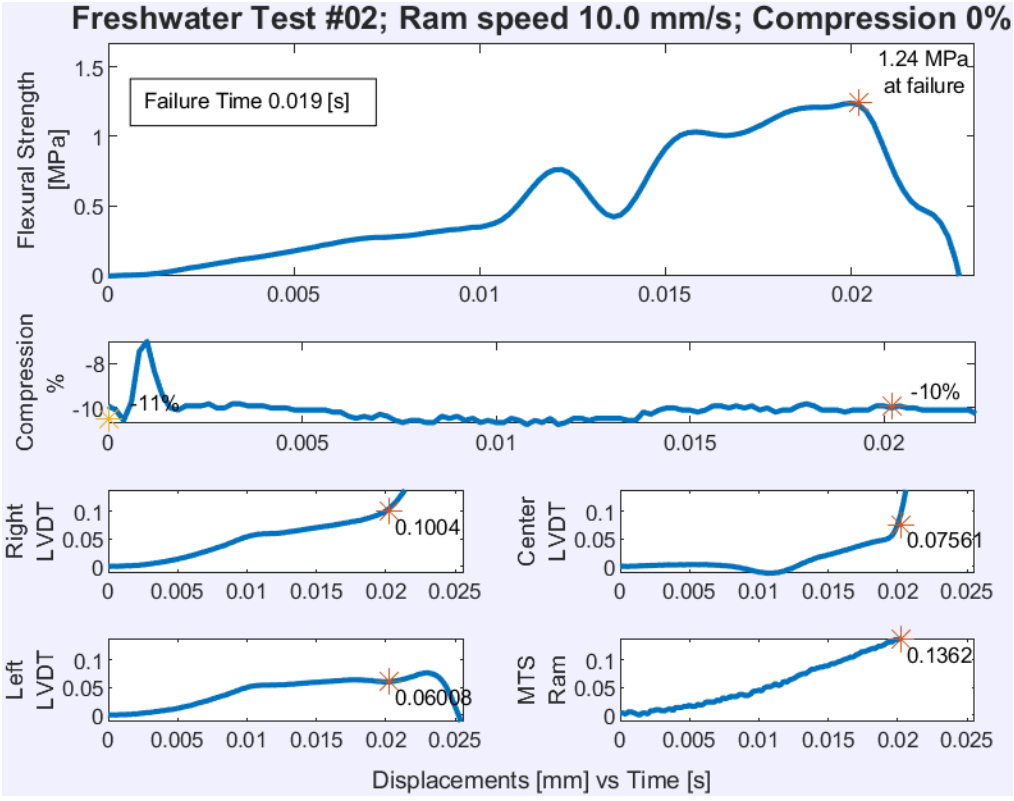
Freshwater Test #02; Ram speed 10.0 mm/s; Compression 0%
Failure Time 0.019 [s]
1.24 MPa
at failure
Flexural Strength [MPa]
Compression %
-11%
-10%
Right LVDT
0.1004
Center LVDT
0.07561
Left LVDT
0.06008
MTS Ram
0.1362
Displacements [mm] vs Time [s]

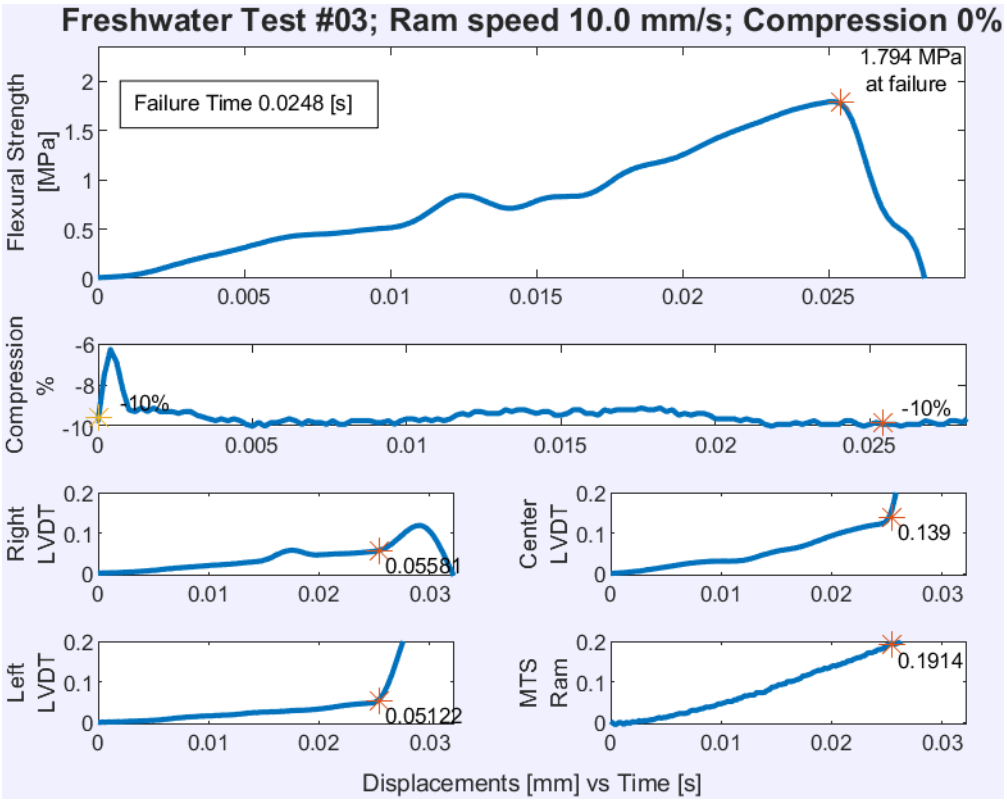
Freshwater Test #03; Ram speed 10.0 mm/s; Compression 0%
Failure Time 0.0248 [s]
1.794 MPa
at failure
Flexural Strength [MPa]
Compression %
-10%
-10%
Right LVDT
0.05581
Center LVDT
0.139
Left LVDT
0.05122
MTS Ram
0.1914
Displacements [mm] vs Time [s]

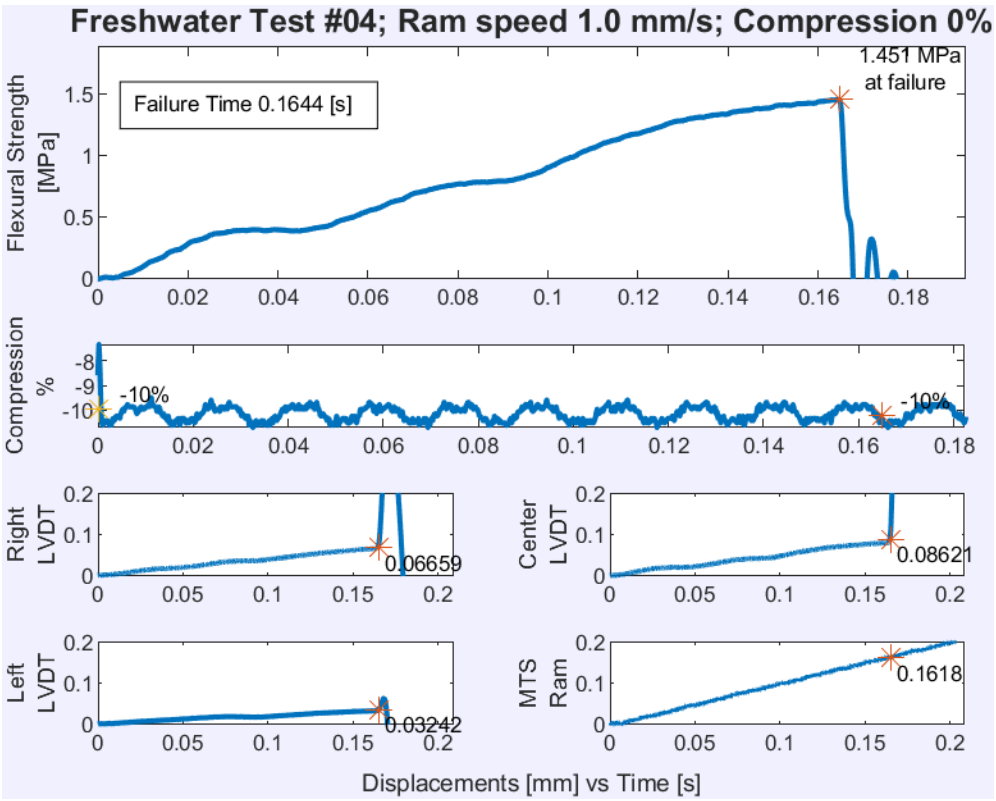
Freshwater Test #04; Ram speed 1.0 mm/s; Compression 0%
Failure Time 0.1644 [s]
1.451 MPa
at failure
Flexural Strength [MPa]
Compression %
-10%
-10%
Right LVDT
0.06659
Center LVDT
0.08621
Left LVDT
0.03242
MTS Ram
0.1618
Displacements [mm] vs Time [s]

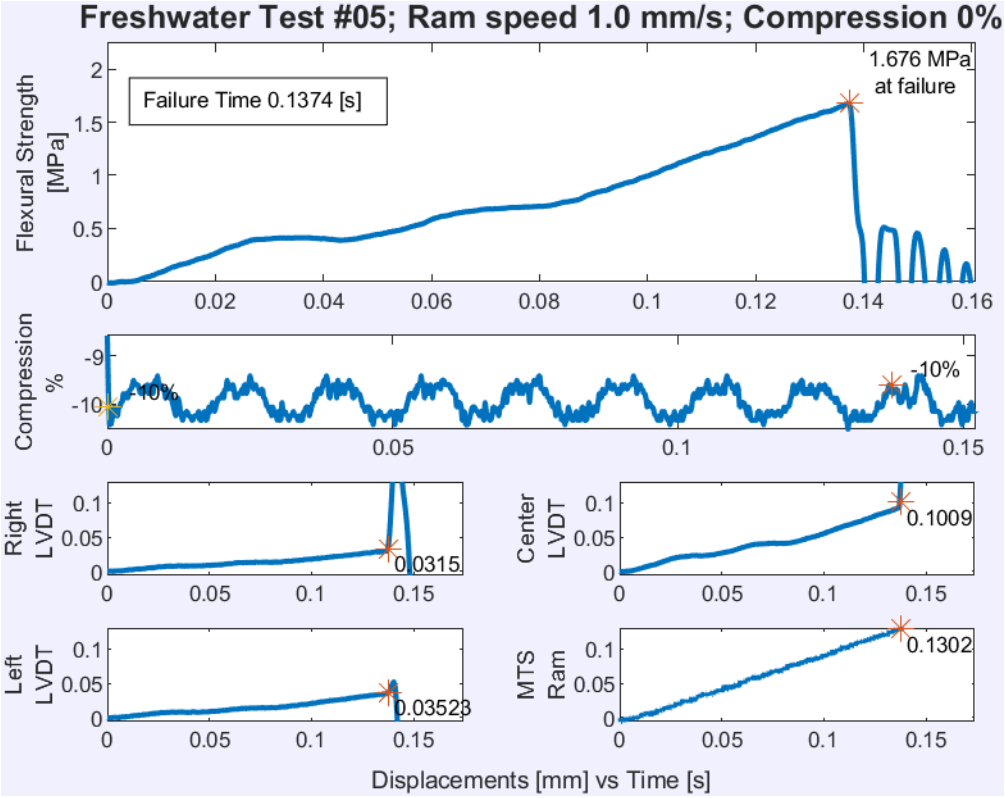
Freshwater Test #05; Ram speed 1.0 mm/s; Compression 0%
Failure Time 0.1374 [s]
1.676 MPa
at failure
Flexural Strength [MPa]
Compression %
-10%
-10%
Right LVDT
0.0315
Center LVDT
0.1009
Left LVDT
0.03523
MTS Ram
0.1302
Displacements [mm] vs Time [s]

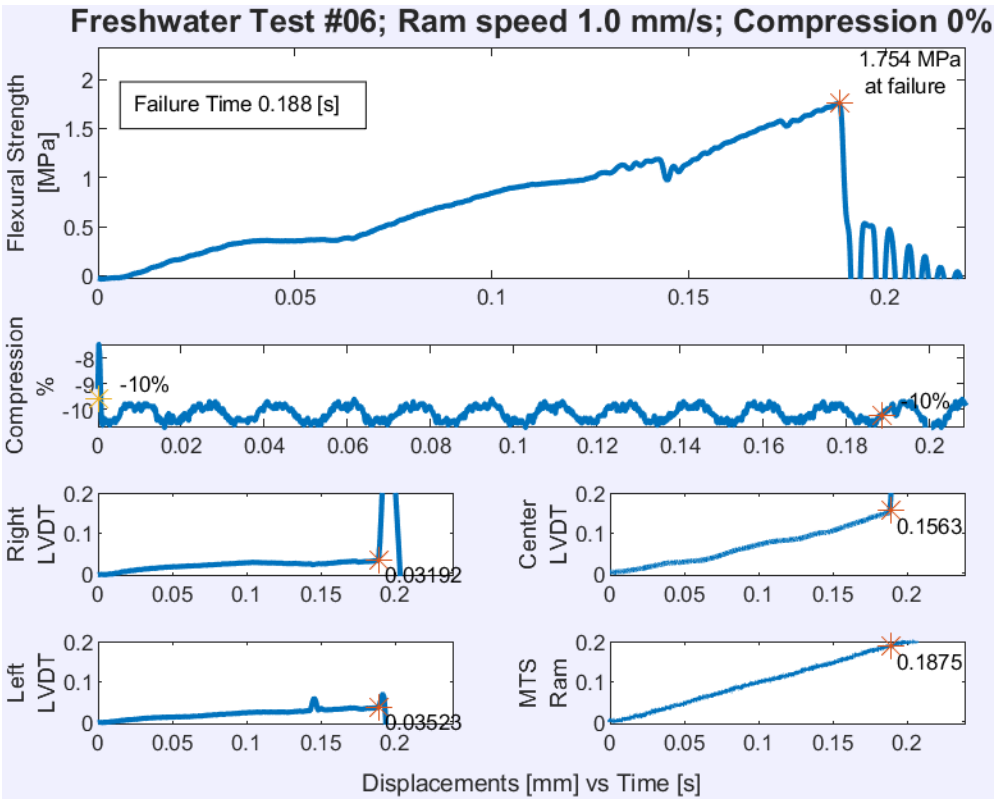
Freshwater Test #06; Ram speed 1.0 mm/s; Compression 0%
Failure Time 0.188 [s]
1.754 MPa
at failure
Flexural Strength [MPa]
Compression %
-10%
-10%
Right LVDT
0.03192
Center LVDT
0.1563
Left LVDT
0.03523
MTS Ram
0.1875
Displacements [mm] vs Time [s]

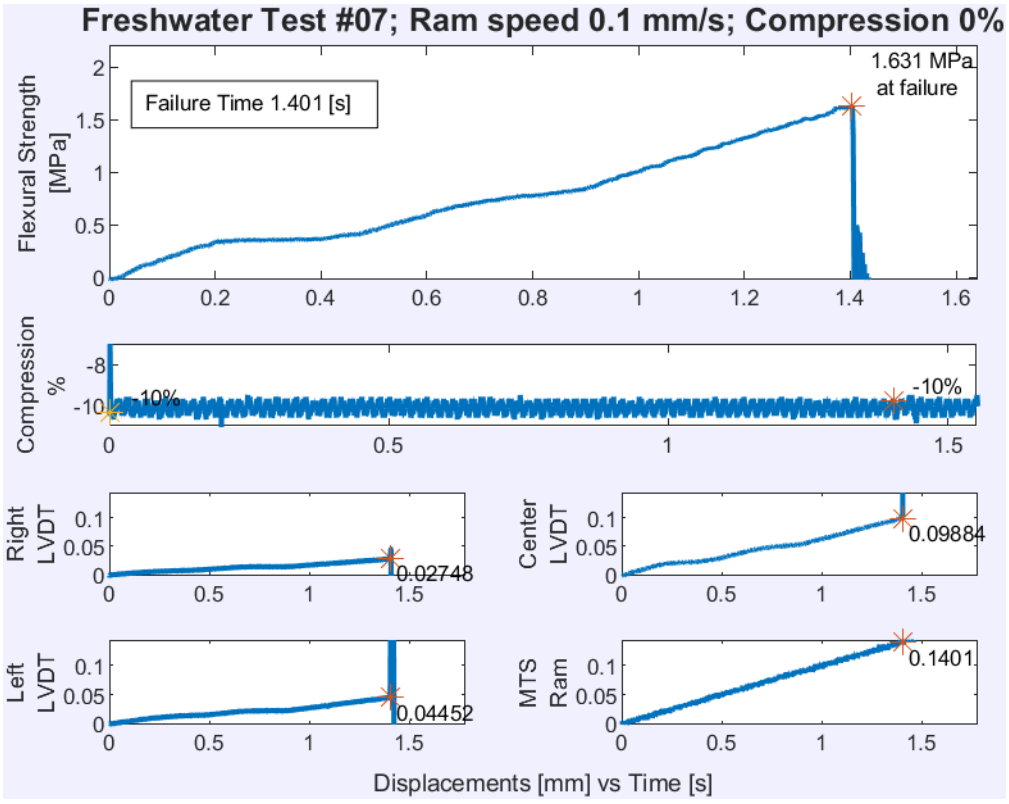
Freshwater Test #07; Ram speed 0.1 mm/s; Compression 0%
Failure Time 1.401 [s]
1.631 MPa
at failure
Flexural Strength [MPa]
Compression %
-10%
-10%
Right LVDT
0.02748
Center LVDT
0.09884
Left LVDT
0.04452
MTS Ram
0.1401
Displacements [mm] vs Time [s]

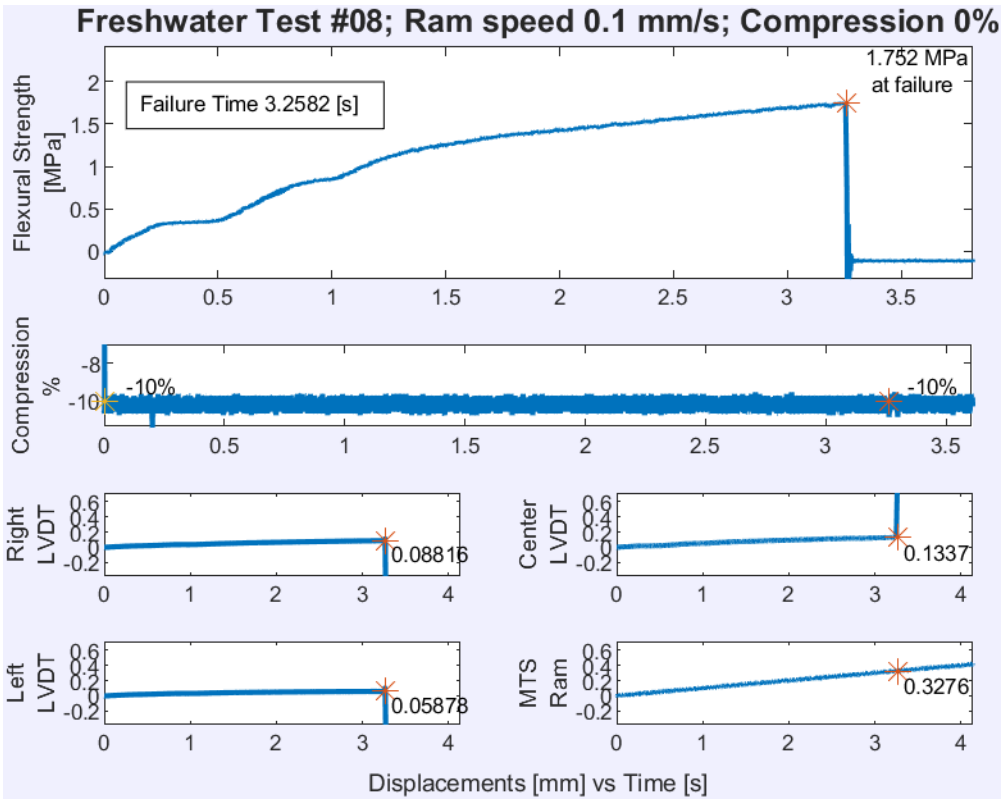
Freshwater Test #08; Ram speed 0.1 mm/s; Compression 0%
Failure Time 3.2582 [s]
1.752 MPa
at failure
Flexural Strength [MPa]
Compression %
-10%
-10%
Right LVDT
0.08816
Center LVDT
0.1337
Left LVDT
0.05878
MTS Ram
0.3276
Displacements [mm] vs Time [s]

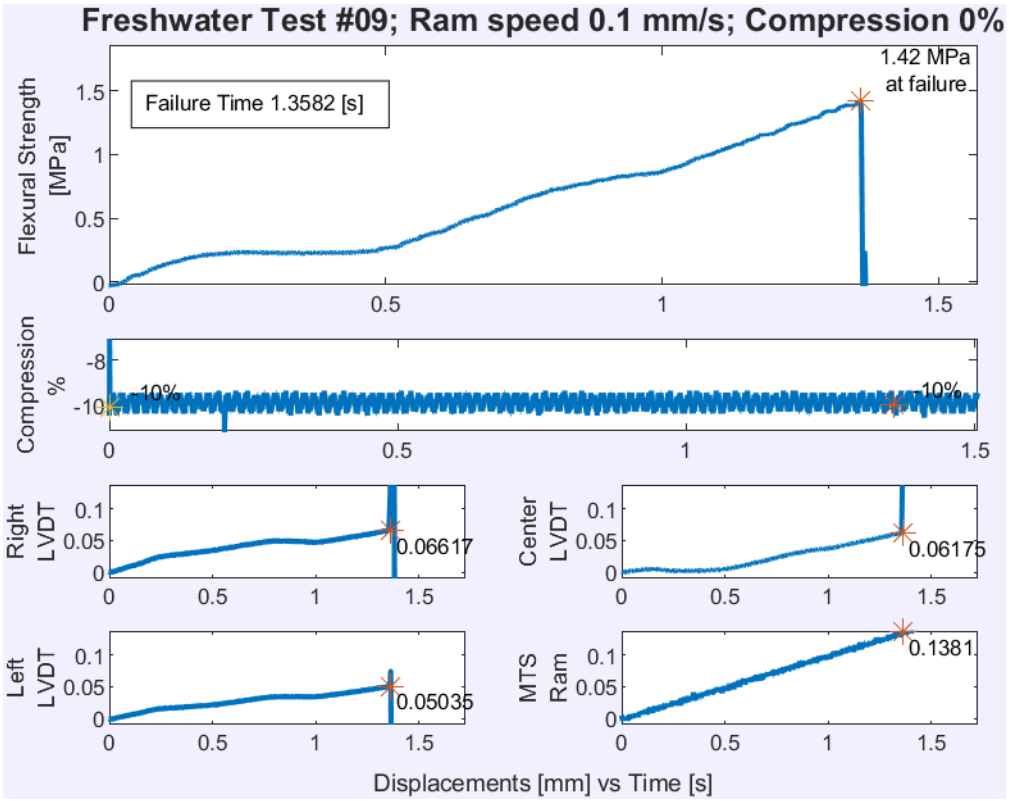
Freshwater Test #09; Ram speed 0.1 mm/s; Compression 0%
Failure Time 1.3582 [s]
1.42 MPa
at failure
Flexural Strength [MPa]
Compression %
-10%
-10%
Right LVDT
0.06617
Center LVDT
0.06175
Left LVDT
0.05035
MTS Ram
0.1381
Displacements [mm] vs Time [s]

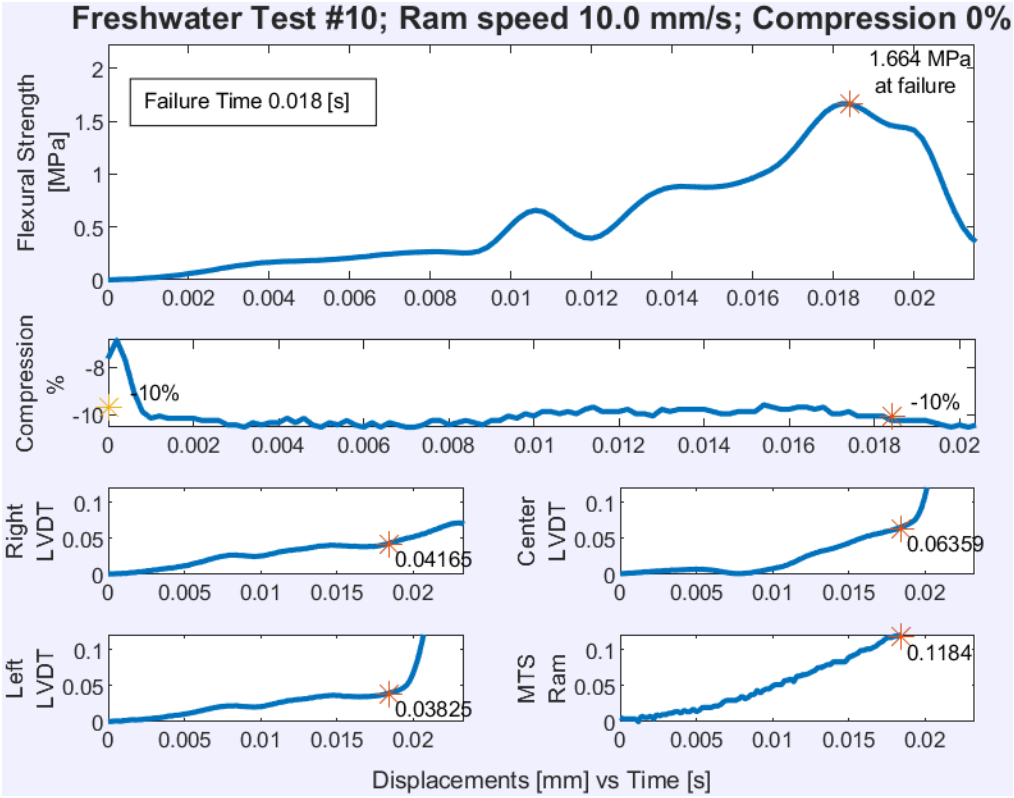
Freshwater Test #10; Ram speed 10.0 mm/s; Compression 0%
Failure Time 0.018 [s]
1.664 MPa
at failure
Flexural Strength [MPa]
Compression %
-10%
-10%
Right LVDT
0.04165
Center LVDT
0.06359
Left LVDT
0.03825
MTS Ram
0.1184
Displacements [mm] vs Time [s]

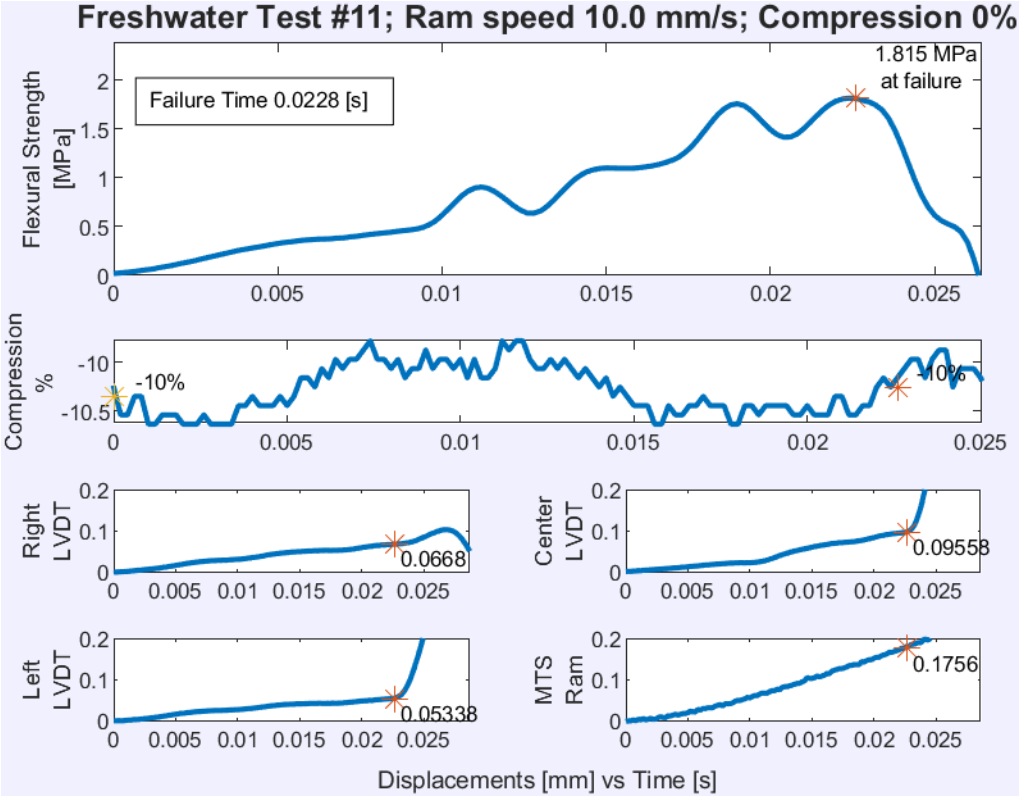
Freshwater Test #11; Ram speed 10.0 mm/s; Compression 0%
Failure Time 0.0228 [s]
1.815 MPa
at failure
Flexural Strength [MPa]
Compression %
-10%
-10%
Right LVDT
0.0668
Center LVDT
0.09558
Left LVDT
0.05338
MTS Ram
0.1756
Displacements [mm] vs Time [s]

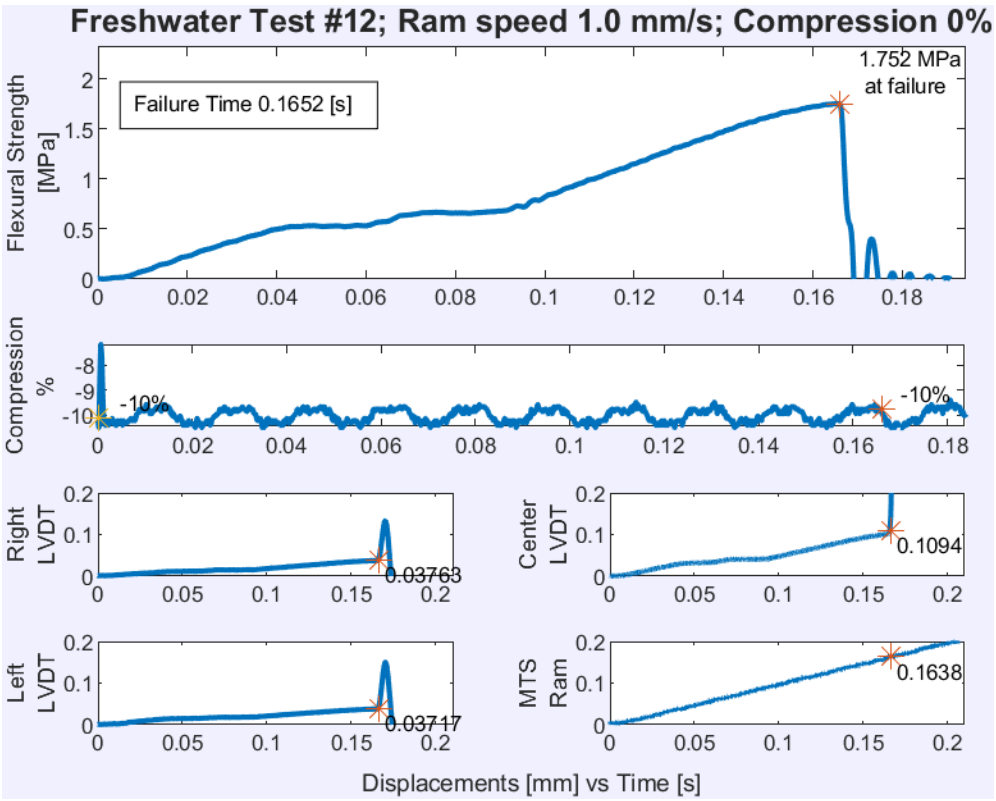
Freshwater Test #12; Ram speed 1.0 mm/s; Compression 0%
Failure Time 0.1652 [s]
1.752 MPa
at failure
Flexural Strength [MPa]
Compression %
-10%
-10%
Right LVDT
0.03763
Center LVDT
0.1094
Left LVDT
0.03717
MTS Ram
0.1638
Displacements [mm] vs Time [s]

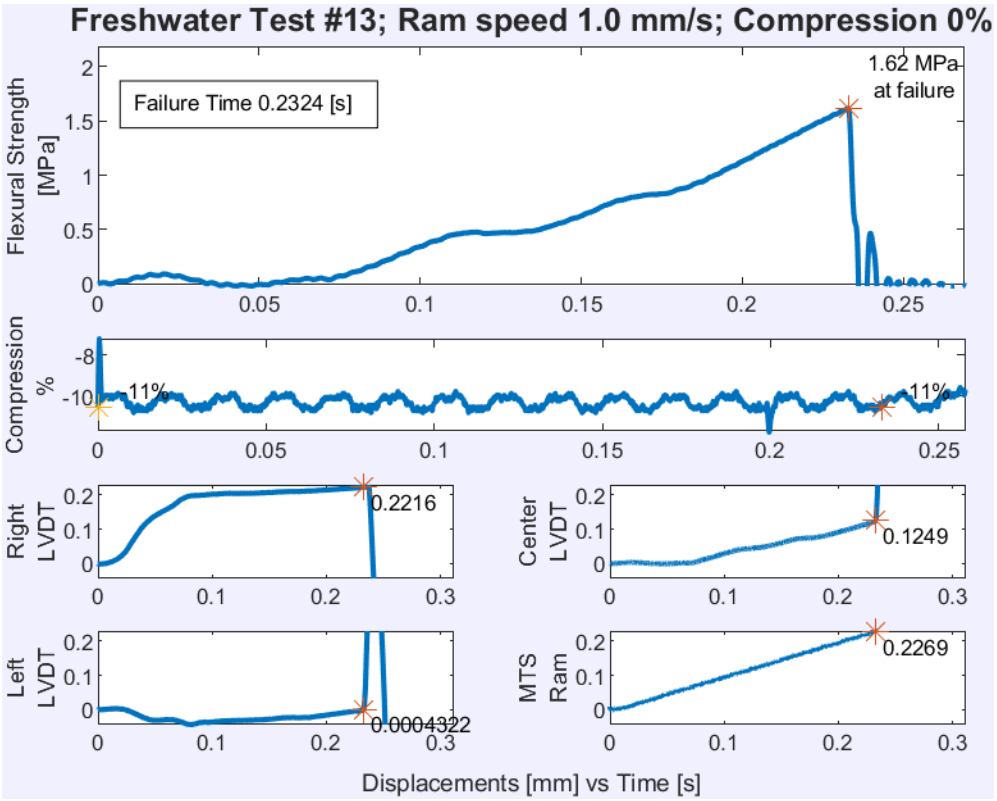
Freshwater Test #13; Ram speed 1.0 mm/s; Compression 0%
Failure Time 0.2324 [s]
1.62 MPa at failure
Flexural Strength [MPa]
Compression %
-11%
-11%
Right LVDT
0.2216
Center LVDT
0.1249
Left LVDT
0.0004322
MTS Ram
0.2269
Displacements [mm] vs Time [s]

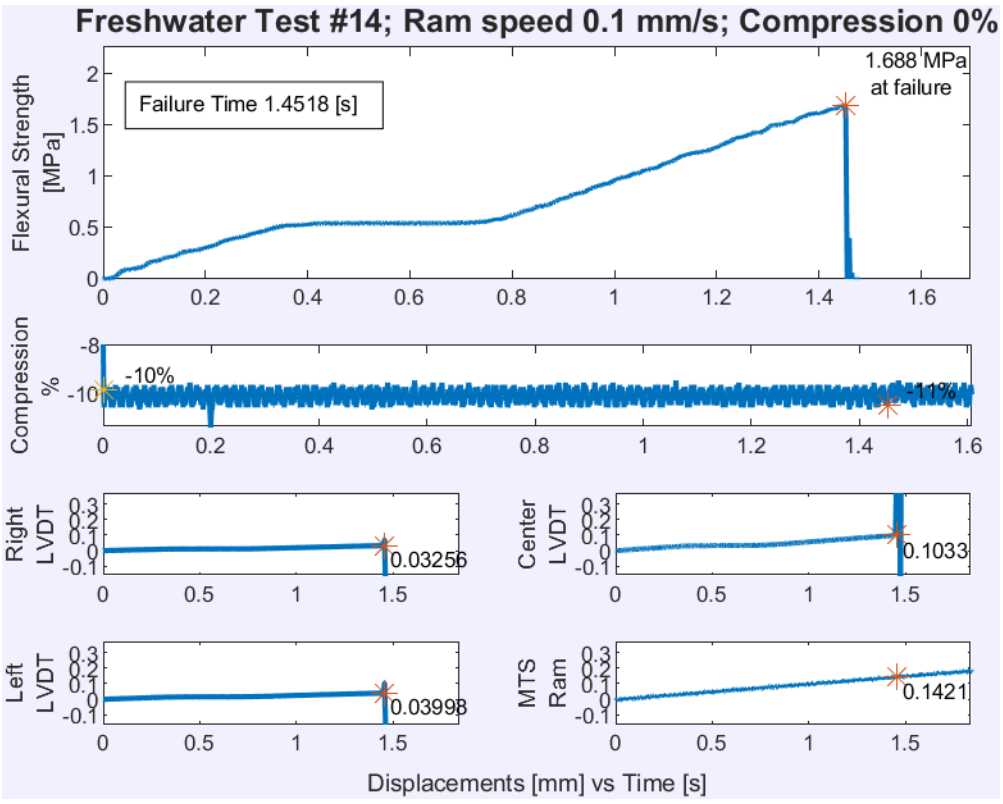
Freshwater Test #14; Ram speed 0.1 mm/s; Compression 0%
Failure Time 1.4518 [s]
1.688 MPa at failure
Flexural Strength [MPa]
Compression %
-10%
-11%
Right LVDT
0.03256
Center LVDT
0.1033
Left LVDT
0.03998
MTS Ram
0.1421
Displacements [mm] vs Time [s]

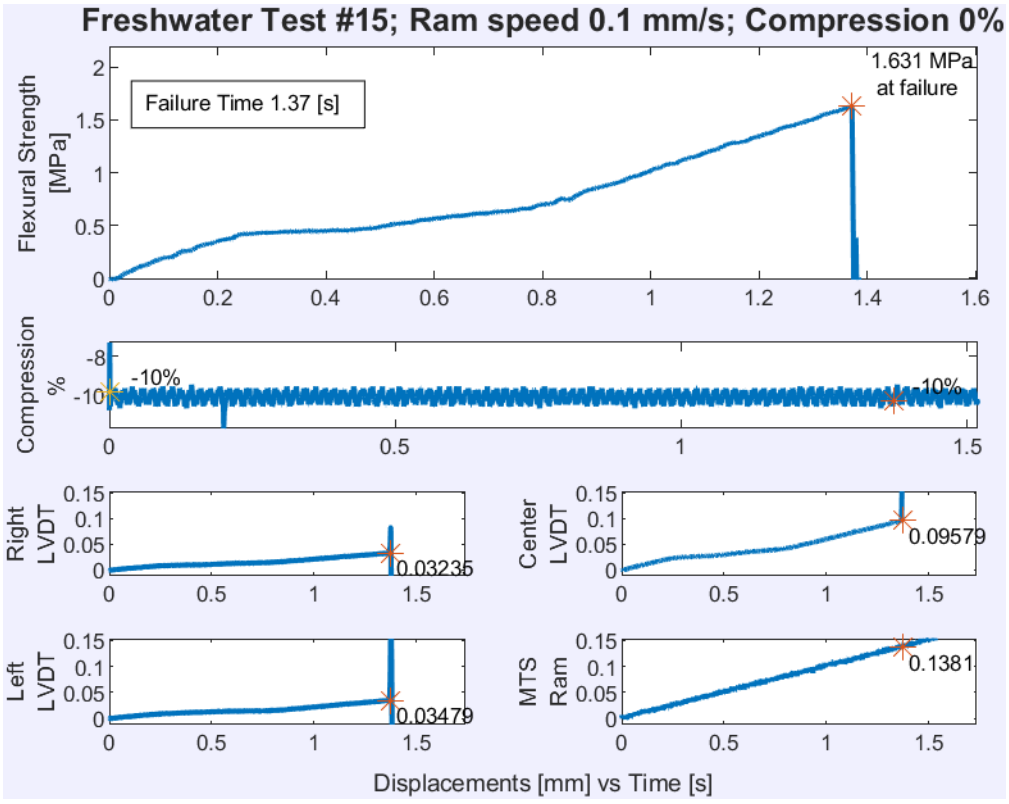
Freshwater Test #15; Ram speed 0.1 mm/s; Compression 0%
Failure Time 1.37 [s]
1.631 MPa
at failure
Flexural Strength [MPa]
Compression %
-10%
-10%
Right LVDT
0.03235
Center LVDT
0.09579
Left LVDT
0.03479
MTS Ram
0.1381
Displacements [mm] vs Time [s]

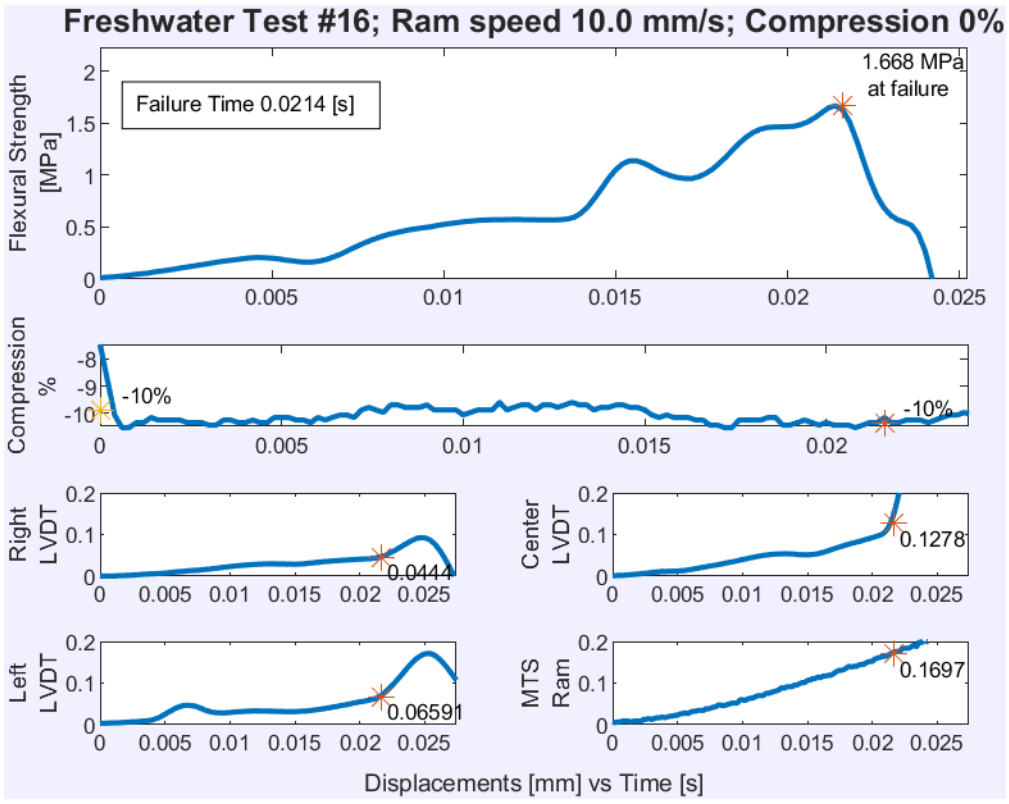
Freshwater Test #16; Ram speed 10.0 mm/s; Compression 0%
Failure Time 0.0214 [s]
1.668 MPa
at failure
Flexural Strength [MPa]
Compression %
-10%
-10%
Right LVDT
0.0444
Center LVDT
0.1278
Left LVDT
0.06591
MTS Ram
0.1697
Displacements [mm] vs Time [s]

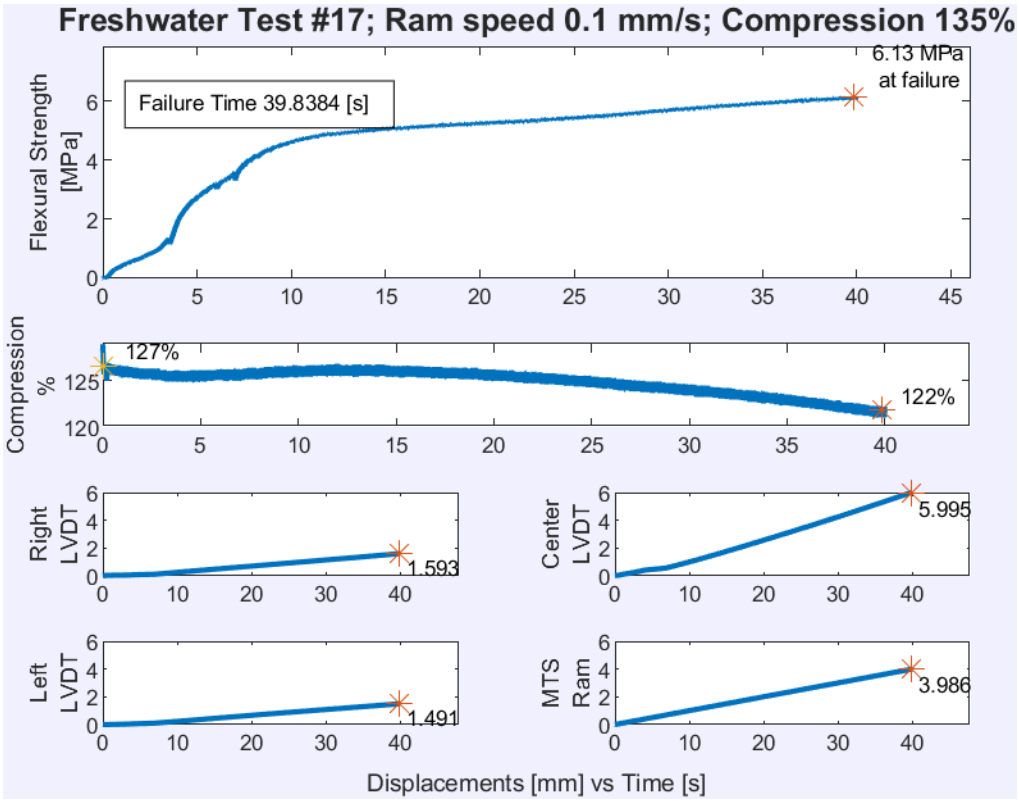
Freshwater Test #17; Ram speed 0.1 mm/s; Compression 135%
Failure Time 39.8384 [s]
6.13 MPa
at failure
Flexural Strength [MPa]
Compression %
127%
122%
Right LVDT
1.593
Center LVDT
5.995
Left LVDT
1.491
MTS Ram
3.986
Displacements [mm] vs Time [s]

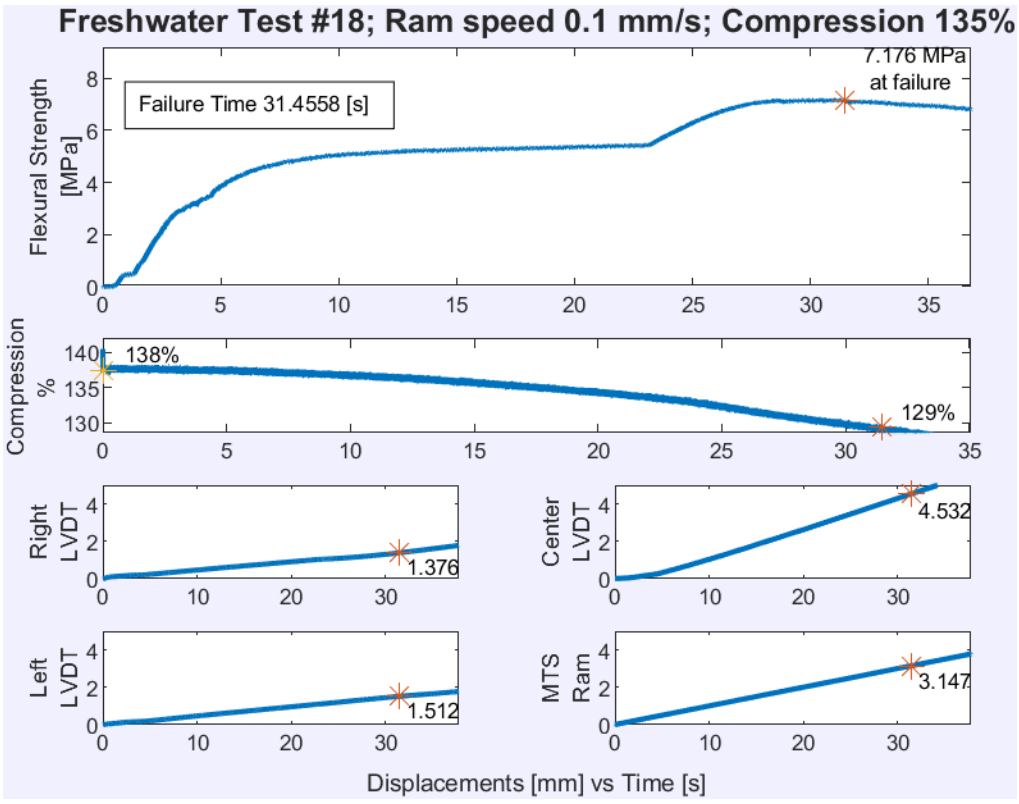
Freshwater Test #18; Ram speed 0.1 mm/s; Compression 135%
Failure Time 31.4558 [s]
7.176 MPa
at failure
Flexural Strength [MPa]
Compression %
138%
129%
Right LVDT
1.376
Center LVDT
4.532
Left LVDT
1.512
MTS Ram
3.147
Displacements [mm] vs Time [s]

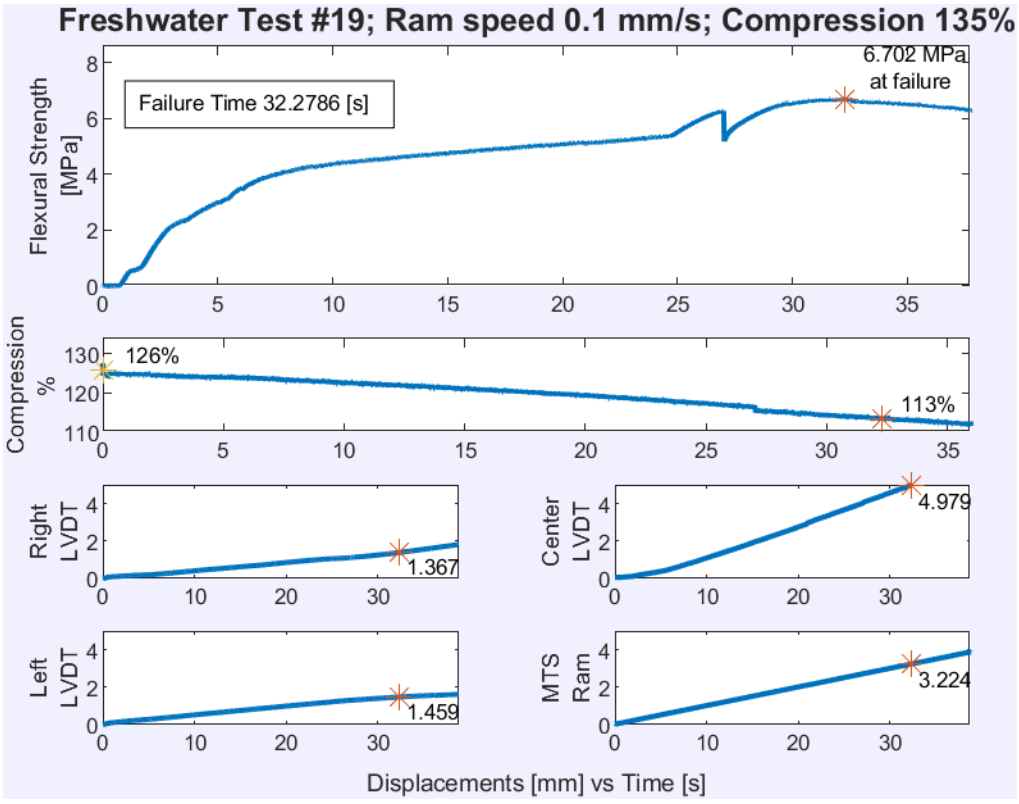
Freshwater Test #19; Ram speed 0.1 mm/s; Compression 135%
Failure Time 32.2786 [s]
6.702 MPa
at failure
Flexural Strength [MPa]
Compression %
126%
113%
Right LVDT
1.367
Center LVDT
4.979
Left LVDT
1.459
MTS Ram
3.224
Displacements [mm] vs Time [s]

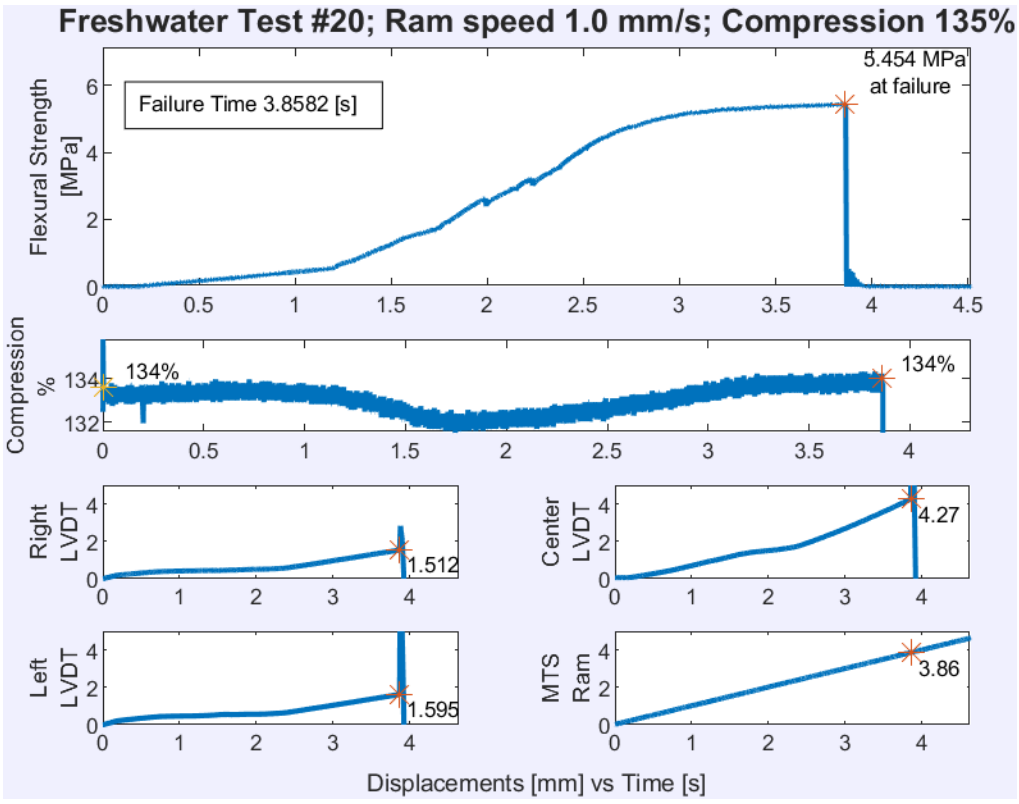
Freshwater Test #20; Ram speed 1.0 mm/s; Compression 135%
Failure Time 3.8582 [s]
5.454 MPa
at failure
Flexural Strength [MPa]
Compression %
134%
134%
Right LVDT
1.512
Center LVDT
4.27
Left LVDT
1.595
MTS Ram
3.86
Displacements [mm] vs Time [s]

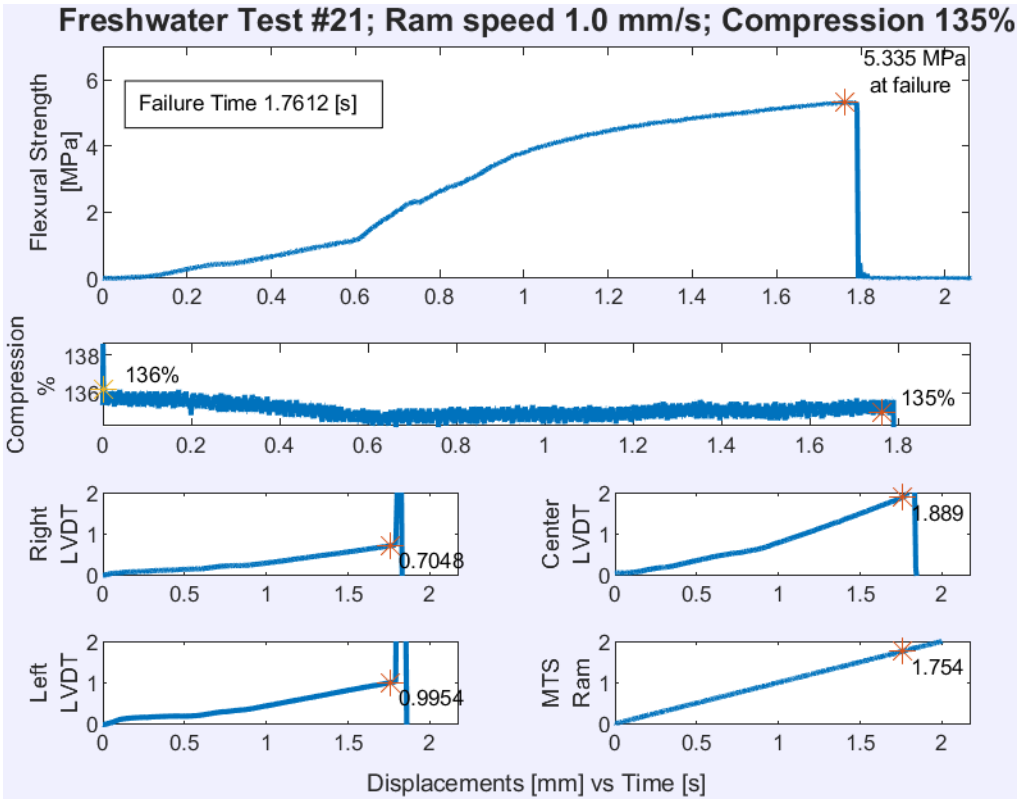
Freshwater Test #21; Ram speed 1.0 mm/s; Compression 135%
Failure Time 1.7612 [s]
5.335 MPa
at failure
Flexural Strength [MPa]
Compression %
136%
135%
Right LVDT
0.7048
Center LVDT
1.889
Left LVDT
0.9954
MTS Ram
1.754
Displacements [mm] vs Time [s]

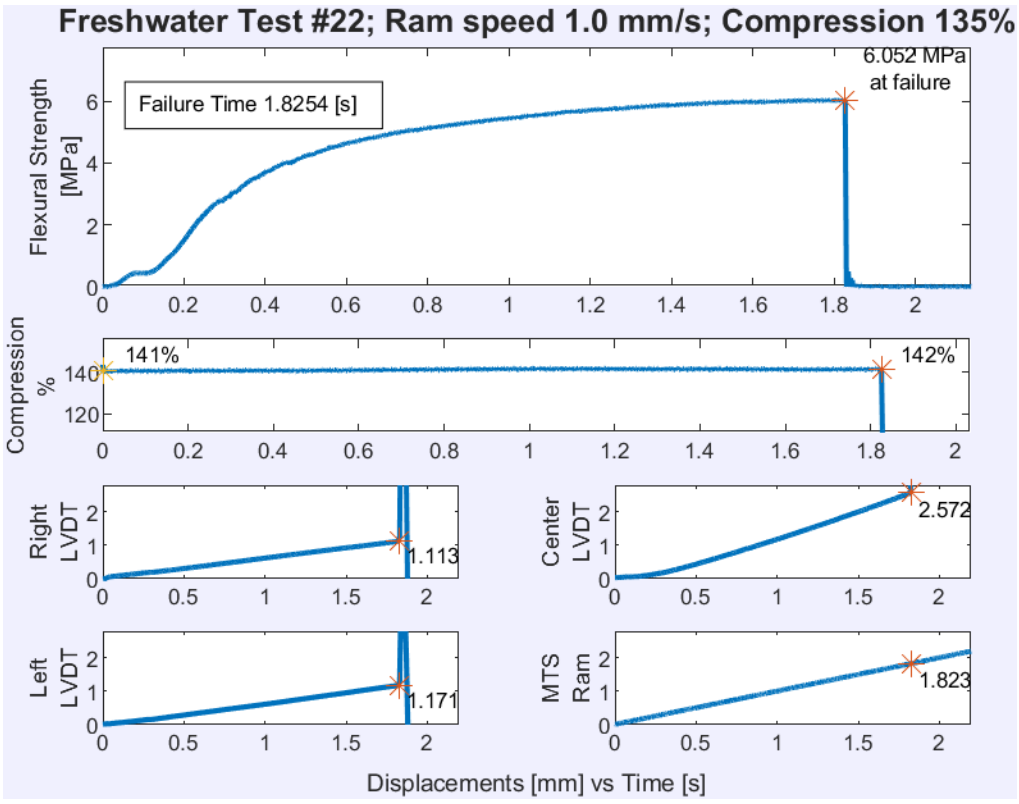
Freshwater Test #22; Ram speed 1.0 mm/s; Compression 135%
Failure Time 1.8254 [s]
6.052 MPa
at failure
Flexural Strength [MPa]
Compression %
141%
142%
Right LVDT
1.113
Center LVDT
2.572
Left LVDT
1.171
MTS Ram
1.823
Displacements [mm] vs Time [s]

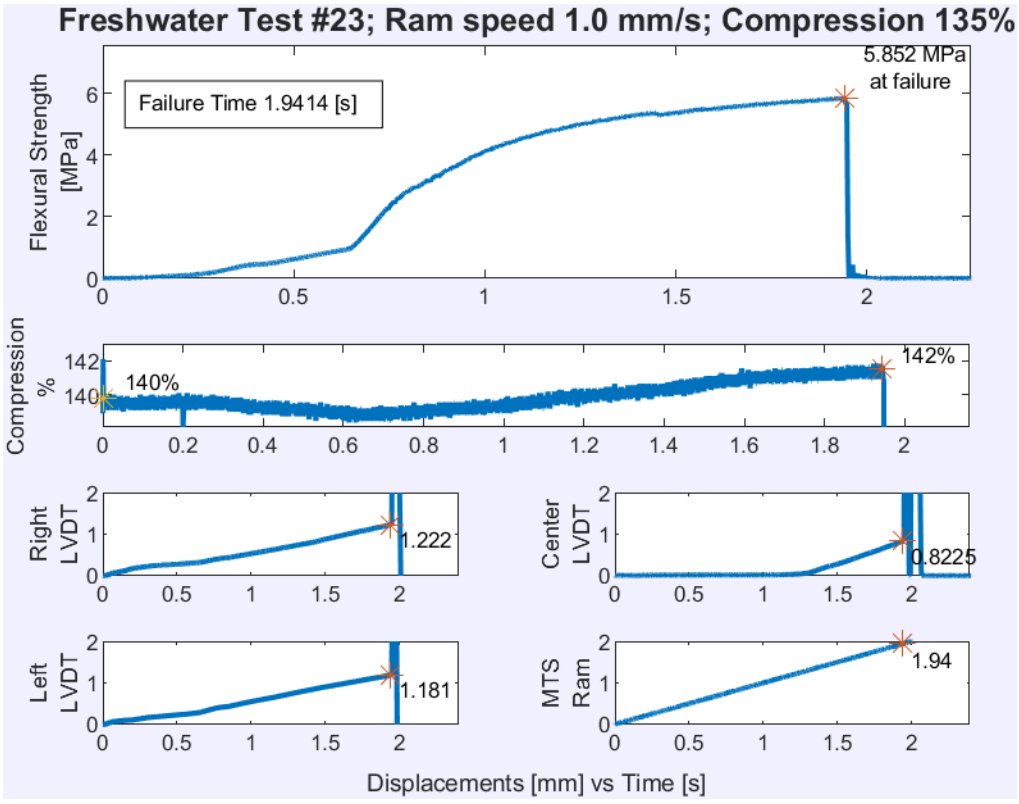
Freshwater Test #23; Ram speed 1.0 mm/s; Compression 135%
Failure Time 1.9414 [s]
5.852 MPa
at failure
Flexural Strength [MPa]
Compression %
140%
142%
Right LVDT
1.222
Center LVDT
0.8225
Left LVDT
1.181
MTS Ram
1.94
Displacements [mm] vs Time [s]

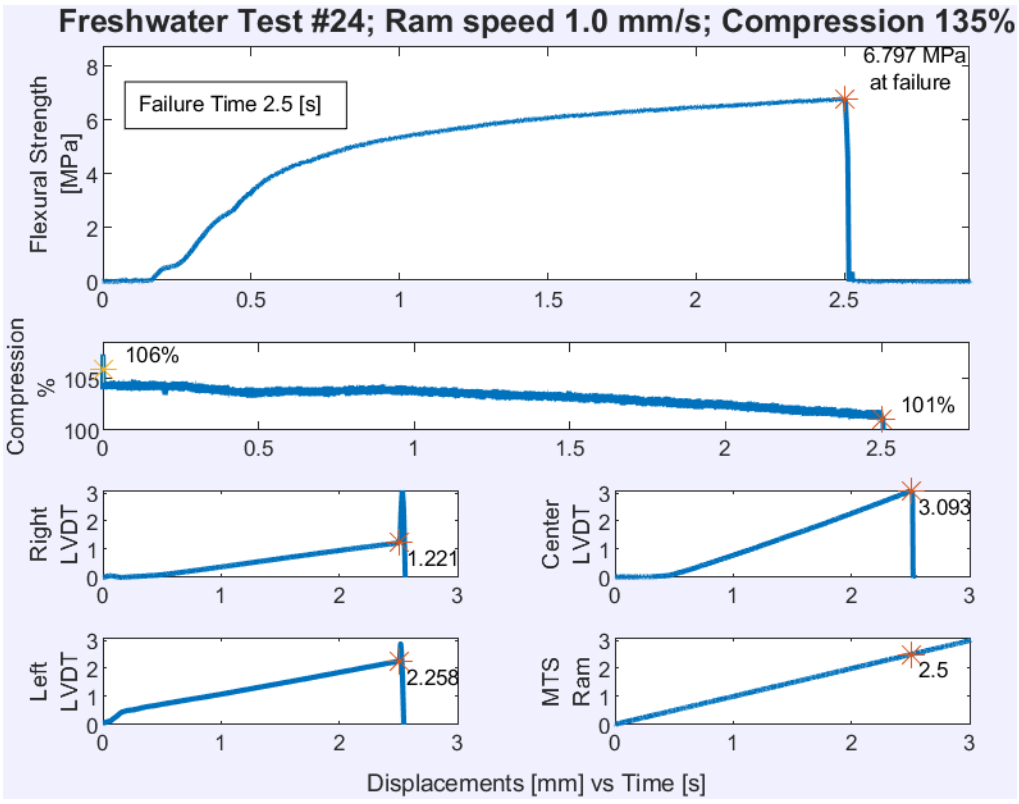
Freshwater Test #24; Ram speed 1.0 mm/s; Compression 135%
Failure Time 2.5 [s]
6.797 MPa
at failure
Flexural Strength [MPa]
Compression %
106%
101%
Right LVDT
1.221
Center LVDT
3.093
Left LVDT
2.258
MTS Ram
2.5
Displacements [mm] vs Time [s]

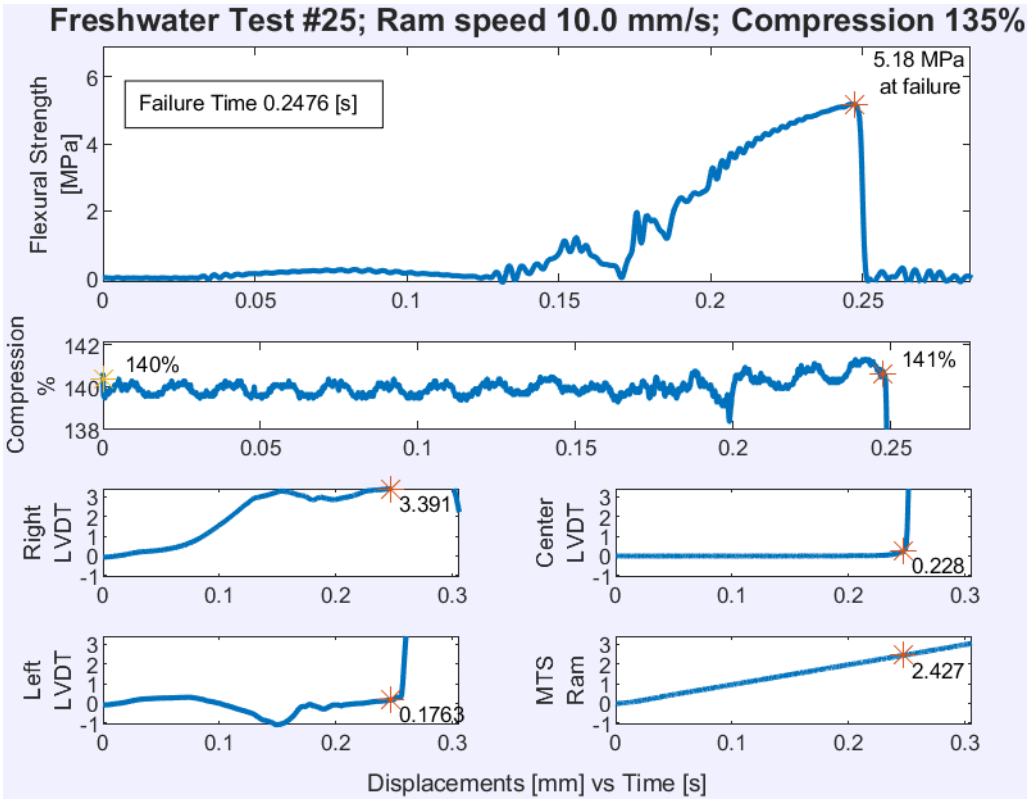
Freshwater Test #25; Ram speed 10.0 mm/s; Compression 135%
Failure Time 0.2476 [s]
5.18 MPa
at failure
Flexural Strength [MPa]
Compression %
140%
141%
Right LVDT
3.391
Center LVDT
0.228
Left LVDT
0.1763
MTS Ram
2.427
Displacements [mm] vs Time [s]

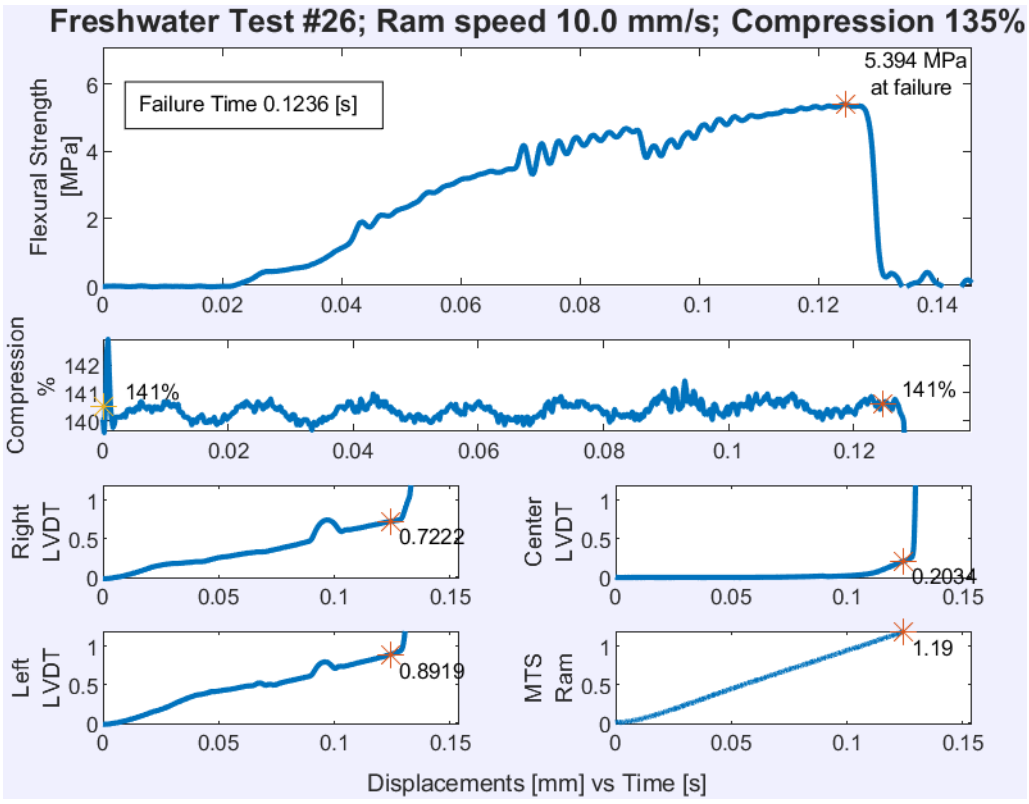
Freshwater Test #26; Ram speed 10.0 mm/s; Compression 135%
Failure Time 0.1236 [s]
5.394 MPa
at failure
Flexural Strength [MPa]
Compression %
141%
141%
Right LVDT
0.7222
Center LVDT
0.2034
Left LVDT
0.8919
MTS Ram
1.19
Displacements [mm] vs Time [s]

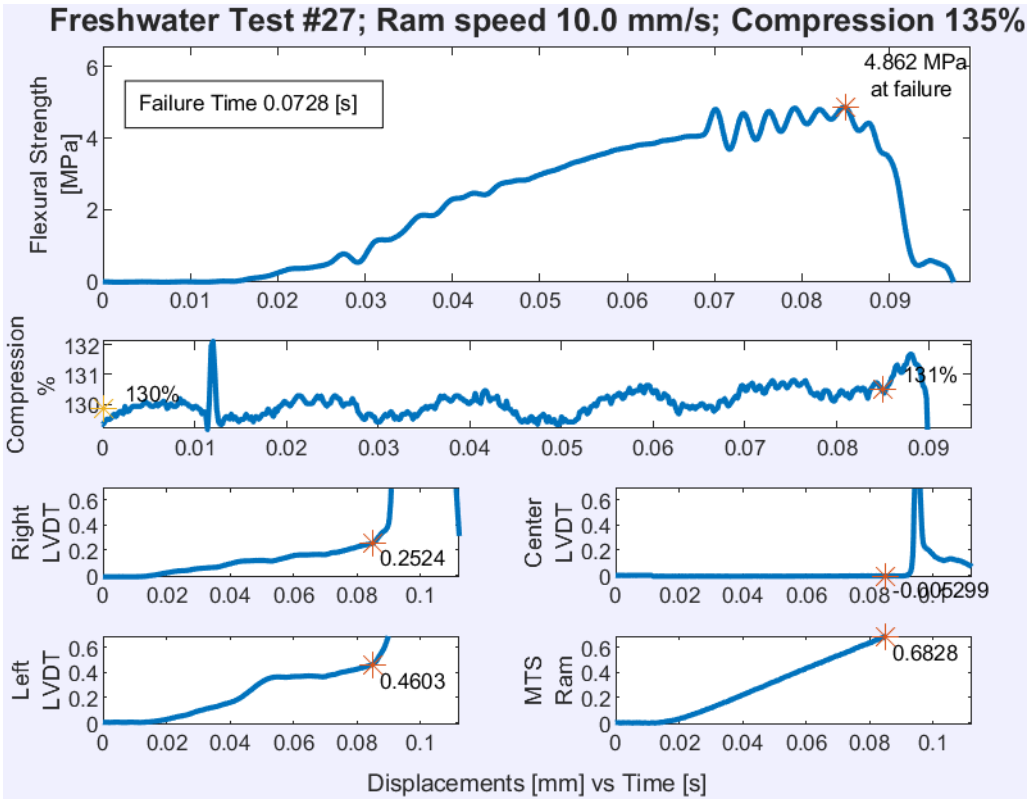
Freshwater Test #27; Ram speed 10.0 mm/s; Compression 135%
Failure Time 0.0728 [s]
4.862 MPa
at failure
Flexural Strength [MPa]
Compression %
130%
131%
Right LVDT
0.2524
Center LVDT
-0.005299
Left LVDT
0.4603
MTS Ram
0.6828
Displacements [mm] vs Time [s]

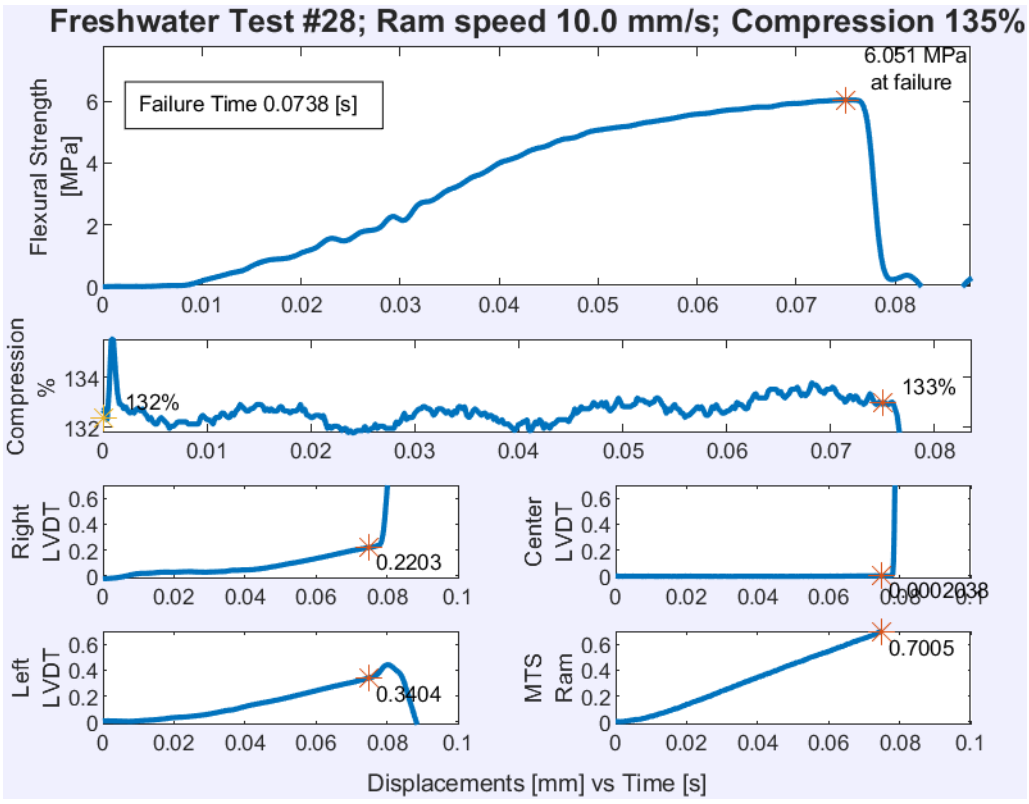
Freshwater Test #28; Ram speed 10.0 mm/s; Compression 135%
Failure Time 0.0738 [s]
6.051 MPa
at failure
Flexural Strength [MPa]
Compression %
132%
133%
Right LVDT
0.2203
Center LVDT
0.0002038
Left LVDT
0.3404
MTS Ram
0.7005
Displacements [mm] vs Time [s]

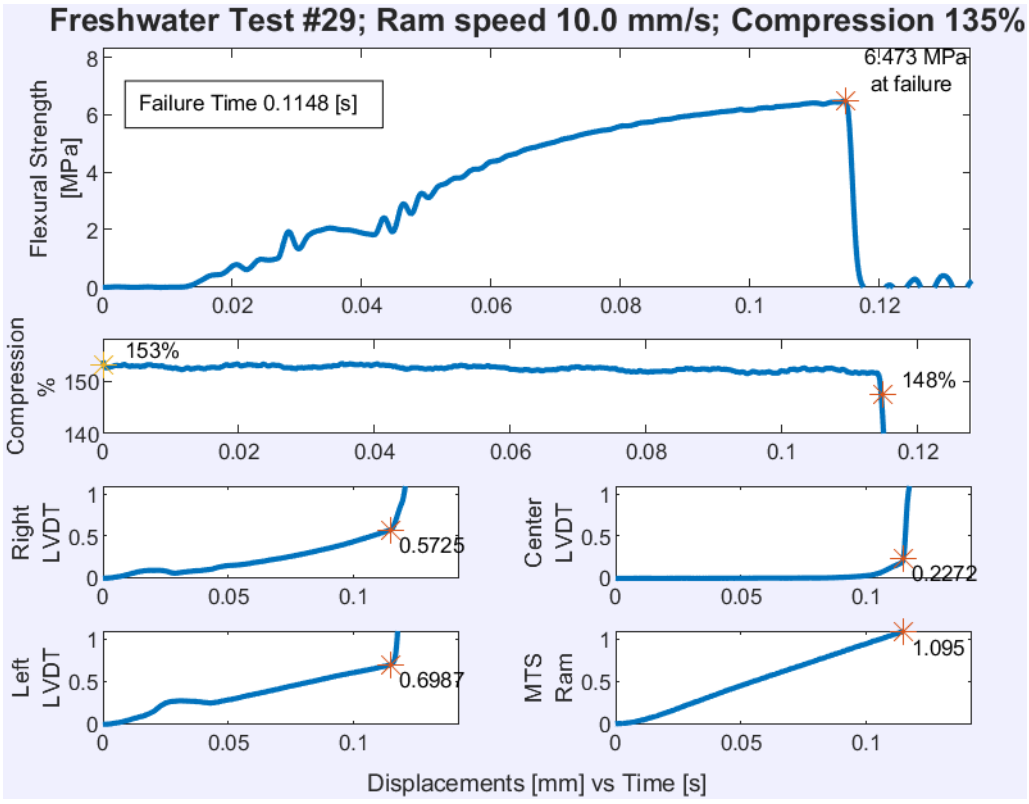
Freshwater Test #29; Ram speed 10.0 mm/s; Compression 135%
Failure Time 0.1148 [s]
6.473 MPa at failure
Flexural Strength [MPa]
Compression %
153%
148%
Right LVDT
0.5725
Center LVDT
0.2272
Left LVDT
0.6987
MTS Ram
1.095
Displacements [mm] vs Time [s]

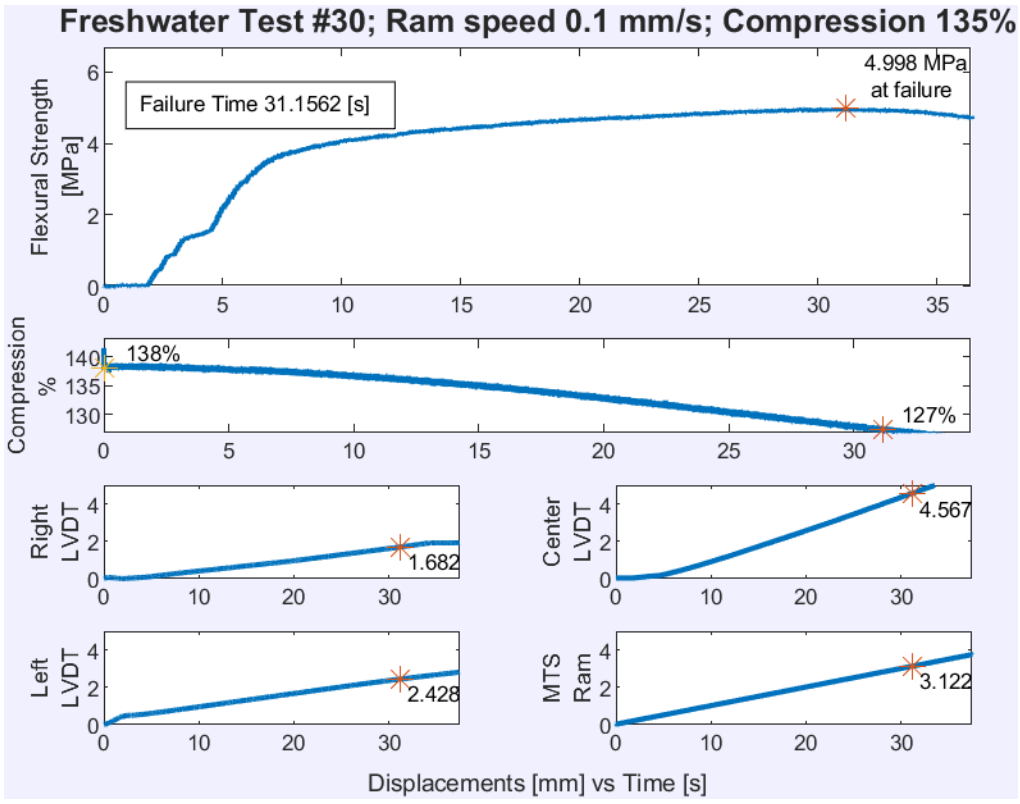
Freshwater Test #30; Ram speed 0.1 mm/s; Compression 135%
Failure Time 31.1562 [s]
4.998 MPa at failure
Flexural Strength [MPa]
Compression %
138%
127%
Right LVDT
1.682
Center LVDT
4.567
Left LVDT
2.428
MTS Ram
3.122
Displacements [mm] vs Time [s]

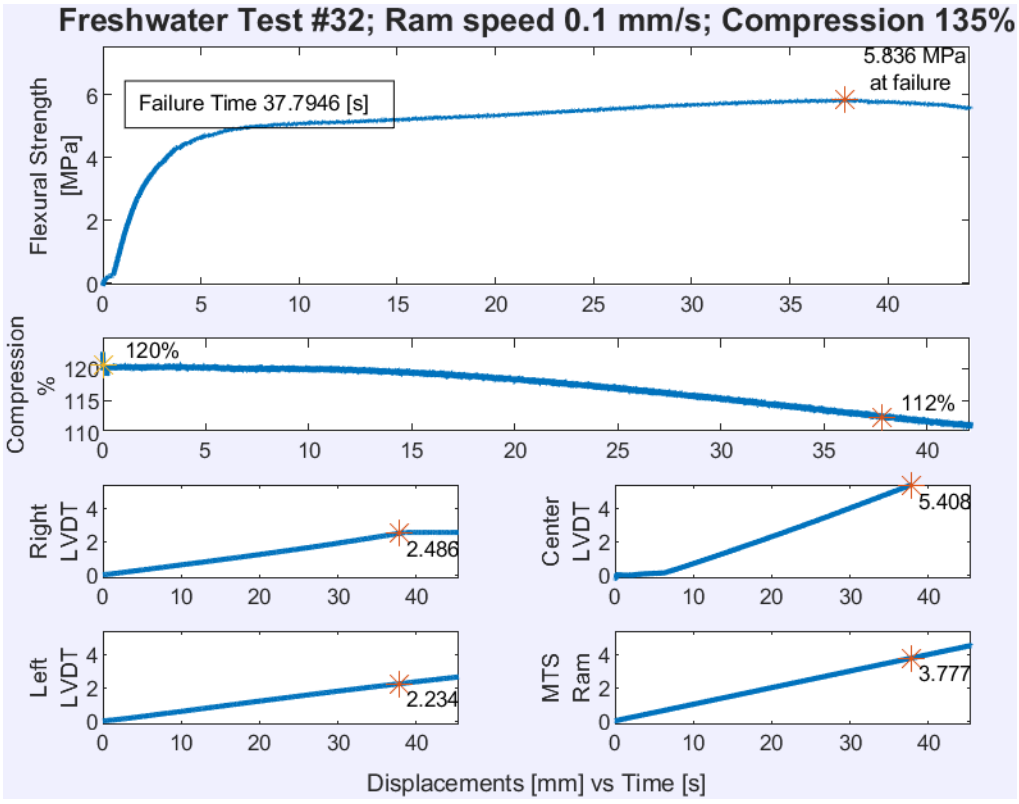
Freshwater Test #32; Ram speed 0.1 mm/s; Compression 135%
Failure Time 37.7946 [s]
5.836 MPa
at failure
Flexural Strength [MPa]
Compression %
120%
112%
Right LVDT
2.486
Center LVDT
5.408
Left LVDT
2.234
MTS Ram
3.777
Displacements [mm] vs Time [s]

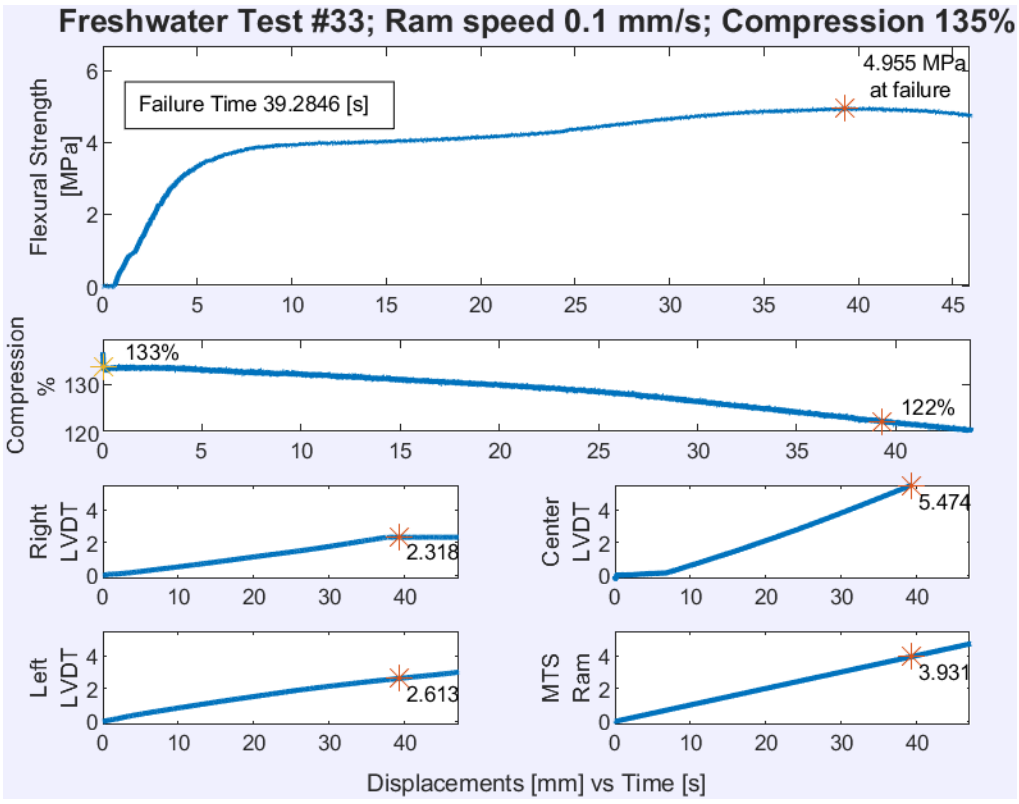
Freshwater Test #33; Ram speed 0.1 mm/s; Compression 135%
Failure Time 39.2846 [s]
4.955 MPa
at failure
Flexural Strength [MPa]
Compression %
133%
122%
Right LVDT
2.318
Center LVDT
5.474
Left LVDT
2.613
MTS Ram
3.931
Displacements [mm] vs Time [s]

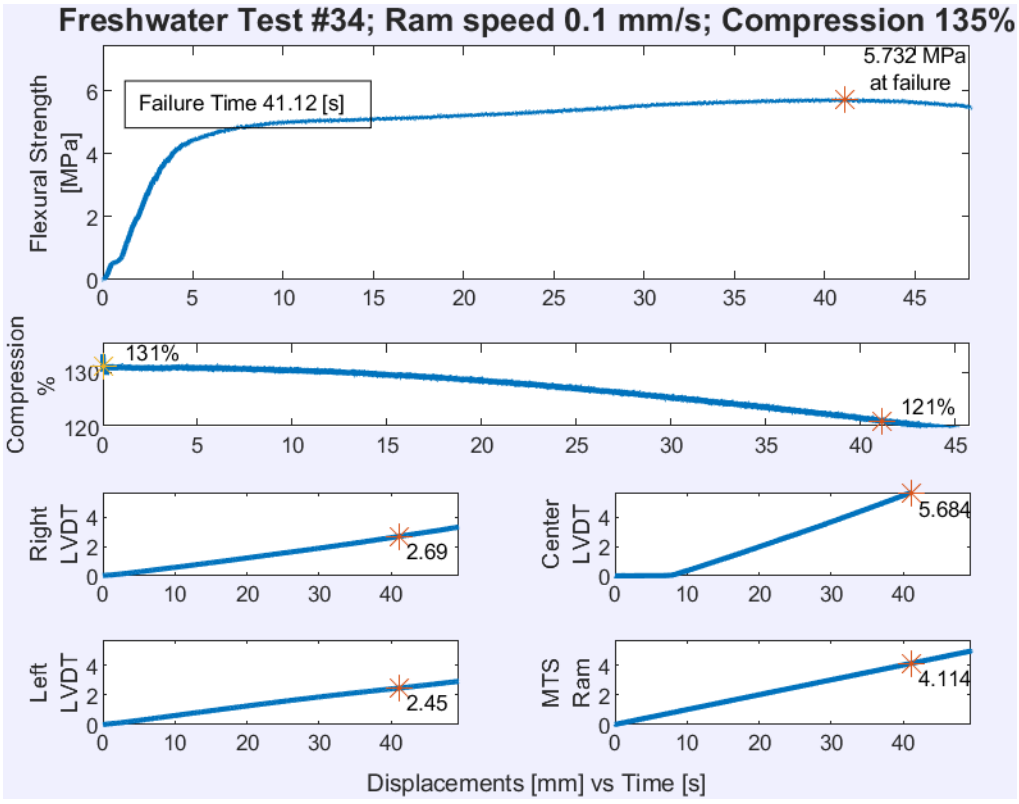
Freshwater Test #34; Ram speed 0.1 mm/s; Compression 135%
Failure Time 41.12 [s]
5.732 MPa
at failure
Flexural Strength [MPa]
131%
121%
Compression %
Right LVDT
2.69
Center LVDT
5.684
Left LVDT
2.45
MTS Ram
4.114
Displacements [mm] vs Time [s]

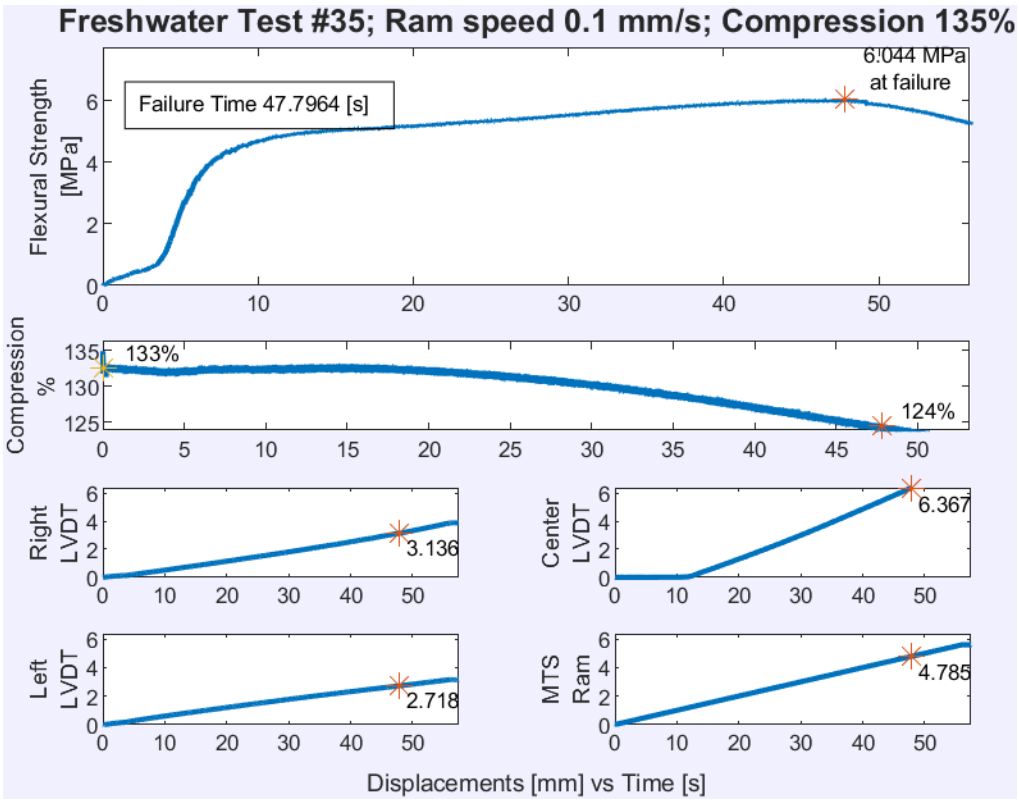
Freshwater Test #35; Ram speed 0.1 mm/s; Compression 135%
Failure Time 47.7964 [s]
6.044 MPa
at failure
Flexural Strength [MPa]
133%
124%
Compression %
Right LVDT
3.136
Center LVDT
6.367
Left LVDT
2.718
MTS Ram
4.785
Displacements [mm] vs Time [s]

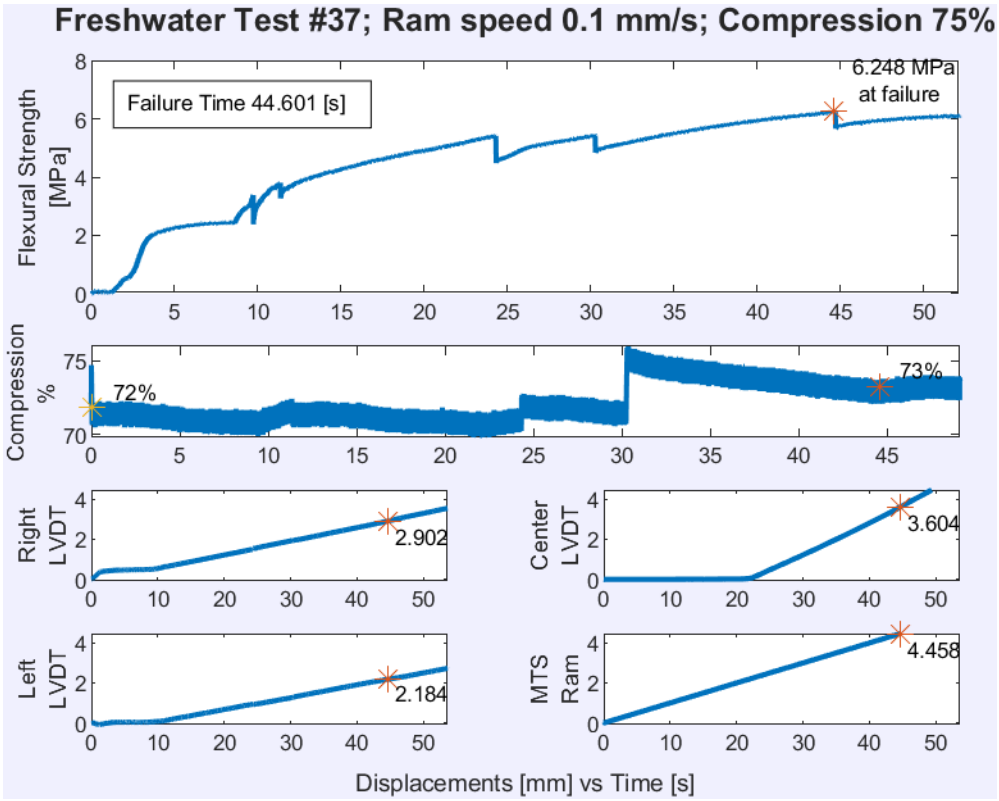
Freshwater Test #37; Ram speed 0.1 mm/s; Compression 75%
Failure Time 44.601 [s]
6.248 MPa
at failure
Flexural Strength [MPa]
Compression %
72%
73%
Right LVDT
2.902
Center LVDT
3.604
Left LVDT
2.184
MTS Ram
4.458
Displacements [mm] vs Time [s]

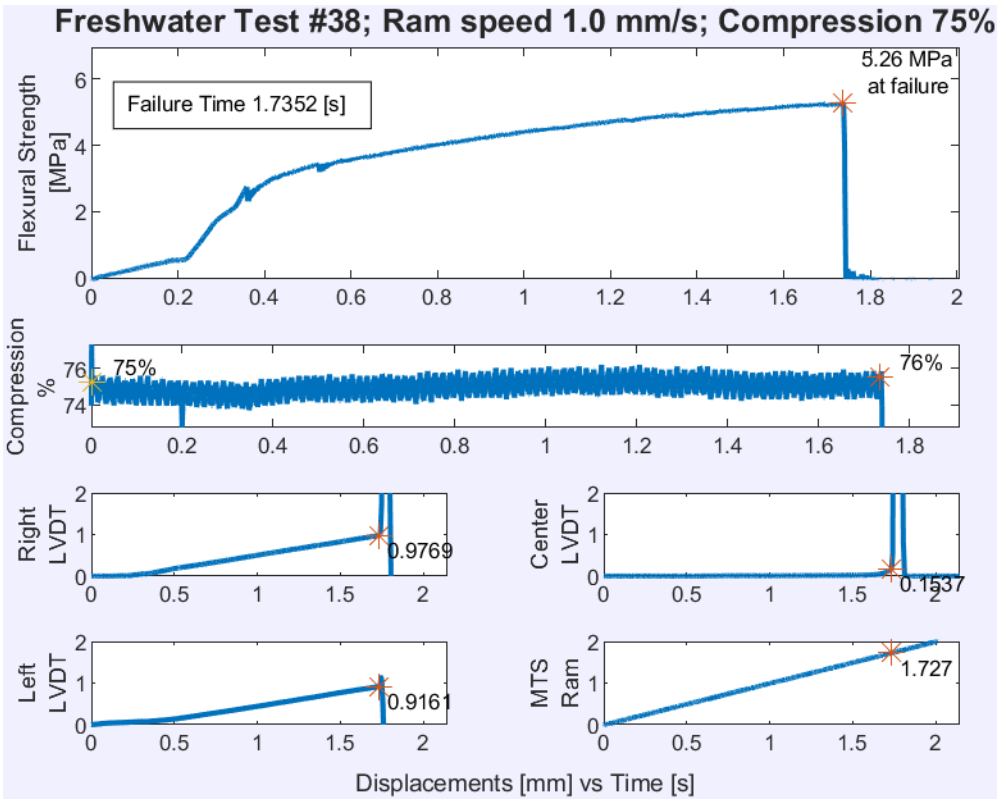
Freshwater Test #38; Ram speed 1.0 mm/s; Compression 75%
Failure Time 1.7352 [s]
5.26 MPa
at failure
Flexural Strength [MPa]
Compression %
75%
76%
Right LVDT
0.9769
Center LVDT
0.1537
Left LVDT
0.9161
MTS Ram
1.727
Displacements [mm] vs Time [s]

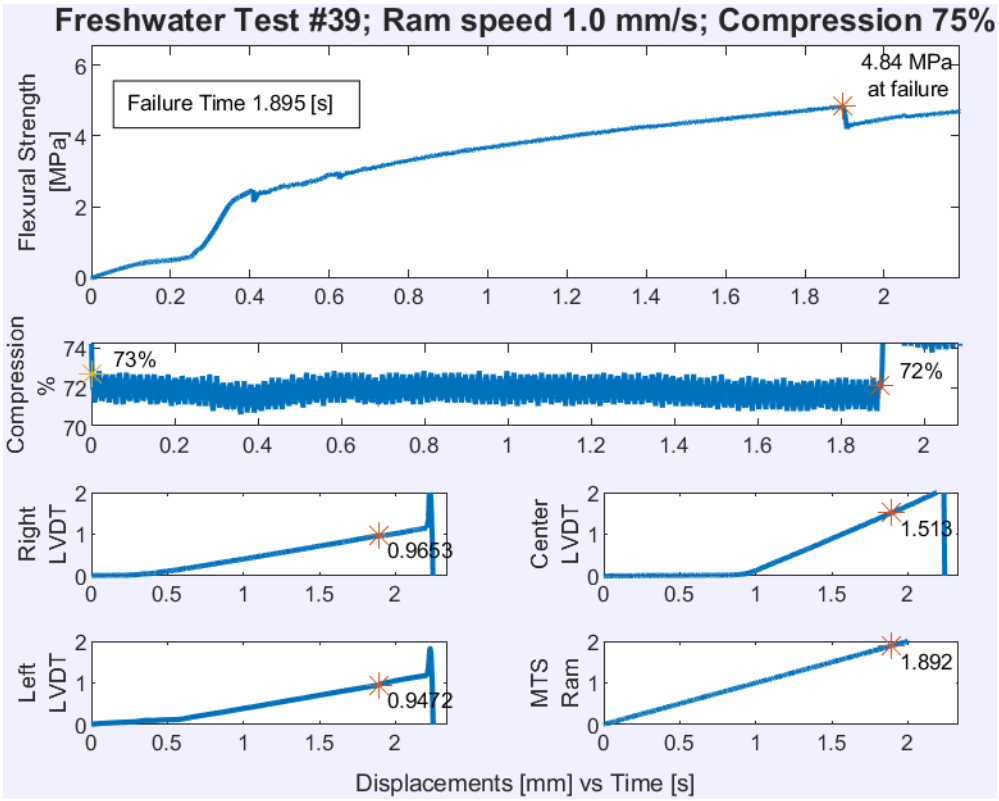
Freshwater Test #39; Ram speed 1.0 mm/s; Compression 75%
Failure Time 1.895 [s]
4.84 MPa at failure
Flexural Strength [MPa]
Compression %
73%
72%
Right LVDT
0.9653
Center LVDT
1.513
Left LVDT
0.9472
MTS Ram
1.892
Displacements [mm] vs Time [s]

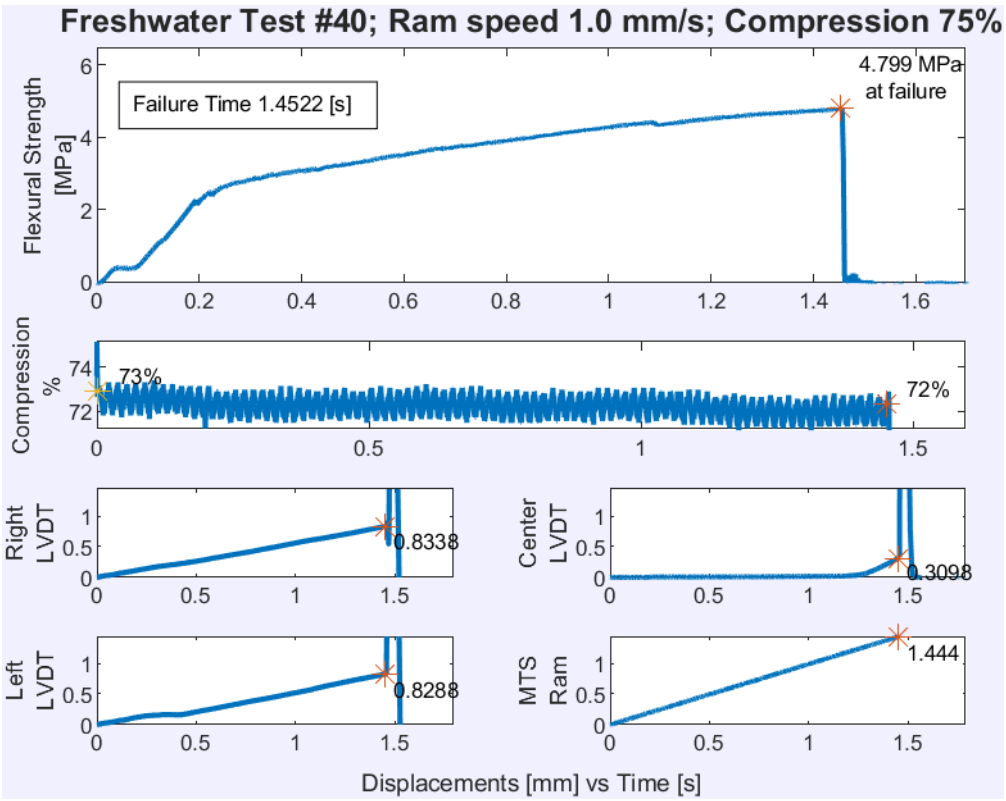
Freshwater Test #40; Ram speed 1.0 mm/s; Compression 75%
Failure Time 1.4522 [s]
4.799 MPa at failure
Flexural Strength [MPa]
Compression %
73%
72%
Right LVDT
0.8338
Center LVDT
0.3098
Left LVDT
0.8288
MTS Ram
1.444
Displacements [mm] vs Time [s]

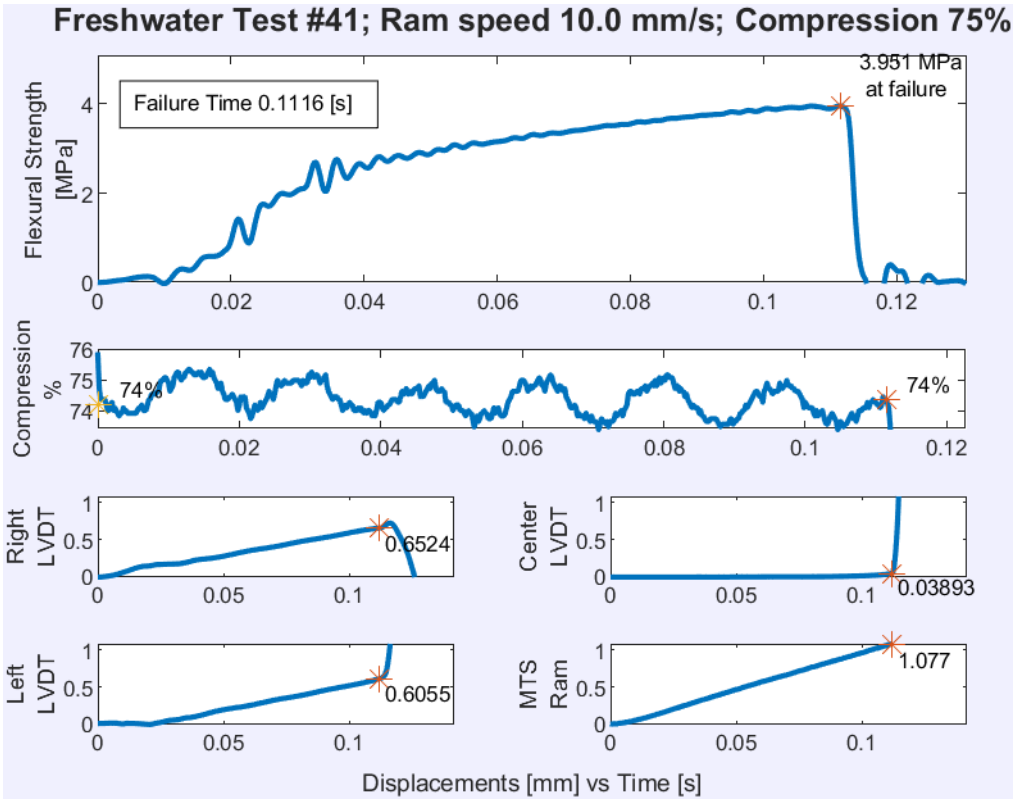
Freshwater Test #41; Ram speed 10.0 mm/s; Compression 75%
Failure Time 0.1116 [s]
3.951 MPa
at failure
Flexural Strength [MPa]
Compression %
74%
74%
Right LVDT
0.6524
Center LVDT
0.03893
Left LVDT
0.6055
MTS Ram
1.077
Displacements [mm] vs Time [s]

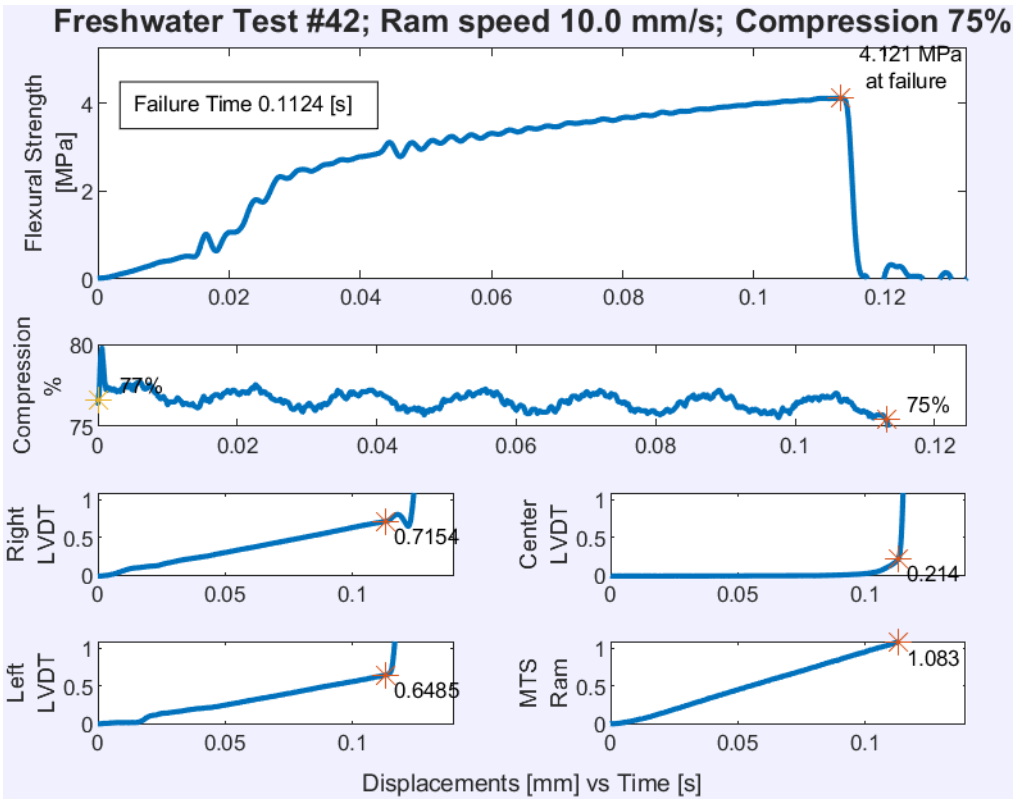
Freshwater Test #42; Ram speed 10.0 mm/s; Compression 75%
Failure Time 0.1124 [s]
4.121 MPa
at failure
Flexural Strength [MPa]
Compression %
77%
75%
Right LVDT
0.7154
Center LVDT
0.214
Left LVDT
0.6485
MTS Ram
1.083
Displacements [mm] vs Time [s]

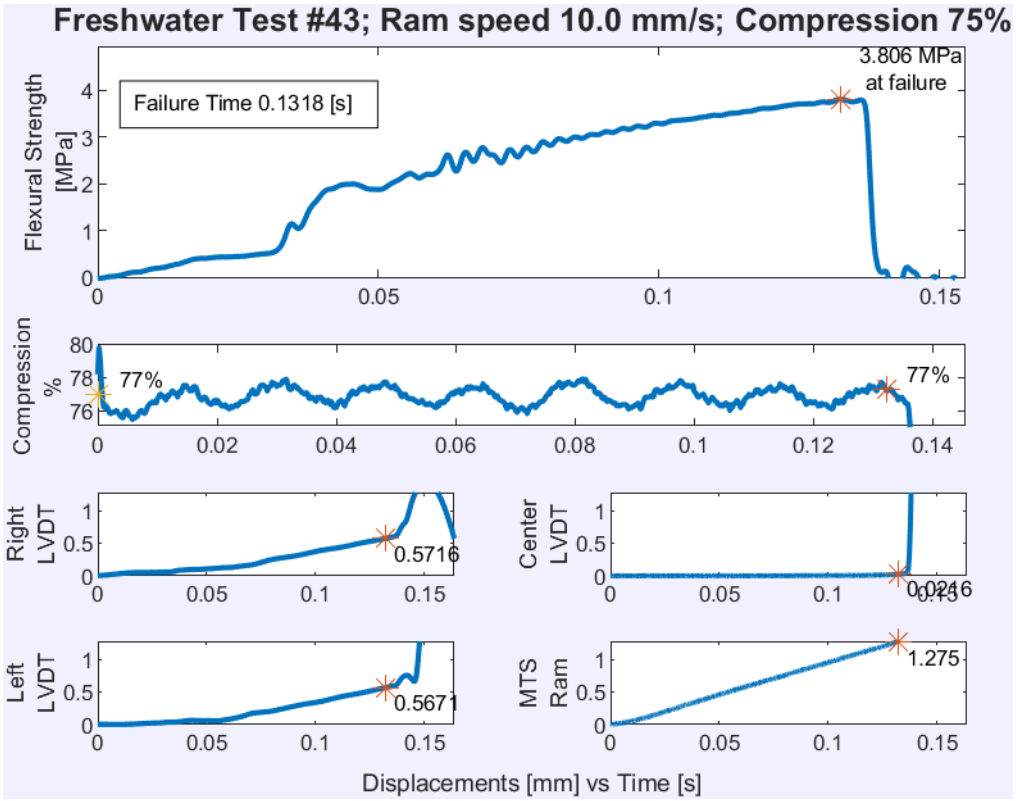
Freshwater Test #43; Ram speed 10.0 mm/s; Compression 75%
Failure Time 0.1318 [s]
3.806 MPa
at failure
Flexural Strength [MPa]
Compression %
77%
77%
Right LVDT
0.5716
Center LVDT
0.0216
Left LVDT
0.5671
MTS Ram
1.275
Displacements [mm] vs Time [s]

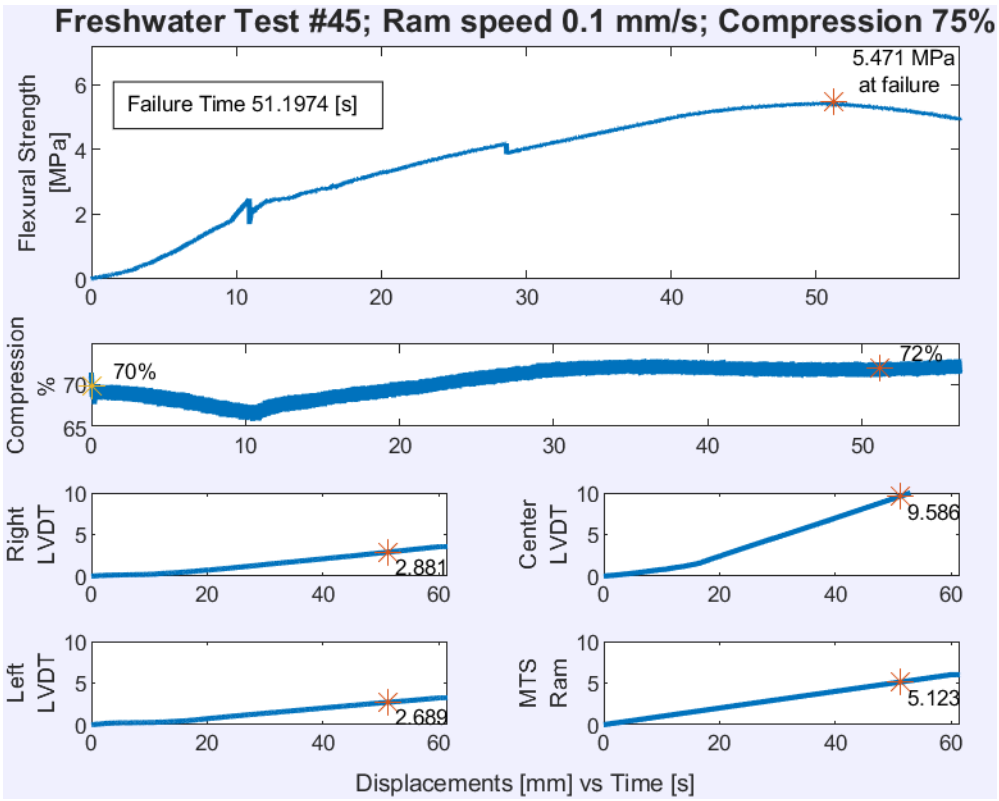
Freshwater Test #45; Ram speed 0.1 mm/s; Compression 75%
Failure Time 51.1974 [s]
5.471 MPa
at failure
Flexural Strength [MPa]
Compression %
70%
72%
Right LVDT
2.881
Center LVDT
9.586
Left LVDT
2.689
MTS Ram
5.123
Displacements [mm] vs Time [s]

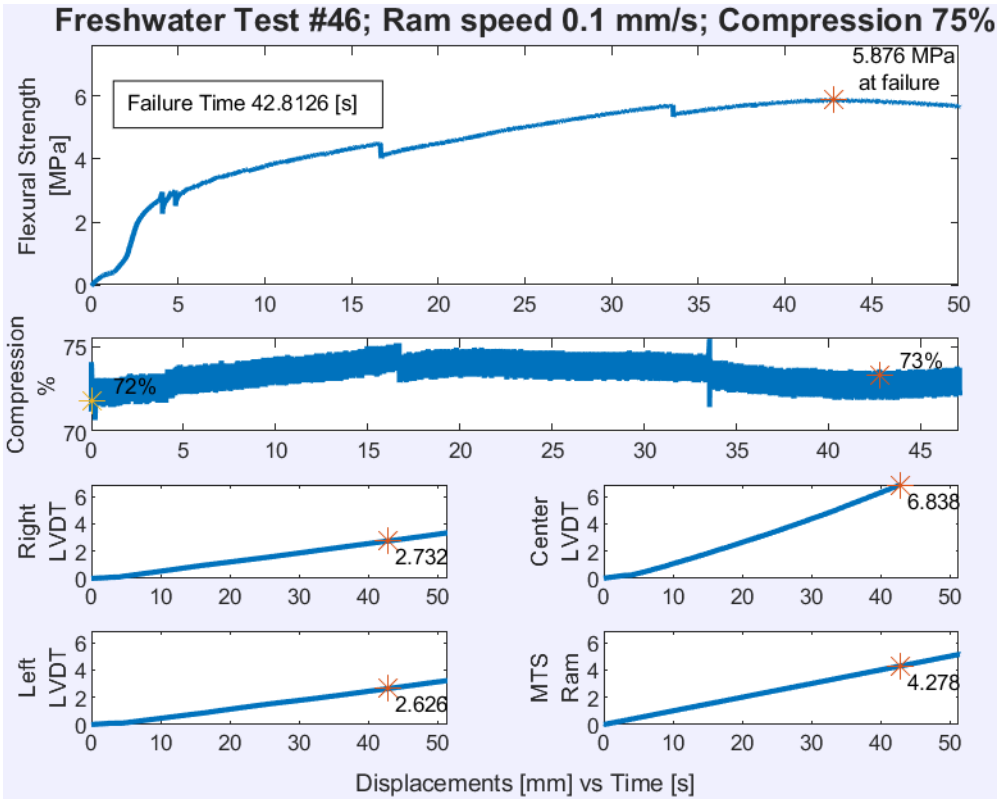
Freshwater Test #46; Ram speed 0.1 mm/s; Compression 75%
Failure Time 42.8126 [s]
5.876 MPa
at failure
Flexural Strength [MPa]
Compression %
72%
73%
Right LVDT
2.732
Center LVDT
6.838
Left LVDT
2.626
MTS Ram
4.278
Displacements [mm] vs Time [s]

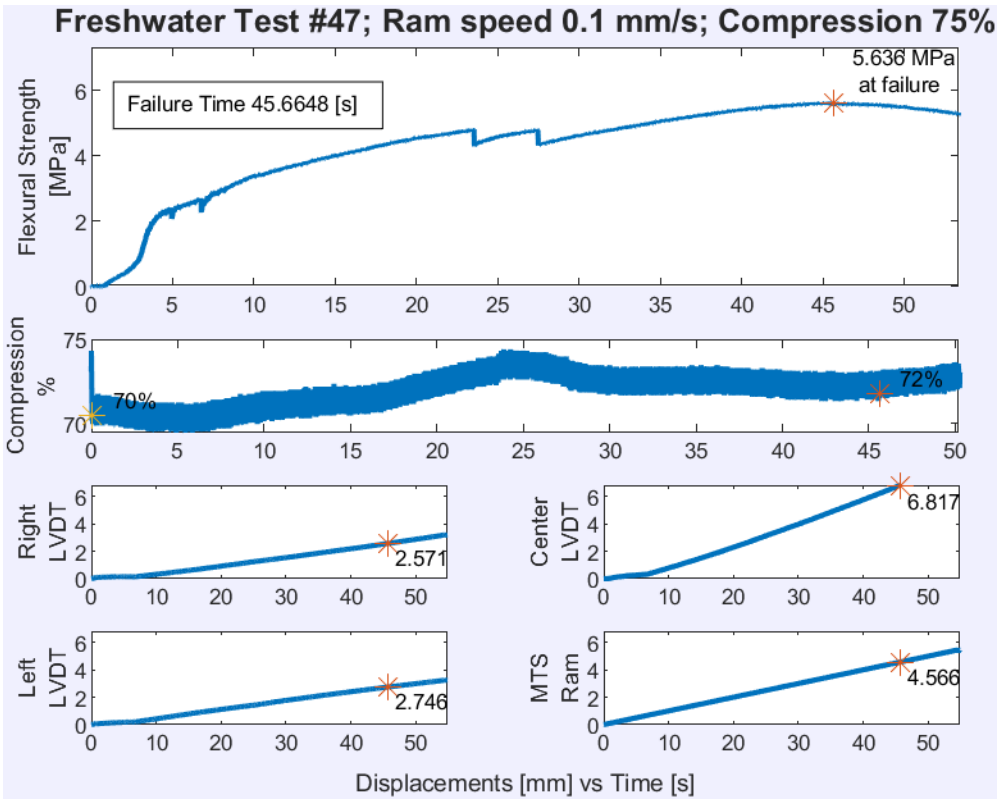
Freshwater Test #47; Ram speed 0.1 mm/s; Compression 75%
Failure Time 45.6648 [s]
5.636 MPa
at failure
Flexural Strength [MPa]
Compression %
70%
72%
Right LVDT
2.571
Center LVDT
6.817
Left LVDT
2.746
MTS Ram
4.566
Displacements [mm] vs Time [s]

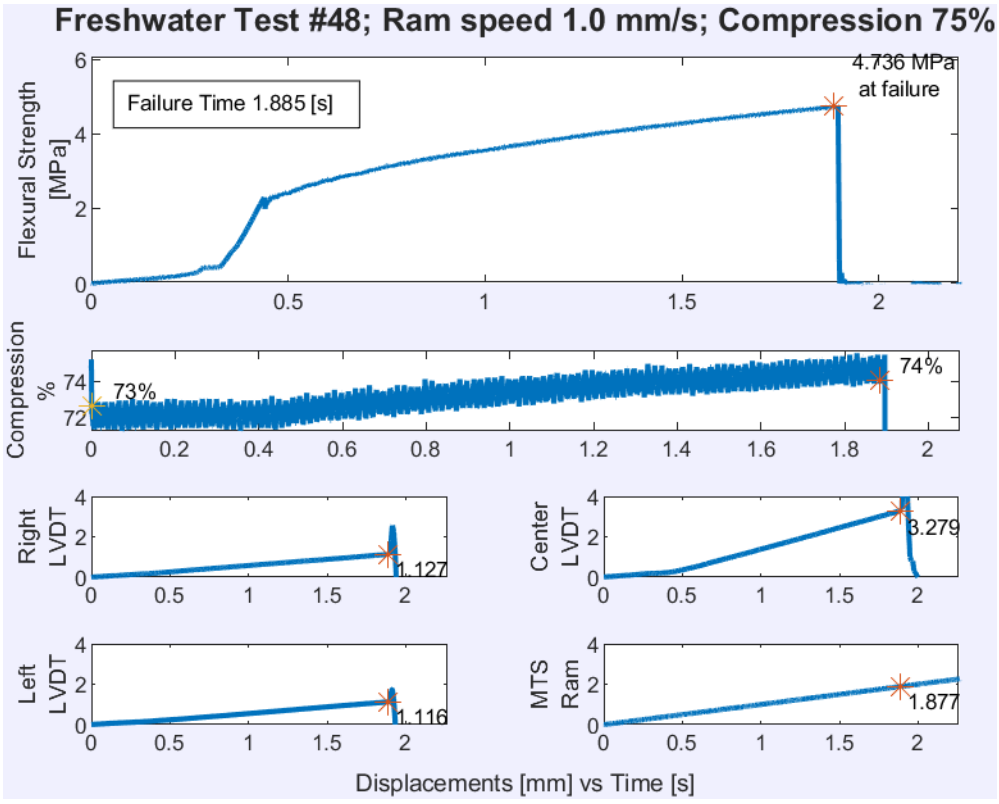
Freshwater Test #48; Ram speed 1.0 mm/s; Compression 75%
Failure Time 1.885 [s]
4.736 MPa
at failure
Flexural Strength [MPa]
Compression %
73%
74%
Right LVDT
1.127
Center LVDT
3.279
Left LVDT
1.116
MTS Ram
1.877
Displacements [mm] vs Time [s]

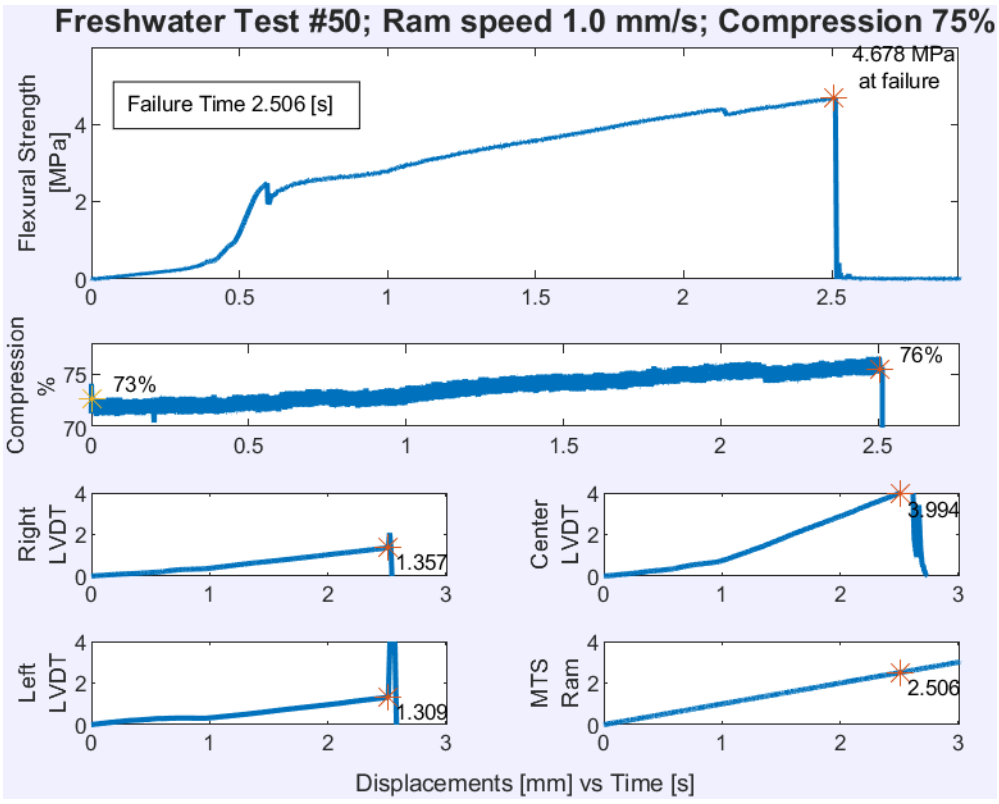
Freshwater Test #50; Ram speed 1.0 mm/s; Compression 75%
Failure Time 2.506 [s]
4.678 MPa
at failure
Flexural Strength [MPa]
Compression %
73%
76%
Right LVDT
1.357
Center LVDT
3.994
Left LVDT
1.309
MTS Ram
2.506
Displacements [mm] vs Time [s]

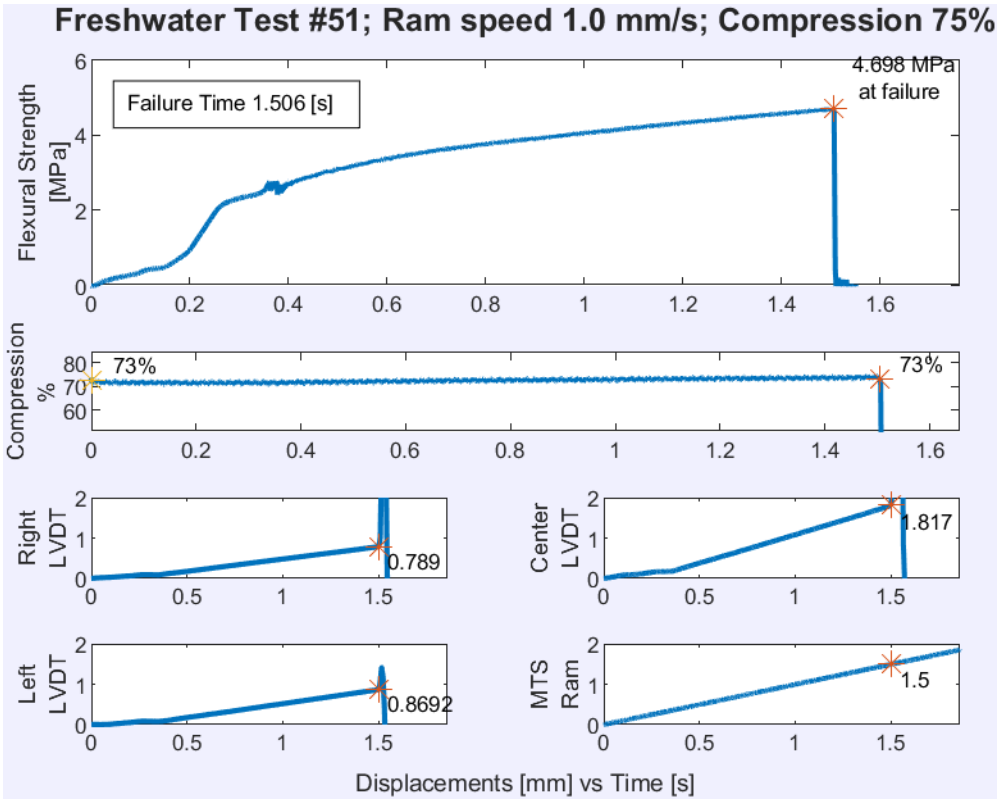
Freshwater Test #51; Ram speed 1.0 mm/s; Compression 75%
Failure Time 1.506 [s]
4.698 MPa
at failure
Flexural Strength [MPa]
Compression %
73%
73%
Right LVDT
0.789
Center LVDT
1.817
Left LVDT
0.8692
MTS Ram
1.5
Displacements [mm] vs Time [s]

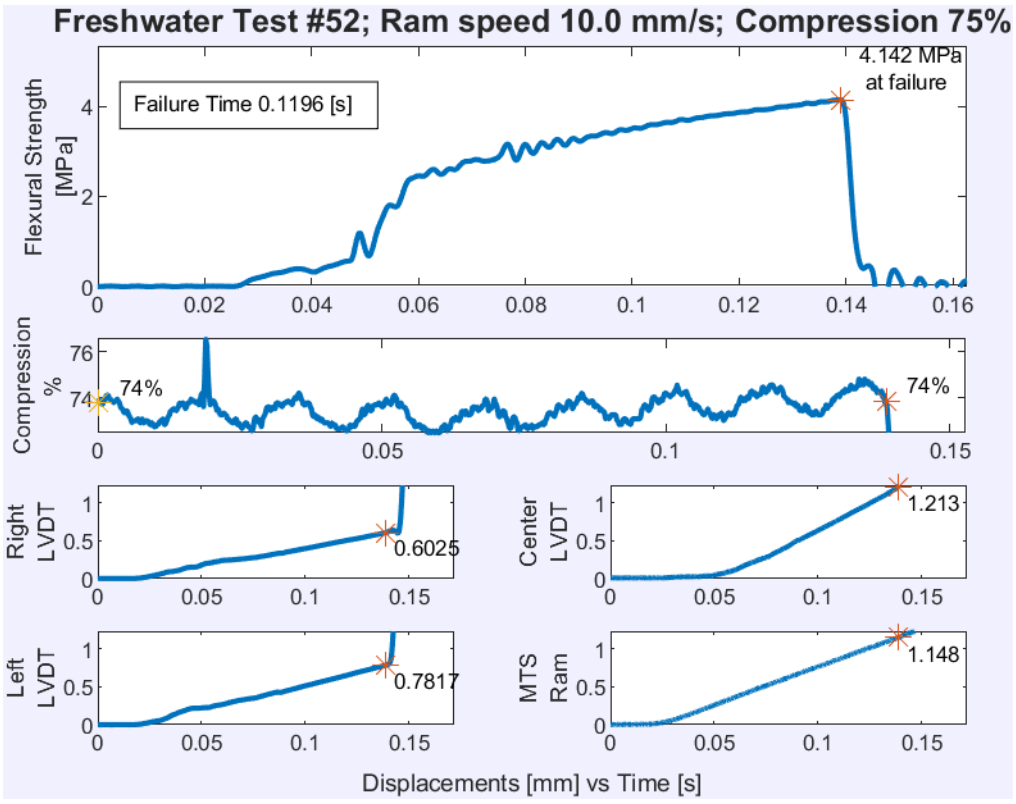
Freshwater Test #52; Ram speed 10.0 mm/s; Compression 75%
Failure Time 0.1196 [s]
4.142 MPa
at failure
Flexural Strength [MPa]
Compression %
74%
74%
Right LVDT
0.6025
Center LVDT
1.213
Left LVDT
0.7817
MTS Ram
1.148
Displacements [mm] vs Time [s]

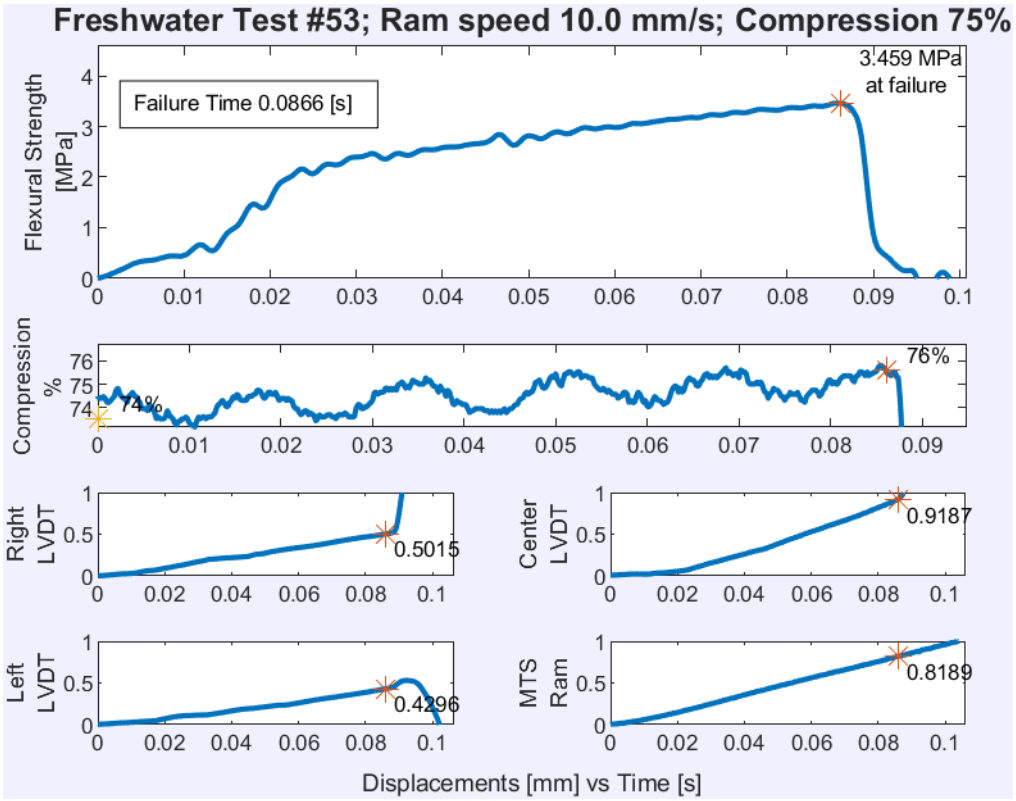
Freshwater Test #53; Ram speed 10.0 mm/s; Compression 75%
Failure Time 0.0866 [s]
3.459 MPa
at failure
Flexural Strength [MPa]
Compression %
74%
76%
Right LVDT
0.5015
Center LVDT
0.9187
Left LVDT
0.4296
MTS Ram
0.8189
Displacements [mm] vs Time [s]

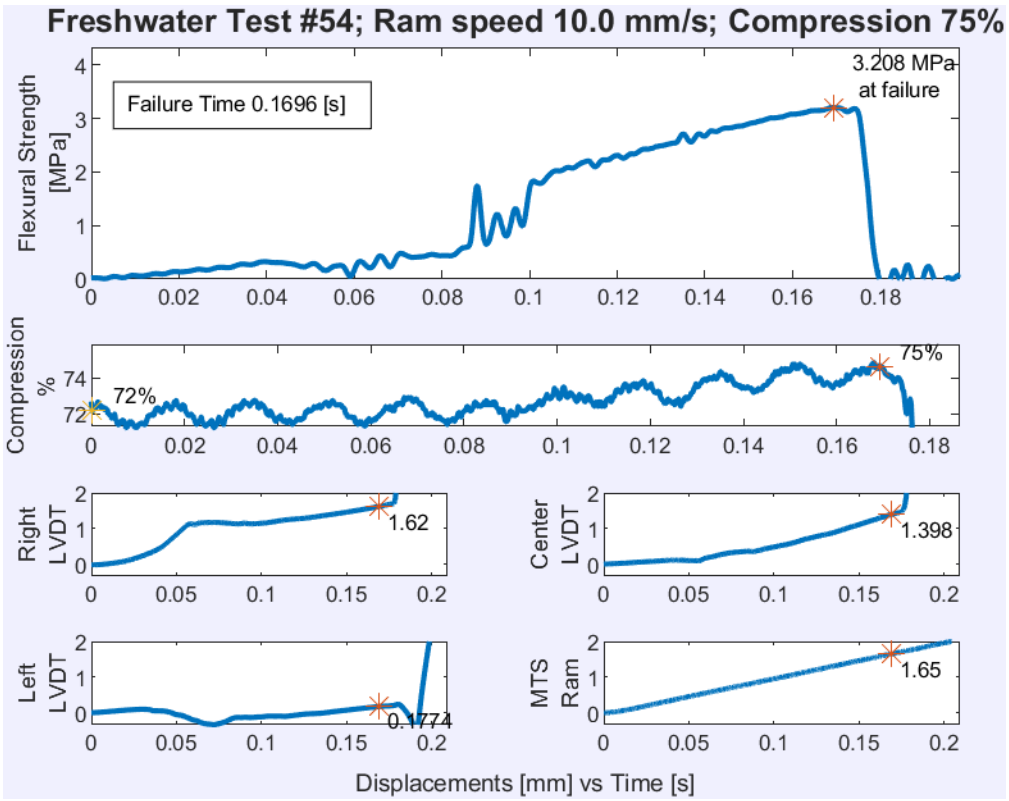
Freshwater Test #54; Ram speed 10.0 mm/s; Compression 75%
Failure Time 0.1696 [s]
3.208 MPa
at failure
Flexural Strength [MPa]
Compression %
72%
75%
Right LVDT
1.62
Center LVDT
1.398
Left LVDT
0.1774
MTS Ram
1.65
Displacements [mm] vs Time [s]

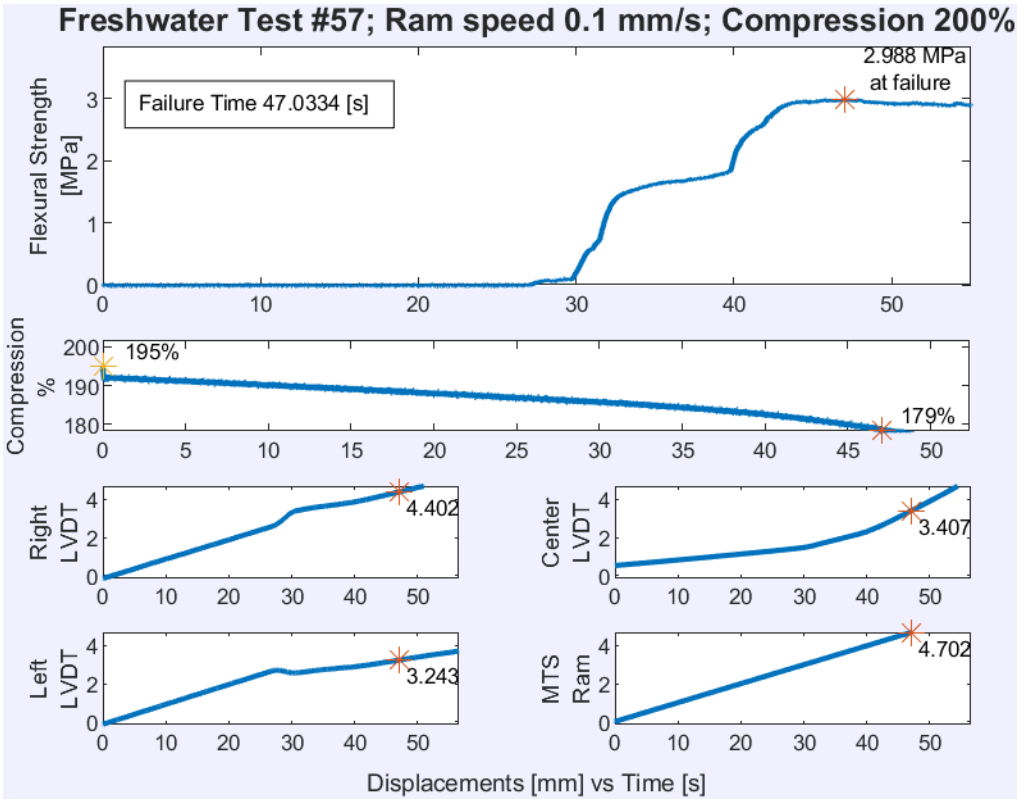
Freshwater Test #57; Ram speed 0.1 mm/s; Compression 200%
Failure Time 47.0334 [s]
2.988 MPa
at failure
Flexural Strength [MPa]
Compression %
195%
179%
Right LVDT
4.402
Center LVDT
3.407
Left LVDT
3.243
MTS Ram
4.702
Displacements [mm] vs Time [s]

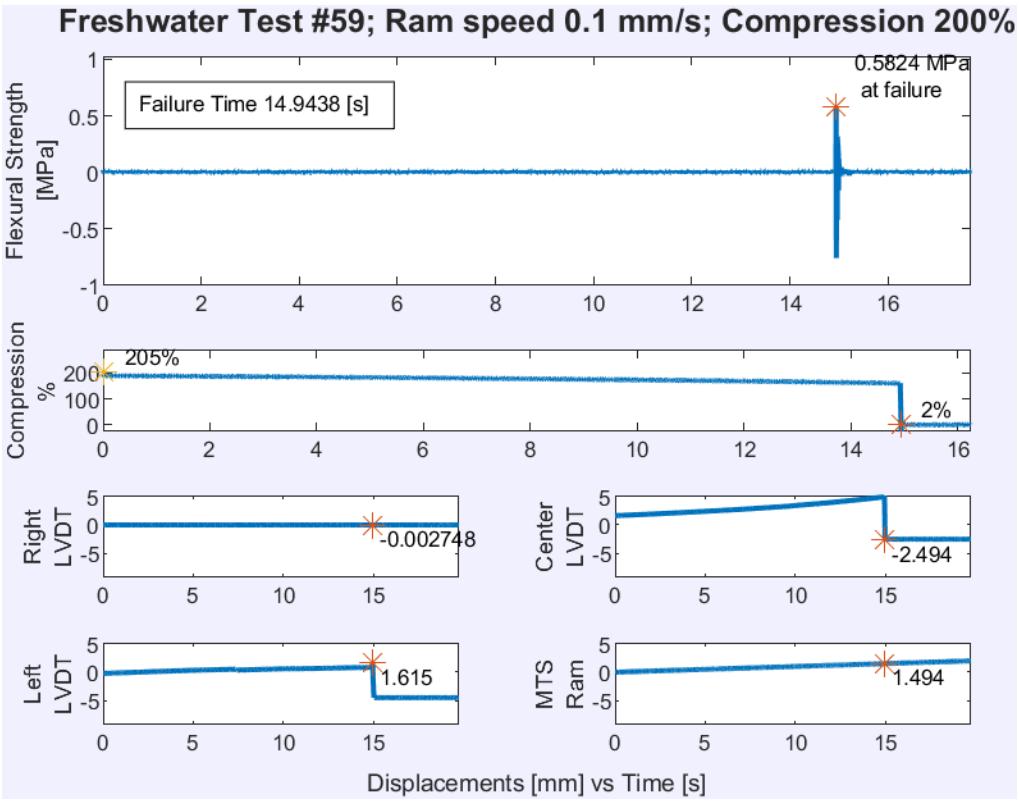
Freshwater Test #59; Ram speed 0.1 mm/s; Compression 200%
Failure Time 14.9438 [s]
0.5824 MPa
at failure
Flexural Strength [MPa]
Compression %
205%
2%
Right LVDT
-0.002748
Center LVDT
-2.494
Left LVDT
1.615
MTS Ram
1.494
Displacements [mm] vs Time [s]

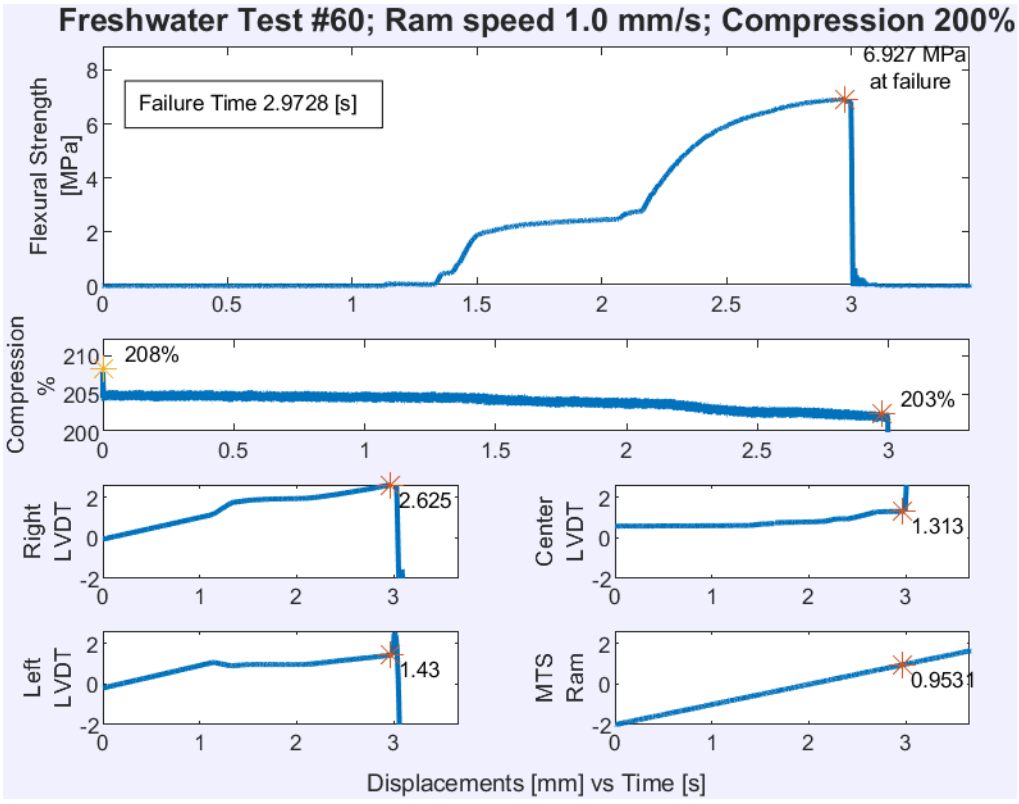
Freshwater Test #60; Ram speed 1.0 mm/s; Compression 200%
Failure Time 2.9728 [s]
6.927 MPa
at failure
Flexural Strength [MPa]
Compression %
208%
203%
Right LVDT
2.625
Center LVDT
1.313
Left LVDT
1.43
MTS Ram
0.9531
Displacements [mm] vs Time [s]

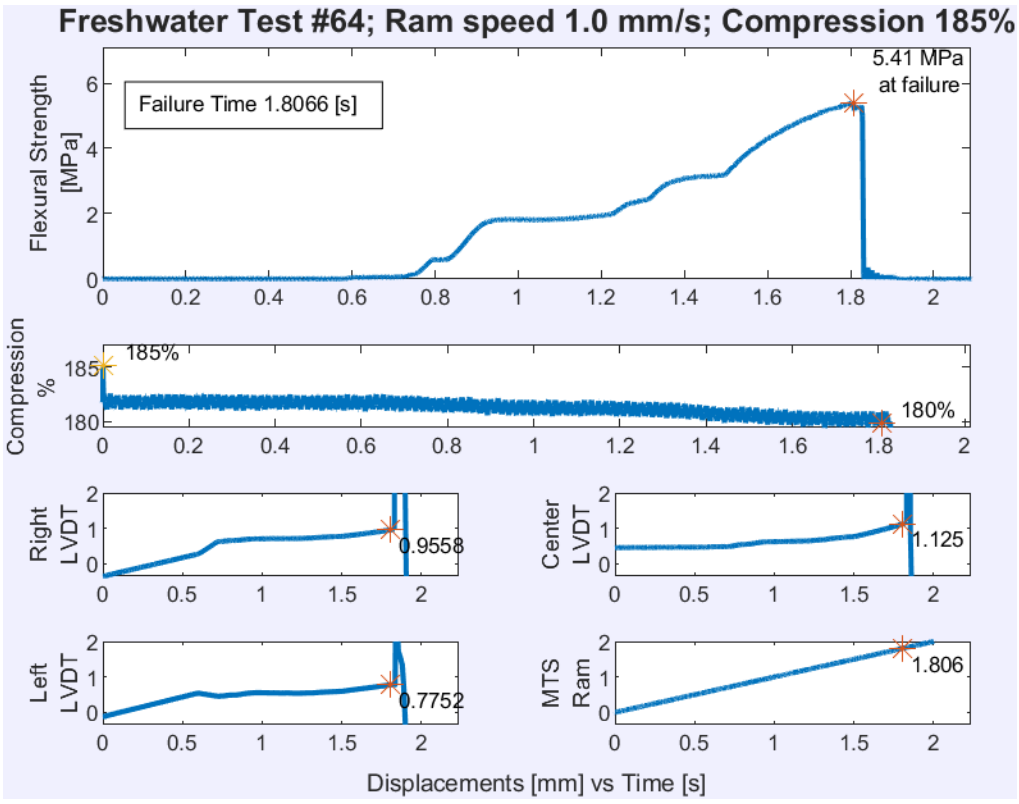
Freshwater Test #64; Ram speed 1.0 mm/s; Compression 185%
Failure Time 1.8066 [s]
5.41 MPa
at failure
Flexural Strength [MPa]
Compression %
185%
180%
Right LVDT
0.9558
Center LVDT
1.125
Left LVDT
0.7752
MTS Ram
1.806
Displacements [mm] vs Time [s]

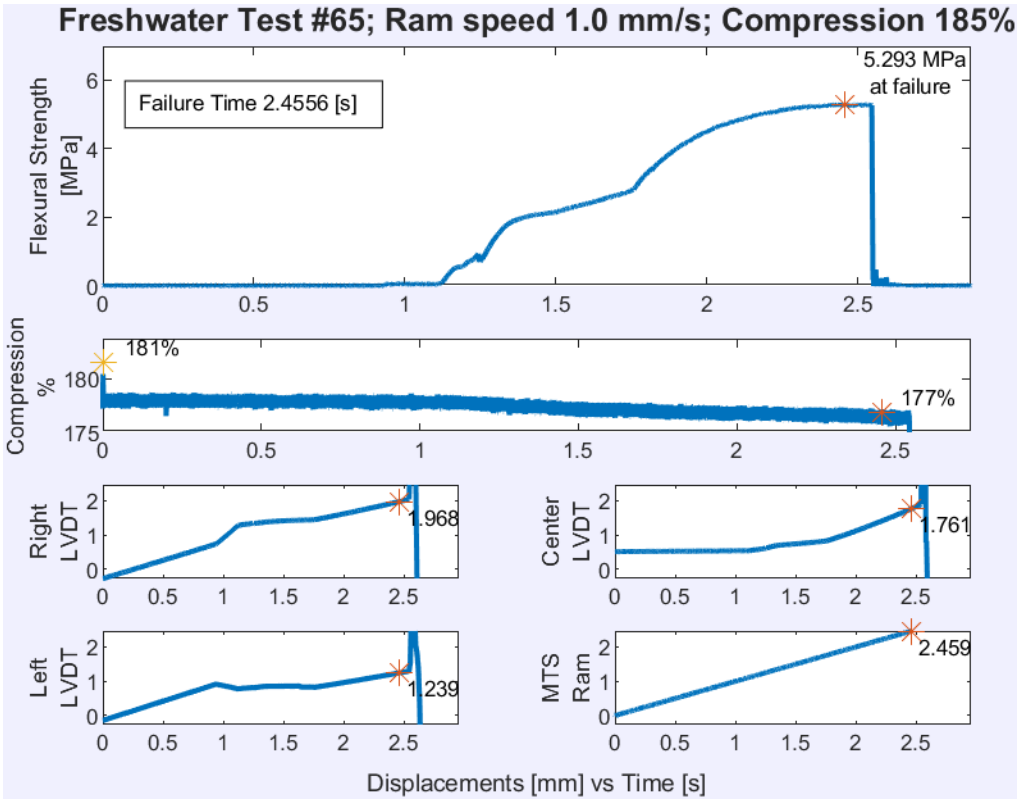
Freshwater Test #65; Ram speed 1.0 mm/s; Compression 185%
Failure Time 2.4556 [s]
5.293 MPa
at failure
Flexural Strength [MPa]
Compression %
181%
177%
Right LVDT
1.968
Center LVDT
1.761
Left LVDT
1.239
MTS Ram
2.459
Displacements [mm] vs Time [s]

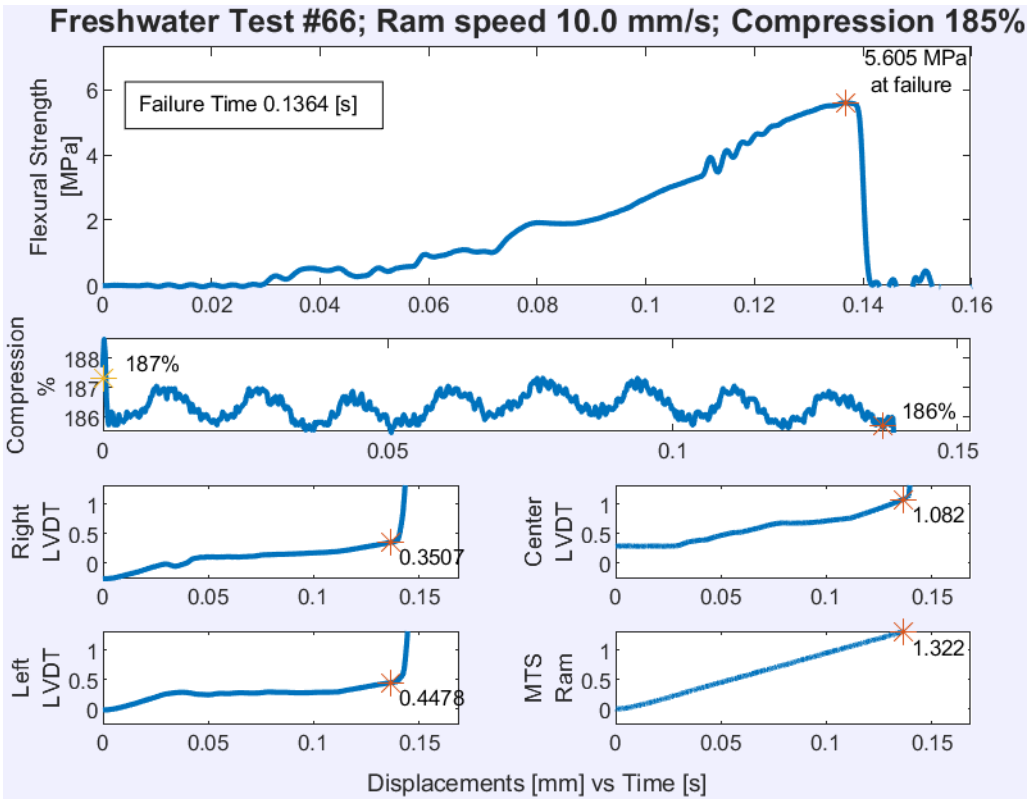
Freshwater Test #66; Ram speed 10.0 mm/s; Compression 185%
Failure Time 0.1364 [s]
5.605 MPa
at failure
Flexural Strength [MPa]
Compression %
187%
186%
Right LVDT
0.3507
Center LVDT
1.082
Left LVDT
0.4478
MTS Ram
1.322
Displacements [mm] vs Time [s]

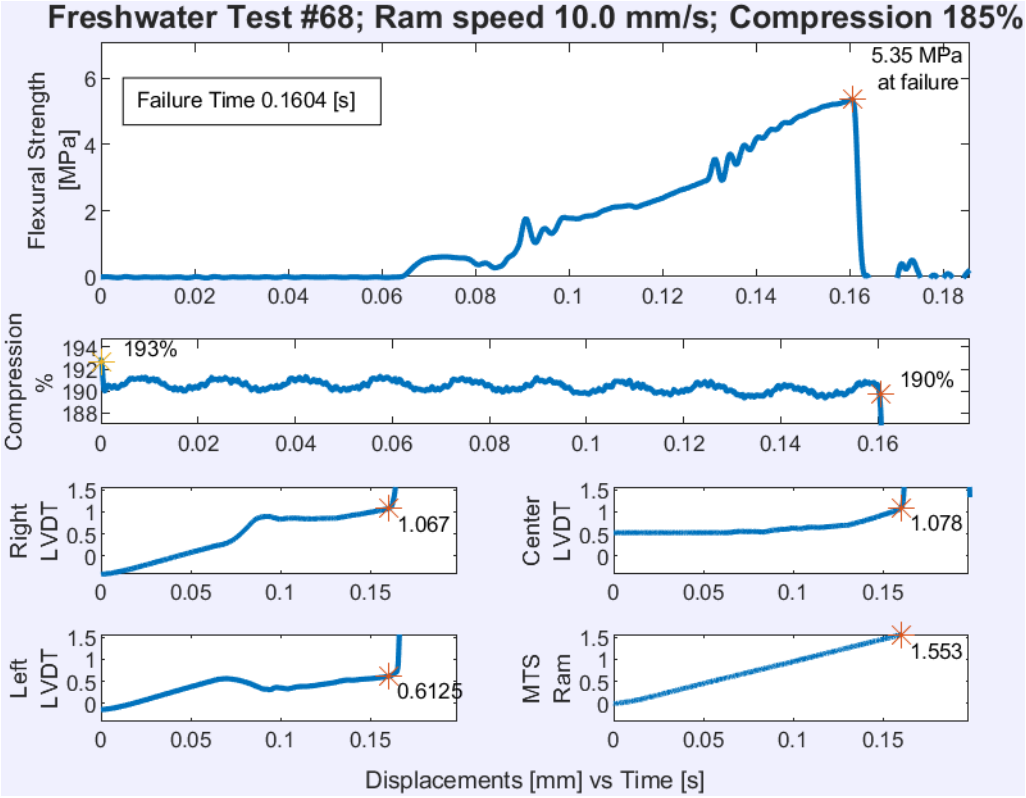
Freshwater Test #68; Ram speed 10.0 mm/s; Compression 185%
Failure Time 0.1604 [s]
5.35 MPa
at failure
Flexural Strength [MPa]
Compression %
193%
190%
Right LVDT
1.067
Center LVDT
1.078
Left LVDT
0.6125
MTS Ram
1.553
Displacements [mm] vs Time [s]

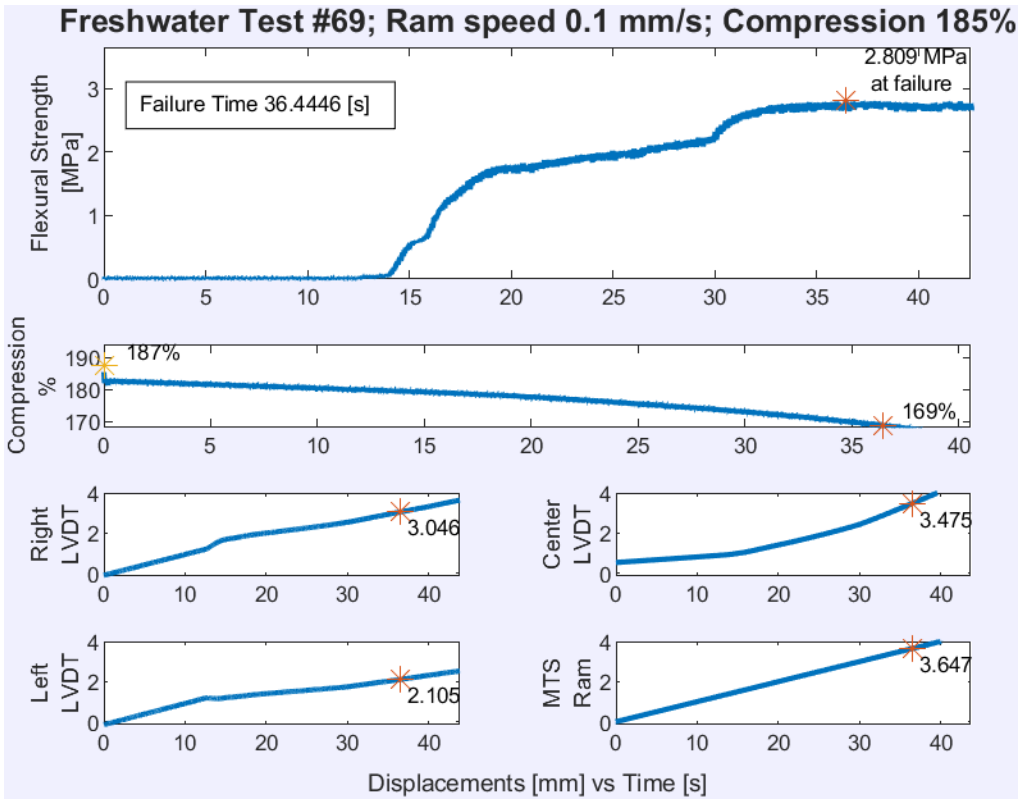
Freshwater Test #69; Ram speed 0.1 mm/s; Compression 185%
Failure Time 36.4446 [s]
2.809 MPa
at failure
Flexural Strength [MPa]
Compression %
187%
169%
Right LVDT
3.046
Center LVDT
3.475
Left LVDT
2.105
MTS Ram
3.647
Displacements [mm] vs Time [s]

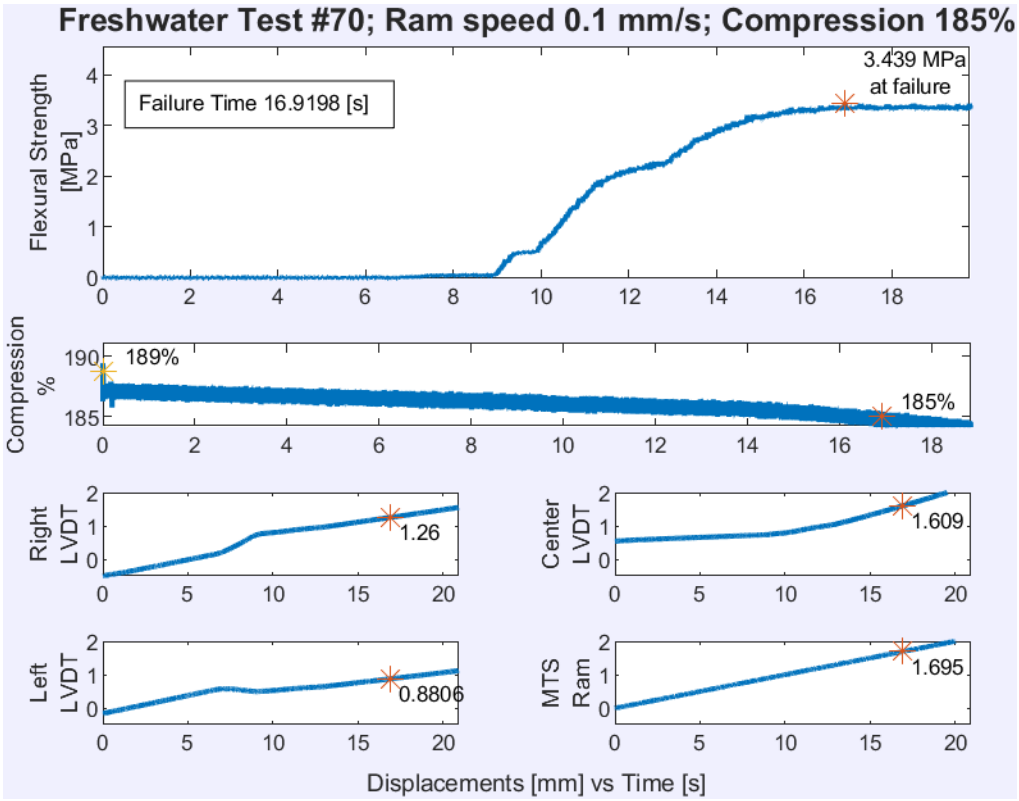
Freshwater Test #70; Ram speed 0.1 mm/s; Compression 185%
Flexural Strength [MPa]
Failure Time 16.9198 [s]
3.439 MPa at failure
Compression %
189%
185%
Right LVDT
1.26
Center LVDT
1.609
Left LVDT
0.8806
MTS Ram
1.695
Displacements [mm] vs Time [s]

Appendix C - Saline Ice Tests Raw Data Table

Table C 1 - Raw Data for 0% Compression Tests on Saline Ice

Index #	Test #	Ram Speed [mm/s]	Failure Time [s]	Target Compression [%]	Flexural Strength [MPa]	MTS Displacement [mm]	Right LVDT [mm]	Left LVDT [mm]	Center LVDT [mm]	Axial Load [N]	Cross-sectional Area [mm2]	Compressive Stress [MPa]	Measured Compression [%]
1	1	0.1	1.988	0	1.767	0.195	0.120	0.132	0.077	-	1308	-	-
2	2	0.1	2.596	0	1.327	0.262	0.063	0.361	0.000	-	1326	-	-
3	3	0.1	5.578	0	2.624	0.558	0.040	0.658	0.166	-	1312	-	-
4	10	0.1	0.393	0	1.592	0.385	0.704	0.086	0.115	-	1274	-	-
5	13	0.1	4.809	0	1.478	0.487	0.032	0.584	0.094	-	1261	-	-
6	4	1	0.132	0	1.202	0.126	0.030	0.058	0.077	-	1266	-	-
7	5	1	0.312	0	0.964	0.306	0.004	0.536	0.034	-	1293	-	-
8	6	1	0.461	0	0.898	0.452	0.312	1.115	0.084	-	1302	-	-
9	11	1	0.448	0	2.494	0.442	0.046	0.064	0.054	-	1392	-	-
10	12	1	0.253	0	1.817	0.247	0.094	0.113	0.132	-	1276	-	-
11	7	10	0.022	0	1.494	0.174	0.132	0.319	0.067	-	1424	-	-
12	8	10	0.018	0	1.400	0.130	0.033	0.050	0.096	-	1258	-	-
13	9	10	0.086	0	1.611	0.805	1.574	1.248	0.390	-	1298	-	-

Note: Ram speeds 0.1, 1 and 10 mm/s correspond to strain rates 4.67×10^{-4}, 4.67×10^{-3} and 4.67×10^{-2} respectively.

Table C 2 - Raw Data for 35% Compression Tests on Saline Ice

Index #	Test #	Ram Speed [mm/s]	Failure Time [s]	Target Compression [%]	Flexural Strength [MPa]	MTS Displacement [mm]	Right LVDT [mm]	Left LVDT [mm]	Center LVDT [mm]	Axial Load [N]	Cross-sectional Area [mm2]	Compressive Stress [MPa]	Measured Compression [%]
14	36	0.1	40.000	35	3.000	2.000	4.895	5.759	5.000	708	1255	0.595	41
15	37	0.1	37.861	35	3.178	3.789	1.809	1.969	6.177	713	1309	0.529	36
16	38	0.1	30.724	35	2.810	3.070	1.812	1.706	3.157	681	1168	0.603	41
17	39	1	4.307	35	3.429	4.310	2.846	2.172	7.871	686	1295	0.531	36
18	40	1	4.208	35	2.959	4.211	2.868	2.342	7.184	689	1193	0.555	38
19	41	1	4.278	35	3.070	4.280	2.552	2.115	7.584	694	1306	0.510	35
20	42	10	0.187	35	2.220	1.825	1.101	0.663	2.494	702	1305	0.526	36
21	43	10	0.123	35	2.265	1.192	0.683	0.576	1.469	713	1235	0.555	38
22	44	10	0.232	35	2.592	2.279	1.458	0.955	3.509	684	1254	0.571	39

Note: Ram speeds 0.1, 1 and 10 mm/s correspond to strain rates 4.67×10^{-4}, 4.67×10^{-3} and 4.67×10^{-2} respectively.

Table C 3 - Raw Data for 70% Compression Tests on Saline Ice

Index #	Test #	Ram Speed [mm/s]	Failure Time [s]	Target Compression [%]	Flexural Strength [MPa]	MTS Displacement [mm]	Right LVDT [mm]	Left LVDT [mm]	Center LVDT [mm]	Axial Load [N]	Cross-sectional Area [mm2]	Compressive Stress [MPa]	Measured Compression [%]
23	26	0.1	26.422	70	3.838	2.642	2.433	0.756	2.171	1188	1194	1.015	69
24	27	0.1	32.943	70	4.639	3.293	2.038	1.900	4.166	1300	1307	0.991	68
25	28	0.1	34.796	70	4.904	3.475	2.230	2.043	4.577	1314	1204	1.071	73
26	29	1	3.895	70	4.234	3.893	2.831	2.213	5.455	1327	1201	1.089	75
27	30	1	3.073	70	4.775	3.076	1.656	1.500	3.996	1330	1253	1.049	72
28	31	1	4.864	70	5.165	4.864	2.888	3.181	8.769	1311	1375	0.975	67
29	35	1	2.038	70	3.722	2.036	1.136	1.339	1.628	1322	1322	1.023	77
30	32	10	0.210	70	3.787	2.056	0.516	1.710	1.906	1391	1222	1.121	78
31	33	10	0.113	70	2.916	1.083	0.592	0.339	0.930	1324	1182	1.140	75
32	34	10	0.133	70	2.914	1.285	0.743	0.626	1.134	1306	1202	1.097	70

Note: Ram speeds 0.1, 1 and 10 mm/s correspond to strain rates 4.67×10^{-4}, 4.67×10^{-3} and 4.67×10^{-2} respectively.

Table C 4 - Raw Data for 135% Compression Tests on Saline Ice

Index #	Test #	Ram Speed [mm/s]	Failure Time [s]	Target Compression [%]	Flexural Strength [MPa]	MTS Displacement [mm]	Right LVDT [mm]	Left LVDT [mm]	Center LVDT [mm]	Axial Load [N]	Cross-sectional Area [mm2]	Compressive Stress [MPa]	Measured Compression [%]
33	14	0.1	39.816	125	5.980	3.982	2.056	2.401	4.565	2459	1319	1.872	128
34	15	0.1	31.527	125	5.095	3.159	2.156	2.029	4.516	2451	1328	1.848	127
35	16	0.1	32.420	125	5.097	3.244	2.099	1.619	4.226	2414	1303	1.874	128
36	17	0.1	49.477	125	7.008	4.945	3.323	2.624	6.010	2566	1340	1.912	131
37	18	1	3.582	125	7.304	3.584	1.915	1.955	0.000	2491	1325	1.874	128
38	19	1	1.708	125	4.949	1.707	0.665	0.790	1.704	1898	1317	1.442	99
39	20	1	3.638	125	6.007	3.637	2.625	1.838	4.824	2323	1372	1.701	117
40	21	1	3.006	125	6.257	3.003	1.647	1.749	4.056	2494	1295	1.938	133
41	22	10	0.091	125	3.545	0.858	0.303	0.498	0.382	2272	1252	1.826	125
42	23	10	0.179	125	4.075	1.752	0.313	1.355	0.926	1546	1299	1.199	82
43	24	10	0.123	125	4.553	1.150	0.484	0.500	0.860	2435	1326	1.834	126
44	25	10	0.119	125	4.924	1.145	0.352	0.712	0.782	2245	1326	1.698	116

Note: Ram speeds 0.1, 1 and 10 mm/s correspond to strain rates 4.67×10^{-4}, 4.67×10^{-3} and 4.67×10^{-2} respectively.

Appendix D - Saline Ice Individual Test Plot

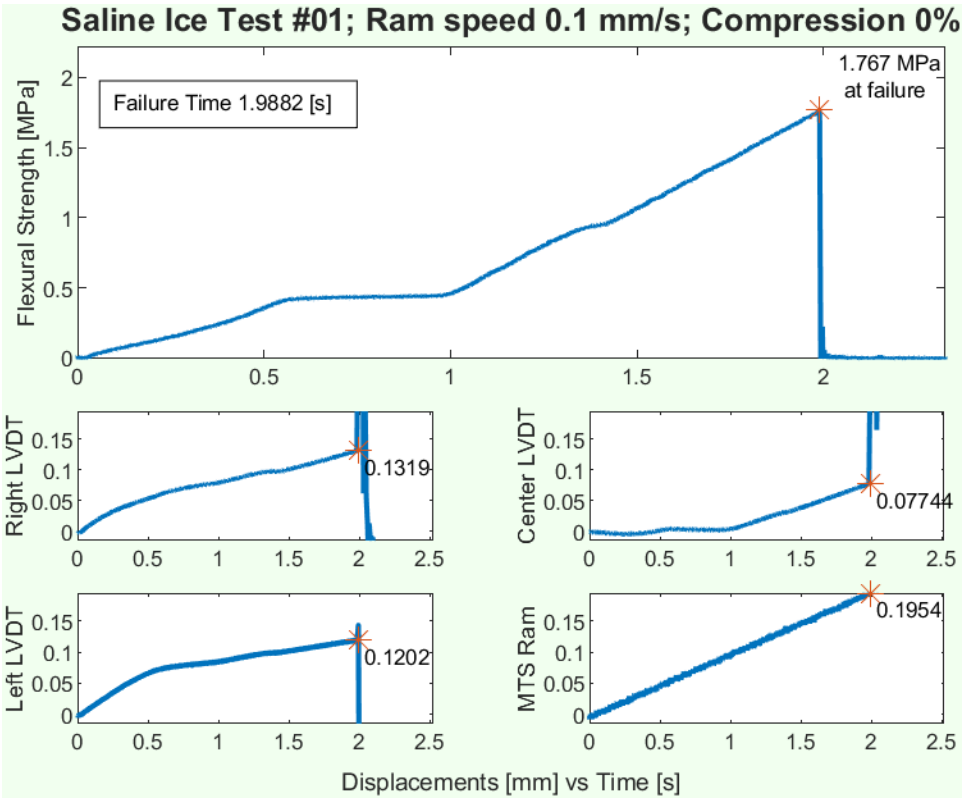
Saline Ice Test #01; Ram speed 0.1 mm/s; Compression 0%
Failure Time 1.9882 [s]
1.767 MPa
at failure
Flexural Strength [MPa]
Right LVDT
0.1319
Center LVDT
0.07744
Left LVDT
0.1202
MTS Ram
0.1954
Displacements [mm] vs Time [s]

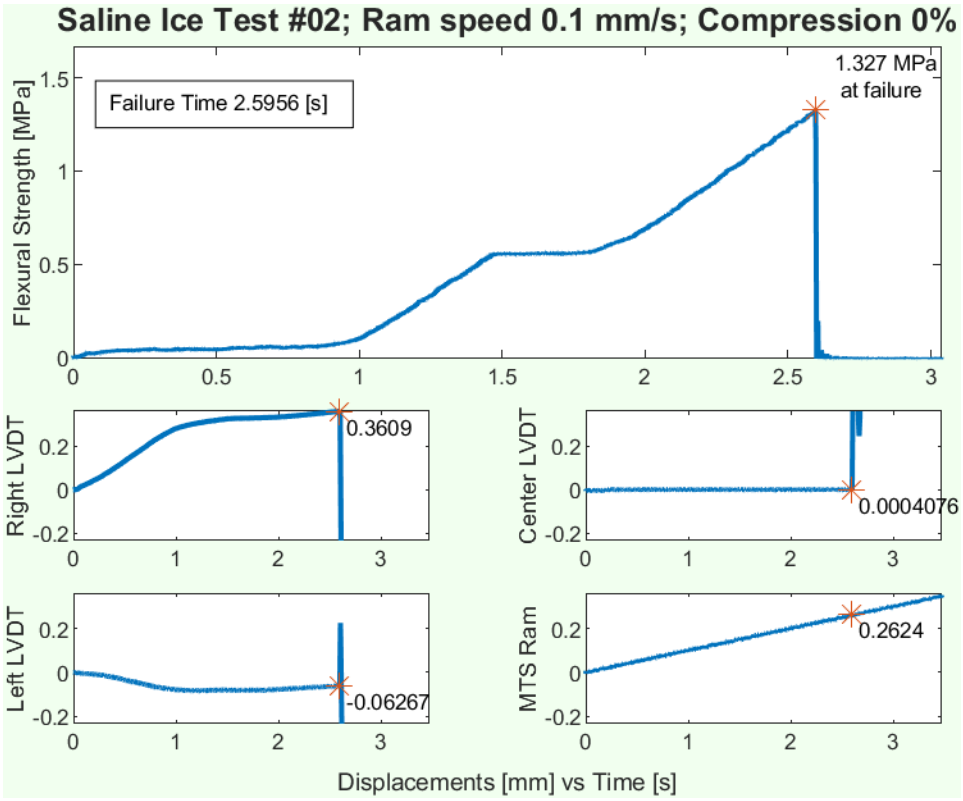
Saline Ice Test #02; Ram speed 0.1 mm/s; Compression 0%
Failure Time 2.5956 [s]
1.327 MPa
at failure
Flexural Strength [MPa]
Right LVDT
0.3609
Center LVDT
0.0004076
Left LVDT
-0.06267
MTS Ram
0.2624
Displacements [mm] vs Time [s]

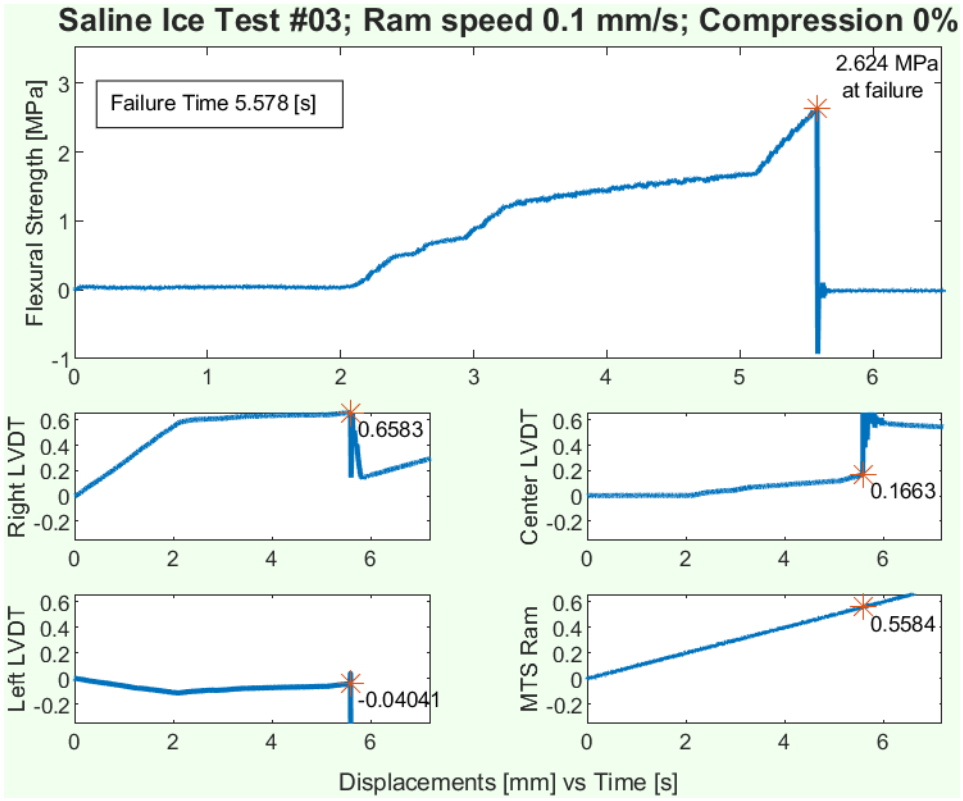
Saline Ice Test #03; Ram speed 0.1 mm/s; Compression 0%
Failure Time 5.578 [s]
2.624 MPa
at failure
Flexural Strength [MPa]
Right LVDT
0.6583
Center LVDT
0.1663
Left LVDT
-0.04041
MTS Ram
0.5584
Displacements [mm] vs Time [s]

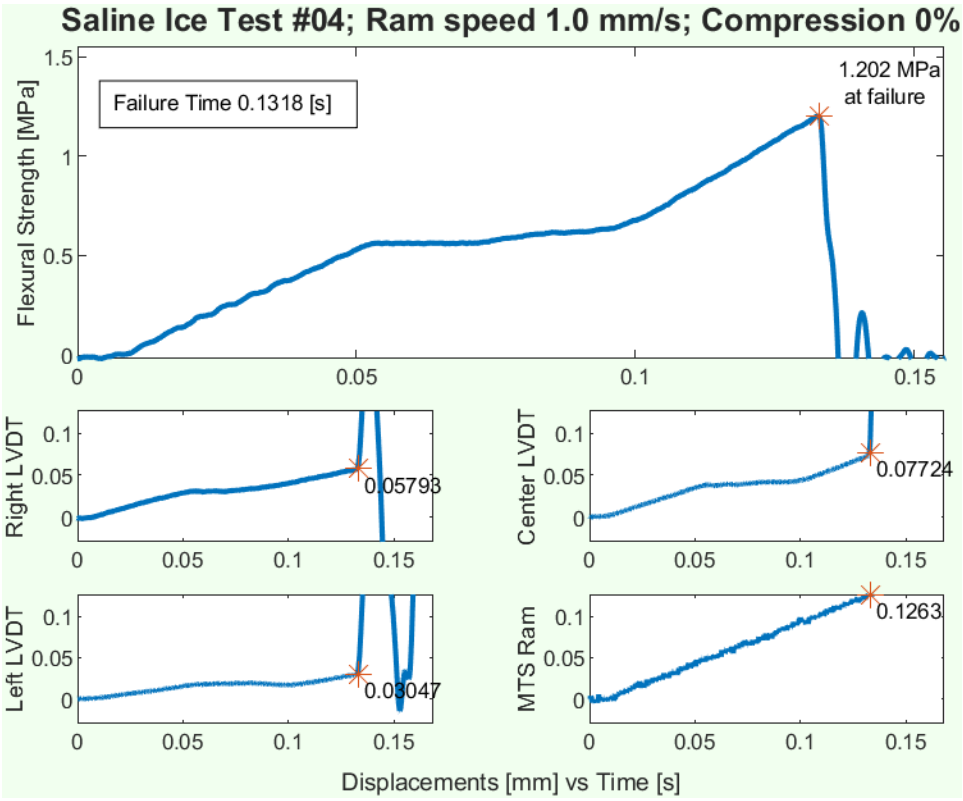
Saline Ice Test #04; Ram speed 1.0 mm/s; Compression 0%
Failure Time 0.1318 [s]
1.202 MPa
at failure
Flexural Strength [MPa]
Right LVDT
0.05793
Center LVDT
0.07724
Left LVDT
0.03047
MTS Ram
0.1263
Displacements [mm] vs Time [s]

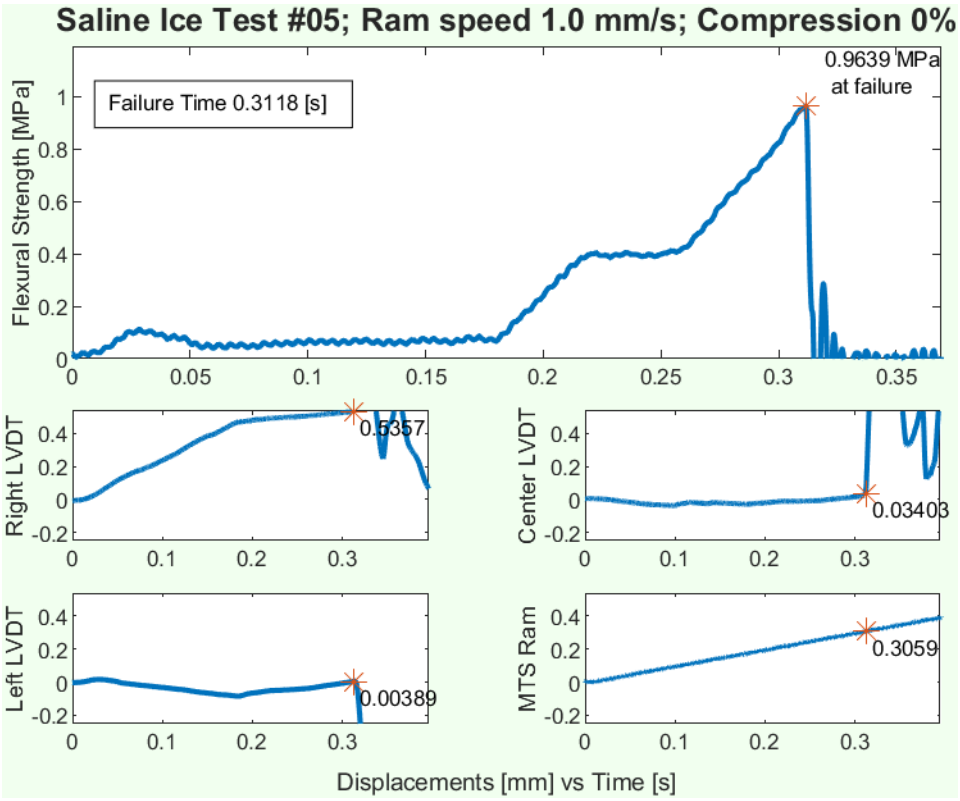
Saline Ice Test #05; Ram speed 1.0 mm/s; Compression 0%
Failure Time 0.3118 [s]
0.9639 MPa
at failure
Flexural Strength [MPa]
Right LVDT
0.5357
Center LVDT
0.03403
Left LVDT
0.00389
MTS Ram
0.3059
Displacements [mm] vs Time [s]

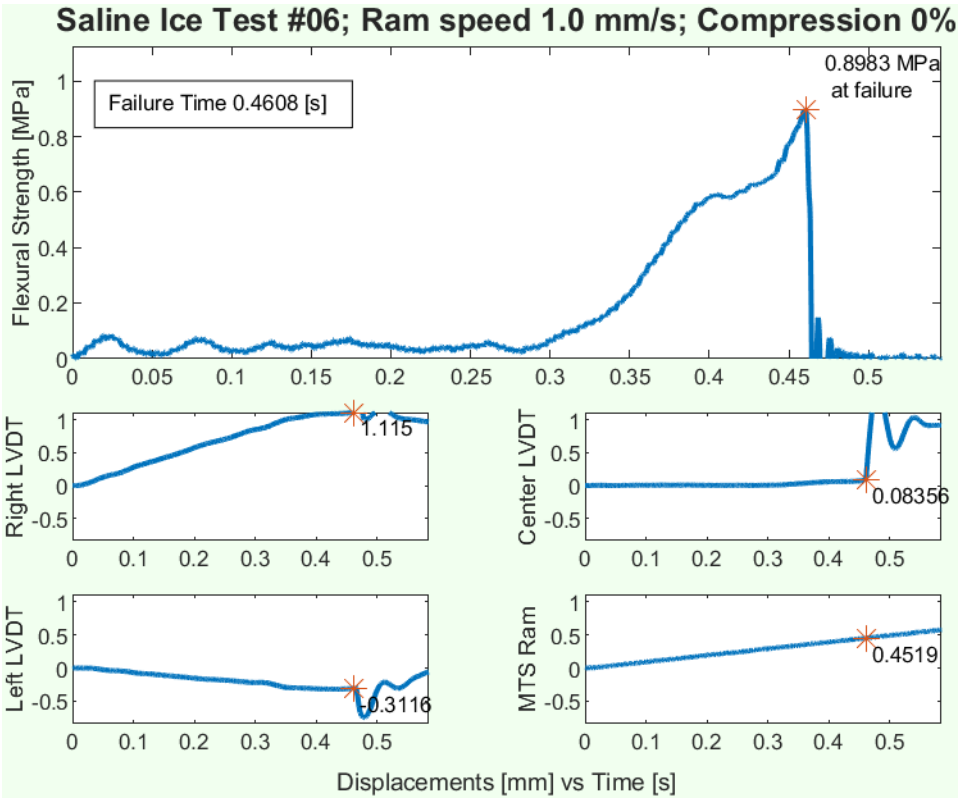
Saline Ice Test #06; Ram speed 1.0 mm/s; Compression 0%
Failure Time 0.4608 [s]
0.8983 MPa
at failure
Flexural Strength [MPa]
Right LVDT
1.115
Center LVDT
0.08356
Left LVDT
-0.3116
MTS Ram
0.4519
Displacements [mm] vs Time [s]

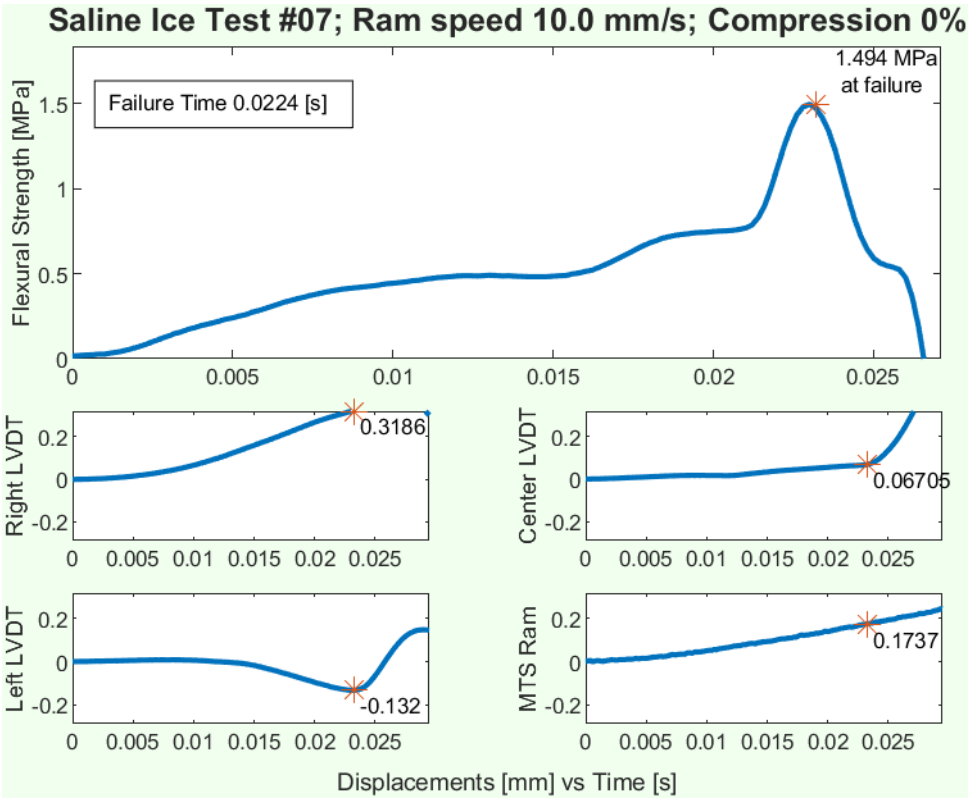
Saline Ice Test #07; Ram speed 10.0 mm/s; Compression 0%
Failure Time 0.0224 [s]
1.494 MPa
at failure
Flexural Strength [MPa]
Right LVDT
0.3186
Center LVDT
0.06705
Left LVDT
-0.132
MTS Ram
0.1737
Displacements [mm] vs Time [s]

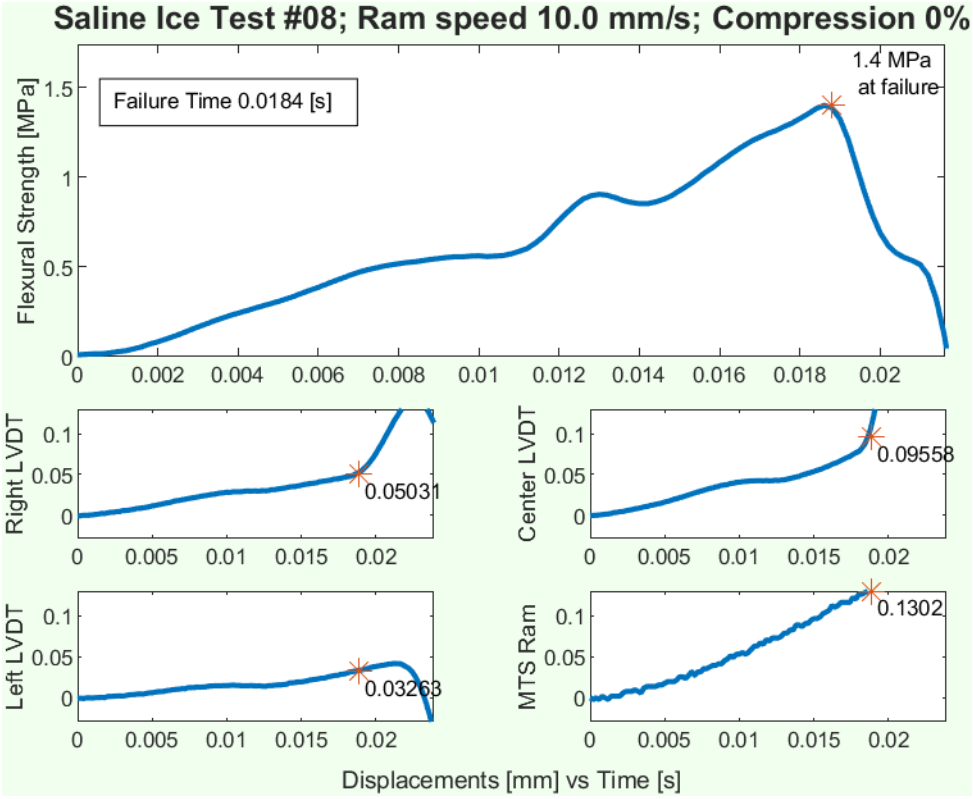
Saline Ice Test #08; Ram speed 10.0 mm/s; Compression 0%
Failure Time 0.0184 [s]
1.4 MPa
at failure
Flexural Strength [MPa]
Right LVDT
0.05031
Center LVDT
0.09558
Left LVDT
0.03263
MTS Ram
0.1302
Displacements [mm] vs Time [s]

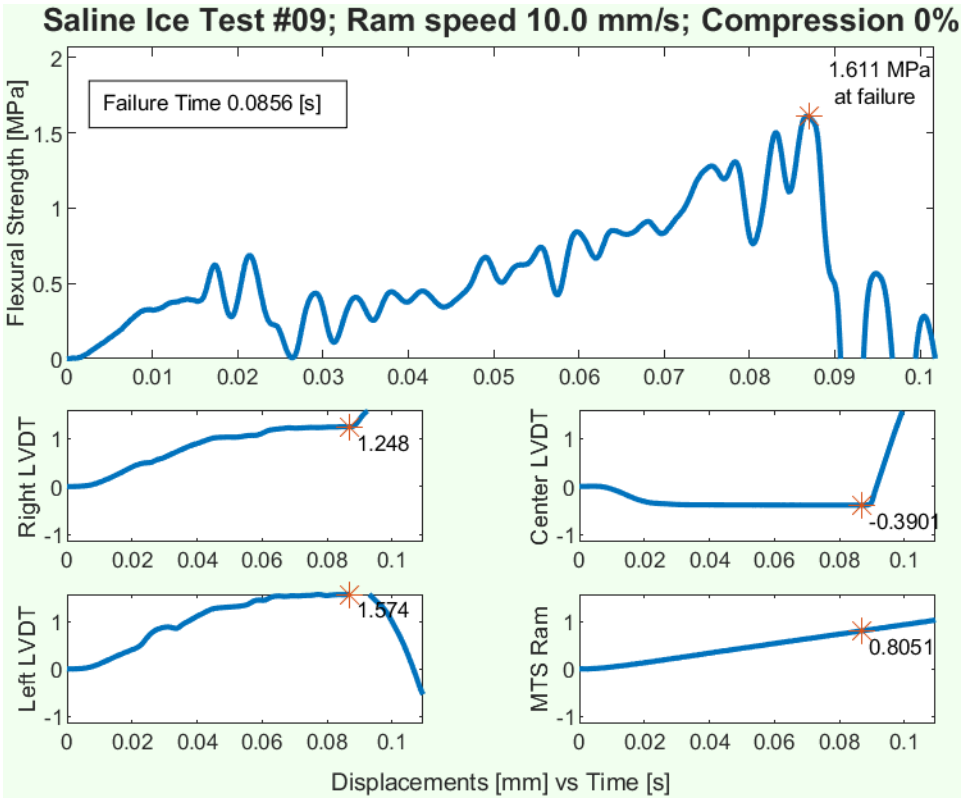
Saline Ice Test #09; Ram speed 10.0 mm/s; Compression 0%
Failure Time 0.0856 [s]
1.611 MPa
at failure
Flexural Strength [MPa]
Right LVDT
1.248
Center LVDT
-0.3901
Left LVDT
1.574
MTS Ram
0.8051
Displacements [mm] vs Time [s]

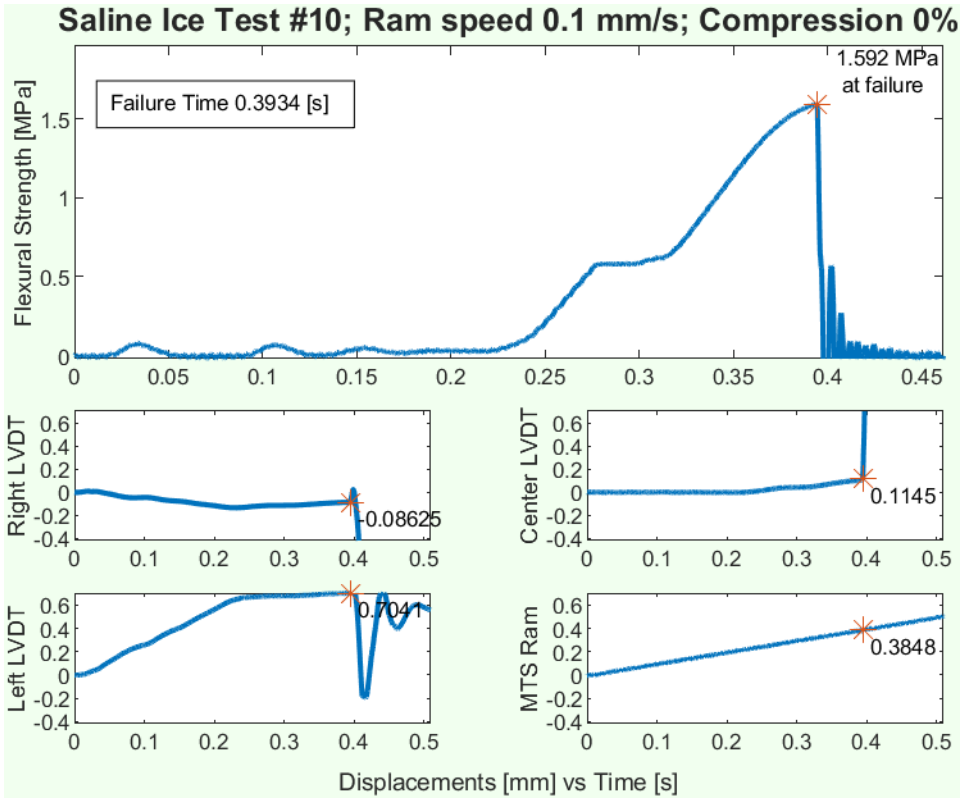
Saline Ice Test #10; Ram speed 0.1 mm/s; Compression 0%
Failure Time 0.3934 [s]
1.592 MPa
at failure
Flexural Strength [MPa]
Right LVDT
-0.08625
Center LVDT
0.1145
Left LVDT
0.7041
MTS Ram
0.3848
Displacements [mm] vs Time [s]

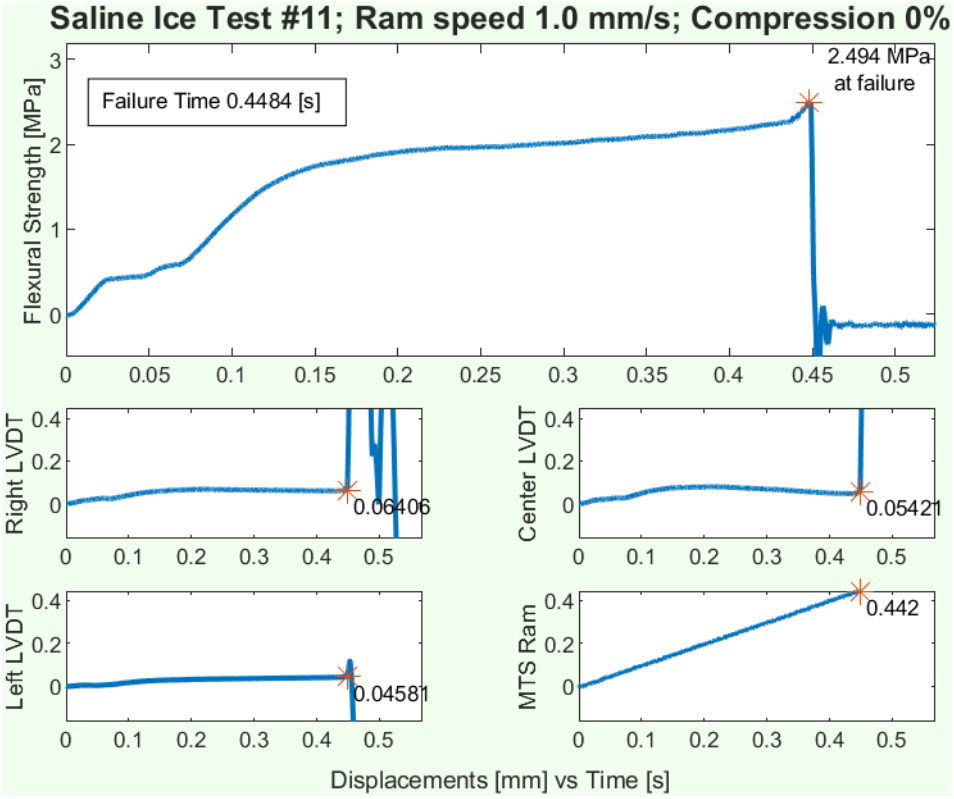
Saline Ice Test #11; Ram speed 1.0 mm/s; Compression 0%
Failure Time 0.4484 [s]
2.494 MPa
at failure
Flexural Strength [MPa]
Right LVDT
0.06406
Center LVDT
0.05421
Left LVDT
0.04581
MTS Ram
0.442
Displacements [mm] vs Time [s]

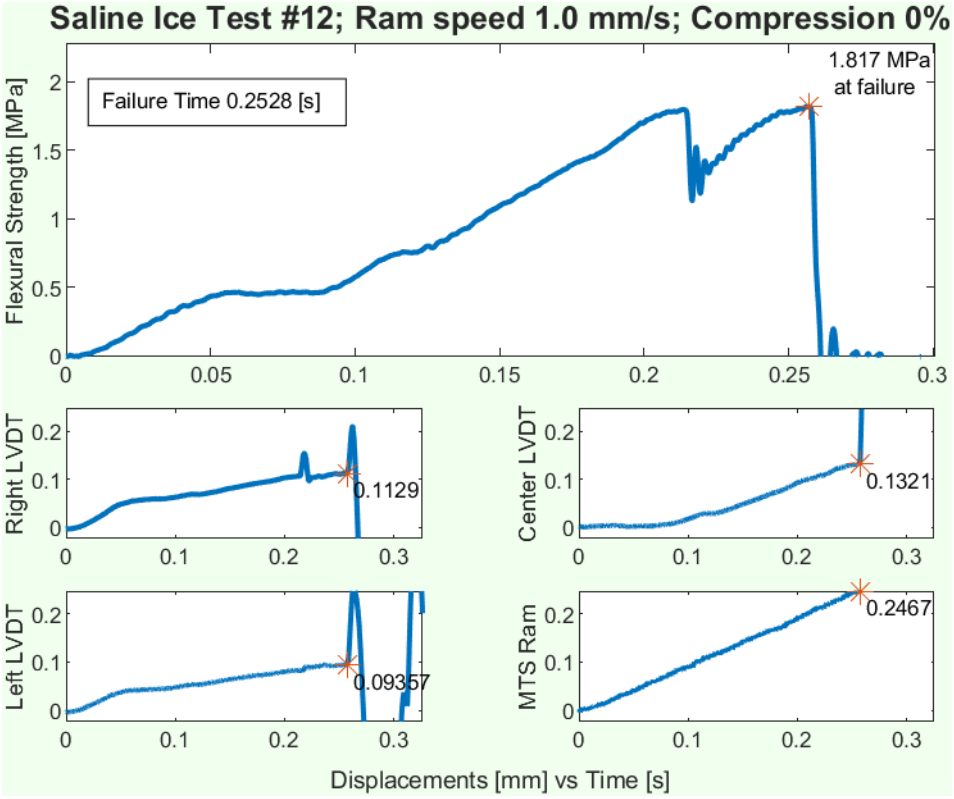
Saline Ice Test #12; Ram speed 1.0 mm/s; Compression 0%
Failure Time 0.2528 [s]
1.817 MPa
at failure
Flexural Strength [MPa]
Right LVDT
0.1129
Center LVDT
0.1321
Left LVDT
0.09357
MTS Ram
0.2467
Displacements [mm] vs Time [s]

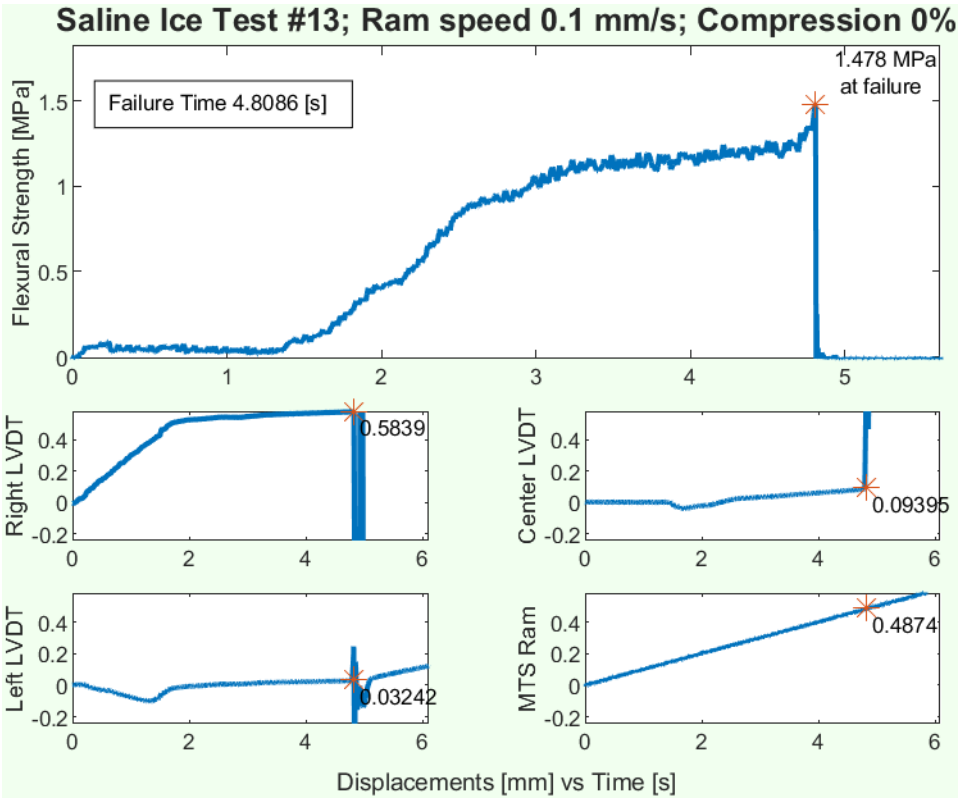
Saline Ice Test #13; Ram speed 0.1 mm/s; Compression 0%
Failure Time 4.8086 [s]
1.478 MPa
at failure
Flexural Strength [MPa]
Right LVDT
0.5839
Center LVDT
0.09395
Left LVDT
0.03242
MTS Ram
0.4874
Displacements [mm] vs Time [s]

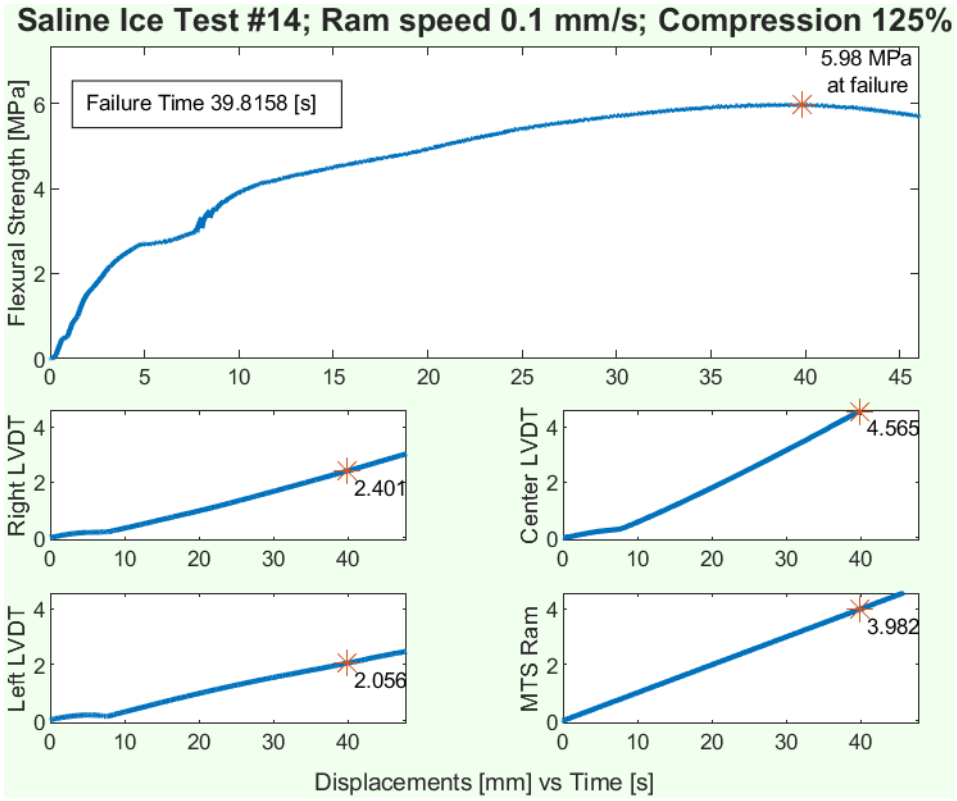
Saline Ice Test #14; Ram speed 0.1 mm/s; Compression 125%
Failure Time 39.8158 [s]
5.98 MPa
at failure
Flexural Strength [MPa]
Right LVDT
2.401
Center LVDT
4.565
Left LVDT
2.056
MTS Ram
3.982
Displacements [mm] vs Time [s]

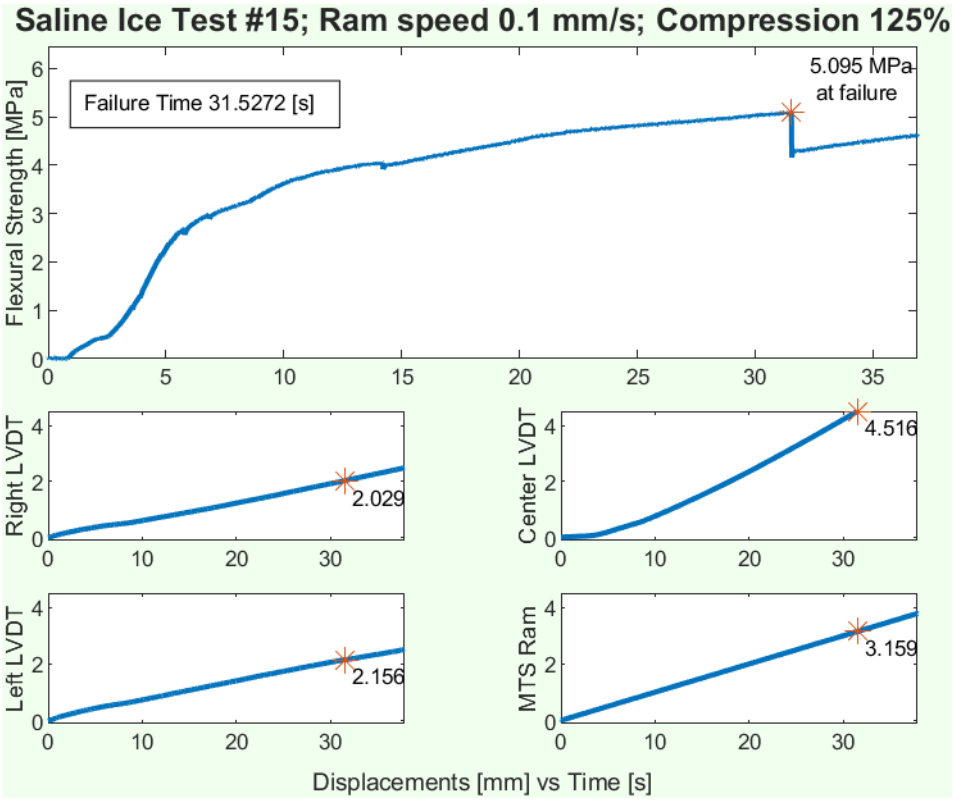
Saline Ice Test #15; Ram speed 0.1 mm/s; Compression 125%
Failure Time 31.5272 [s]
5.095 MPa
at failure
Flexural Strength [MPa]
Right LVDT
2.029
Center LVDT
4.516
Left LVDT
2.156
MTS Ram
3.159
Displacements [mm] vs Time [s]

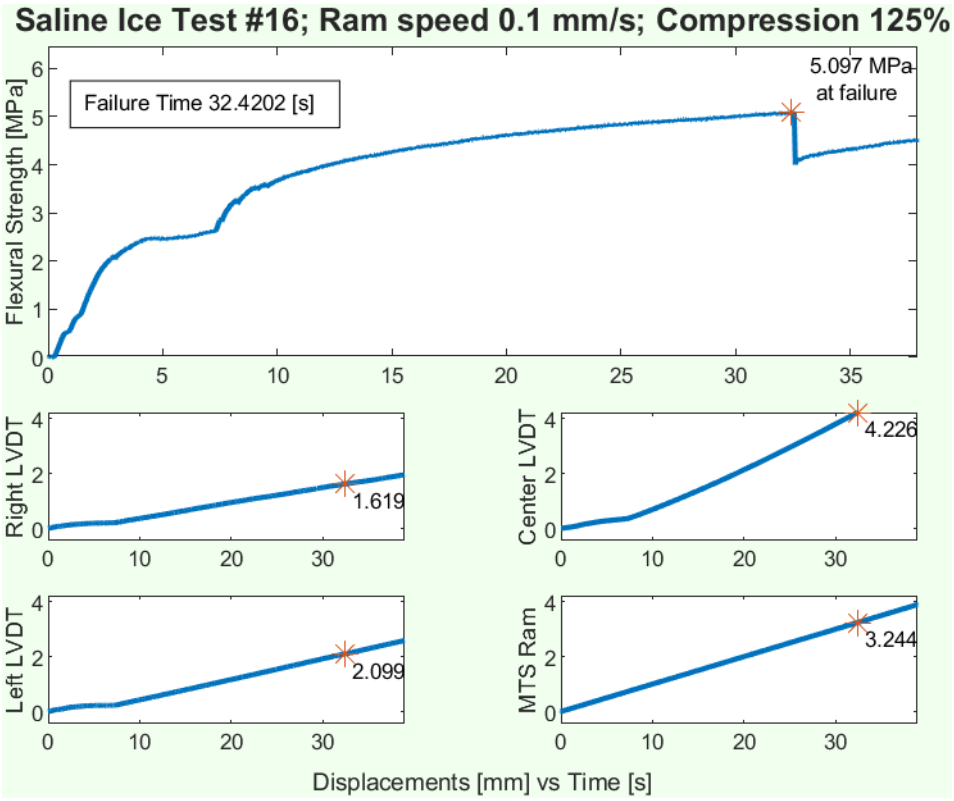
Saline Ice Test #16; Ram speed 0.1 mm/s; Compression 125%
Failure Time 32.4202 [s]
5.097 MPa
at failure
Flexural Strength [MPa]
Right LVDT
1.619
Center LVDT
4.226
Left LVDT
2.099
MTS Ram
3.244
Displacements [mm] vs Time [s]

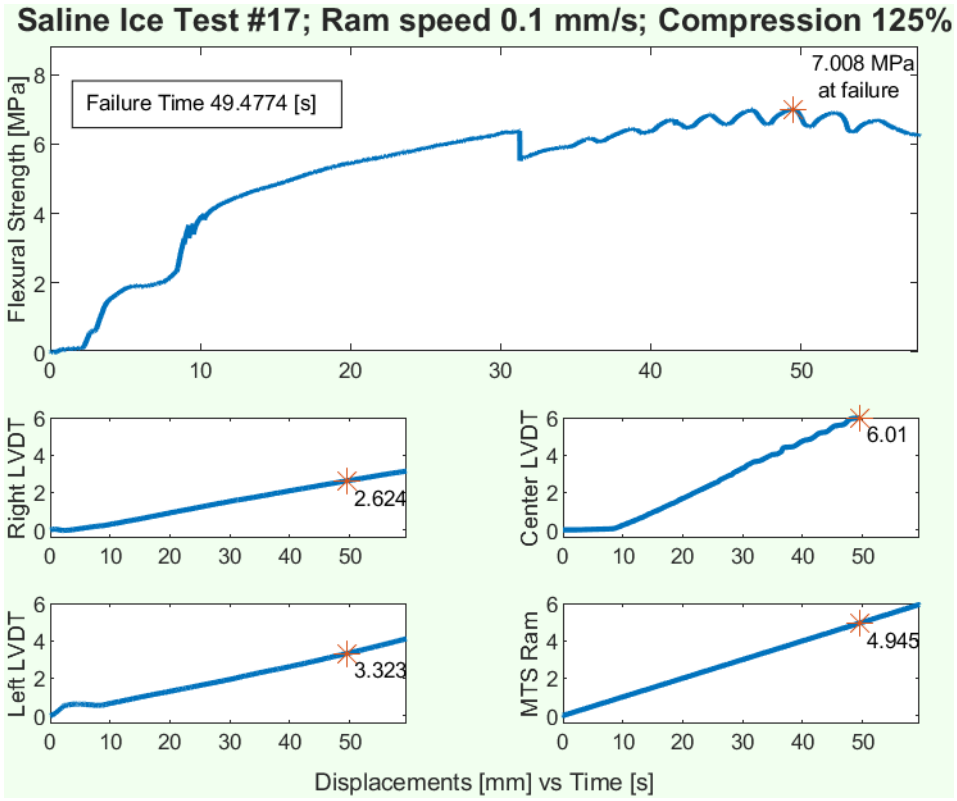
Saline Ice Test #17; Ram speed 0.1 mm/s; Compression 125%
Failure Time 49.4774 [s]
7.008 MPa
at failure
Flexural Strength [MPa]
Right LVDT
2.624
Center LVDT
6.01
Left LVDT
3.323
MTS Ram
4.945
Displacements [mm] vs Time [s]

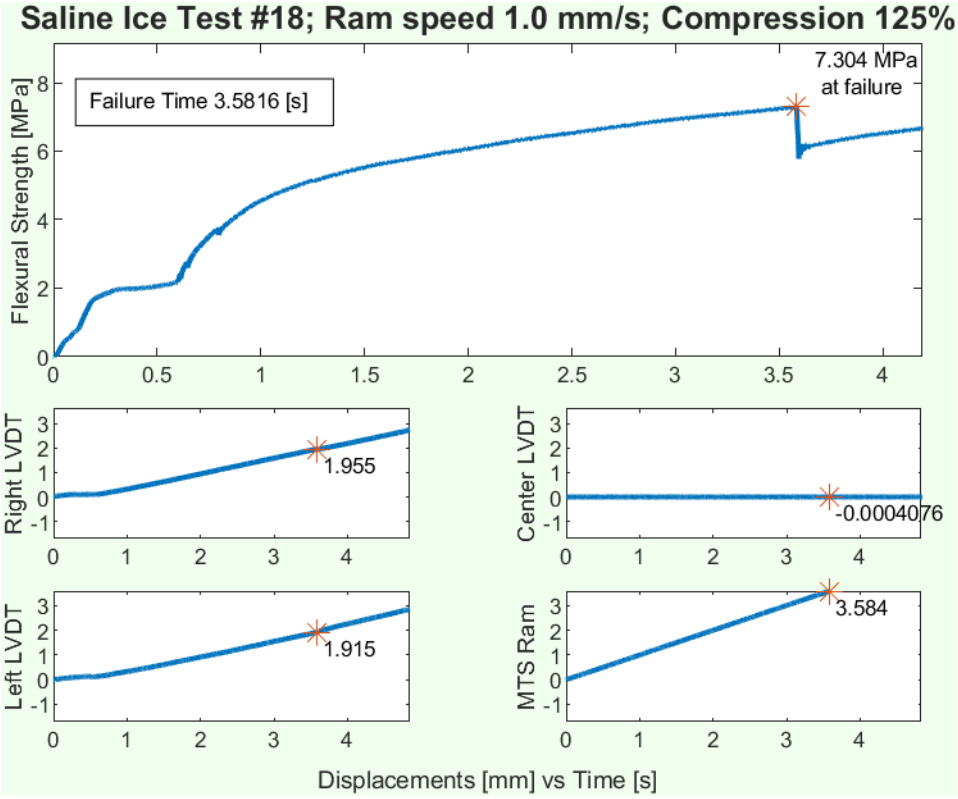
Saline Ice Test #18; Ram speed 1.0 mm/s; Compression 125%
Failure Time 3.5816 [s]
7.304 MPa
at failure
Flexural Strength [MPa]
Right LVDT
1.955
Center LVDT
-0.0004076
Left LVDT
1.915
MTS Ram
3.584
Displacements [mm] vs Time [s]

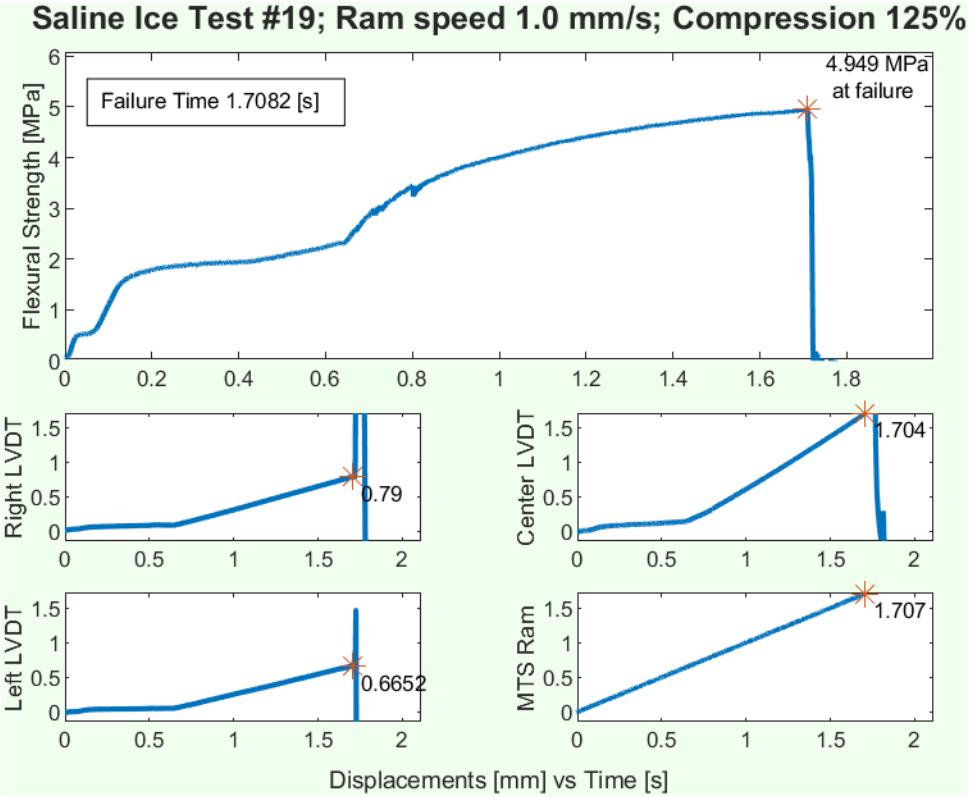
Saline Ice Test #19; Ram speed 1.0 mm/s; Compression 125%
Failure Time 1.7082 [s]
4.949 MPa
at failure
Flexural Strength [MPa]
Right LVDT
0.79
Center LVDT
1.704
Left LVDT
0.6652
MTS Ram
1.707
Displacements [mm] vs Time [s]

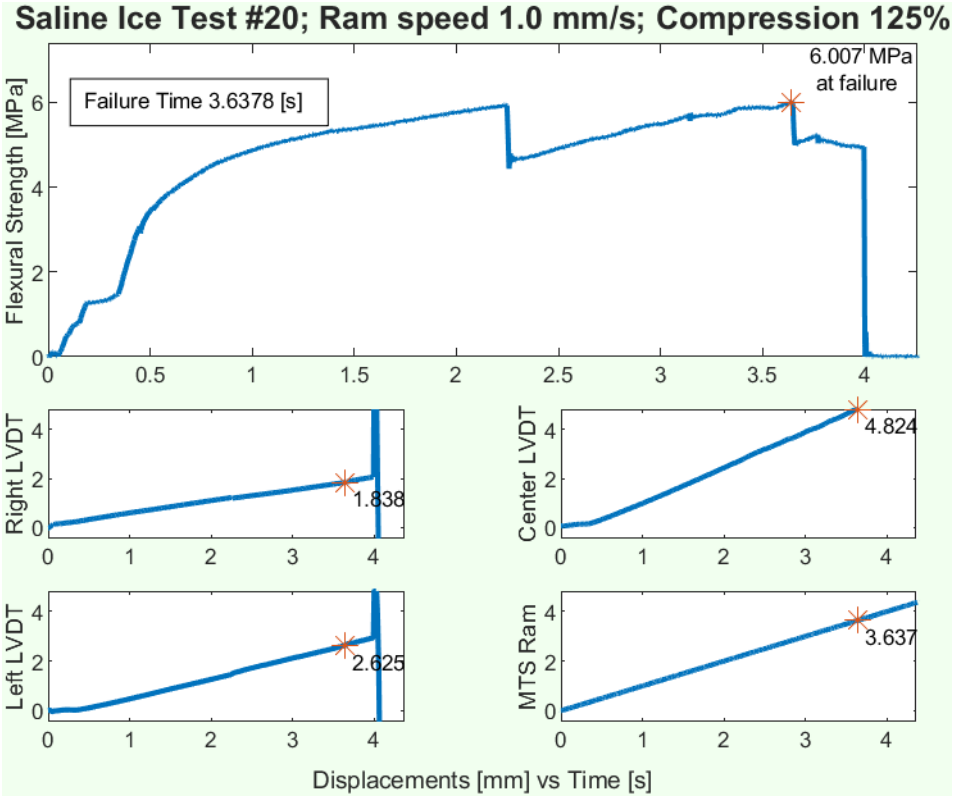
Saline Ice Test #20; Ram speed 1.0 mm/s; Compression 125%
Failure Time 3.6378 [s]
6.007 MPa
at failure
Flexural Strength [MPa]
Right LVDT
1.838
Center LVDT
4.824
Left LVDT
2.625
MTS Ram
3.637
Displacements [mm] vs Time [s]

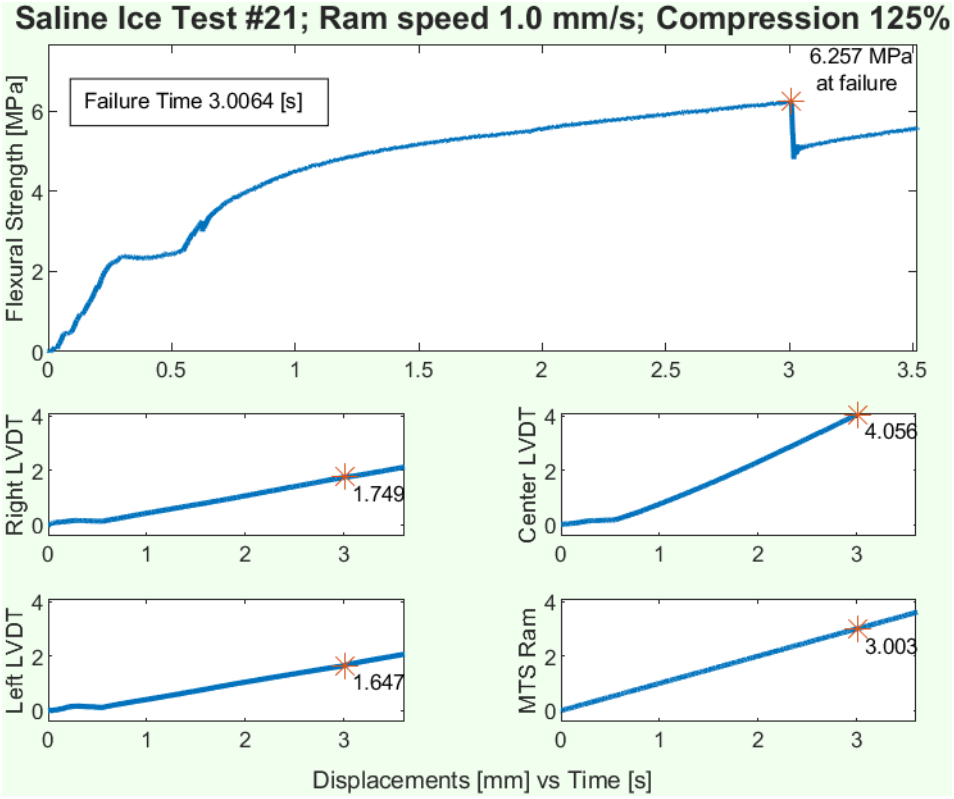
Saline Ice Test #21; Ram speed 1.0 mm/s; Compression 125%
Failure Time 3.0064 [s]
6.257 MPa
at failure
Flexural Strength [MPa]
Right LVDT
1.749
Center LVDT
4.056
Left LVDT
1.647
MTS Ram
3.003
Displacements [mm] vs Time [s]

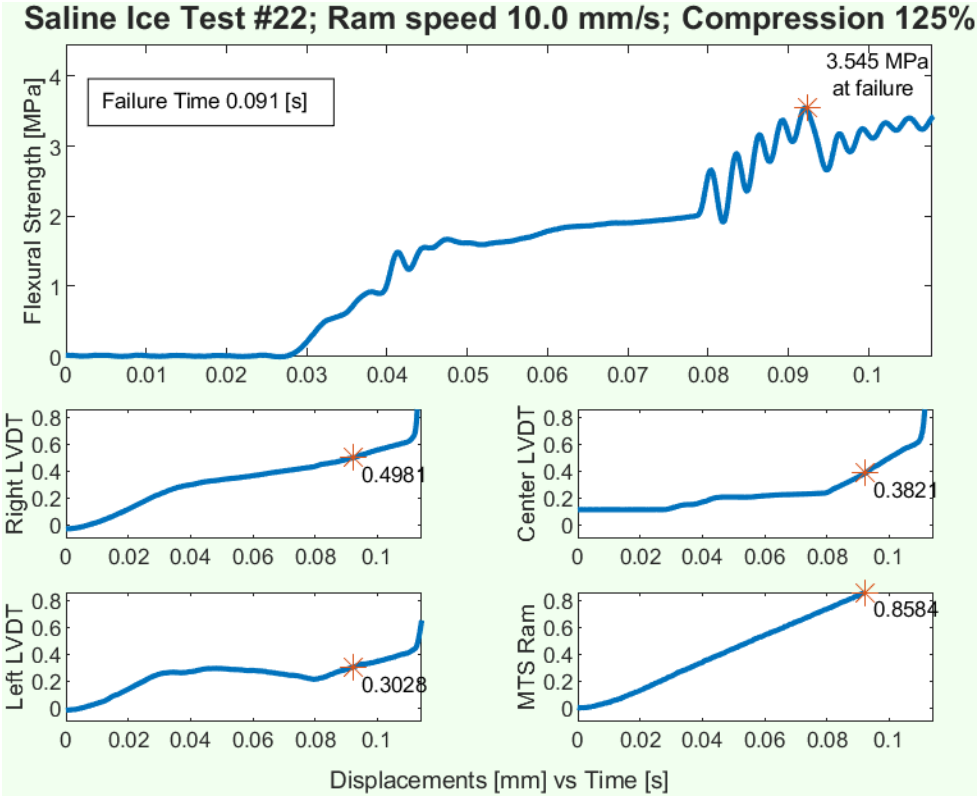
Saline Ice Test #22; Ram speed 10.0 mm/s; Compression 125%
Failure Time 0.091 [s]
3.545 MPa
at failure
Flexural Strength [MPa]
Right LVDT
0.4981
Center LVDT
0.3821
Left LVDT
0.3028
MTS Ram
0.8584
Displacements [mm] vs Time [s]

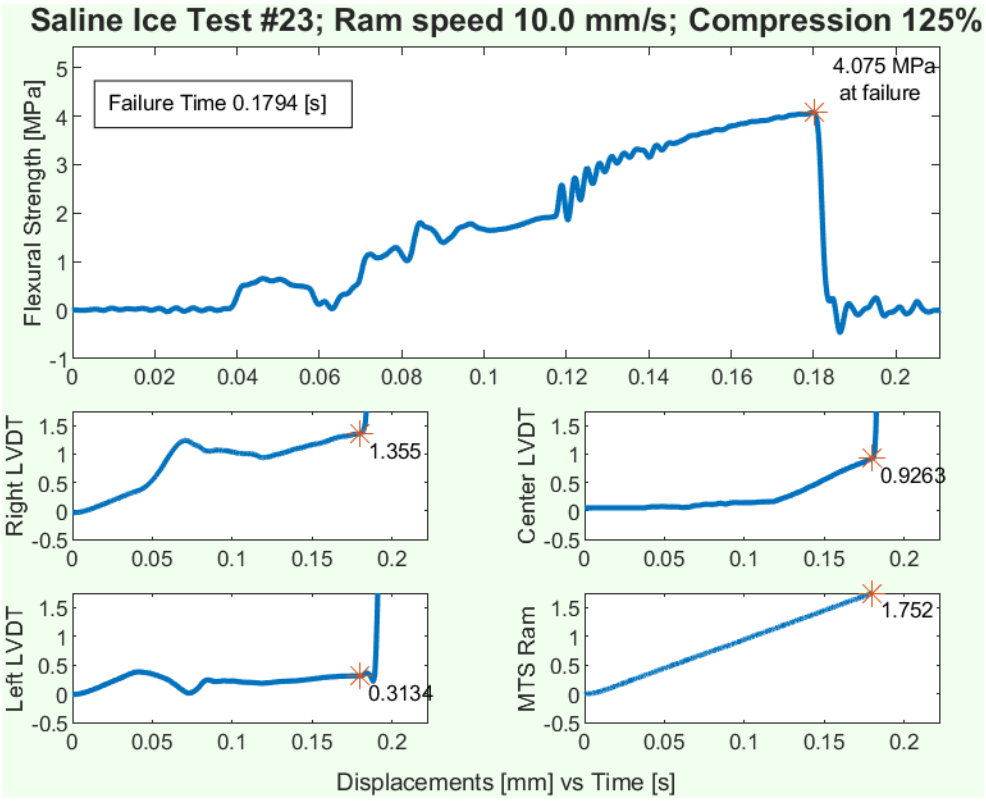
Saline Ice Test #23; Ram speed 10.0 mm/s; Compression 125%
Failure Time 0.1794 [s]
4.075 MPa
at failure
Flexural Strength [MPa]
Right LVDT
1.355
Center LVDT
0.9263
Left LVDT
0.3134
MTS Ram
1.752
Displacements [mm] vs Time [s]

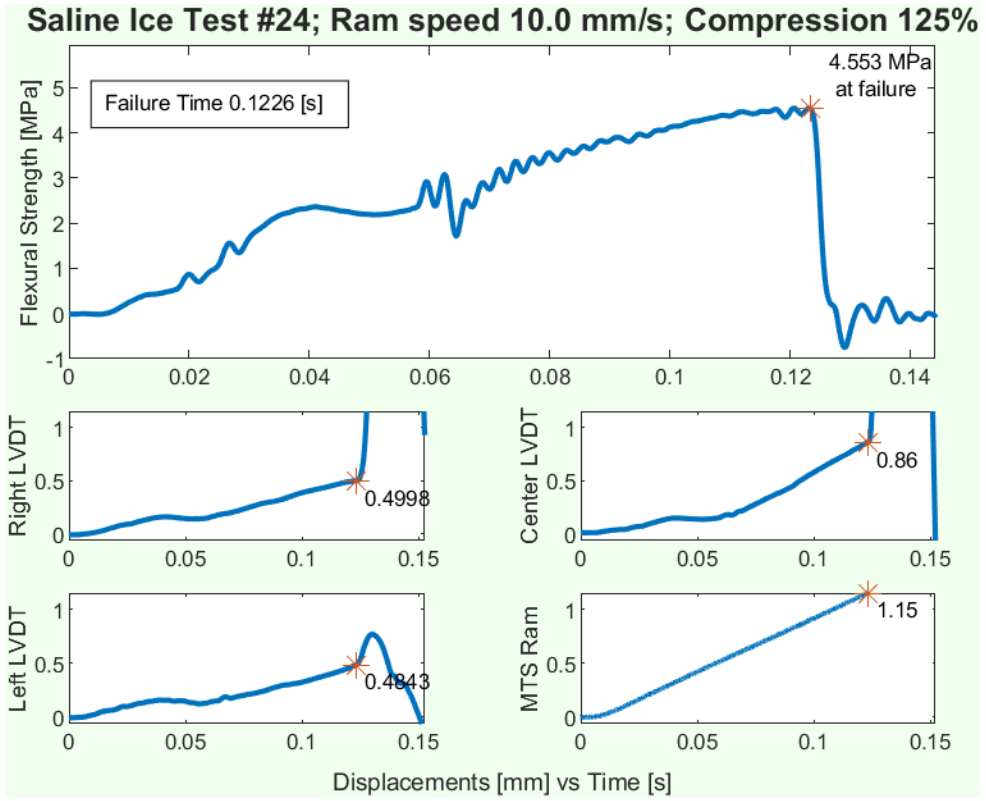
Saline Ice Test #24; Ram speed 10.0 mm/s; Compression 125%
Failure Time 0.1226 [s]
4.553 MPa
at failure
Flexural Strength [MPa]
Right LVDT
0.4998
Center LVDT
0.86
Left LVDT
0.4843
MTS Ram
1.15
Displacements [mm] vs Time [s]

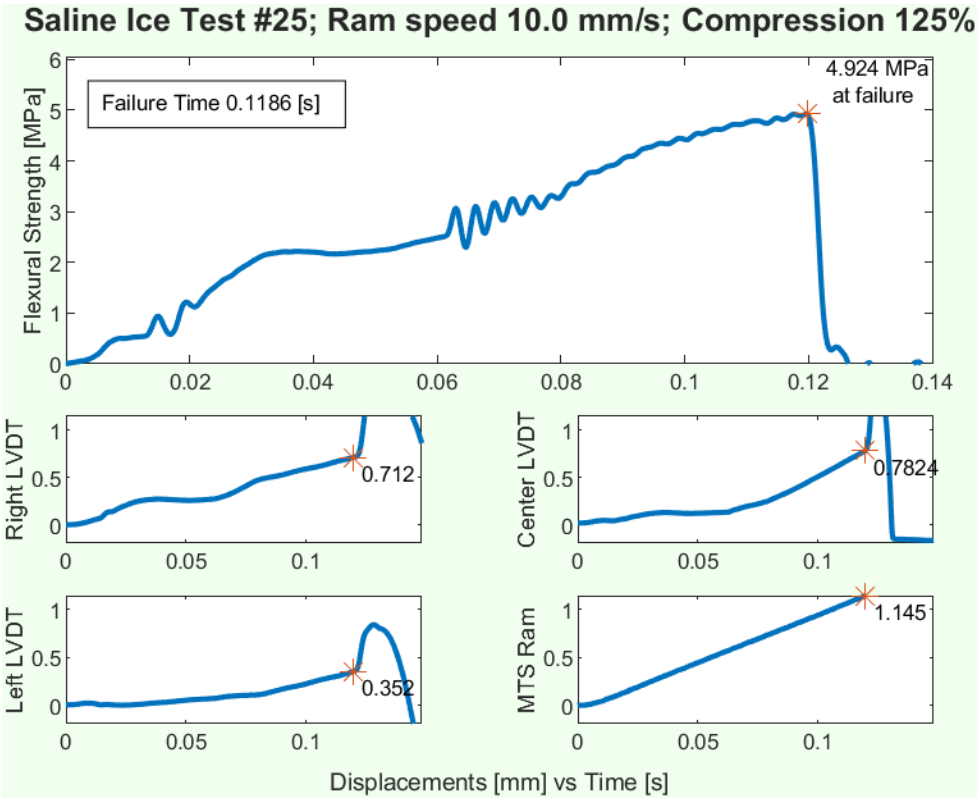
Saline Ice Test #25; Ram speed 10.0 mm/s; Compression 125%
Failure Time 0.1186 [s]
4.924 MPa
at failure
Flexural Strength [MPa]
Right LVDT
0.712
Center LVDT
0.7824
Left LVDT
0.352
MTS Ram
1.145
Displacements [mm] vs Time [s]

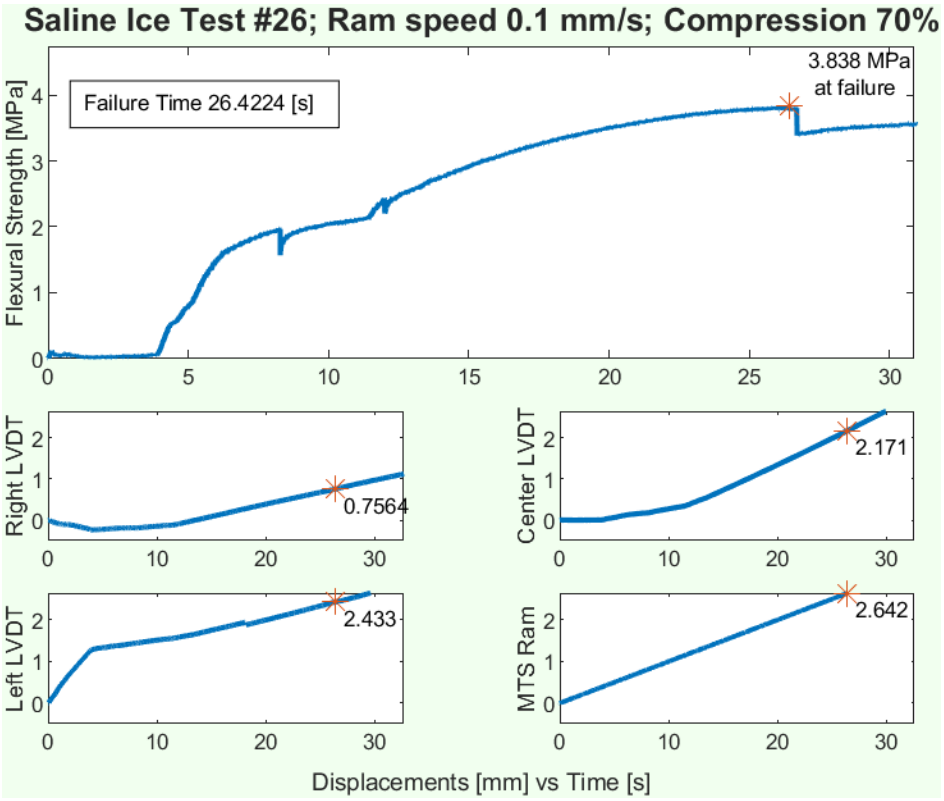
Saline Ice Test #26; Ram speed 0.1 mm/s; Compression 70%
Failure Time 26.4224 [s]
3.838 MPa
at failure
Flexural Strength [MPa]
Right LVDT
0.7564
Center LVDT
2.171
Left LVDT
2.433
MTS Ram
2.642
Displacements [mm] vs Time [s]

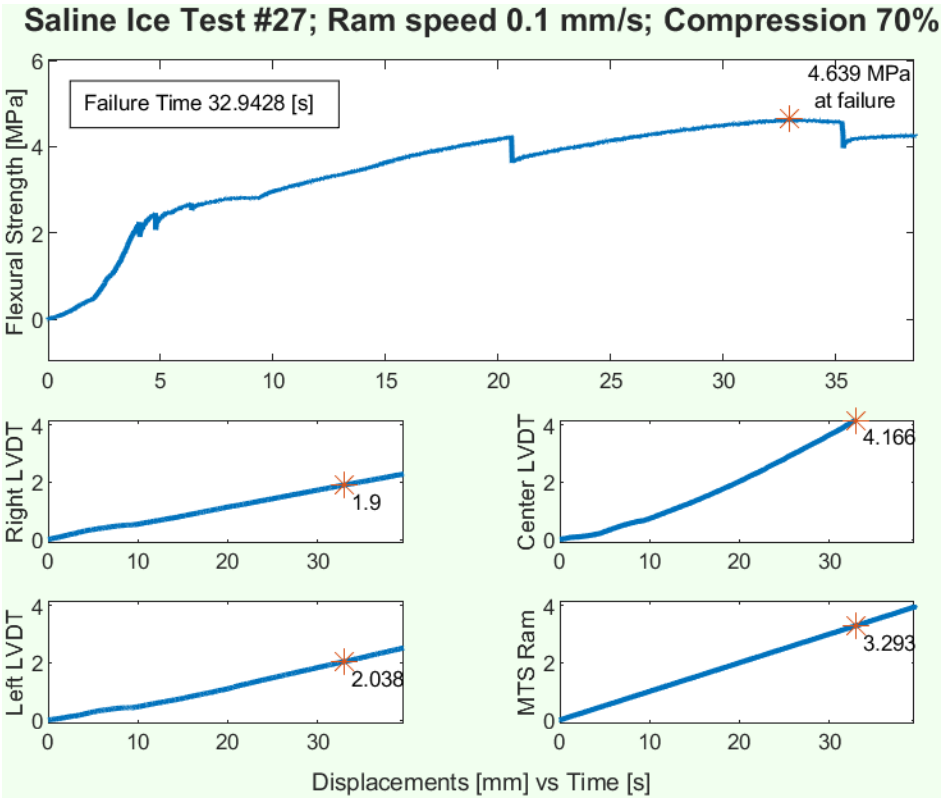
Saline Ice Test #27; Ram speed 0.1 mm/s; Compression 70%
Failure Time 32.9428 [s]
4.639 MPa
at failure
Flexural Strength [MPa]
Right LVDT
1.9
Center LVDT
4.166
Left LVDT
2.038
MTS Ram
3.293
Displacements [mm] vs Time [s]

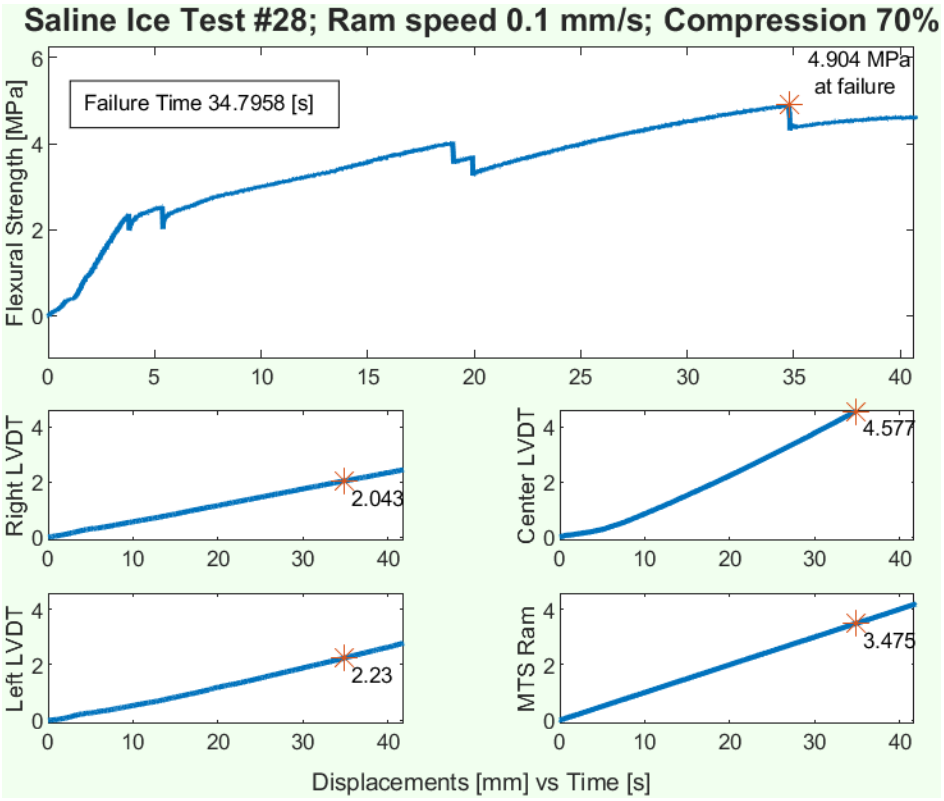
Saline Ice Test #28; Ram speed 0.1 mm/s; Compression 70%
Failure Time 34.7958 [s]
4.904 MPa
at failure
Flexural Strength [MPa]
Right LVDT
2.043
Center LVDT
4.577
Left LVDT
2.23
MTS Ram
3.475
Displacements [mm] vs Time [s]

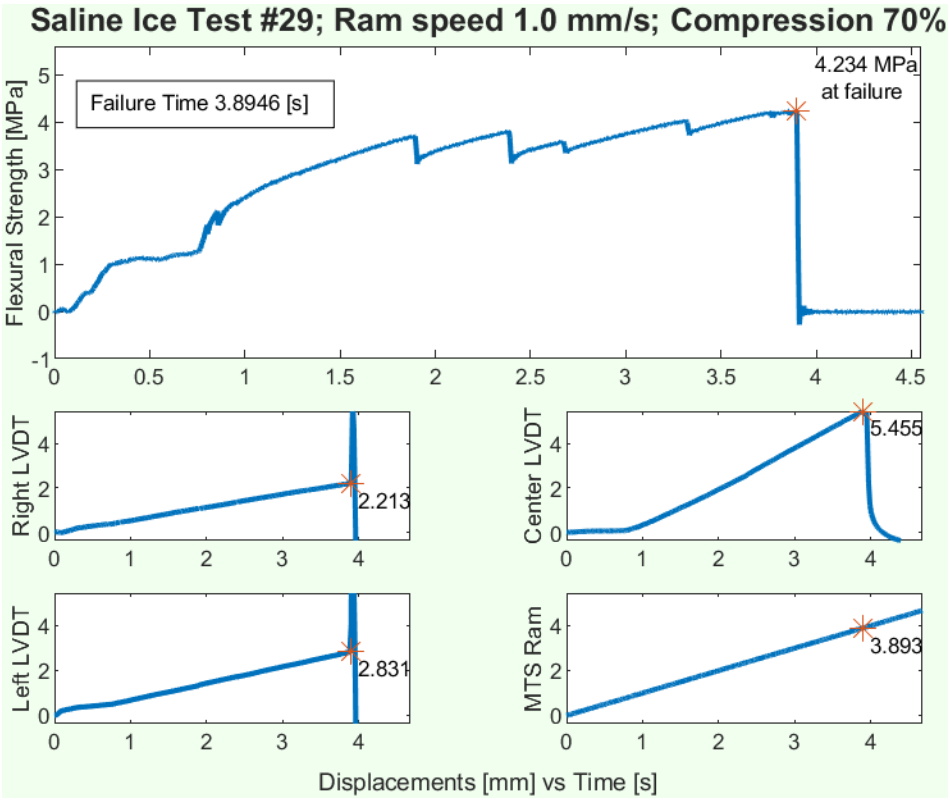
Saline Ice Test #29; Ram speed 1.0 mm/s; Compression 70%
Failure Time 3.8946 [s]
4.234 MPa
at failure
Flexural Strength [MPa]
Right LVDT
2.213
Center LVDT
5.455
Left LVDT
2.831
MTS Ram
3.893
Displacements [mm] vs Time [s]

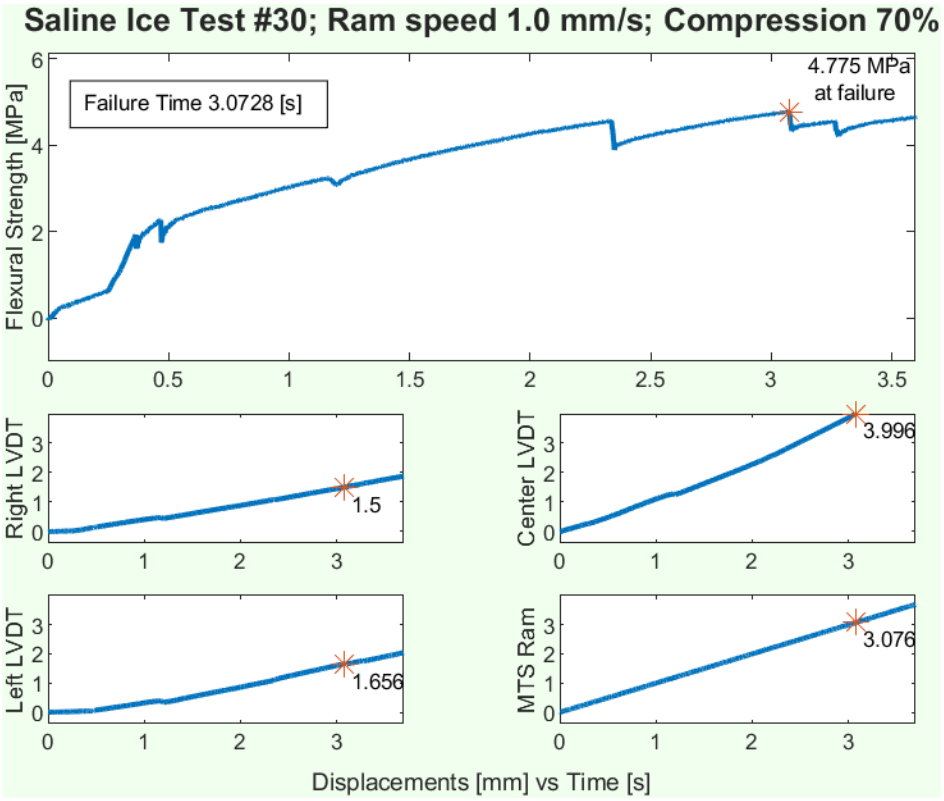
Saline Ice Test #30; Ram speed 1.0 mm/s; Compression 70%
Failure Time 3.0728 [s]
4.775 MPa
at failure
Flexural Strength [MPa]
Right LVDT
1.5
Center LVDT
3.996
Left LVDT
1.656
MTS Ram
3.076
Displacements [mm] vs Time [s]

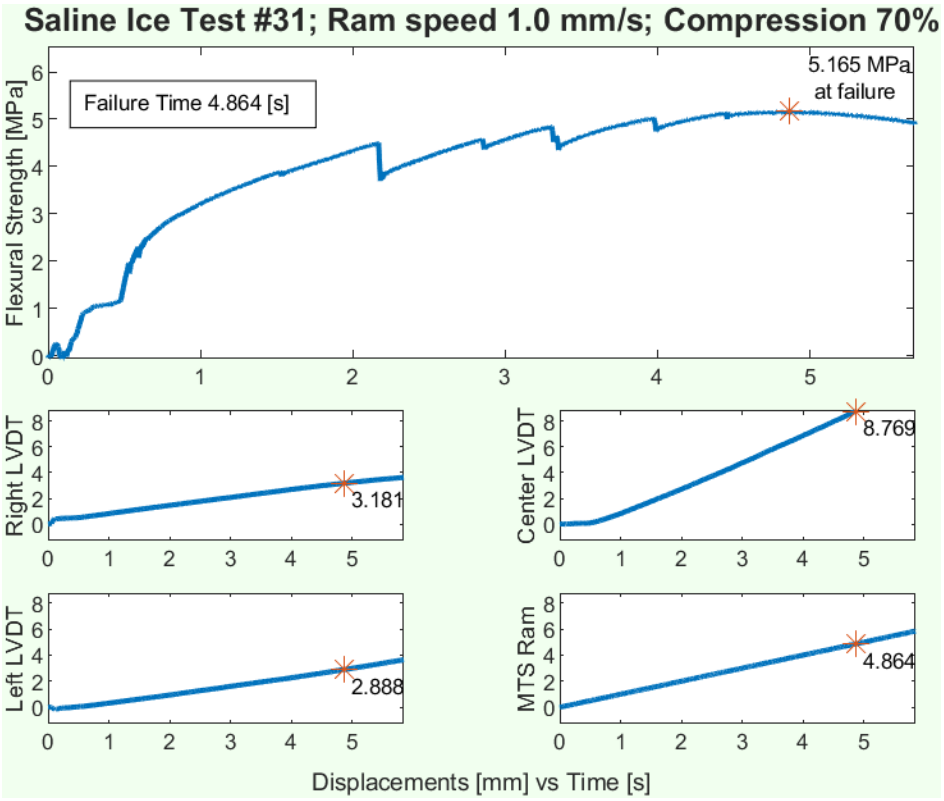
Saline Ice Test #31; Ram speed 1.0 mm/s; Compression 70%
Failure Time 4.864 [s]
5.165 MPa
at failure
Flexural Strength [MPa]
Right LVDT
3.181
Center LVDT
8.769
Left LVDT
2.888
MTS Ram
4.864
Displacements [mm] vs Time [s]

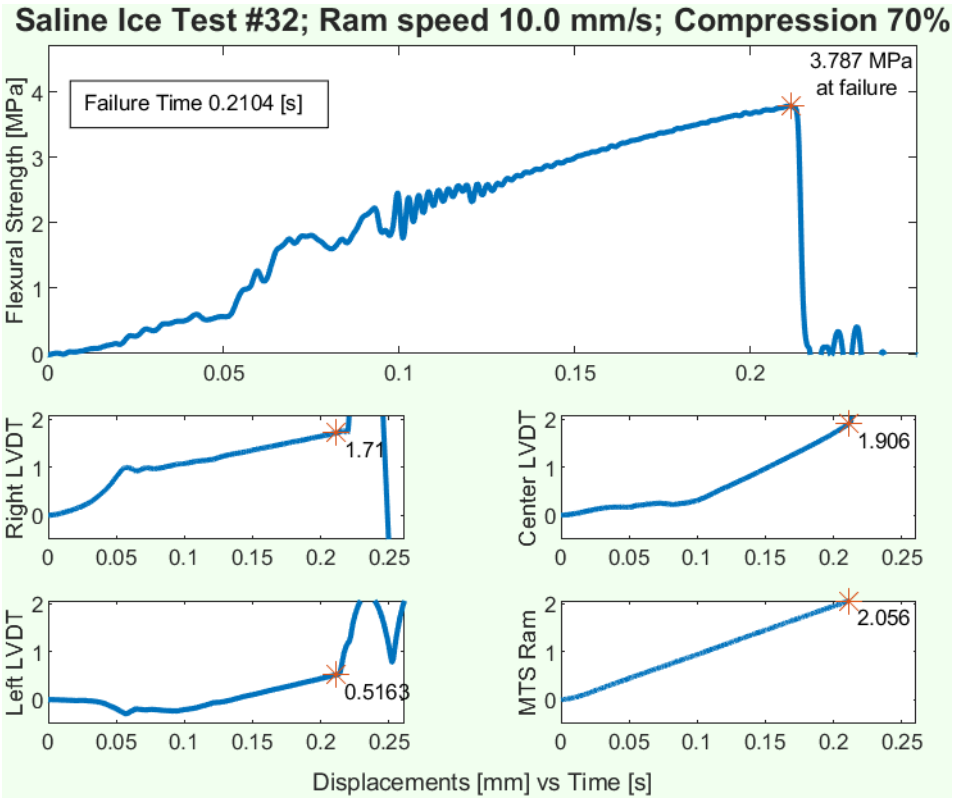
Saline Ice Test #32; Ram speed 10.0 mm/s; Compression 70%
Failure Time 0.2104 [s]
3.787 MPa
at failure
Flexural Strength [MPa]
Right LVDT
1.71
Center LVDT
1.906
Left LVDT
0.5163
MTS Ram
2.056
Displacements [mm] vs Time [s]

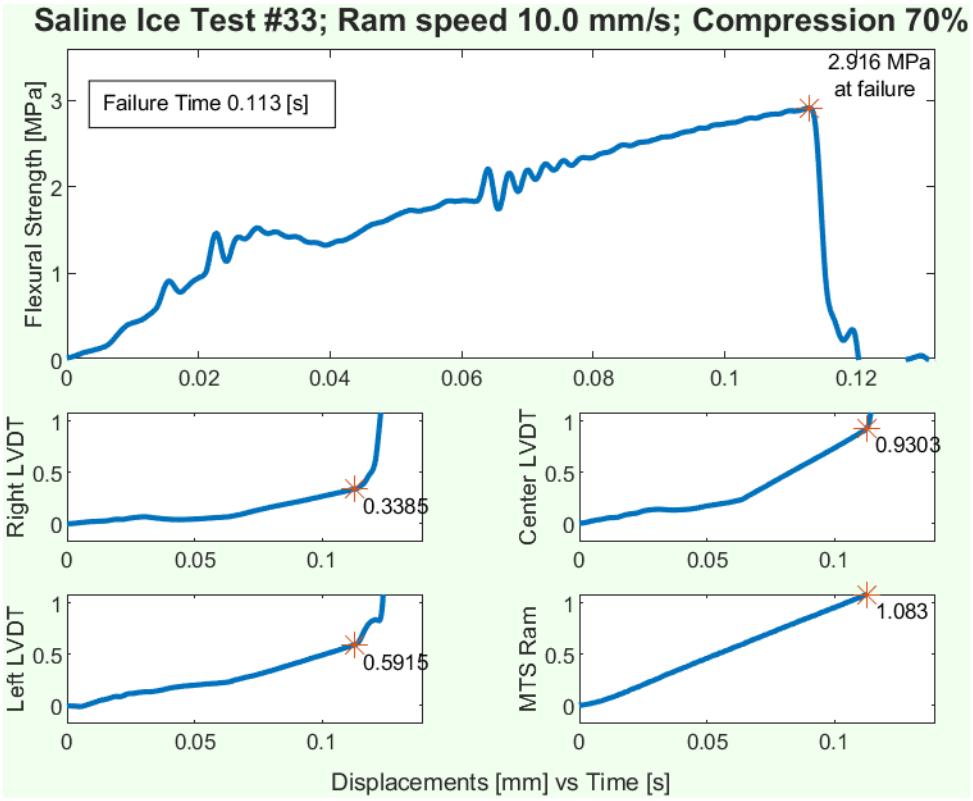
Saline Ice Test #33; Ram speed 10.0 mm/s; Compression 70%
Failure Time 0.113 [s]
2.916 MPa
at failure
Flexural Strength [MPa]
Right LVDT
0.3385
Center LVDT
0.9303
Left LVDT
0.5915
MTS Ram
1.083
Displacements [mm] vs Time [s]

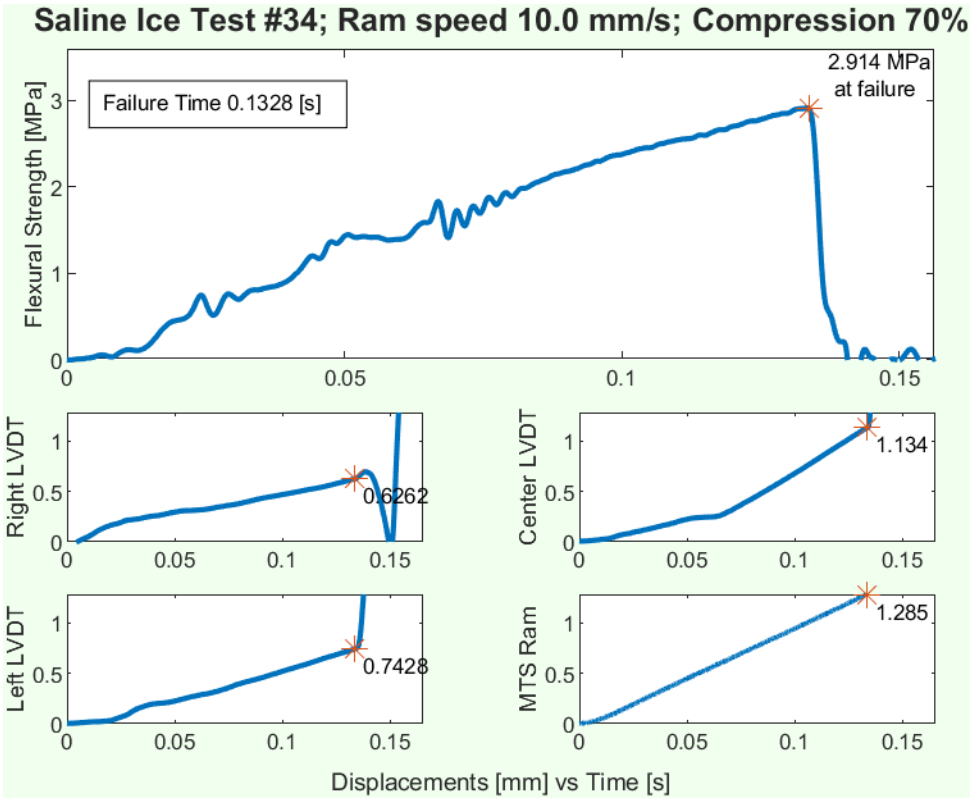
Saline Ice Test #34; Ram speed 10.0 mm/s; Compression 70%
Failure Time 0.1328 [s]
2.914 MPa
at failure
Flexural Strength [MPa]
Right LVDT
0.6262
Center LVDT
1.134
Left LVDT
0.7428
MTS Ram
1.285
Displacements [mm] vs Time [s]

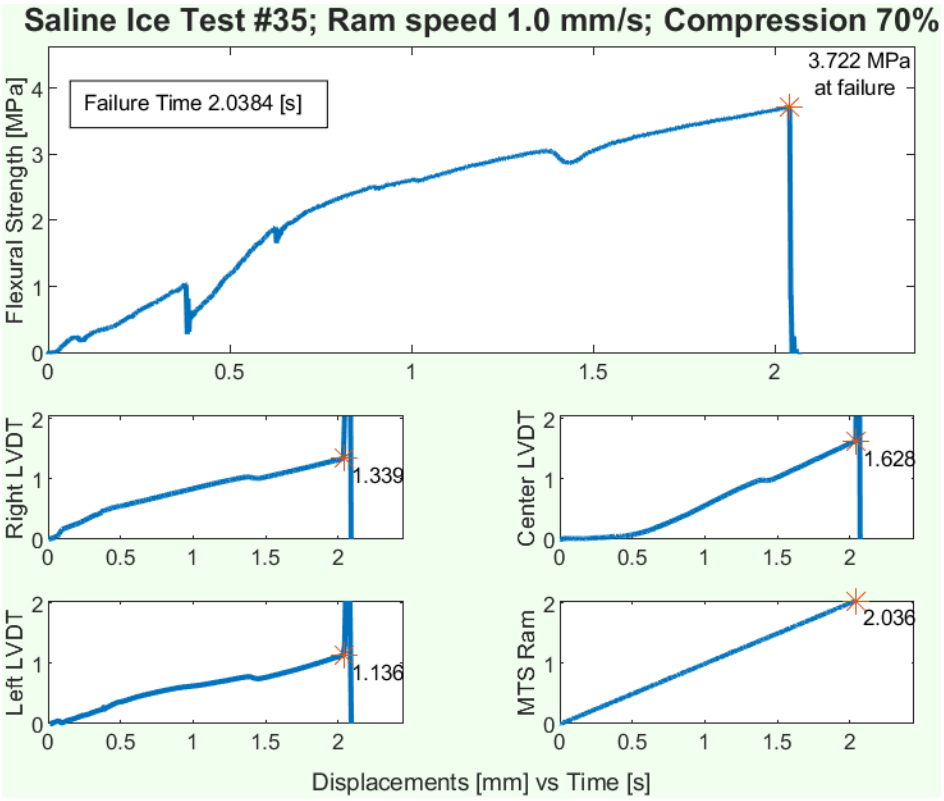
Saline Ice Test #35; Ram speed 1.0 mm/s; Compression 70%
Failure Time 2.0384 [s]
3.722 MPa
at failure
Flexural Strength [MPa]
Right LVDT
1.339
Center LVDT
1.628
Left LVDT
1.136
MTS Ram
2.036
Displacements [mm] vs Time [s]

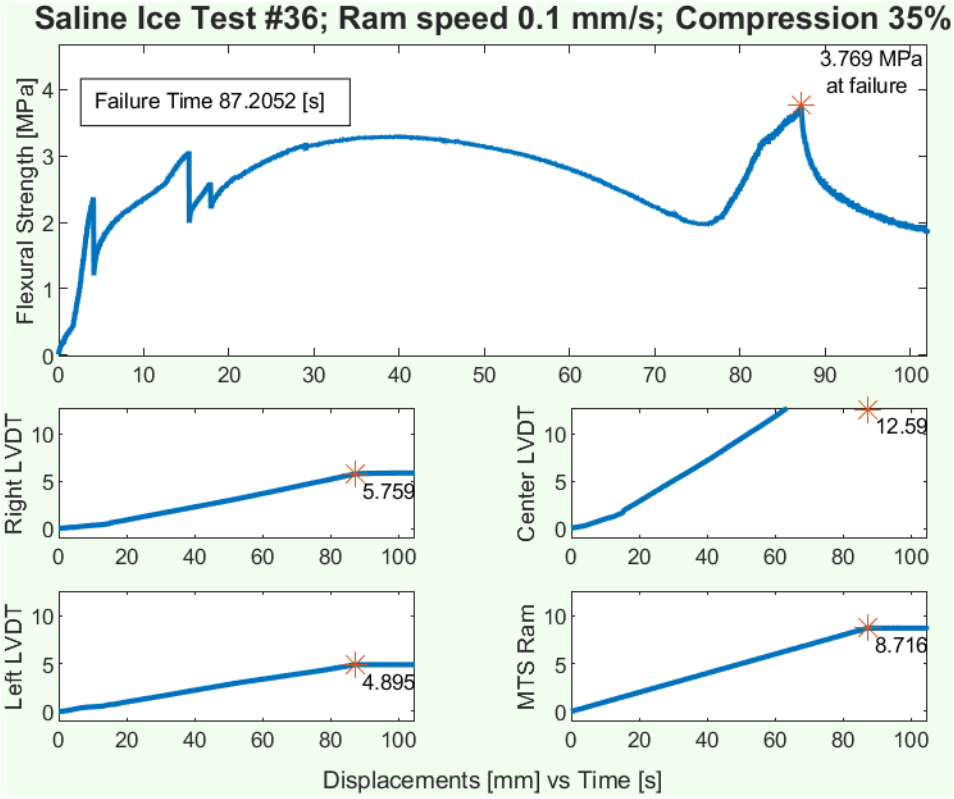
Saline Ice Test #36; Ram speed 0.1 mm/s; Compression 35%
Failure Time 87.2052 [s]
3.769 MPa
at failure
Flexural Strength [MPa]
Right LVDT
5.759
Center LVDT
12.59
Left LVDT
4.895
MTS Ram
8.716
Displacements [mm] vs Time [s]

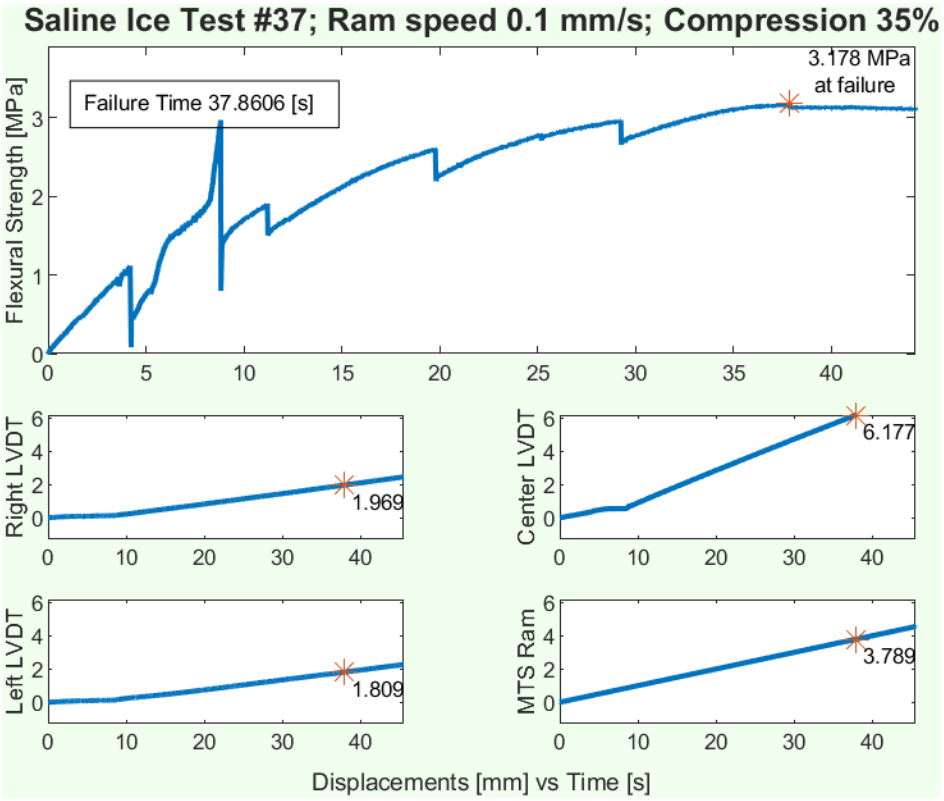
Saline Ice Test #37; Ram speed 0.1 mm/s; Compression 35%
Failure Time 37.8606 [s]
3.178 MPa
at failure
Flexural Strength [MPa]
Right LVDT
1.969
Center LVDT
6.177
Left LVDT
1.809
MTS Ram
3.789
Displacements [mm] vs Time [s]

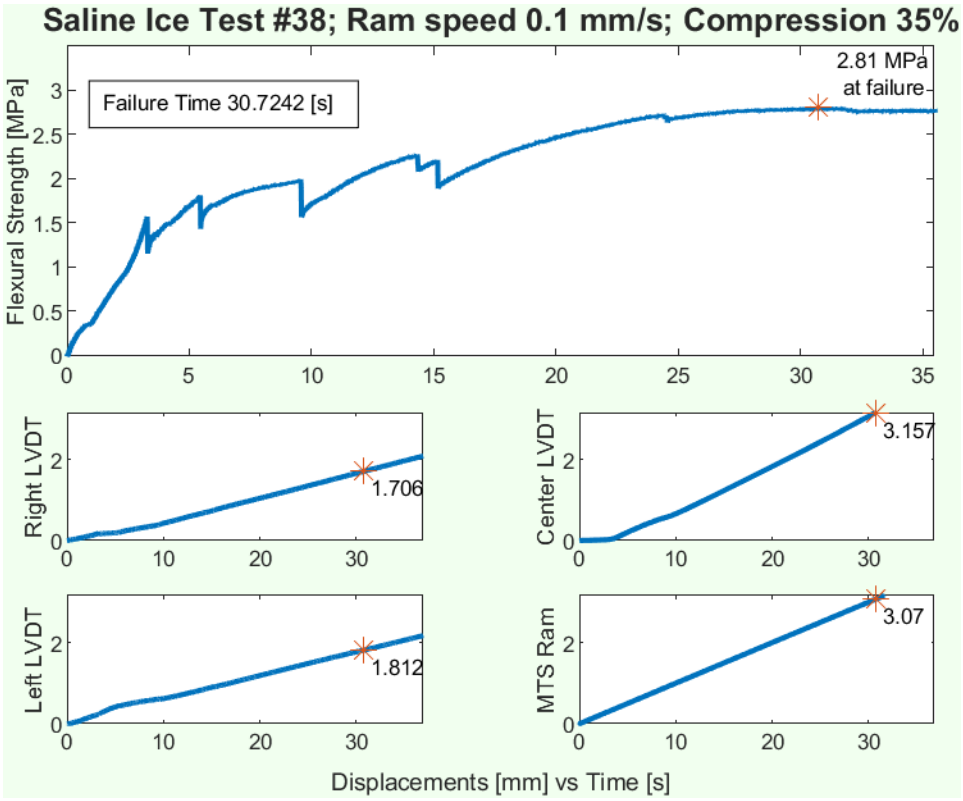
Saline Ice Test #38; Ram speed 0.1 mm/s; Compression 35%
Failure Time 30.7242 [s]
2.81 MPa
at failure
Flexural Strength [MPa]
Right LVDT
1.706
Center LVDT
3.157
Left LVDT
1.812
MTS Ram
3.07
Displacements [mm] vs Time [s]

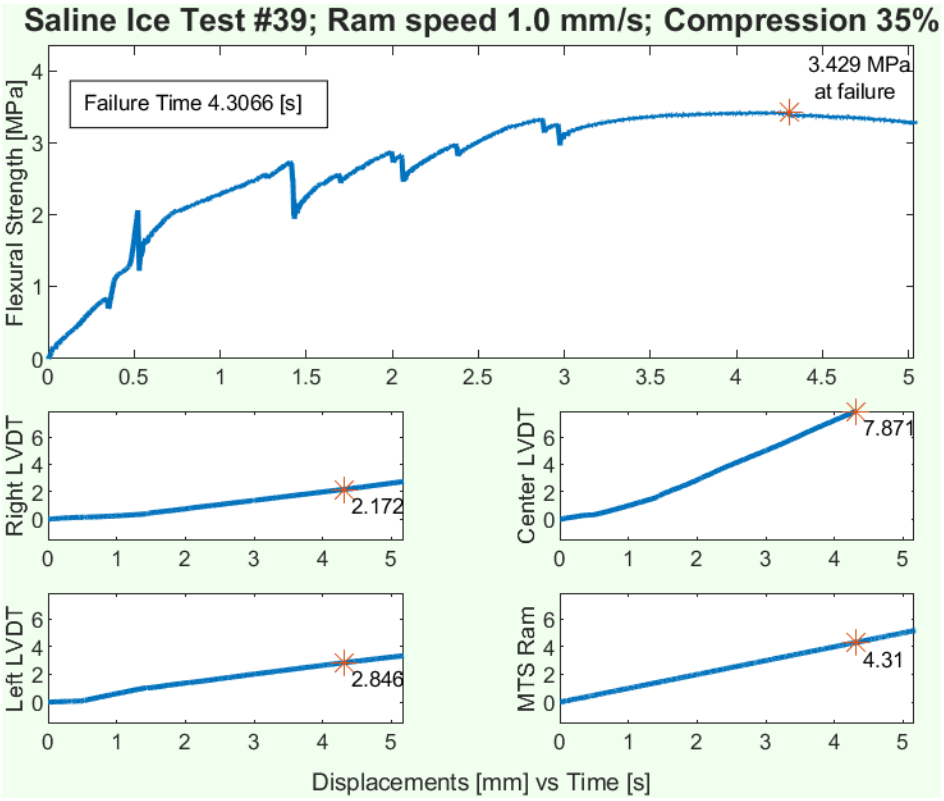
Saline Ice Test #39; Ram speed 1.0 mm/s; Compression 35%
Failure Time 4.3066 [s]
3.429 MPa
at failure
Flexural Strength [MPa]
Right LVDT
2.172
Center LVDT
7.871
Left LVDT
2.846
MTS Ram
4.31
Displacements [mm] vs Time [s]

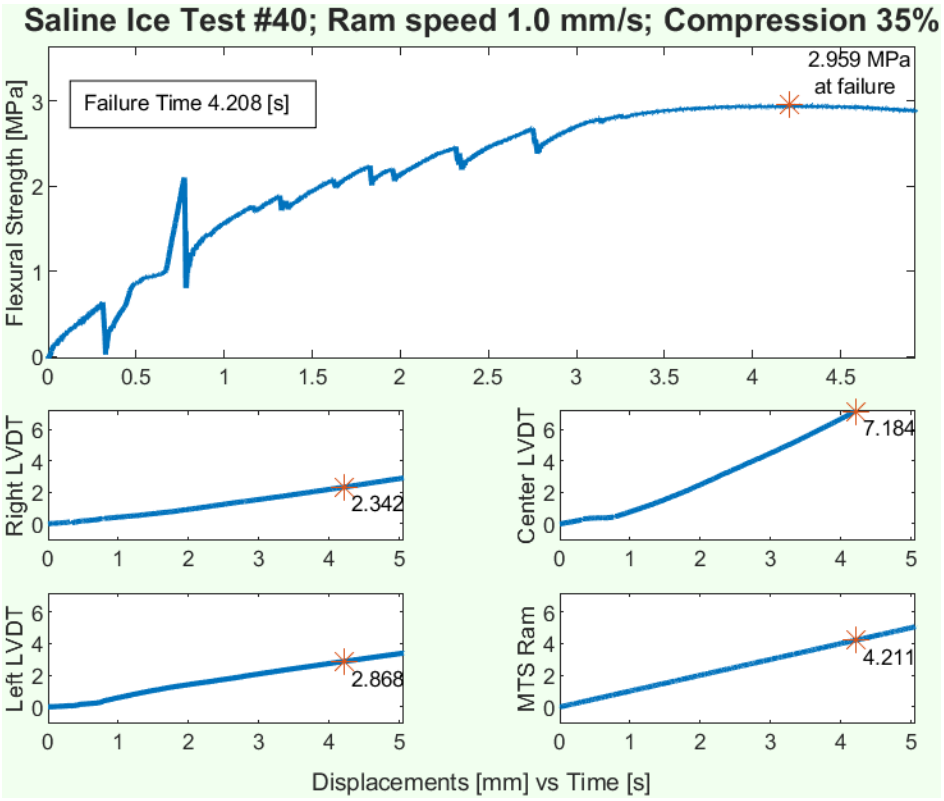
Saline Ice Test #40; Ram speed 1.0 mm/s; Compression 35%
Failure Time 4.208 [s]
2.959 MPa
at failure
Flexural Strength [MPa]
Right LVDT
2.342
Center LVDT
7.184
Left LVDT
2.868
MTS Ram
4.211
Displacements [mm] vs Time [s]

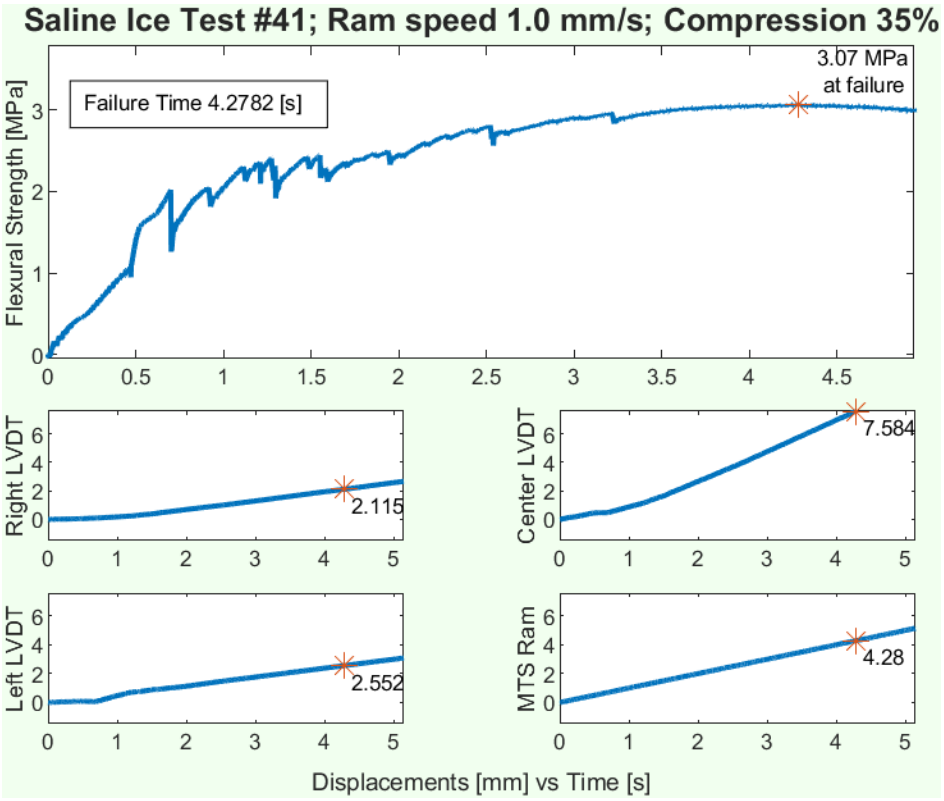
Saline Ice Test #41; Ram speed 1.0 mm/s; Compression 35%
Failure Time 4.2782 [s]
3.07 MPa
at failure
Flexural Strength [MPa]
Right LVDT
2.115
Center LVDT
7.584
Left LVDT
2.552
MTS Ram
4.28
Displacements [mm] vs Time [s]

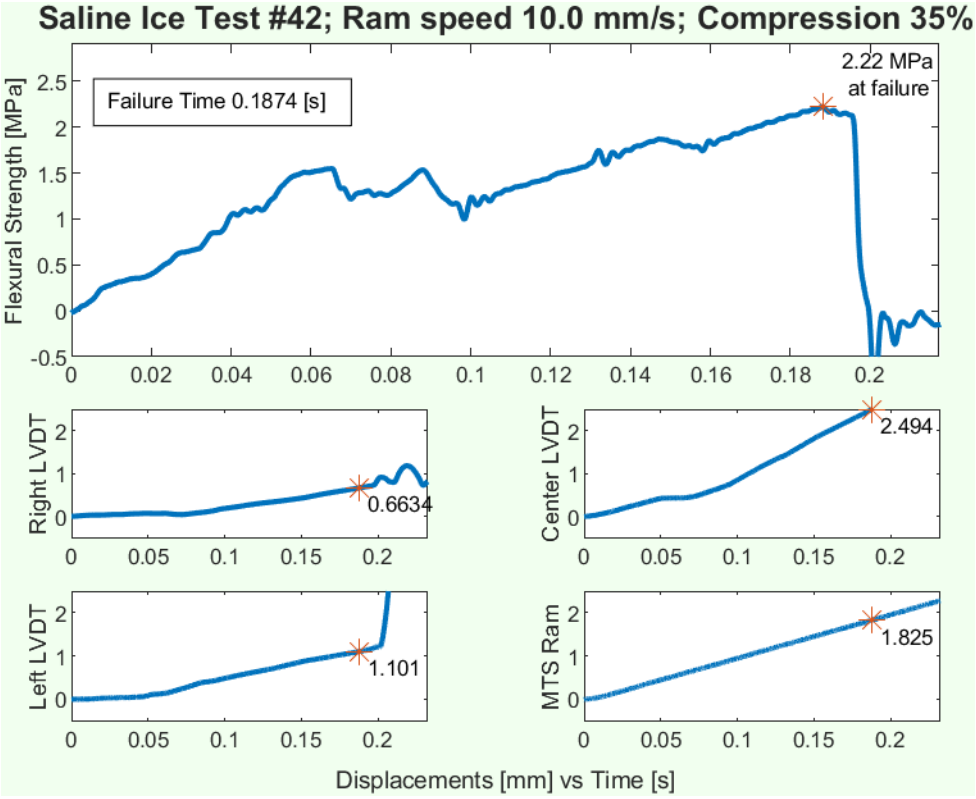
Saline Ice Test #42; Ram speed 10.0 mm/s; Compression 35%
Failure Time 0.1874 [s]
2.22 MPa
at failure
Flexural Strength [MPa]
Right LVDT
0.6634
Center LVDT
2.494
Left LVDT
1.101
MTS Ram
1.825
Displacements [mm] vs Time [s]

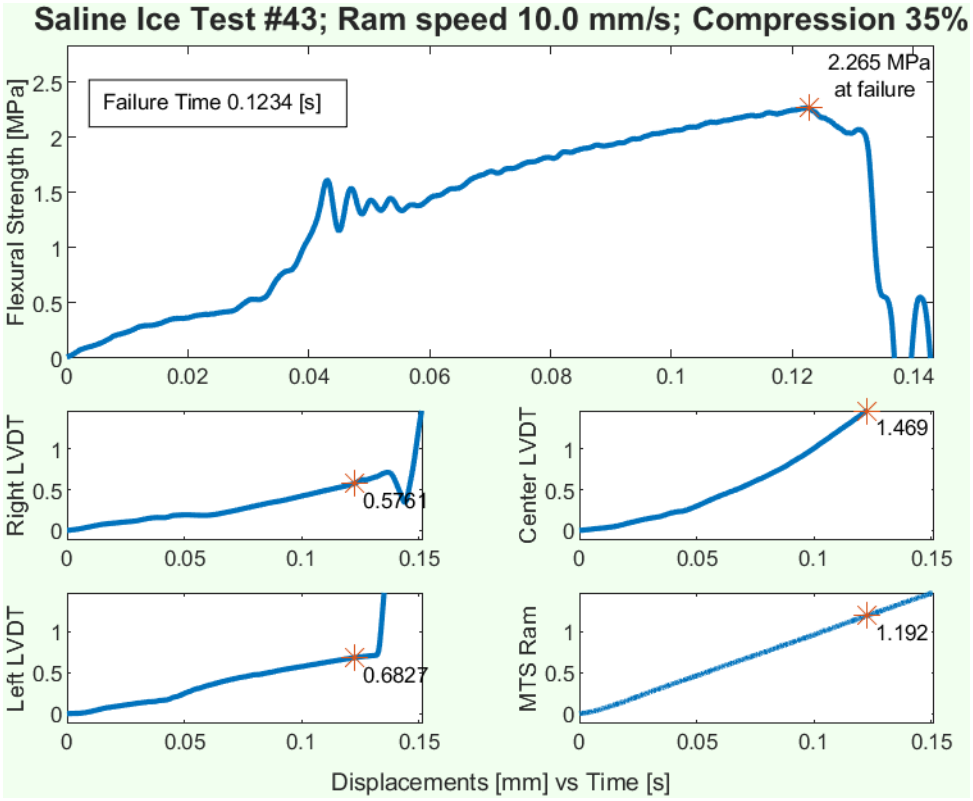
Saline Ice Test #43; Ram speed 10.0 mm/s; Compression 35%
Failure Time 0.1234 [s]
2.265 MPa
at failure
Flexural Strength [MPa]
Right LVDT
0.5761
Center LVDT
1.469
Left LVDT
0.6827
MTS Ram
1.192
Displacements [mm] vs Time [s]

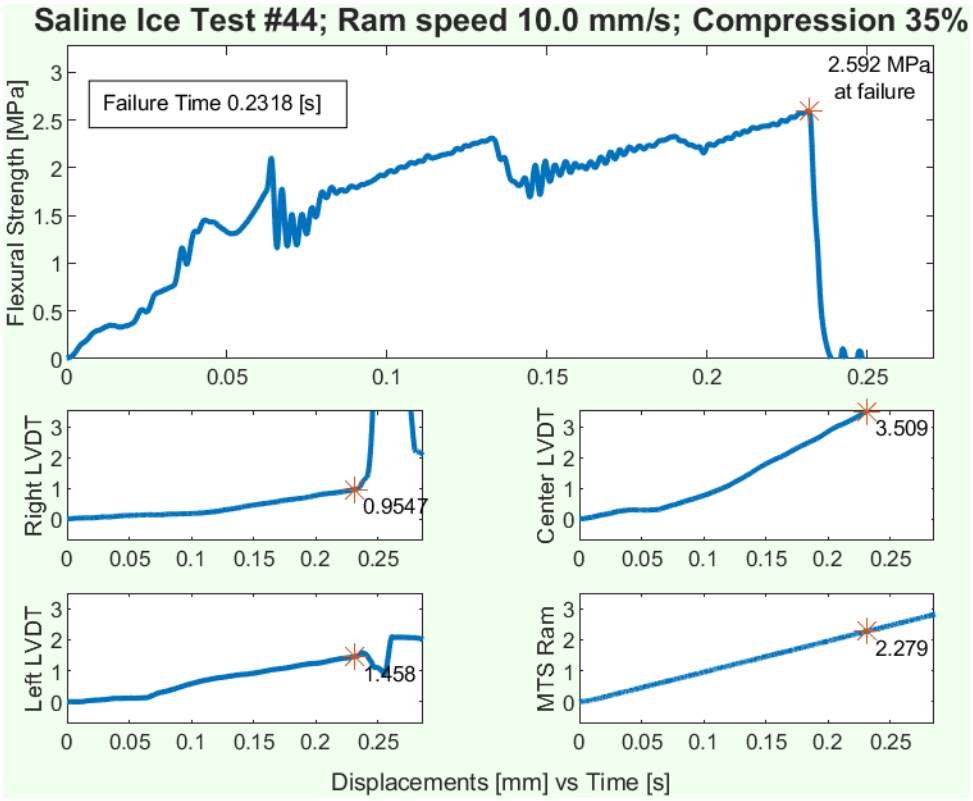
Saline Ice Test #44; Ram speed 10.0 mm/s; Compression 35%
Failure Time 0.2318 [s]
2.592 MPa
at failure
Flexural Strength [MPa]
Right LVDT
0.9547
Center LVDT
3.509
Left LVDT
1.458
MTS Ram
2.279
Displacements [mm] vs Time [s]

Appendix E - Additional Plots and Analysis

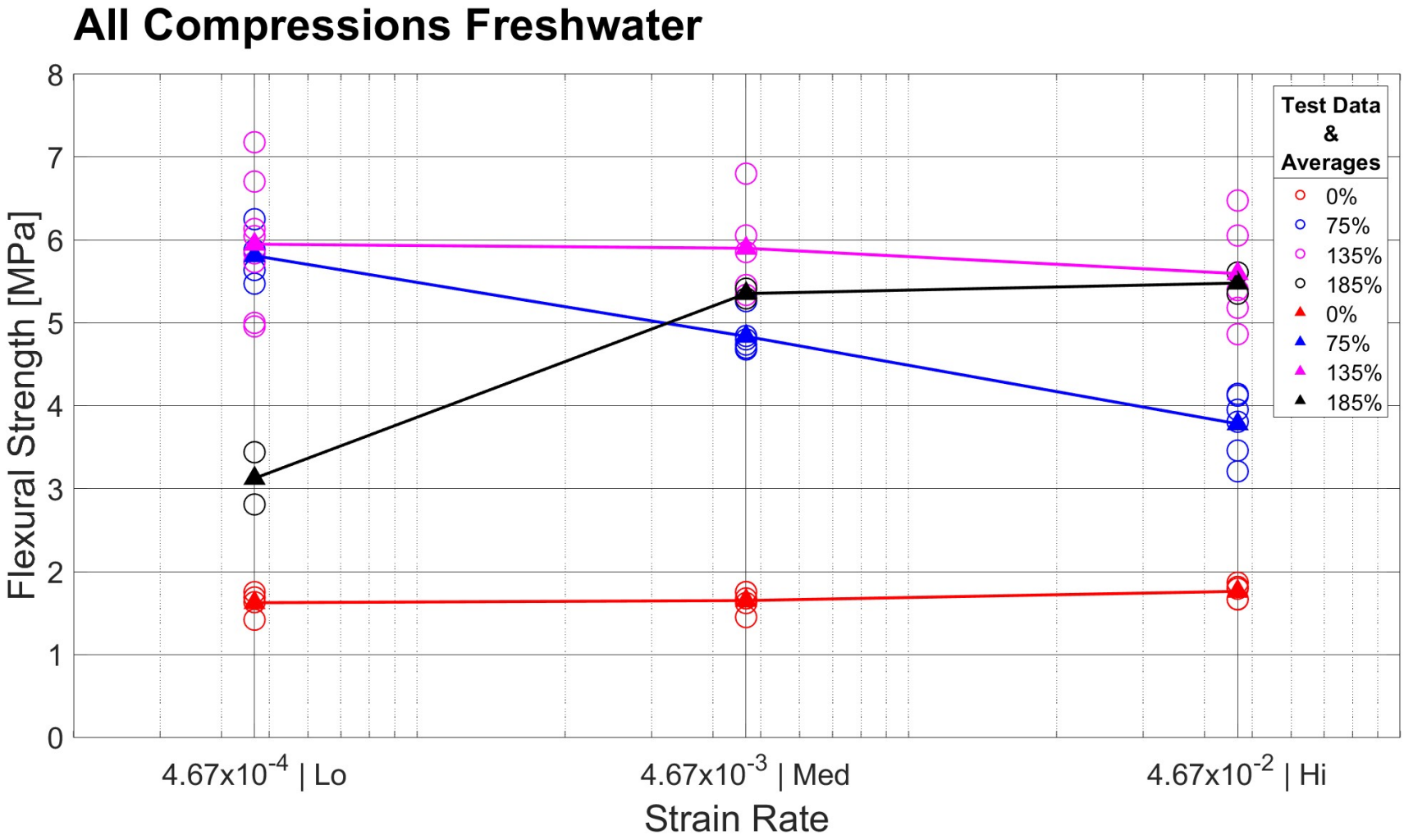

Figure E 1- Individual data points of all freshwater apparent flexural strength tests plotted against strain rates for all compression levels along with their averages.

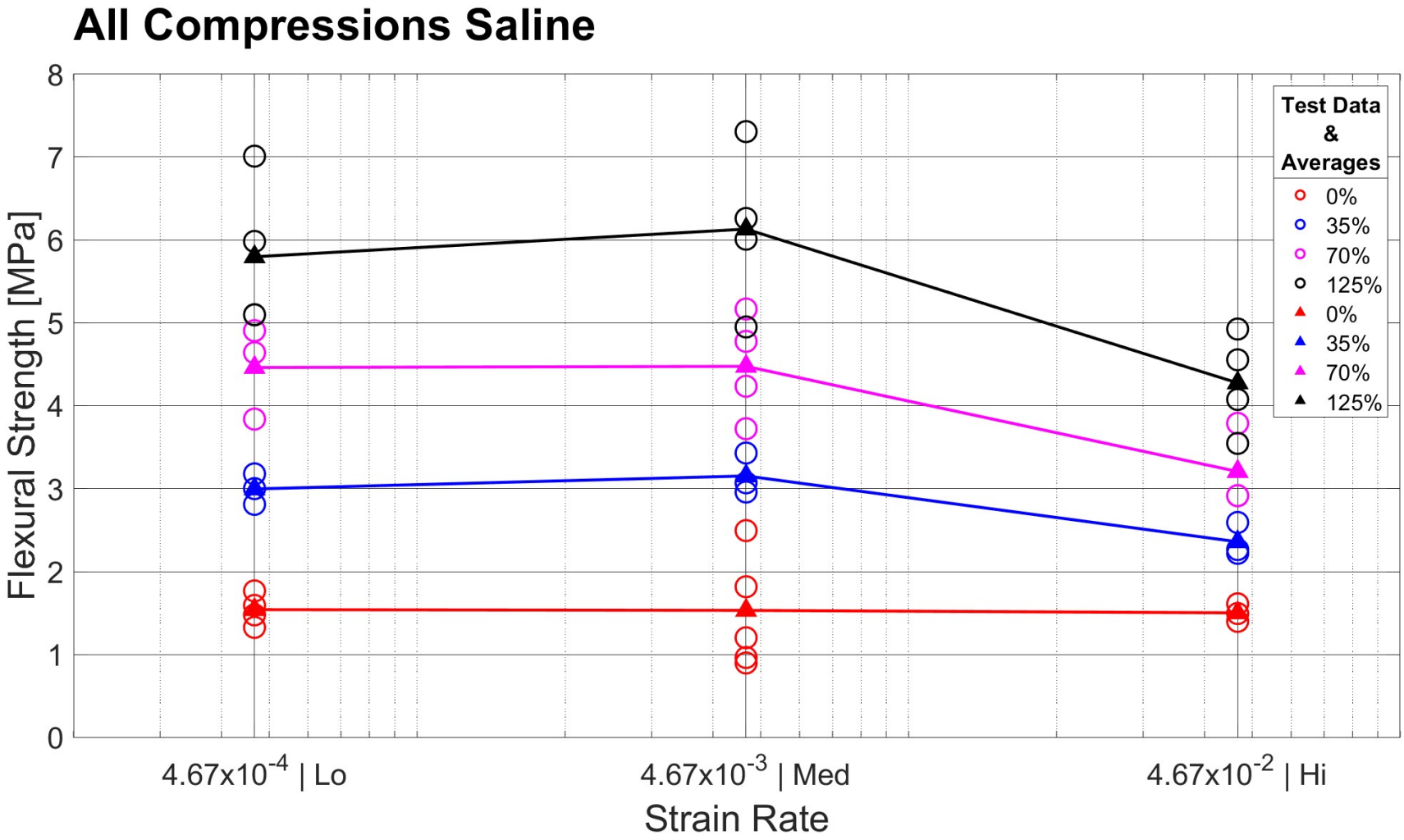

Figure E 2 - Individual data points of all saline apparent flexural strength tests plotted against strain rates for all compression level along with their averages.

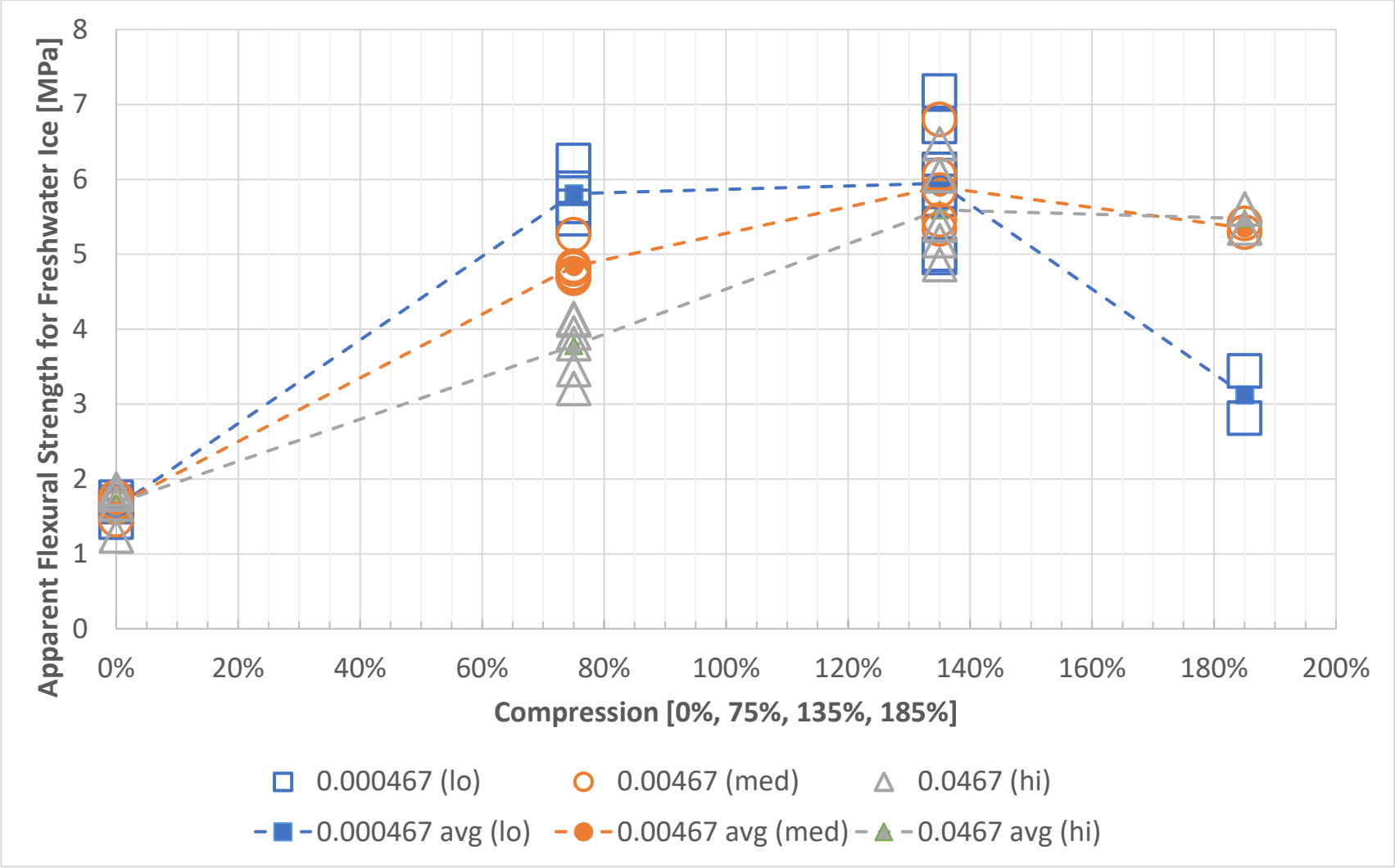

Figure E 3 - All data points and their averages for apparent flexural strength of freshwater ice tests plotted against compression levels for all strain rates.

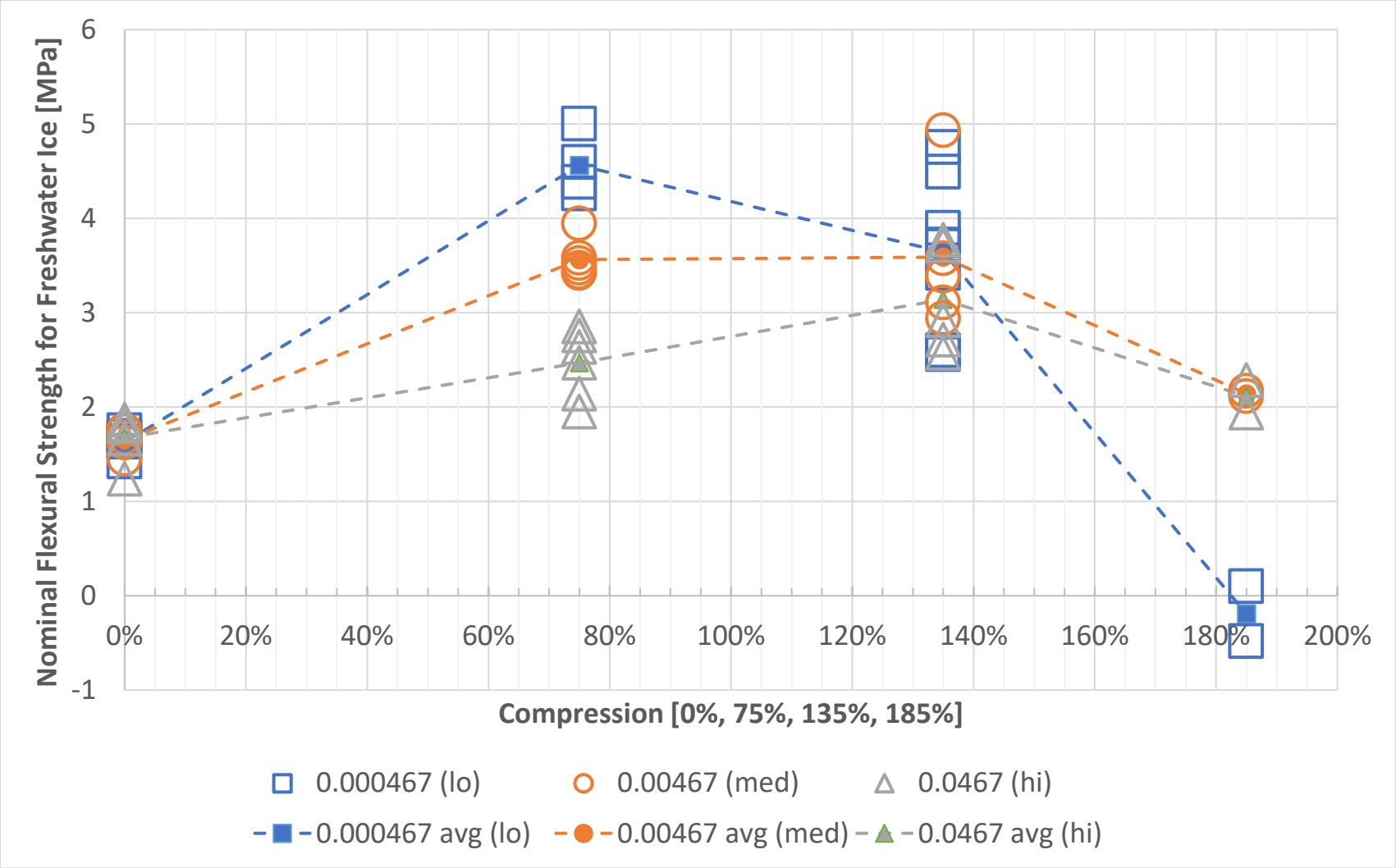

Figure E 4 - All data points and their averages for nominal flexural strength of freshwater ice tests plotted against compression levels for all strain rates.

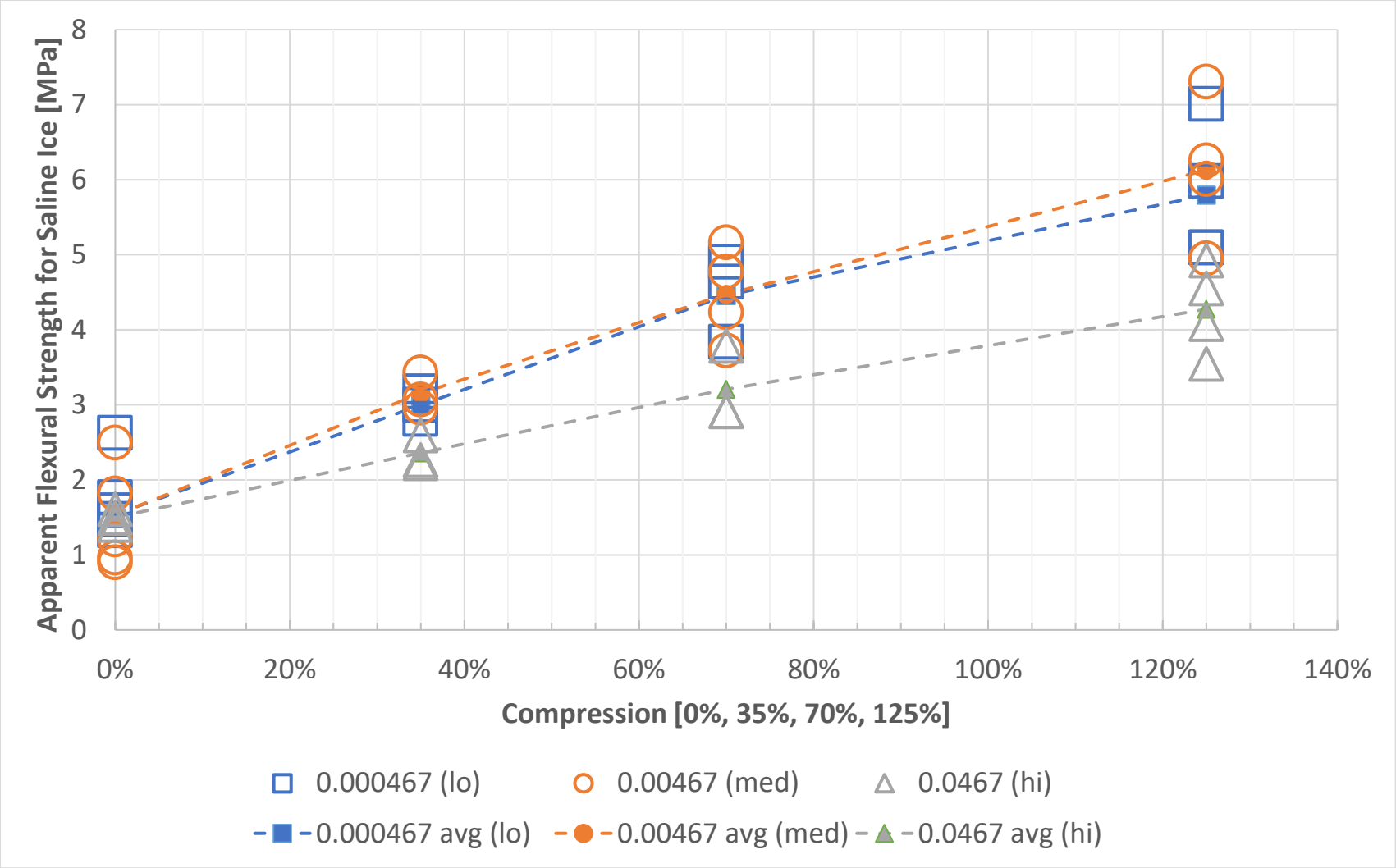

Figure E 5 - All data points and their averages for apparent flexural strength of saline ice tests plotted against compression levels for all strain rates.

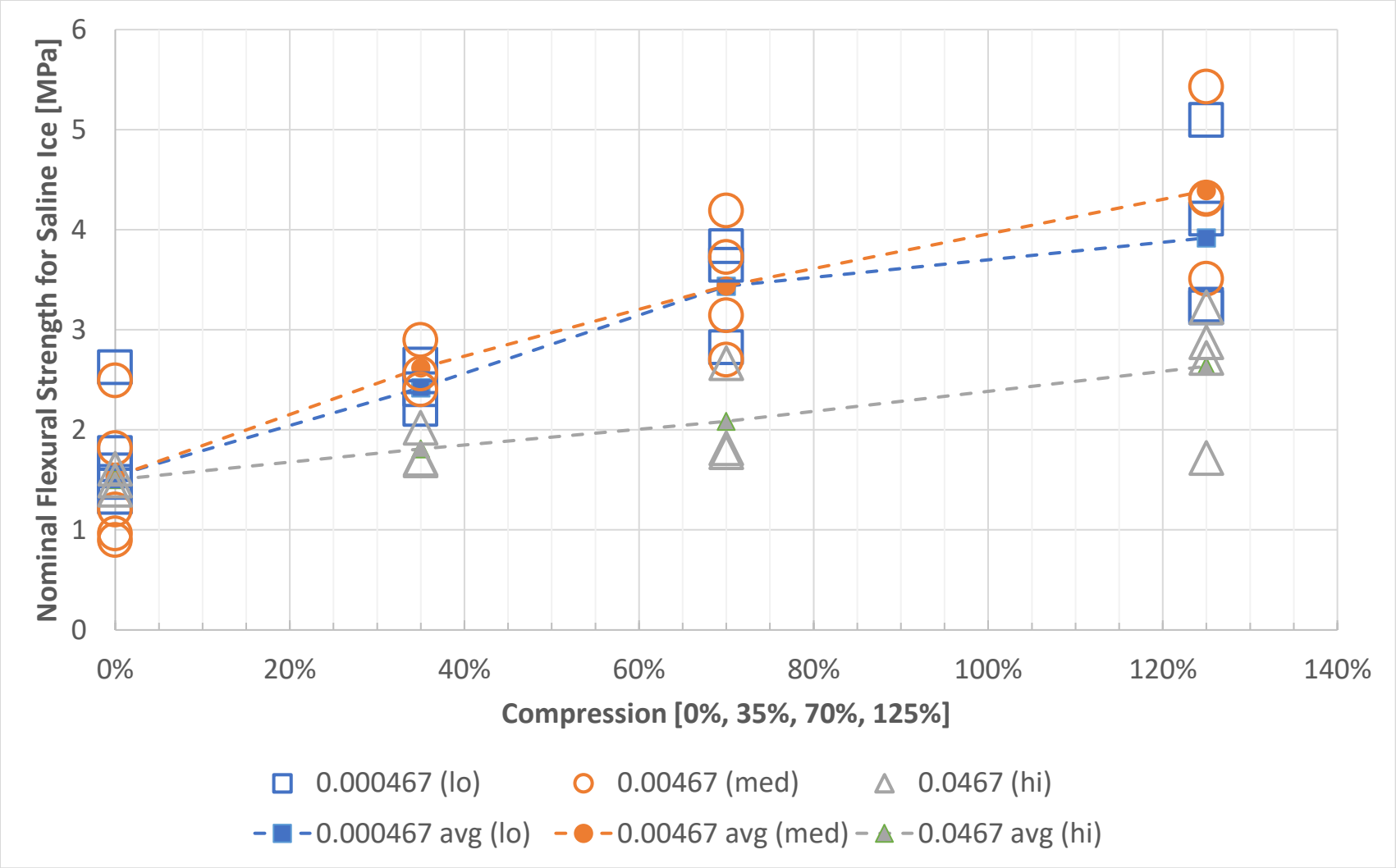

Figure E 6 - All data points and their averages for nominal flexural strength of saline ice tests plotted against compression levels for all strain rates.

Table E 1 - Buckling load calculations for ice beam dimensions used in testing.

End Conditions	*k*	*n*
Fixed-fixed	1	1
Fixed-pivot	0.7	2
Pivot-pivot	0.5	4

Johnson: $\sigma_{cr_J} = S_y - \frac{S_y^2}{4\pi^2 E}\left(\frac{l_e}{r_g}\right)^2$

Young's Modulus	**E**	9000000000	Pa	
width	**b**	0.0508	*m*	(2 in.)
depth	**h**	0.0254	*m*	(1 in.)
area	**A**	0.00129032	*m^2*	(2 in.^2)
length	**L**	0.2	*m*	(200 mm)
moment of inertia	**I**	6.9372E-08	*m^4*	(bh^3)/12
radius of gyration	**r**	0.00733235	*m*	sqrt(I/A)
Max compressive load	**Fcy**	8202	*N*	Compressive failure
Compressive Strength	**Sy**	6356749	*Pa*	Fcy/A
Transition Slenderness Ratio	**Tsr**	167	-	sqrt(2E(pi^2)/Sy)
Slenderness Ratio	**SR**	27	-	L/r

		k		
		Fixed-Fixed	**Fixed-Pivot**	**Pivot-Pivot**
	Pa	**1**	**0.7**	**0.5**
F buckling [N]	9,000,000,000	8,093	8,149	8,175

Transition Slenderness Ratio:

$$\left(\frac{l_e}{r_g}\right)_{trans} = \sqrt{\frac{2\pi^2 E}{S_y}}$$